DESIGN AND CHARACTERIZATION OF ZEOLITE MEMBRANES FOR FLUID SEPARATION

ISLAM HUSSAIN

Doctor of Philosophy

ASTON UNIVERSITY

July 2006

Aston University

Design and Characterization of Zeolite Membranes for Fluid Separation

Islam Hussain

Doctor of Philosophy 2006

Thesis Summary

Experimental and theoretical methods have been used to study zeolite structures, properties and applications as membranes for separation purposes. Thin layers of silicalite-1 and Na-LTA zeolites have been synthesised onto carbon-graphite supports using a hydrothermal synthesis procedure. The separation behaviour of the composite membranes was characterized by gas permeation studies of pure, binary and ternary mixtures of methane, ethane and propane. The influence of temperature and feed gas mixture composition on the separation and selectivity performance of the membranes was also investigated. It was found that the silicalite-1 composite membranes synthesised onto the 4 hour oxidized carbon-graphite supports showed the most promising separation behaviour of all the composite membranes investigated.

Molecular simulation methods were used to gain an understanding of how hydrocarbon molecules behave both within the pores and on the surfaces of silicalite-1, mordenite and LTA zeolites. Molecular dynamic simulations were used to investigate the influence of temperature and molecular loadings on the diffusional behaviour of hydrocarbons in zeolites. For mixed component simulations it was found that molecules of similar sizes (methane/ethane and propane/ethane) underwent a diffusional reversal role as the loading was increased. This unique behaviour observed for the first time is attributed to both the size entropy and coupling effect between diffusing species.

Both hydroxylated (surface termination with hydroxyl groups) and non-hydroxylated silicalite-1 and Na-mordenite surfaces were generated. For both zeolites the most stable surfaces correspond to the {010} surface. For the silicalite-1 {010} surface the adsorption of hydrocarbons and molecular water onto the hydroxylated surface showed a favourable exothermic adsorption process compared to adsorption on the non-hydroxylated surface. With the Na-mordenite {010} surface the adsorption of hydrocarbons onto both the hydroxylated and non-hydroxylated surfaces had a combination of favourable and non-favourable adsorption energies, while the adsorption of molecular water onto both types of surface was found to be a favourable adsorption process.

Key Words: Alkanes, Carbon-graphite, Separation, Molecular simulation, Microporous.

TO

MY WIFE

AND MY CHILDREN

ACKNOWLEDGEMENTS

I wish to express my deepest gratitude and sincere thanks to my supervisor Dr James O Titiloye for his supervision, valuable guidance and constant encouragement throughout the duration of this work.

I am also deeply grateful to Professor Steve Parker for making time in his busy schedule to teach me the potential applications of the METADISE code and for sharing his expert knowledge.

I also acknowledge the DTG funding and support from the School of Engineering and Applied Science, Aston University and UK EPSRC for funding.

Contents

List of Tables

List of Figures

Chapter 1: Introduction

Chapter 1: Introduction

1.0 General description of zeolites

Zeolites are hydrated crystalline alumnio-silicate materials that were first recognized as a new type of mineral in 1756 by A. F. Cronstedt a Swedish mineralogist. The word "zeolite" was derived from the Greek words Zeo and Lithos meaning to boil and a stone. The interest in zeolites started in the late 1930's when the modern founder of zeolite chemistry Professor R. Barrer began the characterization of zeolite structure and chemistry and thus confirmed the molecular sieving properties of these microporous materials. Today more than 200 synthetic zeolite types and 50 natural zeolites are known and owing their unique molecular sieving properties to their uniform pores with diameters up to 20 nm. The classification of zeolites follows established procedures with an identification code of three letters used by the International Zeolite Association (IZA).

The zeolite framework consists of SiO_4 and AlO_4 tetrahedra primary building units linked together by the sharing of oxygen atoms (1). The AlO_4 results in a net negative charge, which is balanced by the inclusion of a cation. This linking of tetrahedra results in the formation of well defined distinct of 1, 2 or 3 dimensional channel systems that are occupied by cations and adsorbed water molecules. These cations are mobile and can be exchanged by other cations and the adsorbed water can be removed leaving behind intact crystalline channels. In general hydrated zeolites can be represented by the formula:

$$M^{+n}_{x/n}\left[(AlO_2)x(SiO_2)y\right].wH_2O \tag{1.1}$$

where M is the cation of valence n, w is the number of water molecules and y/x is the Si to Al ratio in the structure.

The stability of zeolites in acid environments is dependent on the Si/Al ratio such that zeolites with a low Si/Al ratio are unstable in extreme pH environments compared to a high Si/Al ratio zeolites, which are stable (2). The exchange behaviour of cations within the channels/cavities is not only dependent on the locations, sizes, charges and concentrations of the hydrated cations but also on the temperature. Cation exchange can produce considerable change in various other properties of the zeolite, such as thermal stability, adsorption behaviour, and catalytic activity.

Isomorphous substitution of the framework atoms has resulted in an expansion of the zeolite molecular sieve family, resulting in the formation of different zeotypes such as aluminophosphates (AlPOs) and silicoaluminophosphates (SAPOs). Some of these new zeotypes have zeolite analogues, whereas others are unique. The addition of elements such as Mg, Ti, Mn, Co, Fe, or Zn into these structures has made it possible to generate metalloaluminophosphates and metallosilicoaluminophosphate analogues.

Also there has been recent interest in developing molecular sieves with pore diameters in the mesoporous range such as the MCM-41 (Mobile Crystalline Material), which is a silicate, obtained by a templating mechanism. By changing the length of the template molecule, the width of the channels can be controlled to within 20 to 100 Angstroms. These mesoporous silicate materials have large surface areas in excess of 1000 m^2/g and larger pore sizes, which permit high, permeate fluxes thereby extending the range of the potential applications.

1.1 Application of zeolites

Because of their unique structural properties, zeolites are used in a variety of applications with a global multi-billion dollar per year market involving over several million tonnes per annum (3). The three main properties of zeolites which have found wide spread uses in industry are namely catalysis, ion-exchange and adsorption/molecular sieving.

1.1.1 Catalysis

Zeolites are extremely useful as catalysts and can promote a broad range of catalytic reactions. Due to their microporosity and large internal surface areas the bulk of the reactions take place within their pores, which allows a greater degree of product and reaction control. The dimensions of the pores control the access to reactants and products and thus zeolites are often said to act as shape selective catalysts. In 1960, Weisz and Frilette (4) introduced the expression ''Shape-Selective Catalysis'' by demonstrating that Ca-LTA (CaA) zeolite could dehydrated 1-butanol at 260°C but not isobutanol. This observation showed that the conversion took place inside the microporous structure of the CaA zeolite (0.5 nm pore diameter), not available for the branched isobutanol due to its large kinetic diameter. An example of the acid catalyzed reactions is the ZSM-5 zeolite, developed by Mobil Oil with a high silica and low aluminium content. The substitution of an Si4+ with an Al3+ atom requires the presence of an added positive charge. When the positive charge is in the form of a proton (H+), the zeolite becomes very acidic. The catalytic activity of the ZSM-5 is due to this acidity and this has been found to be useful in the petroleum industry for hydrocarbon interconversion (5) and in the upgrading of crude oil and natural gas with zeolites used in fluid catalytic cracking (FCC), isomerisation reactions (6,7).

1.1.2 Adsorption and molecular sieving

The shape-selective properties of zeolites are the basis for their use in adsorption and separation processes via molecular sieving. The ability to preferentially adsorb certain molecules, while excluding others, has opened up a wide range of molecular sieving applications. Thus molecules with dimensions similar to that of the zeolites pores can enter whilst larger molecules will be rejected. Zeolite pores can be fine tuned by changing the size and number of cations in the pores thus effectively increasing or reducing the pore sizes of a given zeolite. Sometimes access into the pores is simply a matter of the size and shape of the molecules but in other cases the polarity of the molecules governs which molecules can enter. For example cation-containing zeolites are extensively used as desiccants due to their high affinity for water, where molecules are differentiated on the basis of their electrostatic interactions with the metal ions. This property has resulted in there use in separating alcohol water mixture and has been exploited commercially (8). Equally, hydrophobic silica zeolites preferentially adsorb organic solvents whilst totally excluding polar molecules. Due to this inherent ability to act as molecular sieves, zeolites have been used widely as membranes. A membrane can be described as a barrier, which is capable of separating fluid components through the direct action of a driving force such as concentration, chemical, electrical or pressure gradient. Zeolite membranes are a relatively new technology and are completely different from simple crystalline zeolite powders.

1.1.3 Ion exchange

The ease of ion exchange is related to the loosely bound nature of extra-framework metal ions in the zeolite. This property of zeolites is exploited in water softening, where alkali metals such as sodium or potassium in the zeolite are exchanged with calcium and magnesium ions from hard water. Many commercial washing powders, detergents and soaps thus contain substantial quantities of zeolite. Commercial wastewater containing heavy metals, and nuclear effluents containing radioactive isotopes can also be cleaned up using the ion-exchange properties of zeolites (9).

1.2 Zeolite synthesis

Zeolites are normally synthesized at hydrothermal conditions from basic reaction gels at temperatures between 60°C to 200°C under an autogeneous pressure and in the presence of a large excess of water.

Most of the highly siliceous zeolites are formed in the presence of an organic molecule, which initiates crystallization upon its addition to the reaction mixture. These molecules are termed templating agents. The most widely known templating agents are the tetramethylammonium (TMA), tetraethylammonium (TEA) and tetrapropylammonium (TPA) ions. These ions can be added to the synthesis reaction mixture as either hydroxides or bromides. A problem which is associated with template assisted synthesis is following crystallization the templating agent becomes trapped and immobilized within the zeolite channel network and thus effectively blocks the pores. This problem is typically overcome by calcination in either air or nitrogen at around 400°C to 700°C, which results in the decomposition of the templating agent leaving behind an intact zeolite channel system. The structure and properties of the zeolite product are highly dependent on the reactants used in preparing the reaction mixture, the type of cations or organic template and the conditions (temperature, pressure and duration) of the hydrothermal treatment. The fabrication of zeolites as membranes is very challenging and various synthesis approaches have been developed for membrane preparation.

1.2.1 Non-supported freestanding zeolite membranes

A dense zeolite membrane, with a surface free of defects (pin holes) with a thickness (<1 nm) would be an ideal candidate for molecular sieving applications. Such films have been grown on temporary supports like Teflon and cellulose or at the interface between two phases (10,11). The preparation of zeolite membranes following this route has not gained widespread use for the simple reason that self-supported zeolite membranes are extremely fragile.

1.2.2 Zeolite filled polymeric membranes

Another method of preparing zeolite-containing membranes is to embed zeolite crystals into a non-porous polymer matrix and thus forming a membrane. The use of this method of membrane preparation is very limited due to blockages of the zeolite pores by the polymer matrix resulting in diffusional problems and a reduction in the porosity and catalytic activity of the zeolite phase. Also gaps between the binder and zeolite or porosity in the matrix could introduce nonselective alternative diffusion pathways leading to poor separation performances. The main drawback of using these zeolite-filled polymeric membranes is that they have relatively low chemical and thermal stabilities, which can result in the decomposition and relative short life of the supporting polymer matrix if used in extremes of these conditions.

1.2.3 Supported (composite) zeolite membranes

The most widely used preparation method seems to be that of the so-called composite membranes. This method of membrane preparation is carried out via hydrothermal synthesis. The crystallization of a relatively thin zeolite layer onto the surface of a porous support results in the formation of the membrane. Materials which have been used a supports include ceramics, metals, glasses, carbon and porous alumina. Porous alumina has been the most popular choice for most of these preparations. The nucleation and crystal growth on the support can be self-induced or induced by a pretreatment of the support (seeding of the support) before the hydrothermal synthesis (12). Zeolite-coated composite membranes have also been prepared by a vapour phase deposition method called 'dry synthesis.' The zeolite layer in this case is prepared by conversion of a previously deposited silica or silica-alumina layer under joint action of vapors containing water and a structure-directing agent (13,14).

1.2.4 Zeolite membrane characterization and evaluation

Various techniques are available for the characterization of zeolites these include: X-ray diffraction (XRD), scanning electron microscopy (SEM), sorption capacity measurement (N2 adsorption) and Fourier transform infrared spectroscopy (FTIR). These techniques all reveal key properties of the zeolites and will be discussed further later in the thesis. The separation properties of the synthesized zeolite membranes in this work are evaluated by gas separations using both pure and mixed light alkane gas permeation experiments and are discussed further in chapter 4.

1.3 Hydrocarbon separations with zeolite membranes

The petrochemical industry is the producer of valuable hydrocarbons, chemical intermediates and plastics. The use of zeolite membranes has been recognized in these industries as a key technological improvement in the separation of light hydrocarbons as there is a continuing need to develop new processes for hydrocarbon separations (15,16). The key process that lies at the heart of the petrochemical industry is the steam-cracking unit. The steam cracker converts naphtha (a light gasoline fraction) into various high value hydrocarbon and various other chemical intermediates. The main driving force behind the entire reaction is a free radical mechanism and as a consequence this it is not a selective process and mixtures of products are formed.

Separating the mixture of products formed from the steam cracker has some major problems; the boiling points of the products formed are very low (Table 1.1) with many of them having very similar boiling points thus making separation very expensive and energy intensive. Distillation is the only reliable commercial technology used to separate such mixtures. A typical separation scheme for separation of the lighter alkanes (methane, ethane and propane) is shown in figure 1.1. Low temperature distillations are preformed at elevated pressures in traditional trayed fractionators. The separation scheme is highly heat integrated requiring three levels of refrigeration to achieve the low temperatures needed. A propylene refrigerant is used to achieve temperatures as low as – 40°C, an ethylene based refrigerant system is used to reach temperatures as low as – 100°C and an expansion of the product methane and hydrogen is used to reach the lowest temperature of –145°C. At this temperature a rough separation of the methane and hydrogen is achieved with a simple flash.

Distillation requires a phase change, which can only take place when the compounds being separated are close to their boiling points. In order to separate the mixture formed from the steam cracker it is necessary to raise the pressure of the products therefore increasing the boiling points of the components in the mixture, but a major problem with this is that it reduces the volatility differences of the products thus making distillation more difficult (171). Molecular sieve zeolite membranes can carry out separations of the cracked gases at temperatures well above their boiling points, this would help to dramatically reduce the amount of gas, which needs to be compressed.

Table 1.1 Main products from steam cracker (171)

Components	**Bpt (°C)**
Hydrogen (H_2)	-253
Methane (CH_4)	-161
Ethane (C_2H_6)	-88
Ethene (C_2H_4)	-104
Acetylene (C_2H_2)	-84
Propane ($CH_3CH_2CH_3$)	-42
Propene ($CH_3CH{=}CH_2$)	-48
Propadiene ($CH_2{=}C{=}CH_2$)	-23
But-1-ene ($CH_2{=}CHCH_2CH_3$)	-6
Butane ($CH_3CH_2CH_2CH_3$)	-1
Benzene (C_6H_6)	80

Figure 1.1 Conventional low-temperature cryogenic distillation process for light hydrocarbons (171)

For the successful development of zeolite membranes for separations of mixtures of light hydrocarbons, information is required on both the diffusion and sorption of pure components, and their mixtures both on the surfaces and within the channels of the zeolites. Experimental and theoretical methods can be used as tools to probe the sorption and diffusion behaviour of light hydrocarbons in zeolites. The understanding of the interactions between mixtures of light hydrocarbons and zeolite channels is important from an industrial viewpoint as such mixtures are currently separated by cryogenic distillation (as mentioned above). The large capital and operating costs associated with these processes (17,18) are the motivation for the ongoing research on alternative separation methods. Alternative adsorption processes with zeolites (e.g. silicalite-1) as adsorbents (19,20) have already been developed but the real benefits will be gained with using zeolites as membranes which will result in continuous separations. The knowledge gained on the behaviour involving both light hydrocarbons and zeolites could result in zeolite membranes being used to complement or even replace current industrial hydrocarbon separation processes resulting in improvements in the processes overall efficiency leading to major financial and environmental benefits.

Zeolites play many roles in industry as discussed earlier but the most important role is based on the adsorption of molecules within their pores, which is key in their uses as catalysts and molecular sieves. To better understand this behaviour a clear picture of both the macro and microscopic mechanism of mass transport through zeolites is needed. Figure 1.2 represents a proposed 5 step model (21,22):

1. Adsorption from the bulk gas phase to the external surfaces of the zeolite.
2. Mass transport from the external surfaces into the zeolite pores
3. Intra crystalline zeolite diffusion (Molecular jumps from adsorption sites to adsorption sites).
4. Mass transport out of the zeolite pores to the external surface.
5. Desorption from the external surface to the bulk gas phase.

Figure 1.2 Mechanism of mass transport through zeolites (21,22)

The above 5 point model is generally applicable to molecular sieving but can also be applied to catalytically active zeolites with a minor modification to step 3 where the adsorption sites are catalytically active and promote reactions. Once the reaction is complete the products then follow steps 4 and 5.

Knowing where a particular molecule in a mixture prefers to adsorb both on the surface and within the zeolite channel network can be used to determine how a mixture should be separated. For example if both molecules are found to adsorb at similar sites or in similar quantities then it may be necessary to change the zeolite type or to use a different method to separate the mixture as the selectivity of the membrane would be poor.

In small pores (relative to the size of the adsorbed molecules) the interaction between the molecule and the pore is the dominant factor controlling the adsorption. It is important to understand the behaviour of different molecules within the zeolites porous network, but what is the best way to investigate the adsorbate-adsorbent (alkane-zeolite) interaction behaviour? The answer to this question on a microscopic scale is molecular simulations and for the macroscopic scale membrane gas permeation experimentations.

1.4 Simulations versus experimentations

There are different types of simulation techniques available to use for investigating adsorption behaviour in zeolites. In this work both molecular dynamic and static simulations have been used. Both methods depend on models which approximate the system that is being studied (these are discussed further in Chapter 3). Each method has its strengths and weaknesses and a degree of caution must be taken when using molecular simulations to ensure that the simulation is accurate and of a suitable time length to obtain relevant data. The diffusional behaviour of adsorbed molecules though the pores of a zeolite are obtained using molecular dynamics simulations, and the global minimum adsorption sites and energies are obtained from static simulations. The information gained from the simulations can then be compared to and verified by experimentation by firstly synthesizing the zeolite in question as a membrane then characterizing and evaluating its separation behaviour for gas mixtures. In general simulations can be used as a tool to screen candidate zeolites for fluid separations in a cost effective manner whereas experimentation is used to verify the separation behaviour observed from the simulations.

1.5 Scope and objectives of this work

The objectives of this research fall into three main areas: The molecular simulation and modelling of zeolite membranes. The synthesis of zeolite layers onto a stable platform resulting in a composite zeolite membrane and finally the subsequent characterization of the zeolite membrane. Further detail on each objective is provided below.

The synthesis of zeolite membrane: the objective here was to carry out the synthesis of both silicalite-1 and Na-LTA defect free zeolite layers onto carbon graphite supports using a standard hydrothermal synthesis method. The effect of surface modification of the carbon-graphite support by chemical oxidation on the membrane synthesis was investigated (chapter 4).

The characterization of the synthesised zeolite membranes: The main focus of this work was to characterization of the synthesized membranes by various experimental techniques including Scanning electron microscopy (SEM), X-ray diffraction (XRD), Fourier transform infrared spectroscopy (FTIR), Thermogravimetric analysis (TGA), Nitrogen sorption capacity measurements and X-ray photoelectron spectroscopy (XPS) (chapter 4). This was then followed by determination of the composite membranes separation behaviours towards binary and ternary mixtures of methane, ethane and propane hydrocarbons. The effect of feed gas composition and temperature on the separation behaviour of the membranes was also investigated (chapter 5).

Molecular simulation modeling of the zeolites: The objective of this work was to use both molecular dynamic and static simulations to obtain information on the microscopic behaviour of the three alkanes (methane, ethane and propane) both within the pores and on the surfaces of the zeolites. The most stable zeolite crystal surface configurations were generated and investigated along with preferential sites of adsorption on both the surfaces and within the zeolite channels (chapter 6). The effect of loading and temperature on the diffusional behavior of mixtures of the three alkanes was also investigated within the pores of silicalite-1 (chapter 7).

The thesis starts with previous related work and literature review in chapter 2. Chapter 3 discusses the theoretical methods behind the work. The synthesis and subsequent characterizations of the silicalite-1 and Na-LTA (NaA) composite zeolite membranes is reported and discussed in chapter 4. While in chapter 5 the separation behaviour of the composite membranes is reported and discussed. Chapters 6 and 7 focus on the molecular simulations of zeolite adsorbate systems with chapter 6 focusing on static simulations of linear alkane adsorption on both the surface and within the bulk zeolite structure. While in chapter 7 the results of the molecular dynamic simulation studies of linear alkane diffusional behaviour within silicalite-1 are reported and discussed. The conclusions of this work and future recommendations are found and reported in chapter 8.

Chapter 2: Literature Review

2.0 Chapter 2: Literature Review

2.1 Zeolite membranes

2.1.1 Introduction

Zeolite membrane are a new emerging technology that promises to deliver separation processes that are more compact, less energy and capital intensive (23,24). They have superior thermal, mechanical and structural stabilities as well as chemical and solvent resistance. Zeolite membranes also allow regeneration through the thermal/oxidative removal of adsorbed species at high temperatures and therefore have longer life expectancies than their polymeric counterparts.

A great deal of progress in the field of zeolite membrane synthesis has been made since Suzuki filled the first patent for the synthesis of zeolite membranes which was accepted in 1987 (25). Since then there has been a wealth of papers and various reviews in the literature on zeolite membranes (Bowen et al. (26), Caro et al. (12), and Lin et al. (27)) all summarizing the significant progress made to date in the synthesis of microporous zeolite membranes. Very recently McLeary et al. highlighted the progress and prospects of zeolite catalytic membrane reactors (24).

All the reviewers raised a number of points on the issue of bringing zeolite membranes and reactors to commercial applications and there were a number of factors which they all agreed needed to be further explored:

1. The synthesis of membranes with defect free preferentially oriented, thin layers of zeolites resulting in high selectivities and permeabilites .

2. Reproducibility and long-term stability of membrane performance.

3. Synthesis of membranes with sufficiently small pores (< 0.3 nm "Ultramicroporous") to allow separation on the basis of size exclusion, and without intercrystalline pores (for potential hydrogen separations).

4. The sealing of the membranes at high-temperatures and pressures.

5. Scaling-up of membrane modules, requiring the ability to prepare large defect-free membranes at reasonable costs.

6. Reducing the current cost of membranes and membrane modules.

7. Clarification of multicomponent transport and separation behaviour through zeolitic and non-zeolitic pathways in the membranes at industrially relevant operating conditions.

The MFI type zeolite membranes (silicalite-1, ZSM-5) supported on either flat or tubular supports, have been the main focus of the current research efforts and have been investigated extensively for application in gas separation and pervaporation(12,26,28,29). An important characteristic of these is that they have an irregular thermal behaviour and often show positive volume expansion coefficients at low temperature and negative volume expansion coefficients at higher temperatures (12,30,31). Thus when synthesising a supported (composite) membrane the choice of support used must take this into account. Zeolites membranes have been successfully synthesized and supported on different materials such as ceramics or metals (31-35), polymers and carbon materials (30,36-38) using a variety of synthesis procedures. Of the supports the most widely used are the ceramic and metallic supports, although each of the supports have drawbacks. The polymer supports have relatively low thermal and chemical stabilities and are often unstable in high pressure drop environments leading to decomposition and a relatively short life span for the membrane. Although the ceramics are much more stable they are brittle and very expensive. The main drawbacks in using ceramics or metals as supports is in the growth of zeolite crystals in the pores of the support, which can give rise to significant loss in the membrane permeability and possible dissolution of the support into the synthesis solution resulting in a non homogeneous zeolite phase (30,39). Microporous carbon-graphite materials are also very promising for use both as membranes and support materials due to their high thermal stability in a non-oxidizing inert atmosphere. They have relatively low thermal expansion coefficients compared to ceramic and metallic supports (36) and are inexpensive when compared to other support materials (40) and exhibit hydrophobic properties (41).

Small pore zeolites such as the LTA type zeolites have also attracted the focus of research efforts due to their small pore sizes, which would in principle, result in the effective molecular sieving of molecules with molecular diameter smaller than 0.41 nm (4.1 Angstroms). Few reports exist for the successful application of the LTA zeolite membranes to gas separation. Most authors report selectivities similar to those expected for Knudsen flow through the membrane - an indication of the presence of significant intercrystalline defects. Yet despite these findings the LTA type zeolites have an inherent ability (due to there hydrophilic properties) to separate with superior selectivities aqueous organic mixtures. For this reason the Na-LTA zeolite membrane was the membrane of choice in the world's first large-scale pervaporation plant, which produces 530 l/h of solvents such as EtOH, IPA, MtOH, etc at less than 0.2 wt.% of water from 90 wt.% solvent at 120 °C. The plant was put into operation by Mitsui Engineering and Shipbuilding Co. Ltd in 1999 and has been running since (8). The plant is equipped with 16 modules, each of which consists of 125 pieces of Na-LTA zeolite membrane tubes. The superior water separation selectivity (>10000) of these membranes is based on the hydrophilic properties of the Na-LTA zeolite membrane and not on molecular sieving (26).

This behaviour was observed by Okamoto et al. (42) who prepared Na-LTA membranes which gave H_2/SF_6 separation selectivities almost the same as the Knudsen separation selectivity, highlighting the presence significant of non-zeolite pores in the membranes. In spite of this finding their membranes showed superior separation selectivities as high as 18,000 and 16,000 for the dehydration of aqueous propan-1-ol and ethanol respectively. This suggested that for the dehydration of organics a defect free membrane was not necessary.

2.1.2 Synthesis of zeolite membranes

Two well known procedures exist for the synthesis of zeolite membranes or thin films onto a support. The first procedure in known as in-situ synthesis, this basically involves a one-step hydrothermal synthesis where the support is placed in direct contact with the synthesis precursor solution. The second type of synthesis procedure is known as secondary or seed assisted growth in which an existing zeolite phase (seed crystals), is attached to the support followed by hydrothermal growth of the applied seeds to form a continuous layer.

2.1.2.1 In-situ synthesis

The major problems encountered during in-situ synthesis is ensuring that the support is sufficient covered with nucleation sites and ensuring good contact of the precursor synthesis solution with the support occurs. If this is not the case then this gives rise to poor quality membranes or larger film thickness than required to ensure complete coverage of all defects. A large amount of the research work has been concentrated on methods to ensure that uniform nucleation takes place on the support. The ability of the zeolite phase to adhere to the support surface during synthesis is strongly influenced by the hydrophilicity of the support surface (e.g. the surface oxygen content). Modification of the support surface by chemical oxidation would increase the number of surface hydroxyl groups therefore resulting in more nucleation sites. Berenguer-Murcia et al. (30) reported the growth of a wide variety of silicalite-1 and ZSM-5 membranes on macroporous carbon discs. The surface oxidation of the carbon support was identified as one of the key parameters for a successful membrane synthesis. In a recent report Van den Berg et al. increased the number of surface defect sites and hydroxyl groups and thus the hydrophilicity of a TiO_2-coated support by using UV-radiation. It was concluded a uniform monolithic LTA film was grown on the support (43,44).

Controlling and restricting the nucleation and growth of the zeolite phase to the support and not the bulk synthesis solution can also be used to successfully synthesis zeolite membranes. Yamazaki and Tsutsumi (45) used a plate heater to heat only the support while the solution was kept static. This resulted in zeolite membrane formation without any powder formation in the bulk solution. The vapor phase transfer synthesis method is a variation of the in situ synthesis method and basically consists of two steps: covering the support with a synthesis gel and crystallization of the dried gel under autogeneous pressure. Since one of the nutrient sources is limited to the support surface, zeolite membrane formation would also be limited to the support surface (46,47).

2.1.2.2 Seed assisted synthesis

For the successful synthesis of a thin, defect-free zeolite film using the two-stage synthesis method the application of a thin, uniform and continuous layer of seed crystals to the support is crucial. The simplest and often used method is to apply seed crystals to the substrate with mechanical rubbing (48,49). This technique was used by Mitsui Engineering and Shipbuilding Corp in the fabrication of tubular LTA, FAU and MFI membranes (50). Very recently Zhang et al. (51,52) synthesized both silicalite-1 and Na-LTA onto carbon supports using a two step synthesis procedure involving seeding of the support followed by hydrothermal synthesis. It was concluded that the resultant composite zeolite/carbon membranes had good permeance properties.

The seed assisted synthesis method appears to be simple however, it is quite difficult to obtain a continuous and even seed layer. Various authors have applied seed crystals to the support by dipcoating the support in a colloidal suspension of sub μm sized zeolite crystals, followed by drying at room temperature and calcination in order to fix the crystals to the support surface. This process is often repeated a few times in order to ensure a sufficiently high coverage of the support with zeolite seed crystals (53,54). Electrostatic attraction could also be used to limit the number of times the dipcoating procedure has to be repeated. This involves charge modification of the support surface by adsorption of an anionic or cationic polymer, which would result in the attachment of the seeds to the surface of the support by electrostatic attraction (55,56). The electrostatic attraction process generally achieves a high coverage of the substrate with well-adhered particles and is one of the most-effective techniques developed to date for seed crystal deposition.

Various other techniques have been used to attach the zeolite phase to the support surface these include:

Electrophoretic deposition (EPD), which can be used to coat supports with charged particles from colloidal suspension. Zeolite particles formed during hydrothermal synthesis assume a net charge due to electrical double layer effects and thus are attracted to the charged support surface. With this technique the pre-treatment of the support is eliminated. Berenguer-Murcia et al. (57) reported a novel seeding method, which eliminated the need for oxidation of the carbon support. The method involved the electrophoretic deposition of silicalite-1 nano-crystals onto the support resulting in a homogenous coating of seeds leading to a defect free and well inter-grown silicalite-1 layer. Oonkhanond et al. (58) also made use of this principle to attract ZSM-5 particles to the surface of a porous alumina tube in order to obtain a 10–15 μm thick, continuous layer. Mohammadi and Pak (59) synthesized a LTA zeolite membrane from Kaolin that was electrophoretically deposited on a cylindrical anode and treated hydrothermally. Shan et al. (60) in there work were able to prepare zeolite films through electrophoretic deposition in a non-aqueous medium. It was concluded that the electrophoretic deposition voltage/time and concentration of suspension, could be used to adjust the film thickness. Very recently Berenguer-Murcia et al. (38) successfully synthesised a zeolite membrane reactor. They deposited a layer of catalytically active metallic platinum onto the surface of a carbon support under potentiostatic conditions. Following this electrophoretic deposition was carried out to attach a layer of zeolite seeds following which a standard hydrothermal synthesis was carried out in order to grow continuous zeolite films on top of the catalytically active species.

2.1.2.3 Microwave synthesis

Microwave synthesis compared with conventional hydrothermal synthesis routes for zeolite membrane formations has the advantages of a very short synthesis times, small zeolite particle size, narrow particle size distribution and high purity. All of these characteristics make microwave synthesis a promising method for rapidly synthesising high quality zeolite membranes. Despite all the above-mentioned advantages only few studies on the use of microwave for zeolite membrane synthesis have been reported. These include the works of Xiao et al. (61) who successfully synthesised Na-LTA membranes on to alpha alumina supports by in-situ microwave heating. It was concluded a synthesis time of only 15–20 min was required for synthesis of very stable and dense membranes. Very recently Yang et al. (62) developed a new method called "in-situ aging - microwave synthesis" for zeolite membrane synthesis. High quality LTA membranes were successfully microwave-synthesized without the need for seeding of the support. It was found that in-situ aging temperature, in-situ aging time and microwave heating time all had impacts on the properties of the synthesized membranes, of which, in-situ aging temperature and microwave heating time were the most significant parameters.

2.1.2.4 Template free synthesis

In synthesis of MFI-type zeolite membranes by the above methods, an organic templating agent is normally used such as tetrapropylammonium (TPA). The templating agent is used in the synthesis for structure directing leading to the formation of the zeolite crystals. A result of this is the pores of the zeolite are effectively blocked by the templating agent and thus a calcination stage is required to remove the templating agent and thus open the pore structure of the zeolite membrane. During the calcination stage, micro cracks tend to form in the membranes due to thermal stress caused by the difference in thermal expansion between the zeolite film and the support as discussed previously and by changes in lattice parameters of the zeolite crystals as a result of the template removal (63).

The synthesis of zeolite membranes without the use of templating agents would result in the elimination of the calcination stage and thus elimination of micro cracks and defects. Various attempts have been made to synthesis MFI-type zeolite membranes without the templating agents. Mintova et al. (64) reported the preparation of template free ZSM-5 films on dense quartz supports. The supports were surface modified with a cationic polymer following which a mono-layer of silicalite-1 seed crystals were adsorbed onto the supports surface after which hydrothermal synthesis was carried out in a template free precursor gel. This resulted in the formation of ZSM-5 film thickness in the range of 230–3500 nm. Hedlund et al. (65) also reported the template free synthesis of ZSM-5 membranes supported on porous alumina with a thickness of 1.5 μm using the secondary (seed assisted) growth method. It was found the template-free zeolite membrane exhibited lower gas permeances but higher separation factors for binary mixtures when compared to other membranes (see references within (65)).

2.1.3 Hydrocarbon separations using zeolite membranes

Little work has been reported on the separation of light hydrocarbons and their mixtures using zeolites membranes. Kapteijn et al. (33) reported the permeation and separation behaviour of C_1 to C_3 alkanes and alkenes on a silicalite-1 coated stainless steel support. It was observed that for single component permeation the alkenes permeated faster than their corresponding alkanes and the permeation fluxes generally decreased with increased molecular size. Bakker et al. (21) also investigated the separation behaviour of C_1 to C_4 alkanes using a silicalite-1 coated metal support and arrived at similar conclusions to Kapteijn et al. on the decrease of single gas permeation fluxes with increasing molecular sizes. A remarkable temperature dependency was observed for i-butane where its permeance increased steadily with increasing temperature. Arruebo et al. (34) used silicalite-1 coated on porous stainless steel membranes in the separation of hydrocarbons from natural gas and found that alkanes such as n-butane permeated preferentially over methane. It was concluded that the best separations correspond to operation at atmospheric pressure, with negligible pressure drop across the membrane and in the presence of a sweep gas. McLeary et al. (66) used silicalite-1 membranes in the separation of n-hexane from its branched isomers in a hydroisomerization membrane reactor. It was found that the linear alkanes were preferentially adsorbed by the zeolite and supplied to a packed bed of catalyst. The control of the feed composition to the reaction resulted in an increased selectivity and conversion. Hedlund et al. (67) prepared 0.5 µm thick silicalite-1 membranes that had light gas permeation fluxes that were 1 or 2 orders of magnitude larger than other silicalite-1 membranes reported in the literature. The reported separation selectivities were as high as 9 for a binary (50/50) n-butan/:iso-butane feed mixture at 298 K. Lai et al. (68) also prepared a 1um thick silicalite-1 membranes that gave better separations for xylene isomers than previously reported in the literature. They obtained separation selectivities as high as 500 for para-/ortho-xylene mixtures. Van de Graaf et al. (69) prepared silicalite-1 membranes on stainless steel supports and investigated there separation capacity towards various hydrocarbon mixtures. It was concluded that the selectivity was significantly affected by operating conditions such as mixture composition, temperature and absolute pressure. It was also concluded that the orientation of the zeolite layer affected the selectivity for example the membranes showed selectivity towards ethane in ethane/methane mixtures only when the zeolite layer was facing the feed side. This selectivity was completely lost when the orientation of the zeolite layer was reversed to that of the permeate side.

Recently Arruebo et al.(70) synthesised MFI-type membranes on stainless-steel tubular supports and separated mixtures of n-pentane/isoprene. It was found the highest n-pentane/isoprene selectivity was 74, which was obtained at 333 K for a B-ZSM-5 membrane. It was concluded the separation was due to faster diffusion of the linear alkane. The single-component permeance of n-pentane was higher than its permeance in the mixture because the slower-diffusing isoprene decreases the rate of n-pentane diffusion. The separation selectivity for an equimolar mixture of n-hexane and 2,2-dimethylbutane was greater than 300 at 373 K for all membranes investigated. Van de Graaf et al. (71) reported the use of a silicalite-1 catalytic membrane reactor in the equilibrium limited metathesis of propene to ethane and 2-butene and of cis-2-butene to trans-2-butene. It was concluded the conversion of propene could be increased to 13% compared to the thermodynamic equilibrium conversion, accompanied by a 34% increase in the ratio in which the two butenes are formed during the reaction. The cis-2-butene conversion to trans-2-butene could be also increased to 4%, yielding 79% trans-2-butene in the product stream.

2.2 Molecular simulations

The understanding of the transport mechanisms in microporous zeolites materials can be investigated on the microscopic scale by applying theoretical techniques. The knowledge gained is of vital importance to both the separation and catalysis industries. In the literature there are numerous papers on the diffusion behaviour of adsorbate molecules in the zeolite bulk crystal structure, however, the role played by the external surfaces of the zeolites in effecting the molecular transport has not been fully addressed.

2.2.1 Surface simulations

Of the limited available literature addressing the simulation and adsorption of molecules on the surfaces of zeolites Whitmore et al. (72) using a combination of molecular dynamic and energy minimization techniques investigated the adsorption of benzene at the external surface and sub-surface of a purely siliceous (111) faujasite surface. They reveal distinct optimal adsorption sites compared to those identified in the bulk zeolite crystalline structure. The external surface adsorption energies (calc 30-43 kJ/mol) were found to be consistent with physisorption. They also identified a minimum energy pathway for benzene diffusion from the external surface to the crystal interior, which showed an energy barrier of 18 kJ/mol (compared to 31 kJ/mol in the bulk) for the adsorption/desorption process.

Ojo et al. (73) also using a combination of molecular dynamic and energy minimization techniques investigated the adsorption and migration of benzene at the external surface of a hydroxylated siliceous faujasite zeolite (111) surface. The faujasite surface was composed of hydroxylated double-6-rings (D6R) terminations. It was concluded that diffusion processes into or out of the crystal, when the benzene is near to the 12 –membered-ring (12MR) will be comparable for the two surface terminations considered but substantially less than the value in bulk migration energy of 31 kJ/mol. This suggested that diffusion into or out of the crystal will occur on a much faster time scale than diffusion in the bulk. Also it was found the diffusion parallel to the surface would be slightly faster than that observed in bulk, whilst diffusion from the external surface into the first supercage and vice versa, would occur much more quickly than the equivalent process in the bulk.

Slater et al. (74) using energy minimization techniques investigated the pure surface structures and effects of water on the geometries and stabilities of zeolite LTA. It was found that dissociative adsorption of water had a stabilising effect on all the zeolite surfaces. From the investigations three stable surface terminations were found for the (100) surface. The first type of termination consisted of double-4-rings (D4R), the second and third types consisted of single-4-rings (S4R) and D4R-edge terminations. The D4R and D4R-edge terminations were found to be in agreement with the work of Sugiyama et al. (75) who used Atomic Force Microscopy (AFM) studies to investigate the surfaces of LTA crystals but no presence of S4R terminations were observed. Sugiyama concluded that D4R were the key building unit for crystal growth of LTA. Slater concluded the absence of the S4R termination was due to it being a short-lived intermediate structure which is quickly evolved out of the growing crystal surface. It was also found that the additions of aluminium and extra-framework cations to the zeolites CaNa-A and Na-A caused the zeolite structure to expand, and the terminal hydroxyl groups on the surfaces were stabilised by coordinating with the zeolites extra-framework cations.

In other works Slater et al. (76) again using atomistic techniques investigated the growth mechanism of zeolite Beta C (100) surfaces and compared this to the findings from high resolution electron microscopy (HREM). They revealed three surface types, type I surfaces consisted of hydroxylated 12 membered-ring (12MR) terminations. Type II and type III surfaces consisted of hydroxylated S4R and D4R terminations. It was concluded that the type II surface termination was not formed or was likely to be a short lived intermediate as it was not seen in the HREM imaging experiments. It was also conclude that the surface structures arise not simply from optimal packing of the silicate tetrahedra but from complex reactions of siliceous oligomers with the zeolite surface.

Chandross et al. (77) simulated the interfaces between single component gases of butane/iso-butane and silicalite-1 using molecular dynamic simulations. They investigated the dynamics of exchange between the gas and the zeolite and concluded that molecules from the gas enter the zeolite primarily via the adsorption layer, where they hop among preferred adsorption sites until entering a pore mouth. Molecules desorbing from the zeolite undergo a similar process in reverse. For both processes, the surface residence time (adsorption time) was found to be on the order of 10 ps. However, in comparison the average bulk transit times were found to be much longer and approximately 20 ps per unit cell.

Jagoda-Cwiklik et al.(78) used Dynamic Monte Carlo simulations to study the adsorption and diffusion of n-butane in silicalite-1. During adsorption two limiting factors were found, firstly the butane could only adsorb directly at the openings of channels and secondly channel blocking caused by adsorbed butane made channels unavailable to adsorption for succeeding molecules. It was concluded that the confinement and channel blocking limit the adsorption and desorption processes. Moreover, they cause the maximum loading in the zeolite structure at moderate pressures to be higher than that predicted by the Langmuir model for a flat and homogeneous system.

Nitta et al. (79) used a combination of Monte-Carlo and non-equilibrium molecular dynamic simulations to investigated the adsorption and permeation behaviour of pure single gas and equimolar mixtures of propane and propylene in ZSM-5 membranes. The ideal separation factor and the permselectivity of propylene to propane calculated from simulations were in good agreement with experimental data. It was found for the pure gas permeation simulations the permeability of propane was lower than that of propylene, while for mixed-gas permeation, it becomes higher than that of propylene due to the competitive adsorption of propane. From the simulations Nitta proposed a permeation mechanism that depended on selective adsorption followed by diffusion in the zeolites.

Lin and Murad (80) used molecular dynamic simulations to investigate the separations of water from aqueous NaCl solutions using thin ZK-4 zeolite membranes. During the simulations the phenomena of both osmosis and reverse-osmosis was observed. It was concluded that ZK-4 zeolite membranes were promising candidates for use in membrane-based separations of aqueous electrolyte solutions.

2.2.2 Bulk simulations

2.2.2.1 Influence of water

Ramachandran et al. (81) simulated the adsorption of water from the vapour phase into the silicalite-1 zeolite using Grand Canonical Monte Carlo simulations. They concluded that in a perfect silicalite-1 crystal, the pore system is hydrophobic and essentially no water adsorbs at low pressures. At some intermediate pressure, a sharp transition occurs where the pores become saturated with water molecules. It was also concluded that the presence of hydrophilic defects, such as silanol sites, in experimental samples leads to the adsorption of small amounts of water at low pressures. In the simulations water molecules preferentially form hydrogen-bonded clusters around the defects. The presence of hydrophilic defects also led to a decrease in the pressure when pore filling occurs.

C. Beauvais et al. (82) performed Monte Carlo simulations of water adsorption in NaY and NaX faujasite zeolites. In the simulations the nonframework cations were allowed to move from place to place within the sample, and were not fixed in their crystallographic sites. Water adsorption in the low cation content faujasite (Na48Y) resulted in cation redistribution but no such cation redistribution was observed in the higher cation content Na76X faujasite. It was concluded that the water adsorption process can be very different, depending on the Si/Al ratio of the faujasite zeolite.

Higgins et al. (83) in there work also highlighted the importance of including the effects of hydration when studying ion-exchange in zeolites. They used energy minimisation techniques to model the effect of hydration on the adsorption behaviour of various extra-framework cations in the zeolite LTA. For the zeolite CaNa-A (Si/Al = 1) the energetically preferred position for water molecules was calculated to be inside the α-cage, in agreement with experimentation. It was concluded the preferential locations for the sodium and calcium ions in the hydrated LTA were governed by the water molecules and in the siliceous structure were found to be in the β-cages (S6R position) for Na+ and β-cages (S6R positions) for Ca2+.

2.2.2.2 Hydrocarbon simulations in zeolites

Titiloye et al. (84) using an energy minimization technique investigated the adsorption of linear C1-C8 hydrocarbons in the silicalite-1, H-ZSM-5 and siliceous faujasite zeolites. The influence of framework flexibility on the heats of adsorption was also investigated. It was concluded that framework flexibility was only significant for the larger alkanes and had little effect on the smaller alkanes. It was also found that the adsorption of hydrocarbons (in silicalite-1 and H-ZSM-5) at the straight channels is preferred to that of the sinusoidal channels and in general the hydrocarbons would sorb preferentially in silicalite-1 and ZSM-5 zeolites than the faujasite zeolite.

Nascimento (85) carried out a series of molecular simulations of light alkanes in Silicalite-1 and concluded that linear alkanes (C_1-C_4) showed an equal probability of being found in both the straight and the sinusoidal channels while the branched alkanes preferred the channel intersections.

Rungsirisakun et al. (86) performed molecular dynamics (MD) simulations of benzene at various loadings in the siliceous zeolites FAU, ZSM-5, and MCM-22. It was concluded that the adsorption energies of benzene/zeolite complexes increased with increasing loadings, due to the intermolecular attraction between benzene molecules. Whereas the self-diffusion coefficient of benzene in the zeolites decreases with increasing loadings due to the hindrance between the sorbates passing each other. It was also found that in the FAU zeolite the benzene molecules prefer to be adsorbed parallel to the surface of the sodalite cage above the six-membered-ring. In the ZSM-5 zeolite it was found at loadings of 2, 4, and 8 molecules the benzenes were orientated in a T-structure. Whereas at a loading of 16 molecules the benzenes were lined up along the straight channel and their movement is highly correlated. For MCM-22 it was found at a loading of 4 molecules the benzenes had an orientation similar to the stacked conformation of benzene dimers in the gas phase.

García-Pérez et al. (87) performed molecular simulations to determine adsorption isotherms and heats of adsorption of linear C1–C10 alkanes in the MFI and FAU-type zeolites containing non-framework sodium cations and framework aluminium atoms. The simulations accurately reproduce the available experimental adsorption data in sodium-exchanged MFI- and FAU-type zeolites over a wide range of cation densities, temperatures, and pressures. From the resulting simulation data they obtained a simple empirical expression that described the n-alkane adsorption enthalpy as a function of sodium density and temperature at low coverage. The expression was applied successfully with both zeolite types thus affording an adequate substitute for the complex configurational-bias Monte Carlo simulations.

Fox et al. (88) used Monte Carlo simulations to investigate the properties of C6 alkanes (linear, branched and cyclic) in silicalite-1 and $AlPO_4$-5 using new potential parameters for cyclohexane. For the adsorption of hexane in silicalite-1 at low pressures it was found the molecules had no preference and adsorb uniformly in both the channels and the intersections. At higher pressures the adsorption was localised to the channels, leaving the intersections free. The adsorption location for the 2-

methylpentane was found to be only at the intersections at low pressure but at higher pressures arranged itself so that adsorption was possible in the sinusoidal channels. Whereas for the cyclohexane it was found it adsorbed only at the intersections over all temperature and pressure ranges investigated. It was concluded that the adsorption isotherms for all three alkanes could be produced with good accuracy over a large temperature and pressure range and that the zeolite potential parameters could be successfully transferred to other zeotypes.

Ndjaka et al. (89) also using Monte Carlo simulations showed that force fields which have been parameterised using experimental data obtained from MFI-type zeolites could be used to successfully model heats of adsorption and adsorption isotherms for small alkanes for a range of different pore sized zeolites.

Krishna and Paschek (90) used configurational bias Monte-Carlo simulations to determine the sorption isotherms of methane, ethane, propane, n-butane and iso-butane in silicalite-1. Using the data obtained for loading distribution in the various channels of the silicalite-1 zeolite Krishna and Paschek proposed a three site Langmuir (3SL) (where the characteristics of the sinusoidal, straight and intersections were left separate) model instead of the traditional dual site Langmuir (DSL) model where the characteristics of the straight and sinusoidal channels are summed together. It was concluded that the 3SL model showed good agreement with the experimental data on pure component sorption of light alkanes.

Van Baten and Krishna (91) used a combination of configurational bias Monte-Carlo and molecular dynamics simulations to study the adsorption and diffusion behaviour of hexane isomers in the zeolites MOR FAU and MFI. For the mordenite it was concluded that adsorption and diffusion only occurred within the 12-ring channels. It was also found that the branched alkanes had higher packing efficiencies than the linear alkanes as a result their adsorption strength and capacity was higher. Also for mixtures of linear and branched alkanes at low loading the linear alkanes were found to have the largest diffusivities. At high loadings close to saturation packing entropy phenomena resulted in reversals in the diffusivities with the branched alkanes having the highest diffusivities. For the MFI it was found the entropy effects acted in a manner opposite to that seen for the mordenite. But it was concluded that in mixtures the presence of the branched slower diffusing isomer resulted in a slowing down of the faster diffusing linear isomer. For the FAU it was found both linear and branched alkanes had similar adsorption strengths and diffusivities. It was concluded this behaviour was due to the large window of the FAU, which did not distinguish between linear or branched alkane isomers.

2.2.3 Influence of framework flexibility

The influence of zeolite framework and adsorbate flexibility during simulations has been demonstrated by different workers showing that framework flexibility can influence the diffusional behaviour of small sorbed molecules. Demontis et al. (92,93) using molecular dynamic simulations investigated the effect of both temperature and framework flexibility on the diffusion of methane in silicalite-1. It was concluded that the diffusivity of the methane was much higher with the flexible framework than with the rigid framework. Fritzsche et al. (94) and Leroy et al. (95) using different sets of interatomic potentials independently reported that the diffusional behaviour of methane in silicalite is strongly enhanced by flexible frameworks, and at higher loadings this influence becomes negligible and only significant at high temperatures. In contrast to this finding Kopelevich and Chang (96) reported that for small molecules such as methane and xenon in silicalite the diffusion is not driven by lattice vibrations and recommended that molecular dynamic simulations involving small sorbates require only a simple rigid framework.

2.3 Generalized Maxwell-Stefan (GMS) model

A number of theoretical techniques have been used and sometimes combined to describe transport behaviours of pure and mixed adsorbates through zeolites and zeolite membranes. Techniques such as molecular dynamics (MD) and energy minimization (EM) have been successfully used as seen earlier. In the current section the use of the Generalized Maxwell–Stefan (GMS) model and its reported applications is reviewed.

The generalized Maxwell-Stefan equations have been successfully applied to many systems (e.g. zeolites, microporous activated carbons and carbon molecular sieves) to describe diffusive transport phenomena in multicomponent mixtures as demonstrated by Krishna and Wesselingh (97) and van den Broeke and Krishna (98). It is generally accepted that the Generalized Maxwell–Stefan equations offer the most convenient and the closest prediction of multi-component diffusion and permeation behaviour of adsorbates through zeolite membranes. In a very recent works Krishna and van Baten (99) investigated the loading dependence of the Maxwell–Stefan diffusivity of C1–C4 linear alkanes in four different zeolites (AFI, MOR, MTW, and MFI) using a combination of Monte Carlo and molecular dynamic simulations. It was found the pore size of the zeolite appeared to have a major influence on the Maxwell-Stefan (M–S) diffusivity vs. molecular loading characteristics. For the large pore AFI, the M–S diffusivity is proportional to the inverse of the thermodynamic correction factor ($1/\Gamma$). This was also found for C1 and C2 diffusion in MOR, which has slightly smaller pore size than AFI. For all other guest–host combinations reported the M–S diffusivity values fall less sharply with molecular loading than $1/\Gamma$, Krishna suggested that the energy barrier for diffusion is influenced by the molecular loading.

In an earlier series of works Krishna and van Baten (100) used molecular dynamics (MD) simulations to determine the Maxwell–Stefan (M–S) diffusivities ($Đ_i$) for linear C5-C8 alkanes in the MFI zeolite for a range of molecular loadings. In all cases considered the M–S diffusivities exhibit inflection behaviour at loadings of 4 molecules per unit cell. This inflection was caused by the presence of the corresponding inflection in the sorption isotherm. This behaviour was also reported In an earlier study by Vlugt et al. (101) . Vlugt used Monte-Carlo simulations showed that the sorption isotherms for linear and branched C6-C8 alkanes in MFI zeolite exhibited inflection behaviour. In the case of the branched alkanes it was concluded this inflection behaviour was a result of the branched alkanes below a loading of 4 molecules per unit cell, occupying only the intersections. At a loading of 4 molecules per unit cell, the intersections are fully occupied, and in order to achieve higher loadings, the branched alkane had to reside in the other channels. This, however, was energetically very demanding and required a significantly high pressure thus resulting in the inflection point.

Krishna and Baur (102) developed an analytic solution of the Maxwell–Stefan equations describing the steady-state diffusion/ permeation fluxes of n-component (alkane) mixtures across a MFI zeolite membrane. It was found that the fluxes of C1–C3 alkanes were all suppressed when the upstream partial pressure of n-C4 was increased. It was concluded this was because n-C4 has much stronger adsorption strength and "hinders" the other species. It was also concluded that the interchange M-S diffusivity coefficient (Đ_{ij}) tended to lead to a significant lowering of the fluxes of C1 and C2 alkanes whereas the flux of n-C4 alkane was enhanced due to the interchange M-S diffusivity coefficient (Đ_{ij}).

Krishna and Paschek (103) using the Maxwell–Stefan theory for diffusion derived a simple formula which related the tracer diffusivity (i.e. self diffusivity (*D*)) and Maxwell–Stefan diffusivity.

$$D = \frac{\text{Đ}}{1 + F\theta_i} \quad \text{where } \text{Đ}_{ij} = \frac{\text{Đ}}{F} \tag{2.1}$$

It was found that the presence of the interchange Maxwell–Stefan diffusivity coefficient (Đ_{ij}) in the Maxwell–Stefan formulation causes the self diffusivity to be lower than the Maxwell–Stefan diffusivity. Kinetic Monte-Carlo simulations of methane, perfluoromethane, 2-methylhexane and iso-butane in silicalite-1 with no repulsive interactions where performed to test and validate the formula derived from the Maxwell–Stefan theory. It was concluded for all four molecules that the formula could reproduce the self diffusivity accurately. Also the formula was tested with data derived from molecular dynamics simulations of methane in silicalite-1. It was concluded that the simulation derived self diffusivities agreed with those predicted by the formula provided that F=3. In an earlier work Krishna (104) evaluated the use of the Maxwell-Stefan equations for the prediction of binary mixture transport behaviour using the MD simulation results of Sanborn and Snurr (105) for diffusion of methane and perfluoromethane in the Faujasite zeolite. It was found the simulation results could not be modelled successfully by the MS equations without the inclusion of the interchange Maxwell–Stefan diffusivity (Đ_{ij}). They concluded that the Maxwell-Stefan theory for binary mixture diffusion in zeolites could be used to predict mixture behaviour with good accuracy from pure single component diffusion data.

Krishna (106) used the Maxwell-Stefan equations to highlight the influences of both size and configurational entropy effects on binary mixture permeation across silicalite-1 zeolite membranes. It was concluded that for mixtures containing components with different saturation capacities (methane and n-butane) size entropy effects tended to favour the sorption of the smaller molecule at high loadings. For mixtures of linear and branched alkanes it was found the sorption selectivity increases in favour of the linear alkane at high loading due to a higher packing efficiency or configurational entropy effects. It was also found that the interchange Maxwell–Stefan diffusivity ($Đ_{ij}$) significantly increased the permeation selectivity of n-butane in a binary methane/n-butane mixture.

Kapteijn et al. (107) using both the ideal adsorbed solution (IAS) theory and generalized Maxwell Stefan equations derived expressions for the diffusion of alkane mixtures (C1-C3) with different saturation loadings in the silicalite-1 zeolite. It was found that for binary mixtures of components with large differences in individual diffusivities the presence of the interchange Maxwell–Stefan diffusivity ($Đ_{ij}$) was necessary. If the difference in diffusivities was small then the influence of this term is negligible. Also Kapteijn concluded that superior permeation predictions could be obtained by incorporating a mixture adsorption model (in this case IAS theory), which accounted for differences in saturation loadings with the generalized Maxwell-Stefan equations.

In other works van de Graaf et al. (108) investigated the influence of composition, total hydrocarbon pressure and temperature on the separation of ethane/methane and propane/methane mixtures in a siliclaite-1 membrane. This was then compared to the predicted behaviour obtained from the generalized Maxwell-Stefan equations based on separately determined single component adsorption and diffusion parameters, which was found to be in excellent agreement with the experimental data. It was concluded that the permeation phenomena was much better described by the complete Maxwell-Stefan model (with the interchange Maxwell–Stefan diffusivity ($Đ_{ij}$) describing adsorbate-adsorbate interaction).

Krishna et al. (109) using configurational bias Monte-Carlo simulations generated the both the single component and mixture isotherms of benzene, p-xylene, n-hexane and iso-butane, which showed inflection behaviour. It was found that the dual site Langmuir (DSL) isotherm model could accurately predict the isotherms generated by the CBMC simulations. Following this the Maxwell-Stefan theory was used to predict the separation of C6 isomers (n-hexane and 3-methylpentane). For a binary 50:50 mixture it was found the selectivity was 32, this high selectivity was entirely due to the strong inflection observed from the DSL isotherms for the branched alkane.

2.4 Economic considerations

A limited number of economic assessments of zeolite membranes versus traditional separation processes (e.g. distillation) have been reported in the literature. Caro and co-workers (12) reported zeolite membrane module costs of approximately US$3000/m2 of which 10–15% was contributed to the membrane itself. Meindersma and de Haan (110) conducted an economic feasibility study for the separation of aromatics from Naphtha feedstocks and concluded due to the high costs (€2000/m2) of zeolite membrane modules, that unless membrane module costs were reduced by a factor of 10 and the flux were increased by a factor of 25 the investments would be uneconomical. Van Hoof et al. (111) carried out the dehydration of isopropanol/water mixtures using both traditional distillation and a hybrid system consisting of distillation followed by pervaporation. It was concluded that the hybrid system lead to a decrease in the total cost (operation, investment and maintenance costs) by approximately 49%. Hinchliffe and Porter (112) conducted a comparison of membrane separations versus distillation and concluded that zeolite membranes offer an attractive alternative to distillation for many separations with significant reductions in the operating costs.

Chapter 3: Theoretical Methods

Chapter 3: Theoretical Methods

3.1 Introduction

Computer simulation techniques have received a notable amount of attention due to increases in computation speed and performance. The result of this is that they provide an inexpensive and time-effective way to determine the properties and behaviour of adsorbents within the channels of zeolites. This is in contrast to experimental techniques which are often time-consuming, and subject to errors with result which may be difficult to interpret and sometimes ambiguous. The benefits of using molecular simulations methods are that different parameters of interest such as different pore structures, adsorbate concentration, influence of temperature and pressure can be easily varied, and their influence on the system of interest can be readily investigated. Furthermore, the knowledge gained from molecular simulations at the microscopic level can be used to explain and understand the results from experimentation.

3.1.1 Atomistic simulation potential models

Atomistic simulation methods are based on the Born model of solids (113) which assumes that the ions in the crystal interact via long-range electrostatic and short-range forces. The long-range electrostatic forces are calculated either by using the Ewald method (114) or by the Parry method (115) depending on the periodicity of the simulation cell while the short-range forces are described by parameterised analytical expressions such as Buckingham, Lennard-Jones and Morse potential models (see below). The electronic polarizability of the ions is included via the shell model of Dick and Overhauser (1958) (116) in which each polarizable ion in the simulation cell is represented by a core and a massless shell, connected by a spring.

3.1.2 Two-body potentials

Interactions between the atoms are usually modelled by using two-body potentials. For the adsorption and diffusion of alkanes, short-range dispersive forces are the dominating interactions, and are represented by either a Lennard-Jones or by a Buckingham potential. The Lennard-Jones potential has the form:

$$U_{LJ} = \frac{A_{ij}}{(r_{ij})^{12}} - \frac{B_{ij}}{(r_{ij})^{6}} \qquad 3.1$$

U_{LJ} is the interaction potential between two atom centres separated by a distance r_{ij}, A and B are constants of repulsion and attraction due to dispersive forces, respectively, where $A_{ij} = 4\varepsilon_{ij}\sigma_{ij}^{12}$ and $B_{ij} = 4\varepsilon_{ij}\sigma_{ij}^{6}$. Thus the above equation can be rewritten as:

$$U_{LJ} = 4\varepsilon_{ij}\left[(\frac{\sigma_{ij}}{r_{ij}})^{12} - (\frac{\sigma_{ij}}{r_{ij}})^{6} \right] \qquad 3.2$$

The Buckingham potential is represented by:

$$U_{BUCKS} = A_{ij} \exp\left(-\frac{r_{ij}}{\rho_{ij}} \right) - \frac{C_{ij}}{r_{ij}^{6}} \qquad 3.3$$

Where *i* and *j* are two atoms with separation r_{ij} . A_{ij} and ρ_{ij} are constants describing repulsion, and C_{ij} is a term that takes dispersion effects into account. Plotting the functions of both potentials (equations 2 and 3) gives a potential energy curve as shown in Figure 3.1. It is seen from this potential energy curve there are a number of important characteristics: at a close range the potential energy is very large and positive indicating an unfavourable proximity of the atoms resulting in strong repulsion forces. At long range the potential energy is small and negative and due to London dispersion forces an instantaneous dipole-dipole attraction occurs. This indicates that at this distance repulsion is minimal and attraction forces are significant. In between these two distances the energy is found to be at a minimum indicating the most stable interaction distance.

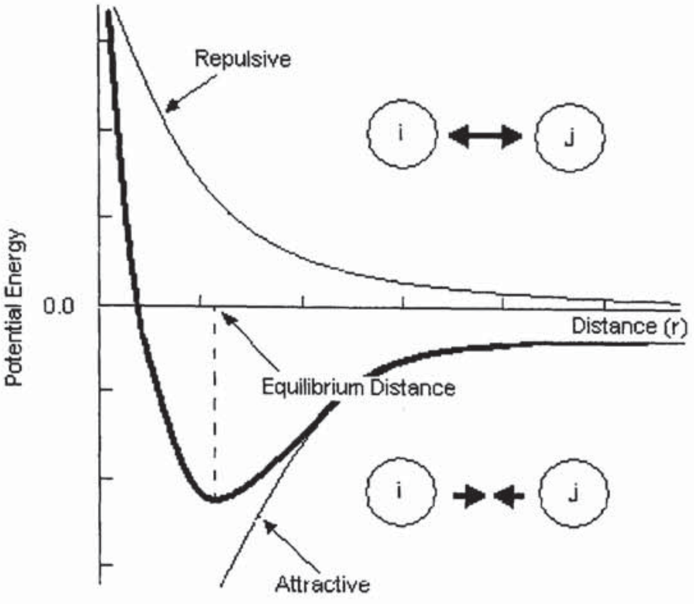

Figure 3.1 Buckingham and Lennard-Jones potential energy curve

In addition to these short-range interatomic potentials, the intramolecular behaviour of the adsorbates is represented by a Harmonic (spring like) potential:

$$U_{BOND-STRETCH} = \frac{1}{2} K_b (b - b_0)^2 \tag{3.4}$$

Equation 3.4 is the approximation to the energy of a bond as a function of displacement from the ideal bond length, b_0. The force constant, K_b, determines the strength of the bond. Generally both ideal bond lengths b_0 and force constants K_b are specific for each pair of bound atoms.

A more realistic representation of the bond stretching behaviour can be represented by using the anharmonic Morse potential, which can be used for large deviations from equilibrium:

$$U_{MORS} = D_{eq} (1 - \exp(-a(b - b_{eq}))^2 \tag{3.5}$$

Where b_{eq} is the equilibrium bond length and D_{eq} the potential energy for bond formation and "a" a parameter controlling the width of the potential well. If we plot the function of both the simple Harmonic and Morse potentials (Equations 3.4 and

3.5) we can see from Figure 3.2 that the Morse potential is more suitable for larger deviations from equilibrium.

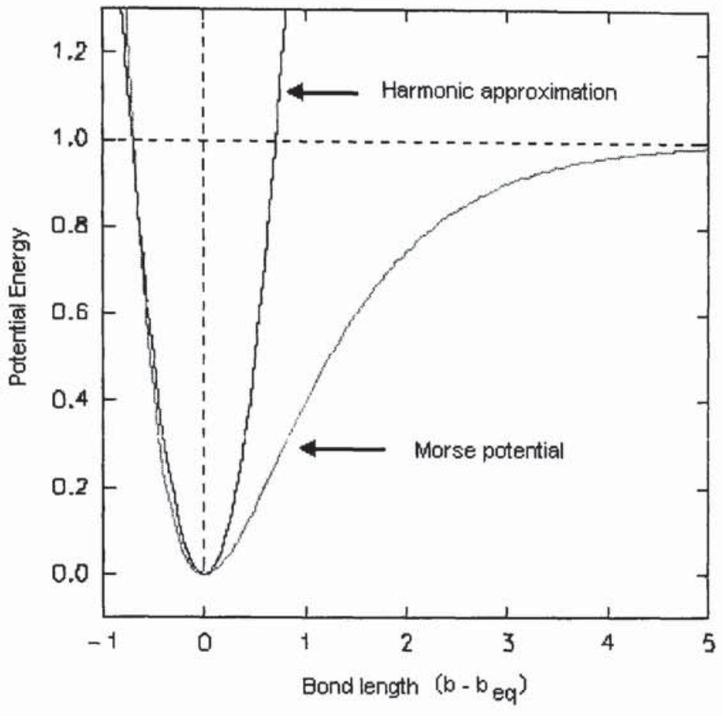

Figure 3.2 Harmonic and Morse potential energy curve

3.1.3 Three-body potentials

This is a bond bending potential model associated with alteration of bond angles Θ from ideal values Θ_0, and is represented by a Harmonic potential:

$$U_{BOND-BEND} = \frac{1}{2} K_{\theta} (\theta - \theta_0)^2 \tag{3.6}$$

Values of Θ_0 and K_Θ depend on the chemical nature of the atoms forming the angle. Once all interactions are defined, the total potential energy experienced by a single atom can be calculated by summing all individual interaction energies of the system.

3.1.4 All atomistic and modified united atom potentials

In this study both all atomistic potentials (AAP) and a modified united atom potential (UAP) models have been used to simulate the adsorbate molecules whereas the zeolite structure has been modelled using only an all atomistic potential model. In the united atom potential, (UAP) the CH_3, CH_2 and CH_4 groups of the adsorbate alkanes are represented and considered as single interaction centres. The potential parameters used in this study are shown in Table 3.1 (modified united atom potential model) and Table 3.2 (all atomistic potential model). The Lennard-Jones parameters for interactions between two unlike atoms *i* and *j* are determined using a set of combining rules. The most common means is to use a geometric mean for ε (the Berthelot rule) and an arithmetic mean for σ (the Lorentz rule):

$$\varepsilon_{ij} = \left(\varepsilon_{ii}\varepsilon_{jj}\right)^{\frac{1}{2}} \;,\; \sigma_{ij} = \frac{1}{2}\left(\sigma_{ii} + \sigma_{jj}\right) \tag{3.7}$$

Table 3.1 Modified United Atom Potentials (UAP)

Molecule	**Sites***	**Sigma (σ)** (Å)	**Epsilon (ε/K_B)** (K)	**Ref**
Methane	**CH_4---CH_4**	3.73	147.933	Smit (117)
	O_z---CH_4	3.694	90.792	Smit (117)
Ethane	**CH_3---CH_3**	3.923	72	Ryckaert & Bellemans (118)
	O_z---CH_3	3.364	83.8	June et al., (119)
Propane	**C_3/C_1---C_3/C_1**	3.870	88.06	Smit (117)
	C_2---C_2	3.870	59.38	Jorgensen et al., (120)
	O_z--- $C_3/C_2/C_1$	3.636	73.4	Fritzsche et al., (94)
Mixed	**CH_4---C_3/C_1**	3.799	114.136	This Work
	CH_4---C_2	3.799	93.724	This Work
	CH_4---CH_3	3.825	103.205	This Work
	CH_3---C_3/C_1	3.896	79.626	This Work
	CH_3---C_2	3.896	65.386	This Work

Morse Potential Parameters

Sites	D_b	α	r_o	
C---C	3.819	1.92	1.53	Titiloye et al., (84)

Three-Body Potential Parameters

Sites	K (eV rad^{-2})	θ_0 (deg)	
C--C--C	4.045	110.5	Titiloye et al., (84)

(*z represents zeolite atoms. C_3/C_1 and C_2 represents the CH_3 and CH_2 groups of the propane molecule)

Table 3.2 All Atomistic Potentials (AAP)

Lennard-Jones Potential Parameters

Sites	A_{ij} (eV $\mathring{A}^{12}$)	B_{ij} (eV $\mathring{A}^{6}$)	
C_{sp3}----O_z	11825.615	17.661	Titiloye et al., (84)
H_s---- O_z	1557.522	5.574	Titiloye et al., (84)

Morse Potential Parameters

Sites	D_b	α	r_o	
C_{sp3}---C_{sp3}	3.819	1.92	1.53	Titiloye et al., (84)
C_{sp3}--- H_s	4.713	1.77	1.1	Titiloye et al., (84)

Three-Body Potential Parameters

Sites	K (eV rad^{-2})	θ_0 (deg)	
H_s--C_{sp3}--H_s	3.428	106.4	Titiloye et al., (84)
C_{sp3}--C_{sp3}-- Hs	3.854	110.0	Titiloye et al., (84)
C_{sp3}--C_{sp3}--C_{sp3}	4.045	110.5	Titiloye et al., (84)
O_z--Si--O_z	2.09724	109.47	Sanders et al., (121)
O_z--Al--O_z	2.09724	109.47	Sanders et al., (121)
H_w--O_w--H_w	4.199780	108.69	de Leeuw (122)

Buckingham Potential Parameters

Sites	Å (eV)	ρ (Å)	C (eV.$Å^6$)	
Si -- O_z	1283.907	0.32052	10.66158	Sanders et al(121)
O_z -- O_z	22764.0	0.149	27.88	Catlow (123)
Na -- O_w	2336.222	0.2387	0.0	Higgins et al.,(83)
Na -- OH	4088.384	0.2387	0.0	Higgins et al.,(83)
Na -- O_z	5836.814	0.2387	0.0	Post (124)
Si -- O_w	562.032	0.32052	10.66158	Higgins et al.,(83)
Si -- OH	983.556	0.32052	10.66158	Higgins et al.,(83)
Al -- O_z	1460.3	0.29912	0.0	Higgins et al.,(83)
Al -- OH	1142.6775	0.29912	0.0	Higgins et al.,(83)
Al -- O_w	584.12	0.29912	0.0	Higgins et al.,(83)
OH -- OH	22764.3	0.149	6.97	de Leeuw (122)
O_z -- OH	22764.3	0.149	13.94	de Leeuw (122)
O_z -- O_w	22764.3	0.149	28.92	de Leeuw (122)
OH -- O_w	22764.3	0.149	17.14	de Leeuw (122)
H -- O_z	396.27	0.25	0.0	de Leeuw (125)
H -- O_w	396.27	0.25	0.0	de Leeuw (125)
H_w -- O_z	396.27	0.25	0.0	de Leeuw (125)
H – OH	311.97	0.25	0.0	de Leeuw (122)
H_w -- OH	311.97	0.25	0.0	de Leeuw (122)

(Note the subscripts z, s and w represent zeolite atoms, sorbate atoms and water atoms respectively)

3.2 Molecular dynamics simulations

Molecular dynamic simulations are a very powerful aid in the study of the dynamics of a given system. Newton's equations of motion are at the core of molecular dynamics and it is the precise numerical solution of these upon which molecular dynamics is based. In a simulation Newton's equation is used to simulate atomic motion:

$$\text{Force} = \text{mass x acceleration} \;\; (F_i = m_i.a_i) \tag{3.8}$$

The rate and direction of motion (velocity) is governed by the forces that the atoms of the system exert on each other. The calculation of the force on each atom is vital in molecular dynamics as from this knowledge, the position of each atom throughout a specified period of time can be obtained (typically on the order of picoseconds = 10^{-12} seconds). The force acting on an atom can be obtained from the differences in energy between its initial position and its final position a small distance away. This is known as the derivative of the energy with respect to the change in the atom's position:

$$-\frac{dE}{dr_i} = F_i \tag{3.9}$$

With the knowledge of the atomic forces and masses the resultant positions of each atom along a series of very small time steps (scale of femtoseconds = 10^{-15} seconds) can be calculated. The resulting series of configuration changes over time is called a trajectory. The use of this method to compute trajectories can be more easily seen when Newton's equation is expressed in the following form:

$$-\frac{dE}{dr_i} = m_i \frac{d^2 r_i}{dt^2} \tag{3.10}$$

First, the atomic accelerations are calculated from the forces and masses. The velocities can then be calculated from the accelerations using the following relationship:

$$a_i = -\frac{dv_i}{dt}$$

3.11

Where r_i is the atomic coordinate and v_i the velocity of atom, i, with mass, m_i. Finally the positions are calculated from the velocities:

$$v_i = -\frac{dr_i}{dt}$$

3.12

3.2.1 Setting up and running a molecular dynamics simulations

In this work all molecular dynamic simulations were performed using the DLPoly code developed by Forrester and Smith. (126). In a molecular dynamics simulation, the time dependent behaviour of the molecular system is obtained by integrating Newton's equations of motion. The result of the simulation is a HISTORY file (containing a time series of configuration coordinates); this is the trajectory or the path followed by each atom or molecule. Most molecular dynamics simulations are performed in the Microcanonical ensemble (NVE). This is the thermodynamic state characterized by a fixed number of atoms, N, at a fixed volume, V, and a fixed energy, E. There exist different ensembles with different characteristics:

(1). Canonical Ensemble (NVT): Here the thermodynamic state is characterized by a fixed number of atoms, N, a fixed volume, V, and a fixed temperature, T.

(2). Isobaric-Isothermal Ensemble (NPT): This ensemble is characterized by a fixed number of atoms, N, a fixed pressure, P, and a fixed temperature, T.

(3). Grand canonical Ensemble (μVT): The thermodynamic state for this ensemble is characterized by a fixed chemical potential, μ, a fixed volume, V, and a fixed temperature, T.

In order to run a successful molecular dynamics simulation with meaningful results a sequence of steps is required to set-up and run the simulation. Figure 3.3 shows the basic steps taken to run a successful simulation.

3.2.1.1 Initiation

An initial configuration of the system i.e a starting point (t=0) is needed to begin a molecular dynamics simulation. The choice of the initial configuration must be done with care as this can influence the outcome of the simulation. It is recommended to use an energy minimized configuration of the system prior to starting the molecular dynamics simulation. This removes any unfavourable structural configurations which may exist leading to an unstable structure.

3.2.1.2 Heating the system

Initial velocities at a low temperature are assigned to each atom of the system and Newton's equations of motion are integrated to initiate the system in time. As the simulation proceeds new velocities at slightly higher temperatures are assigned at regular intervals until the set temperature is reached.

3.2.1.3 Equilibration

Once the set temperature is reached, the simulation proceeds and during this stage properties of interest such as pressure, temperature and the energy are monitored. The reason for the equilibration period is to run the simulation until there are minimal fluctuations in these properties resulting in a stable system.

3.2.1.4 Full simulation run

The final stage of the simulation is to run the actual simulation over the required time period (typically ps to ns or more). It is during this stage that properties of interest can be calculated and stored for subsequent analysis.

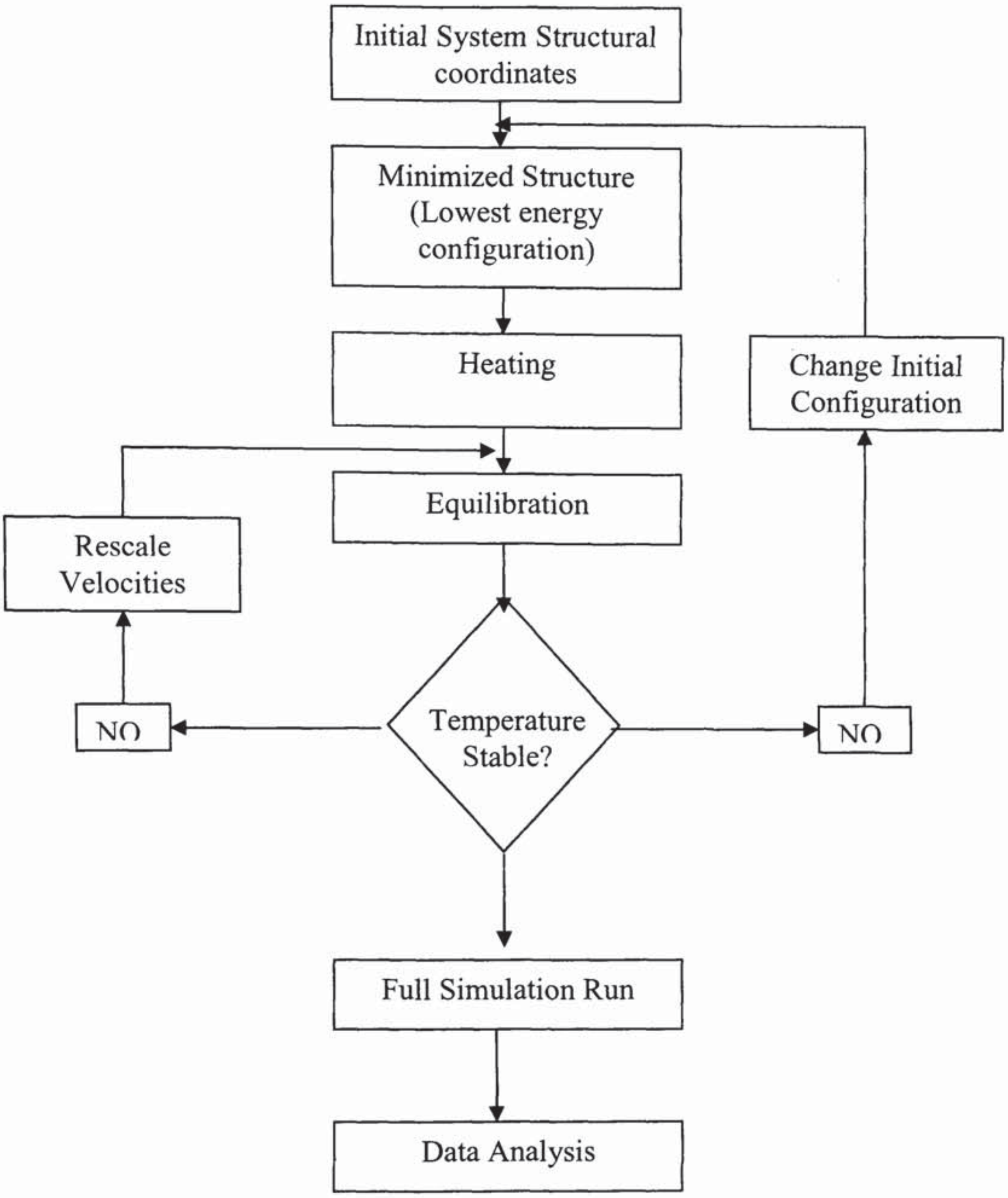

Figure 3.3 Stages of a molecular dynamics simulation

3.2.1.5 Analysis of simulation data

When carrying out an MD simulation, coordinates and velocities of the system are saved; these are then used for the analysis. These time dependent properties can be displayed graphically, where one of the axis corresponds to time and the other to the property of interest, such as the z-density, mean square displacements (msd) and radial distribution functions (rdf). Molecular dynamics simulations can be visualized with the aid of suitable molecular graphic programs which can display the structural parameters of interest in a time dependent way. From this we can gain an understanding of the behaviours of components in a given system for example preferred diffusional pathways, the competition between adsorbate molecules for adsorption sites etc. Properties that can be obtained from a molecular dynamics simulation include:

3.2.1.5.1 Radial Distribution Function (RDF)

To gain an understanding of the behaviour of molecules within the zeolite channels, atom-atom radial distribution functions (RDF) have been analysed. The RDF shows the probability density of finding an atom/particle of type ***b*** within a sphere of radius ***r*** around an atom/particle of type ***a***.

3.2.1.5.2 Mean Square displacements (MSD)

The mean square displacements (MSD) obtained from the simulations are used in analysing the diffusion coefficients following the 3-D Einstein equation:

$$D = \frac{1}{6}\frac{d}{dt}\left\langle \left| r(t - t_o) \right|^2 \right\rangle \tag{3.13}$$

Where D is the diffusion coefficient of species i, $\left\langle \left| r(t - t_o) \right|^2 \right\rangle$ is the mean square displacement, t is the simulation elapsed time and t_0 is an arbitrary starting point. The angular brackets denote that the quantity is an ensemble average property.

3.2.1.5.3 Z-density profile

The density profile plots are valuable in determining the focal points of sorbate and diffusional activities. The position of channel systems located on the plots are determined by considering measurements of channel position in one unit cell along the z-crystallographic axis and translated to the z-density graphs. These plots are particularly useful for identifying competitive adsorption and preferred activity sites for mixed components in the channels.

3.3 Static simulation

3.3.1 Surface generation simulations

The surface stabilities and energies of zeolites surfaces can be modelled at 0 K using atomistic simulation techniques with the computer code METADISE (Minimum Energy Techniques Applied to Dislocation, Interface and Surface Energies) (127). Following the approach of Tasker (128), a crystal consists of a series of charged planes parallel to the surface and periodic in two dimensions. Tasker identified three different types of surfaces (Figure 3.4):

(Type 1) An uncharged plane with cations and anions in stoichiometric ratio.

(Type 2) A stack of charged planes where the repeat unit perpendicular to the surface has no dipole moment.

(Type 3) A stack of charged planes where the repeat unit has a dipole moment perpendicular to the surface. In this instance, the surface needs to be reconstructed to remove the dipole. This is often achieved by creating vacancies in the surface.

A simulation cell is modelled as two blocks (Figure 3.5) each comprising of two regions, region 1 and region 2, which are periodic in two dimensions lateral to the surface. Region 1 contains the surface layer of atoms and a few layers immediately below, and these atoms are allowed to relax to their equilibrium positions to reveal the surface configuration. Region 2 contains those atoms, which are further away and represent the rest of the bulk crystal structure and are kept fixed at their bulk equilibrium positions. The bulk of the crystal is simulated by the two blocks together while the surface is represented by a single block with the top of region I representing the free surface. Both regions 1 and 2 need to be sufficiently large for the energy to converge.

The energy of the generated surface configurations (surface energy γ) is calculated from the energy per unit area required to form the surface relative to the energy per unit area for the same number of bulk atoms, and is given by:

$$\gamma = \frac{U_s - \frac{1}{2}U_b}{A}$$

3.14

U_s is the energy of the surface block of the crystal, U_b is the energy of an equal number of atoms of the bulk crystal and A is the surface area. The surface energy γ is a measure of the thermodynamic stability of the surface with a low, positive value indicating a stable surface. For the hydrated surfaces the surface energies were calculated with respect to liquid water in order to assess the stability of the surface in an aqueous environment:

$$\gamma = \frac{U_d - (U_b + U_{H2O})}{A}$$

3.15

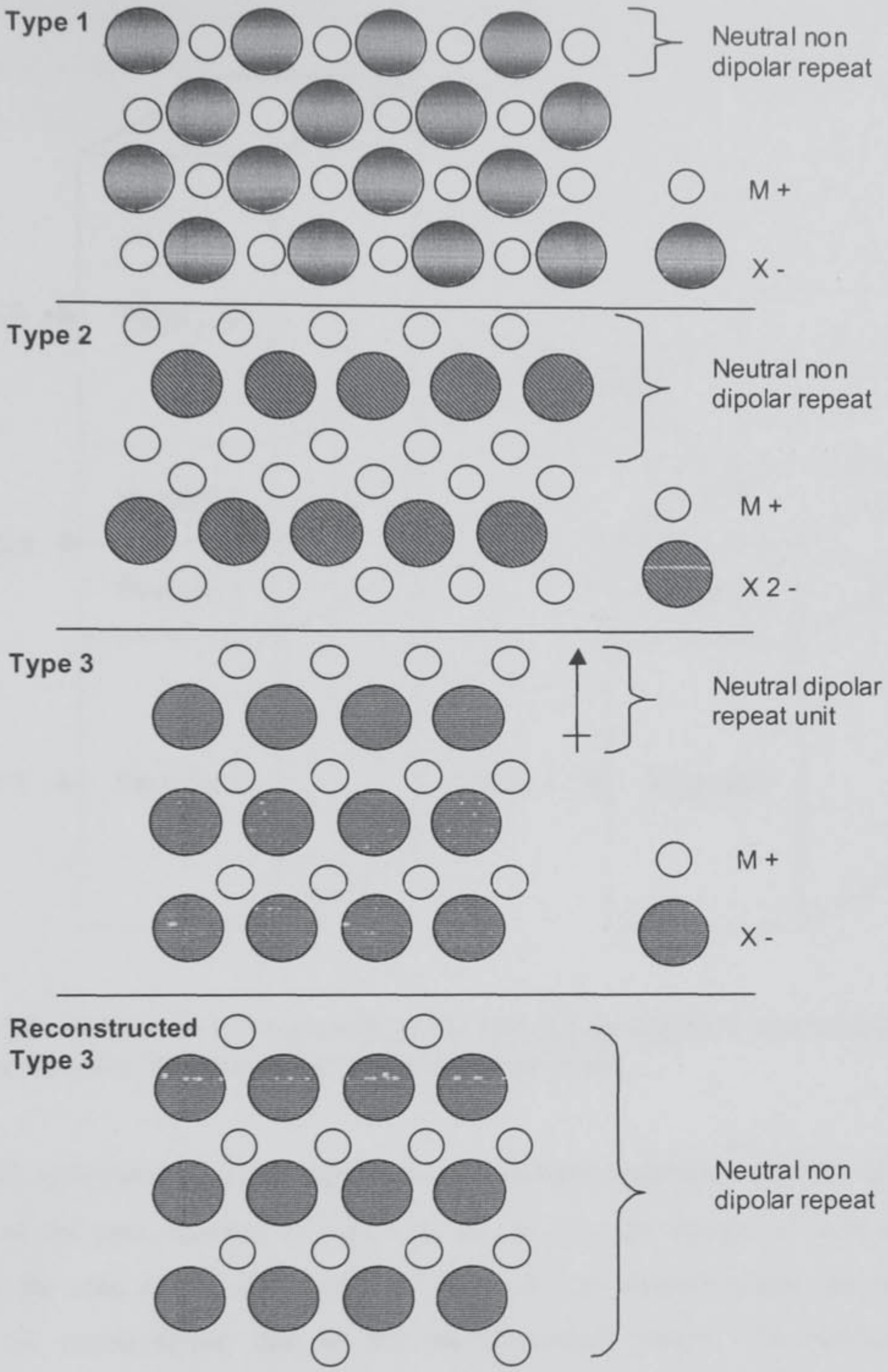

Figure 3.4 Schematic representation of type 1, 2 and 3 surfaces and reconstructed type 3 surface.

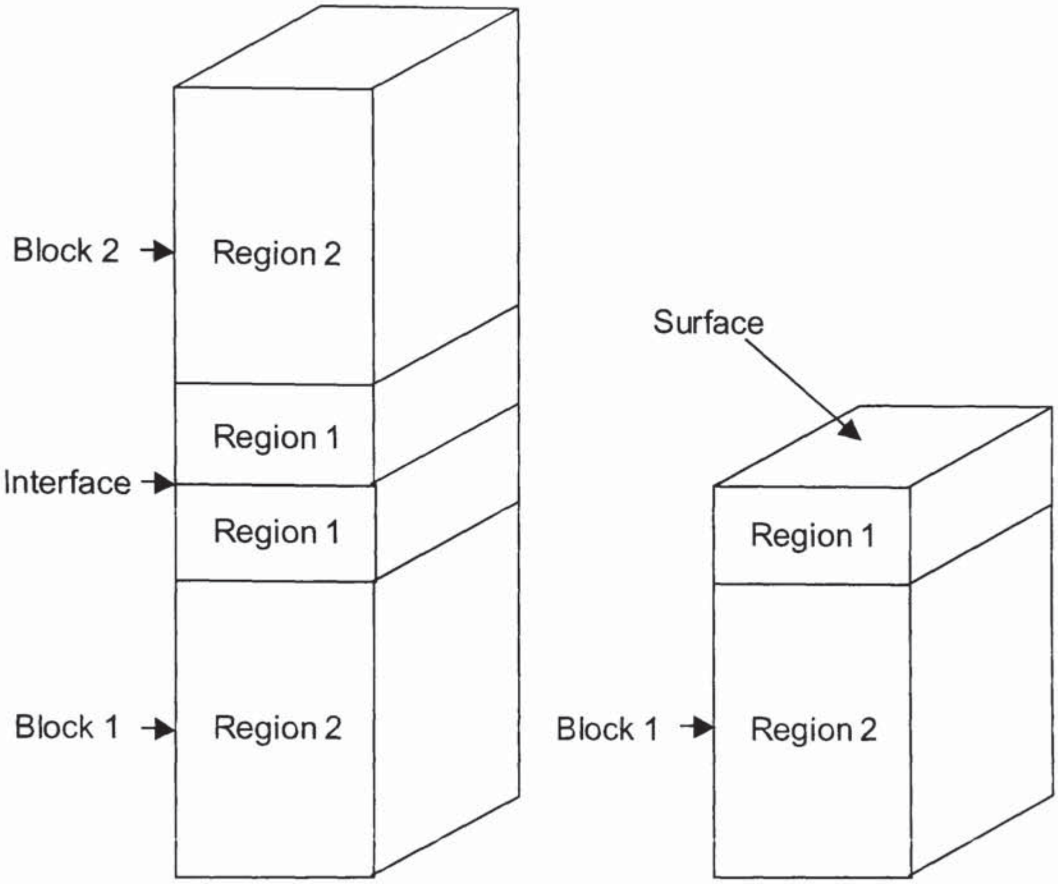

Figure 3.5 Schematic representation of the two region approach used to model an interface between two blocks and a single surface block

where U_d is the energy of the surface block, suitably hydrated, while U_b is again the energy of the same number of bulk ions and U_{H2O} is the energy of bulk water. The latter is the sum of the self-energy of water due to intramolecular forces, and the energy of condensation due to the intermolecular forces. The self-energy for associative adsorption of water is -878.0 kJ mol^{-1} (129) and the energy of condensation of water is -43.0 kJ mol^{-1} from molecular dynamics simulations (122,129) which agrees well with the experimental value of -43.4 kJ mol^{-1} (130). Thus the new surface energy is simply equivalent to the sum of the energy required to cleave the crystal and then add water to the surface.

We need to be confident that in each case the most stable configuration of the surface with adsorbed water layer is found, locating as far as possible the global rather than a local minimum. Thus, several possible configurations need to be investigated, varying both adsorption sites and the initial position of the adsorbed molecules. The calculation of the surface and adsorption energies of dissociative adsorption of water required a value for the energy of dissociation of a water molecule:

$$H_2O(g) + O^{2-}(g) \rightarrow 2(OH)^-(g)$$

Reaction 3.1

However, this requires the second electron affinity of oxygen, which is material dependent (131). This can be overcome by using experimental heats of formation for the reaction:

$$SiO_2(s) + 4H_2O(g) \rightarrow Si(OH)_4(g)$$

Reaction 3.2

The reaction enthalpy for reaction 3.2 was found to be –30.7 kJ mol^{-1} (132-134) and using this, with the calculated lattice energies given in Table 3.3, the energy of dissociation in reaction 3.1 was calculated to be –755.5 kJ mol^{-1}. This value then becomes the effective self-energy of water, U_{H2O}, and can be used directly in Equation 3.14 when dissociative adsorption is modelled.

Table 3.3. Calculated lattice energies, where the lattice energy is the energy released when ions at infinity are brought together into the lattice

	Lattice Energy / kJ mol^{-1}
$SiO_2(s)$	-12414.0
$Si(OH)_4(g)$	-10784.6

The full energy cycle used to calculate the disassociation energy is given in equation 3.16 below where reaction (d) is the sum of (a),(b) and (c) according to Hess's law:

$$\begin{tikzcd}
SiO_2(s) + 2H_2O(g) \arrow[r, "(a)", "\Delta H_f = 30.7\ \text{kJ mol}^{-1}"'] & Si(OH)_4 \arrow[d, "(c)"', "\begin{array}{l}-E(latt)\\ Si(OH)_4(g)\end{array}"] \\
Si^{4+}(g) + 2O^{2-}(g) + 2H_2O(g) \arrow[u, "\begin{array}{r}E(latt)\\ SiO_2(s)\end{array}", "(b)"'] \arrow[r, "(d)"] & Si^{4+}(g) + 4OH^-(g)
\end{tikzcd} \tag{3.16}$$

3.3.2 Surface and bulk crystal adsorption simulations

The static energy minimization simulation code METADISE was also used to determine the lowest energy adsorption site for the sorbed molecules both on the surfaces and within the bulk zeolite crystal channels. Again the static simulation is carried out at 0 K with the energy minimized zeolite lattice structure obtained by one of two methods:

(1). *Constant Volume Minimization*: this is obtained by adjusting the atomic positions within the unit cell until a global minimum is reached.

(2). *Constant Pressure Minimization*: this is obtained by adjusting both the atomic positions and unit cell parameters thus reducing the total strain on the lattice to zero.

The simulation was then used to determine the lowest energy site within the zeolite for the sorbed molecule. The enthalpy of adsorption (q_{st}) of the adsorbed molecules in the zeolites is determined from the following equation:

$$q_{st} = -\mu(Z + mol) + \mu(Z) + \mu(mol)$$

3.17

Where $\mu(Z + mol)$ is the potential energy of the zeolite with sorbed species at equilibrium, $\mu(Z)$ is the potential energy of the zeolite crystal alone and $\mu(mol)$ is the self-energy of the isolated adsorbed molecule.

The potential energies are determined analytically from:

$$\mu = \sum_{ij} \frac{q_i q_j}{r_{ij}} + \sum_{ij} V_{ij}(r_{ij}) + \sum_{ijk} V_{ijk}(r_{ij}, r_{ik}, r_{jk})$$

3.18

Where the first term represents the long-range electrostatic interactions for the zeolite lattice and the adsorbate molecule. The second term represents the two-body potential for the short-range interactions. The third term represents the three-body potential representing the bond bending forces in the zeolite and the adsorbate molecules.

3.4 Gas adsorption in micropores

When a gas is brought into direct contact with a solid the process of sorption occurs where the solid takes up the gas. The gas molecules are then removed from the bulk gas phase by one of two ways.

1. The gas enters the inside of the solid a phenomena known as absorption

2. The gas remains on the outside attached to the surface a phenomena known as adsorption

When both adsorption and absorption occur simultaneously the process is known as sorption. The gas taken up on the surface is called the adsorbate and the solid that takes up the gas is called the adsorbent. Adsorption is a combination of physical and chemical processes in which a substance accumulates on a solid surface when a gas is present near to a solid surface, the gas molecules begin striking the surface and will either adsorb onto the surface or rebound off. Over time this will result in a higher concentration of gas molecules located at the surface of the solid than in the bulk gas phase.

Gas molecules can attach themselves onto surfaces in one of two ways:

1. Physical adsorption (physisorption): this is the result of weak electrostatic forces, which cause the attraction of the adsorbate to the surface. These forces include dipole-dipole interactions, van-der-Waals forces and hydrogen bonding.

2. Chemical adsorption (chemisorption): this is a result of the adsorbate forming strong chemical bonds with the surface. This type of interaction is of several orders of magnitude stronger than physisorption. Chemisorption can only occur at specific surface locations known as chemically active sites (e.g. enzymes / catalysts).

In general porous solids can be classified according to their pore sizes .

1. Porous solids with pores openings exceeding 500 Å in diameter are classified as being macroporous.

2. Porous solids with pore diameters not exceeding 20 Å are termed as microporous (eg molecular sieve zeolites).

3. Porous solids with pores of intermediate size are called mesoporous (20 Å < Pore Diameter < 500 Å)

Construction of an adsorption isotherm is the most convenient way of gaining an understanding of the surface area and porosity of an adsorbent. When the quantity of adsorbate on a surface is measured over a range of relative pressures at a constant temperature, the result is an adsorption isotherm. The adsorption isotherm is constructed by exposing the adsorbent sample to successive known volumes of adsorbate and then measuring the equilibrium pressure. Similarly desorption isotherms are obtained by measuring the quantities of gas removed from the sample as the relative pressure is lowered. All adsorption isotherms may be classified into one of the five types as shown in Figure 3.6 according to Brunauer (135).

- **Type I** or Langmuir isotherms are concave to the relative pressure (P/P_o) axis and the amount of adsorbate approaches a limiting value as (P/P_o) approaches 1 . This type of adsorption isotherm is exhibited by micorpourous solids having relatively small external surfaces, for example molecular sieve zeolites. The limiting uptake of adsorbate is governed by the accessible micropore volume rather than by the internal surface area.
- **Type II** isotherms are the normal form of isotherm obtained with a nonporous or macroporous adsorbent. This type of isotherm represents unrestricted monolayer-multilayer adsorption. The start of the linear central region of the isotherm is usually taken as the relative pressure at which monolayer coverage is complete.

- **Type III** isotherms are convex to the relative pressure axis over its entire range. These isotherms are rarely encountered.
- **Type IV** isotherms are associated with capillary condensation in mesopores, indicated by the steep slope at higher relative pressures. The initial part of the isotherm is similar to that of the type II.
- **Type V** isotherms are uncommon and correspond to the type III, except that the pores in the mesopore range are present.

The phenomenon of adsorption depends on the degree to which the available surface is covered with adsorbate molecules. The fractional coverage of a surface is defined by the quantity θ:

$$\theta = \frac{N_O}{N_T} = \frac{V}{V_m} = \frac{W}{W_m} \tag{3.19}$$

Where N_O is the number of occupied adsorption sites and N_T is the total number of possible adsorption sites. V is the volume of gas adsorbed at a relative pressure (P/P_o) and V_m is the volume of gas, which could cover the entire adsorbing surface with a monomolecular layer. W is the weight of adsorbate at a given relative pressure (P/P_o)and W_m is the weight of adsorbate in a monomolecular layer.

In general there are two main models on the theory of adsorption the Langmuir and the Brunauer, Emmett and Teller (BET) models. A full explanation of these models can be found in references (136-138).

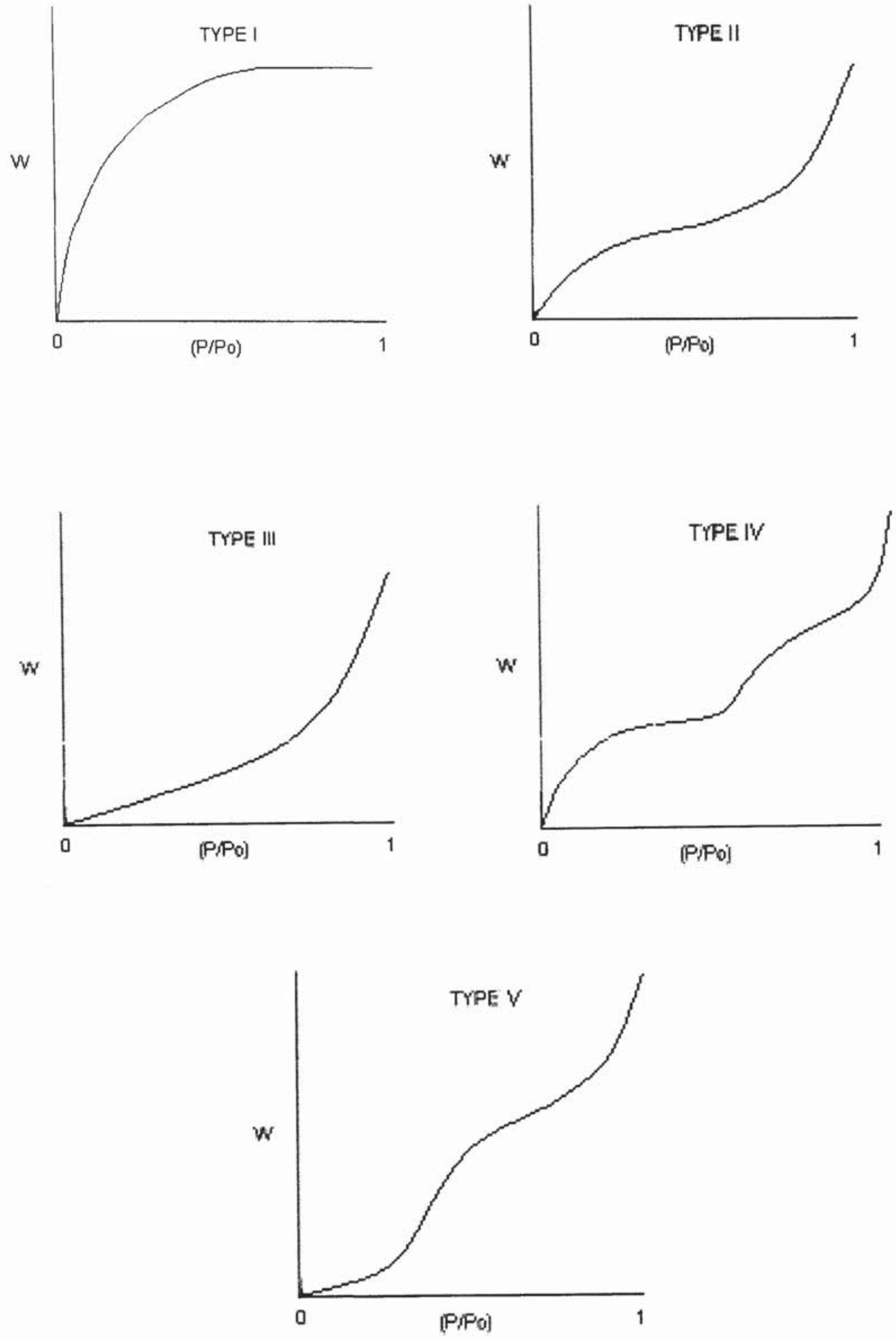

Figure 3.6 Isotherm types (135)

Chapter 4: Synthesis and Characterization of Zeolite Membranes

Chapter 4: Synthesis and Characterization of Zeolite Membranes

4.0 Introduction

In this chapter the procedures for synthesizing silicalite-1 and NaA zeolite layers onto carbon-graphite supports using a standard hydrothermal synthesis method is reported and discussed. The subsequent characterization of the composite membranes by Scanning electron microscopy (SEM), X-ray diffraction (XRD), Fourier transform infrared spectroscopy (FTIR), Thermogravimetric analysis (TGA), Nitrogen sorption capacity measurements and X-ray photoelectron spectroscopy (XPS) is also reported and discussed.

4.1 Experimental procedures:

4.1.1 Synthesis of silicalite-1/carbon-graphite composite membranes

4.1.1.1 Carbon-graphite support preparation

Carbon-graphite discs each with diameter 40 mm and thickness 2 mm were cut from a graphite rod grade Y597 purchased from Olmec (see figure 4.1 for picture of discs). The carbon-graphite discs were analysed by X-ray photoelectron spectroscopy (XPS) to determine the initial surface oxygen content. In this research, XPS was used to study the carbon-graphite supports surface to determine the oxygen to carbon ratios before and after chemical oxidation of the supports. The XPS investigations were performed in a VG ESCALAB 200-D spectrometer with MgKα X-ray radiation. In XPS the sample is irradiated with monochromatic X-rays which produce photoelectrons from core levels in the atoms near to the surface. Measurement of the photoelectron energies allows the identification of the elements present in the near surface region and gives information on the chemical compounds present. Measurement of the numbers of electrons emitted at a given energy allows atomic concentrations to be determined. The XPS measurements were carried out by Aston Surface Analysis, Aston University. The surface oxygen content has been shown to be vital in the successful growth of zeolite onto carbon graphite surfaces (30,36). The calculated initial average surface oxygen to carbon ratio for the graphite supports was found to be 0.006 with a standard deviation of 0.001 (see Table 4.1).

A total of nine carbon-graphite discs were fabricated of which three carbon-graphite discs were oxidized in boiling HNO_3 solution (70% wt) for 4 h and another set of three oxidized for 24 h. The last set of three were left unmodified. Following the acid treatment the supports were thoroughly washed with distilled water and dried for 15 h in an oven at 130°C. An XPS analysis was carried out on the 4 h and 24 h oxidized samples giving average surface oxygen to carbon ratios of 0.028(6) and 0.029(4) respectively.

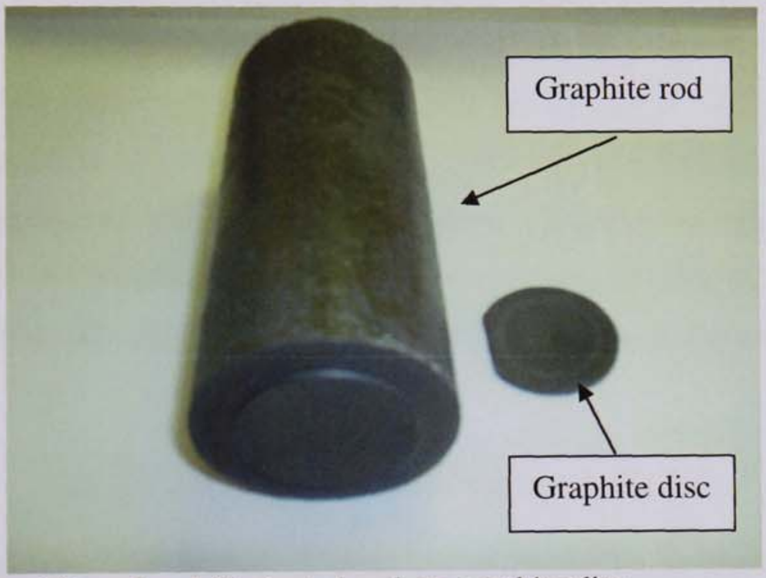

Figure 4.1 Graphite rod and fabricated carbon-graphite disc

Table 4.1 Graphite samples surface oxygen : carbon ratios determined from XPS.

Graphite Sample	HNO_3 Oxidation Duration (hours)	O (1s) (AT)%	C (1s) (AT)%	O : C ratio
A	0	0.573	99.427	0.006
B	0	0.57	99.43	0.006
C	0	0.696	99.304	0.007
D	4	2.765	97.235	0.028
E	4	3.2	96.8	0.033
F	4	2.111	97.889	0.022
G	24	2.558	97.442	0.026
H	24	2.768	97.232	0.028
I	24	3.206	96.794	0.033

4.1.1.2 Silicalite-1 membrane synthesis

Silicalite-1 layers were grown onto all the three sets of graphite supports using standard hydrothermal synthesis method. The resulting silicalite-1/carbon-graphite composites were labelled as follows: 4 hour oxidized carbon-graphite: SIL1, SIL2 and SIL3, 24 hour oxidized carbon-graphite: SIL4, SIL5 and SIL6; unmodified (non-oxidized) carbon-graphite: SIL7, SIL8 and SIL9. The batch preparation of the reaction mixture follows that of Grose and Flanigan (139) using tetrapropylammonium bromide and is as follows:

1.4 g of NaOH (Alfa Aesar, J2524A) was added to 10g of deionised water and stirred for 10 minutes or until the NaOH pellets dissolved. Following this 44g of an aqueous colloidal silica sol containing 30% by weight SiO_2 (Alfa Aesar, 10097749) was added to the NaOH solution resulting in an alkaline silica solution. 2.4g of the templating agent tetrapropylammonium bromide (Alfa Aesar, H4726C) was added to 15g of deionised water and stirred until dissolved. The template solution was then added to the above alkaline silica solution. This resulted in a reaction mixture with molar composition:

$$1\ \mathrm{SiO2} : 0.041\ \mathrm{TPA\text{-}Br} : 0.159\ \mathrm{NaOH} : 14.09\ \mathrm{H_2O}.$$

The graphite supports were placed vertically into a 200 ml Teflon lined stainless steel autoclave vessel (see figure 4.2). The autoclaves temperature can be controlled from -5 to 250°C with a maximum operating pressure of 60 Bars. The synthesis solution was poured into the autoclave and the graphite supports subjected to 3 h ageing time followed by hydrothermal synthesis at 200°C for 24 h. The as-synthesized membranes were washed with distilled water and dried overnight in an oven at 120–130°C. The drying temperature was found to have no effect on the synthesised composite membranes. It was found that for the silicalite-1/carbon-graphite membranes, that only one hydrothermal synthesis was necessary to obtain full coverage of the support. This was true for all oxidized support membranes except for SIL6, which required two hydrothermal synthesis to obtain full coverage of the support.

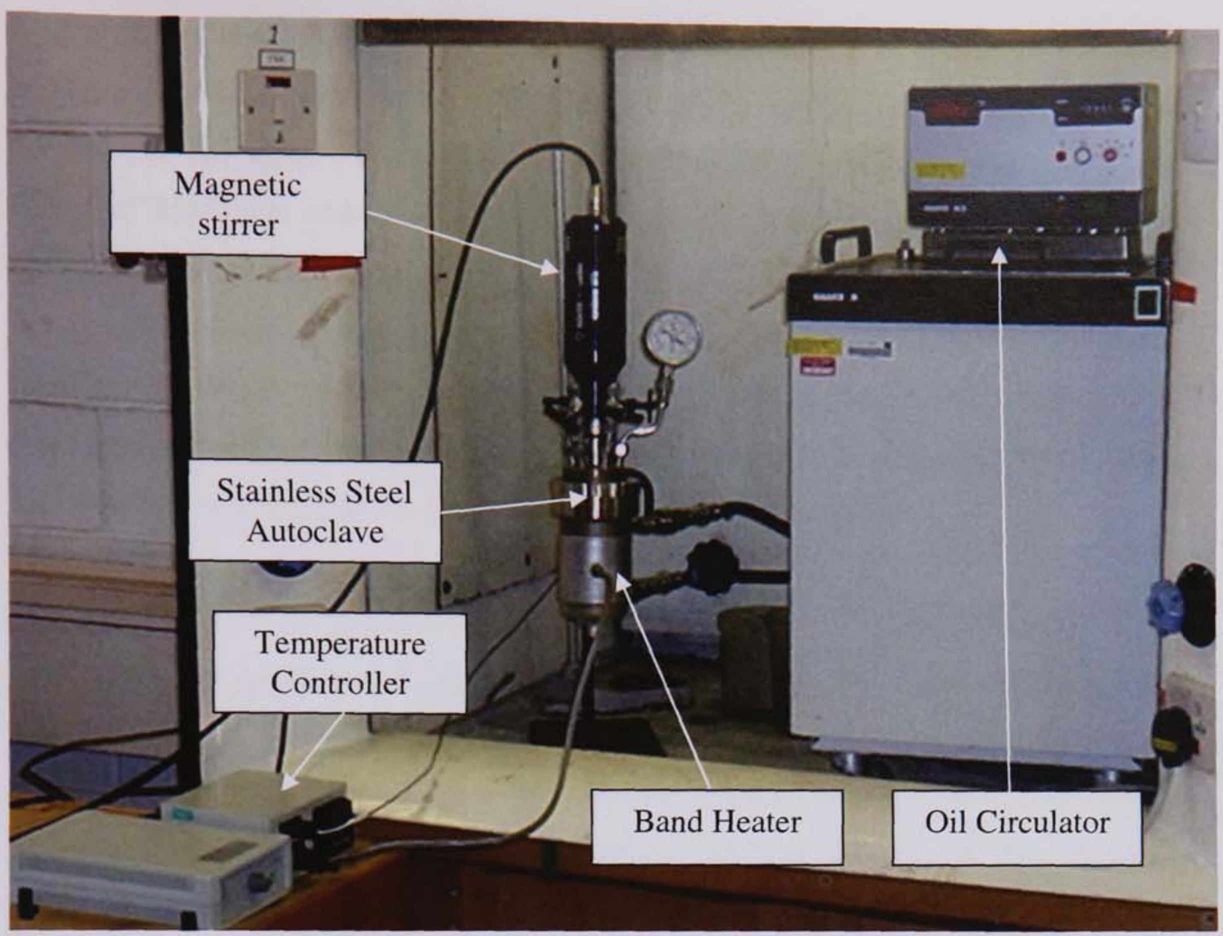

Figure 4.2 Membrane synthesis 200 mL stainless steel autoclave vessel

In order to remove the templating agent from the prepared silicalite-1/carbon-graphite composite membranes the prepared samples were placed in a vertical muffle furnace and heat treated at 700°C (30) under a constant flow of nitrogen (200 cm^3/min). The oven was allowed to reach the 700°C temperature over a two hour period. After a further two hours at this temperature the oven was switched off and allowed to cool down overnight under a constant flow of nitrogen.

4.1.2 Synthesis of NaA/carbon-graphite composite membranes

Another set of three carbon-graphite discs, oxideized for 24 hours were prepared and used for the NaA composite membrane synthesis. NaA layers were grown onto all three graphite supports (NaA membrane NaA1, NaA2 and NaA3) using standard hydrothermal synthesis method. The batch preparation of the reaction mixture follows that Thompson and Huber (140) and is as follows:

0.723g of NaOH (Alfa Aesar, J2524A) was dissolved into 80 mL of deionised water and mixed until the NaOH pellets were completetly dissolved. This solution was then divided into two equal volume parts. To one part 8.258 g of sodium aluminate (Alfa Aesar, I27M35) was added and mixed for 30 minutes until completely dissolved. To the second half of the sodium hydroxide solution 15.48 g of sodium metasilicate (Alfa Aesar, I3990A) was added and mixed for 30 minutes until the solution became clear. Finally the silicate solution was poured quickly into the aluminate solution and thoroughly mixed until homogenized. It was observed a thick colourless gel formed. The resultant reaction mixture formed had a molar composition of:

$$1\ Na_2O.\ Al_2O_3 : 2.518\ Na_2SiO_3 : 0.359\ NaOH : 88.232\ H_2O$$

The graphite supports were placed vertically into the Teflon lined stainless steel autoclave vessel. The synthesis gel was poured into the autoclave, which was then sealed and subjected to a hydrothermal synthesis at 90°C for 24 h. The as-synthesized membranes were washed with distilled water and dried overnight in an oven at 120–130°C. It was found in all cases that the NaA coating on the supports was not consistent and thus a further hydrothermal synthesis was required to form a uniform layer of NaA onto the carbon-graphite.

In order to remove any adsorbed water within the cages of the NaA zeolite layer the prepared NaA/carbon-graphite composite membranes were placed in a vertical muffle furnace and heat treated following a similar procedure as treated for silicalite-1 composite membranes.

4.1.3 Blank carbon-graphite membranes

In comparing the permeation properties of the prepared zeolite/carbon-graphite composite membranes with blank carbon-graphite membranes two blank carbon-graphite discs (without zeolite deposition) were prepared of which one was oxidized with HNO_3 solution for 24 h (BGCO1) while the other disc was left unmodified (BCGN1). In addition both blank carbon-graphite discs were subjected to similar calcination conditions as given to the zeolite/carbon-graphite composite membranes.

4.2 Zeolite/membrane characterization

Different characterization methods were used to elucidate the properties of the synthesised composite membranes. The characterization techniques used are Scanning Electron Microscopy (SEM), X-ray Diffraction (XRD), N_2-Physisorption analyses, Fourier Transform Infrared (FTIR) investigations and Thermogravimetric Analyses (TGA).

4.2.1 Scanning Electron Microscopy (SEM)

Scanning Electron Microscopy (SEM) was used in this research for high magnification imaging, elemental analysis and for the determination of the orientation of the zeolite layer of the prepared composite zeolite membranes. A Cambridge Stereoscan 90 (SEM) coupled to an Energy Dispersive X-ray Analyser (EDXA) for analysing sample chemical composition was used for the analysis. In the preparation of the samples, the membranes surfaces were coated with gold using the sputter technique. The samples were held in position with carbon tape in order to obtain top views of the membranes. The thickness of the zeolite layers were obtained by taking a cross-sectional cut through the membrane and viewing under SEM. The cross-sectional cuts were prepared by one of two methods firstly by cutting and viewing under SEM or mounting the cut section in bakelite to form a pellet which was then polishing down to 1 µm finish and viewed under SEM to obtain zeolite layer thickness. The SEM analyses were carried out at Aston Microscopy and Engineering, Aston University.

The morphology of the synthesized membranes was examined and selections of micrographs obtained for the silicalite-1/carbon-graphite and NaA/carbon-graphite composite membranes are given in Figures 4.3 and 4.4 respectively (the remaining micrographs can be found in appendix A). In general the silicalite-1 layer on all composite membranes had random non-preferential crystallographic orientation with no visible cracks or pinholes. For all composite membranes the carbon-graphite materials were weighed before and after membrane synthesis. The weight gains on each carbon-graphite are given in Tables 4.2a to 4.2d. This enables the calculation of the membrane thickness accessible for gas permeation. The calculated thicknesses based on the weight increase and assuming a density of 1.76 g/cm^3 (141,142) for silicalite-1 and 1.99 g/cm^3 for NaA (143) are also given in Table 4.2a to 4.2d. This was compared to the measured thicknesses obtained from the SEM images of a cross section through the membrane. For the silicalite-1 the SEM images shown in figure 4.3d clearly show the characteristic hexagonal shape of the silicalite-1 crystals thus indicating the deposition of silicalite-1 on the carbon-graphite. It was observed that the silicalite-1 growth on the non-oxidized carbon-graphite (Figure 4.3f) was not entirely uniform in comparison to the oxidized carbon-graphite (Figures 4.3a and 4.3d and see appendix A). This was reflected in the wide range of observed thicknesses obtained from the SEM and regions of little or no surface coverage. The consistent coverage of silicalite-1 on the oxidized support suggest the oxygen groups act as defect nucleation sites on the carbon-graphite surfaces promoting crystal growth. This confirms the work of Garcia-Martinez et al. (36) who suggested the influence of surface chemistry and porosity of carbon support favours the growth of zeolite phases. However, the findings in this work did not support their conclusion that no zeolite growth occurred on non-oxidized carbon-graphite. This is probably due to the differences in the raw carbon-graphite material used in both studies even though the initial surface oxygen to carbon ratio of 0.006 as calculated in this work is much lower than their reported value of 0.052.

For the NaA the SEM images shown in figure 4.4b and in appendix A clearly show cubic shaped crystals which are characteristic of the LTA type zeolites thus indicating the deposition of NaA on the carbon-graphite. It was observed that the NaA growth on the carbon-graphite was not uniform (Figures 4.4a and 4.4b and see appendix A) which was reflected in the larger range of observed thicknesses obtained from the SEM compared to that of silicalite-1. It was seen overall that even though the NaA /carbon-graphite composite membranes required two hydrothermal synthesis they still had comparable thicknesses to that of the silicalite-1/carbon-graphite composite membranes.

Table 4.2a 4 hour oxidized carbon-graphite supports calculated and observed silicalite-1 layer thicknesses.

Membrane	Weight Before Hydrothermal Synthesis (g)	Weight After Hydrothermal Synthesis (g)	Weight gain (g)	Calculated Thickness (μm)[d]	Observed thickness from SEM (μm)[e]
	4 hour oxidized carbon-graphite support composites				
SIL1	4.0914	4.3384	0.247	50.76	50-70
SIL2	4.1201	4.2431	0.123	25.28	30-70
SIL3	4.0901	4.2396	0.1495	30.73	30-60

(a) 1st hydrothermal synthesis (b) 2nd Hydrothermal synthesis (c) Total membrane thickness (d) Assuming uniform thickness over entire surface of graphite support (e) Thickness based on a cross section cut through the membrane.

Table 4.2b 24 hour oxidized carbon-graphite supports calculated and observed silicalite-1 layer thicknesses.

Membrane	Weight Before Hydrothermal Synthesis (g)	Weight After Hydrothermal Synthesis (g)	Weight gain (g)	Calculated Thickness (μm)[d]	Observed thickness from SEM (μm)[e]
	24 hour oxidized carbon-graphite support composites				
SIL4	4.0939	4.2733	0.1794	36.87	30-50
SIL5	4.0173	4.2216	0.2043	41.99	25-50
SIL6	4.0989 (a) 4.4733 (b)	4.4733 (a) 4.8791 (b)	0.3744 (a) 0.4058 (b)	76.95 (a) 83.40 (b)	100-180 (c)

Table 4.2c Non-oxidized carbon-graphite supports calculated and observed silicalite-1 layer thicknesses.

Membrane	Weight Before Hydrothermal Synthesis (g)	Weight After Hydrothermal Synthesis (g)	Weight gain (g)	Calculated Thickness (μm)[d]	Observed thickness from SEM (μm)[e]
	Non-oxidized carbon-graphite supports composites				
SIL7	3.9789	4.0436	0.0647	13.30	0-30
SIL8	3.8384	3.9666	0.1282	26.35	0-150
SIL9	4.103	4.1747	0.0717	14.74	0-150

Table 4.2d 24 hour oxidized carbon-graphite supports calculated and observed NaA layer thicknesses.

Membrane	Weight Before Hydrothermal Synthesis (g)	Weight After Hydrothermal Synthesis (g)	Weight gain (g)	Calculated Thickness (μm)[d]	Observed thickness from SEM (μm)[e]
24 hour oxidized carbon-graphite support composites					
NaA1	3.9271 (a)	3.9989 (a)	0.0718 (a)	13.05 (a)	11-44 (c)
	3.9989 (b)	4.0874 (b)	0.0885 (b)	16.09 (b)	
NaA2	4.2546 (a)	4.3455 (a)	0.0909 (a)	16.52 (a)	6-68 (c)
	4.3455 (b)	4.3852 (b)	0.0397 (b)	7.22 (b)	
NaA3	4.1219 (a)	4.2040 (a)	0.0821 (a)	14.92 (a)	4-14 (c)
	4.2040 (b)	4.2282 (b)	0.0242 (b)	4.40 (b)	

(a) 1st hydrothermal synthesis (b) 2nd Hydrothermal synthesis (c) Total membrane thickness (d) Assuming uniform thickness over entire surface of graphite support (e) Thickness based on a cross section cut through the membrane.

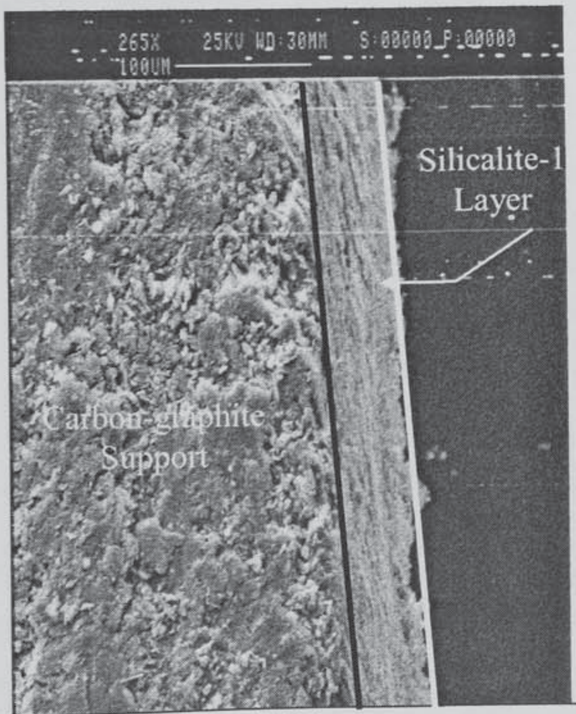

(4.3a)

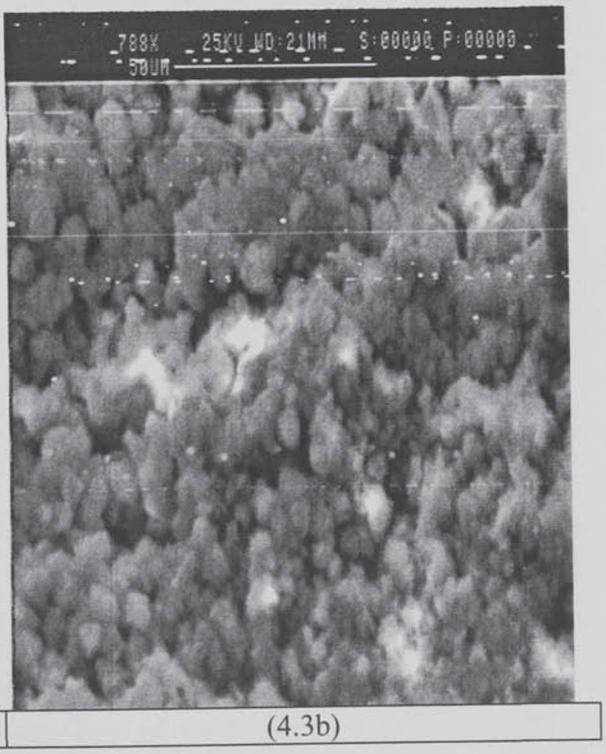

(4.3b)

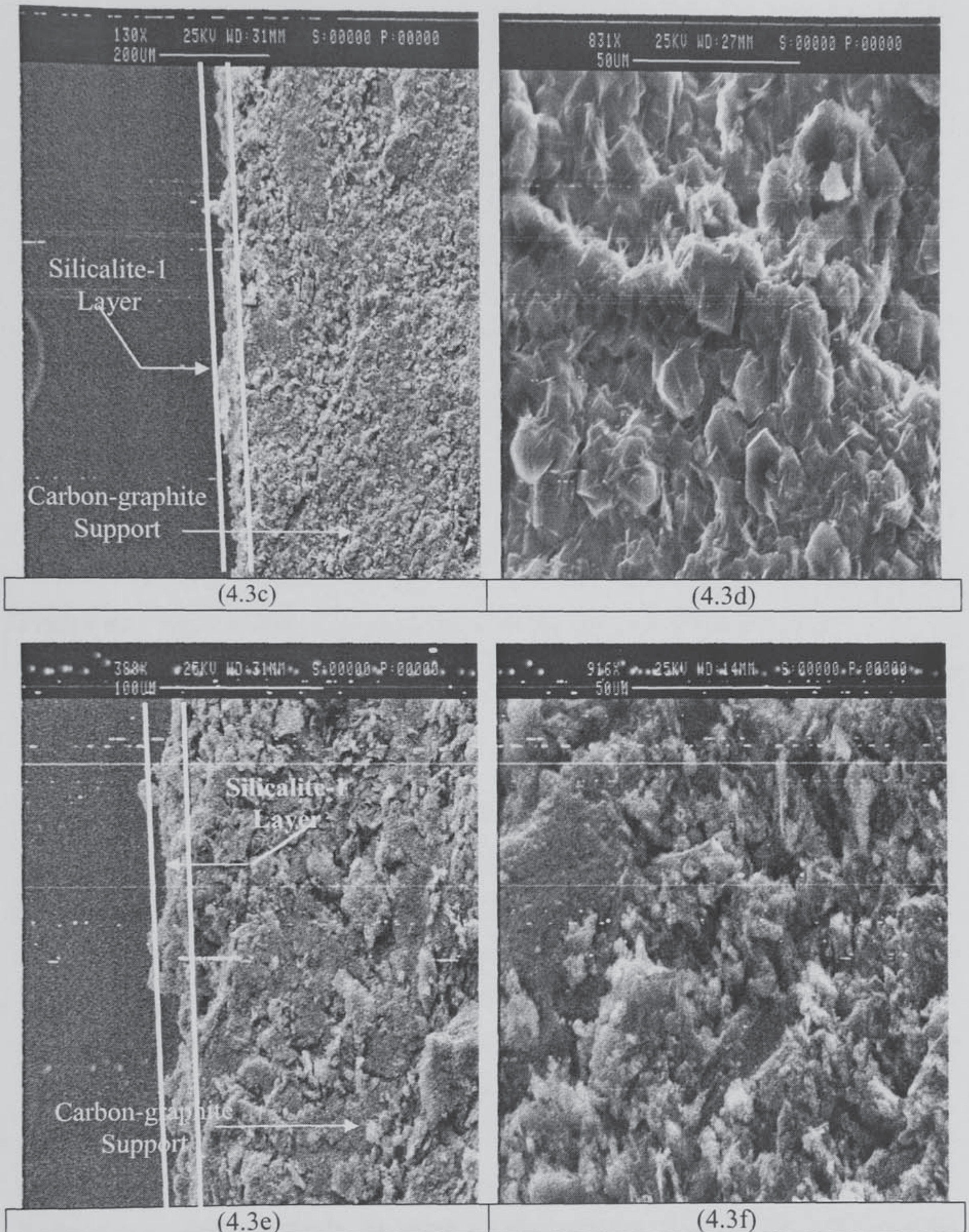

(4.3c) (4.3d)

(4.3e) (4.3f)

Figure 4.3 Representative micrographs of silicalite-1/carbon-graphite composite membranes*: (a) and (b) Cross section and top view of SIL3; (c) and (d) Cross section and top view of SIL4; (e) and (f) Cross section and top view of SIL7 .

*SIL3 – Carbon-graphite oxidized for 4 h, SIL4 – Carbon-graphite oxidized for 24 h SIL7 – Non-oxidized carbon-graphite support.

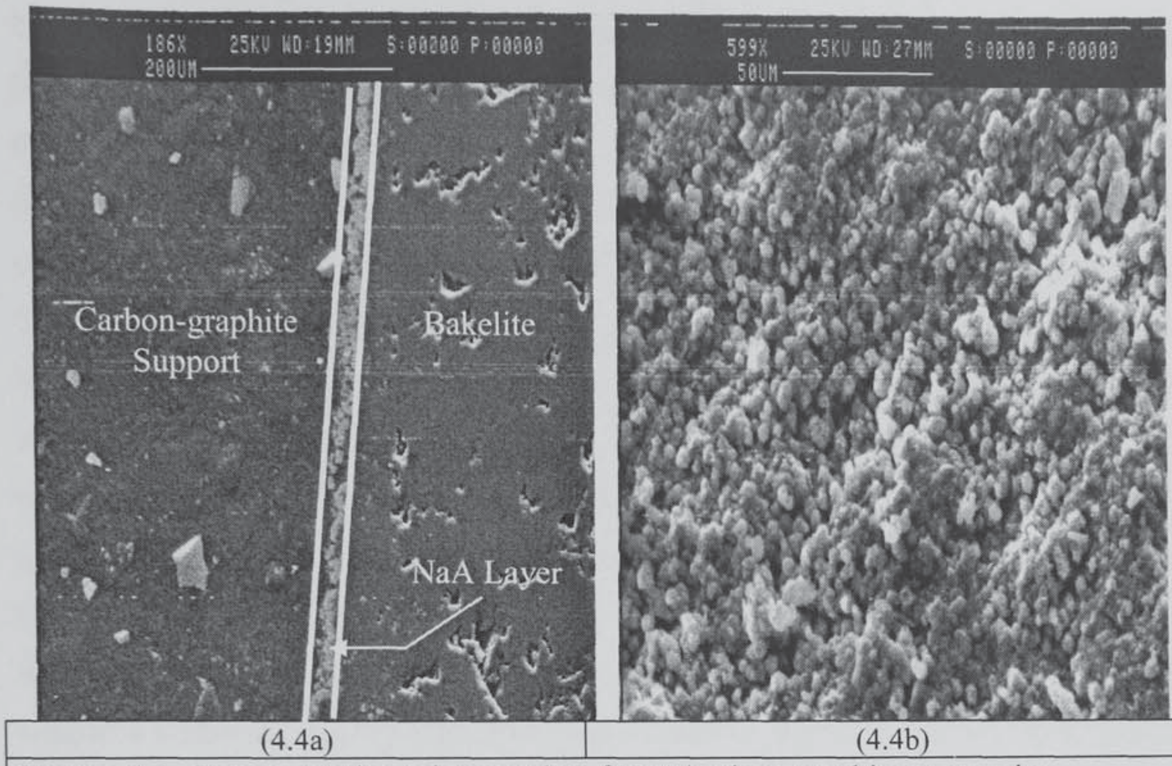

(4.4a) (4.4b)

Figure 4.4 Representative micrographs of NaA/carbon-graphite composite membranes: (a) Cross section view of NaA1; (b) Top view of NaA1.

4.2.2 N_2-Physisorption analyses

Measurements of gas adsorption isotherms are widely used for determining the surface area and pore size distribution of solids. The first step in the interpretation of a physisorption isotherm is to identify the isotherm type. This in turn allows for the correct methods for evaluation of the samples properties. The Brunauer-Emmett-Teller (BET) (144) method is the most commonly used standard procedure to measure surface areas, despite of the oversimplification of the model on which the method is based. In this work, N_2 adsorption measurements were carried out to determine physical characteristics of the composite membranes. Specific surface areas (m^2/g) and pore volumes were measured according to the standard BET (144) and Dubinnin-Radushkevich (145) methods, by using a Quantachrome NOVA 1200 Gas Sorption equipment. The specific surface areas and pore volumes of the samples were obtained from N_2 adsorption isotherms at -196°C. The samples were outgassed in a vacuum at 350°C overnight before conducting the analysis. The micropore size distributions for the samples were calculated from N_2 -adsorption isotherms by the HK (Horvath-Kawazoe) (146) method.

Nitrogen gas adsorption analysis was carried out on the synthesized silicalite-1 and NaA samples taken from each of the membranes and also on small samples cut from the blank carbon-graphite supports. Each sample was degassed for 24 h at 350°C (maximum degassing temperature of NOVA 1200 equipment) under vacuum. In each case the pore size and surface area were determined and the results are presented in Table 4.3. The pore width for the silicalite-1 samples calculated by the Horvarth-Kawazoe (HK) (146) method are in the range 0.54-0.56 nm which is in agreement with actual pore width of silicalite-1. But for the NaA the Horvarth-Kawazoe (HK) (146) method predicts pore sizes in the range of 0.89-1.03 nm these are clearly much larger than the actual pore widths of 0.41 nm for the NaA zeolite. A possible reason for this my be due to the fact as discussed earlier that the NaA zeolite may not have been fully degassed at 350°C and that significant quantities of water may have remained within the cages of the NaA. This is also evident from the low BET surface areas obtained for all three NaA samples.

The blank carbon-graphite samples (BCGN1 and BCGO1) were noticed to have much larger pore sizes than the silicalite-1 and NaA samples. The Dubinin-Radushkevich (145) micropore volume shows significant differences between the samples and in general the microporosity of the silicalite-1 samples is much broader compared to either the blank carbon-graphite or NaA. The blank non-oxidised carbon-graphite membrane BCGN1 (without silicalite-1 deposition), showed a much higher BET micropore surface area than its oxidized form. This confirms the work of Moreno-Castilla et al. (147) who found a reduction in the surface area following chemical oxidation by HNO_3 and concluded this was due to destruction of the pore walls by oxidant treatment.

The nitrogen gas adsorption analysis confirms that the samples are microporous in nature and in the absence of any significant defects the molecular sieving and separation properties of the membranes should be duly observed.

Table 4.3 N_2 adsorption analysis at -196°C of silicalite-1, NaA and the carbon-graphite materials.

Samples	BET Surface Area	Micropore Volumea	HK Pore Width
	(m^2/g)	(cm^3/g)	(nm)
SIL1	180.7	0.09	0.55
SIL2	241.2	0.10	0.56
SIL3	167.7	0.09	0.54
SIL4	195.7	0.06	0.56
SIL5	189.4	0.14	0.56
SIL6	147.0	0.04	0.55
SIL7	197.7	0.04	0.55
SIL8	138.8	0.04	0.55
SIL9	103.8	0.07	0.56
BCGN1	15.3	0.01	1.89
BCGO1	10.9	0.01	1.82
NaA1	102.5	0.04	0.89
NaA2	65.5	0.02	1.03
NaA3	69.2	0.02	1.01

[a] Micropore volume obtained from Dubinin-Radushkevich (145) method.

4.2.3 X-Ray diffraction (XRD)

Powder X-Ray diffraction (XRD) was used to investigate the zeolite crystal phases present in the sample. X-rays are energetic enough to penetrate into the material and their wavelengths are of the same order of magnitude as interatomic distances in solids. Thus as seen in figure 4.5, a beam of X-rays is diffracted by the crystalline phases in the sample according to Bragg's Law:

$$n\lambda = 2d \sin\theta_{diff} \tag{4.1}$$

where λ is the wavelength of the X-rays, d is the distance between two atomic planes in the crystalline phase, n is the order of the diffraction, and θ_{diff} the incoming diffraction angle. The X-ray powder diffractograms were obtained using a Philips PW1730 diffractometer with a CuKα 1.54 Å radiation source. Diffraction patterns were compared and referenced to those obtained from the International Zeolite Association (IZA) diffraction pattern libraries (148). XRD facilities at the School of

Applied Sciences, University of Wolverhampton were used. Powder X-ray diffraction was carried out on all silicalite-1 and NaA samples grown and compared to reference silicalite-1 and NaA X-ray diffraction data (see figures 4.7, 4.11 and 4.12).

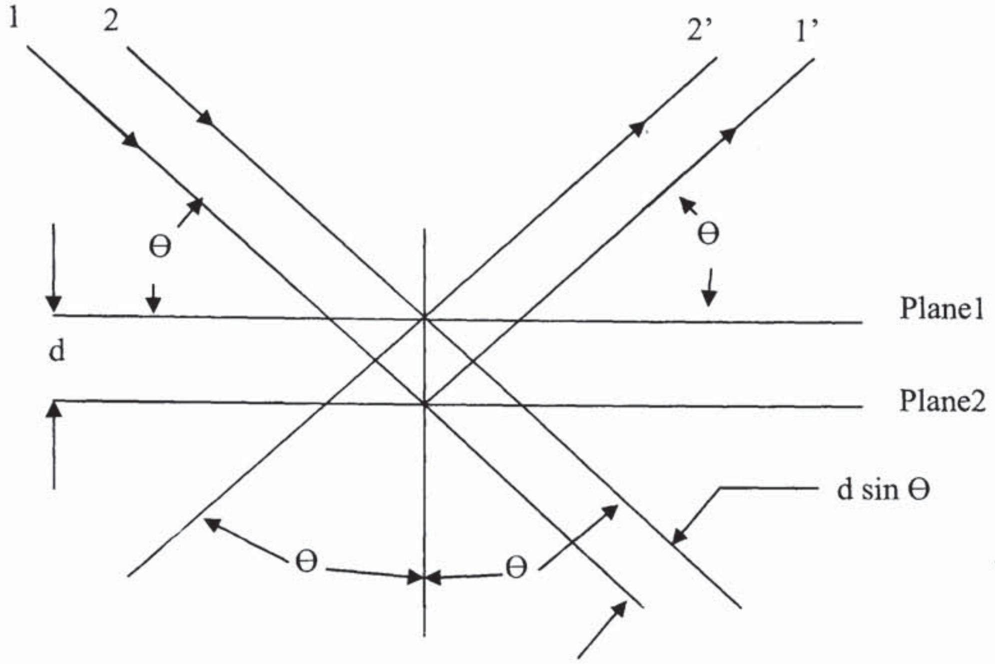

Figure 4.5 Diffraction of x-rays by crystal lattice planes of separation d

For the silicalite-1 membranes it was confirmed that only the MFI type zeolite was present. For the NaA membranes it was found that two different zeolite types were present namely NaA and Sodalite (SOD). Both NaA and SOD zeolites have beta cage type structures, the difference between the two is that in NaA the beta cages are linked together by double-4-rings (D4R) while in the SOD the beta cages are linked by single-4-rings (S4R) as seen in figure 4.6. Typical XRD patterns for silicalite-1 and NaA/SOD obtained following the composite membrane synthesis are shown in figures 4.8-4.10 and figure 4.13 respectively (the remaining XRD patterns can be found in appendix B) confirming the presence of silicalite-1 and NaA/SOD structures.

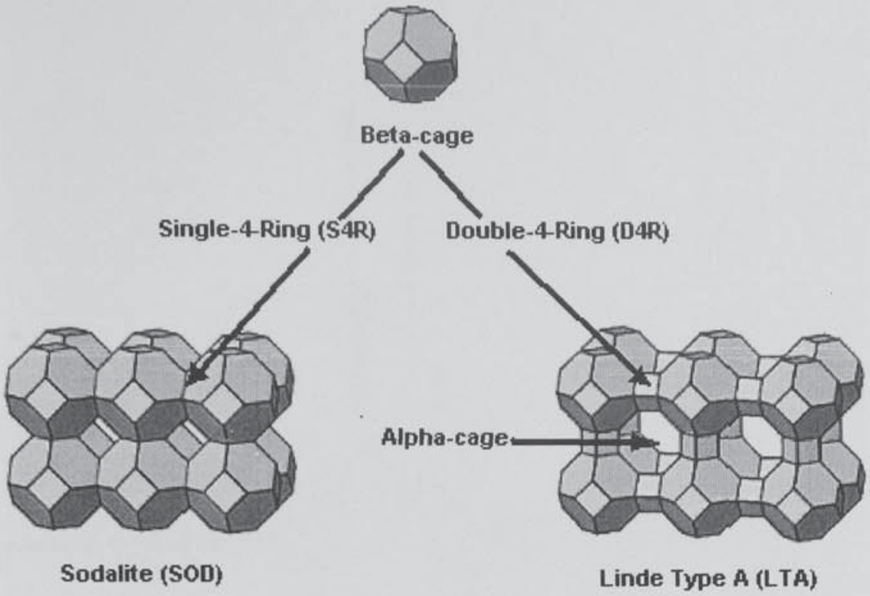

Figure 4.6 Structure of Sodalite and Linde Type A zeolites.

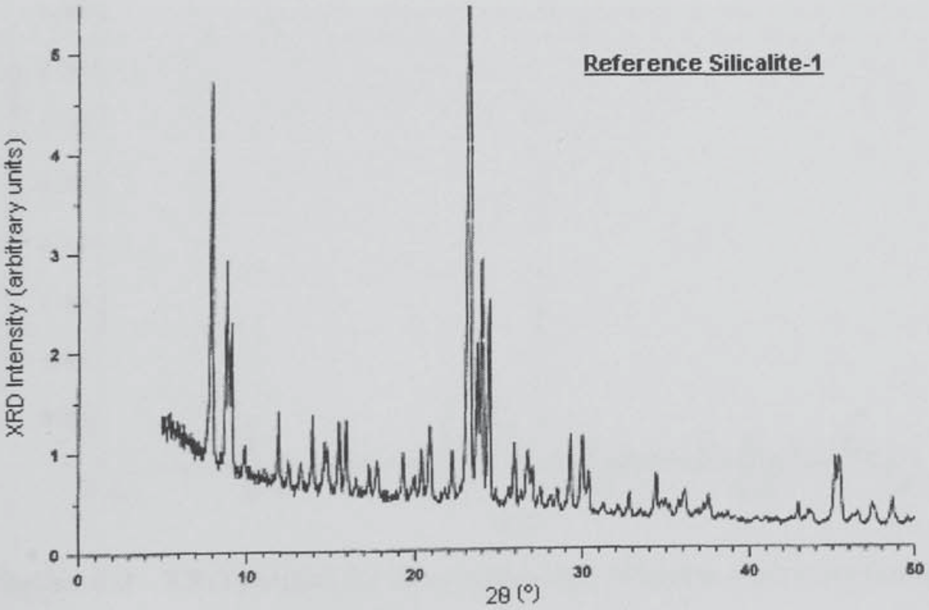

Figure 4.7 Reference XRD pattern for silicalite-1 (148)

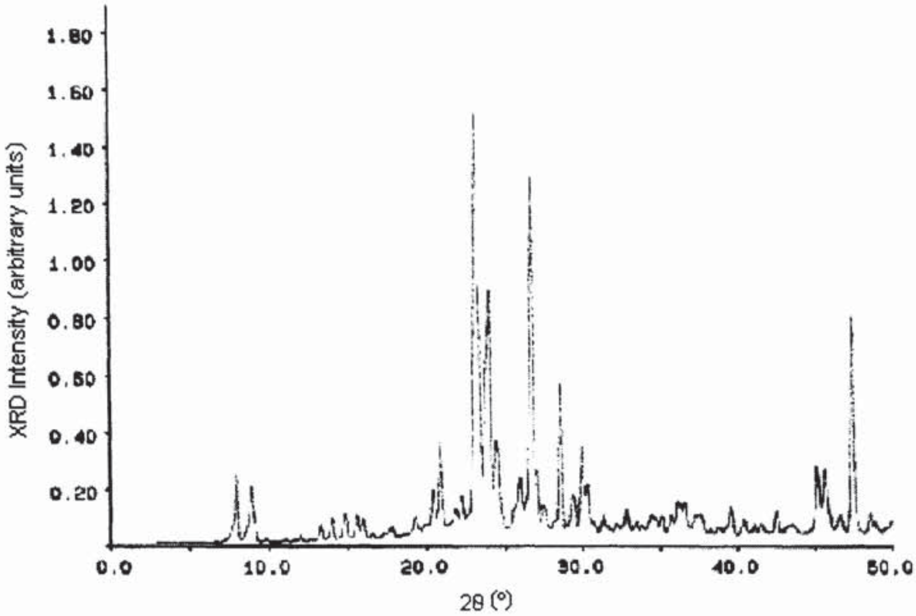

Figure 4.8 XRD pattern for the synthesized silicalite-1 powder (Sample: SIL2)

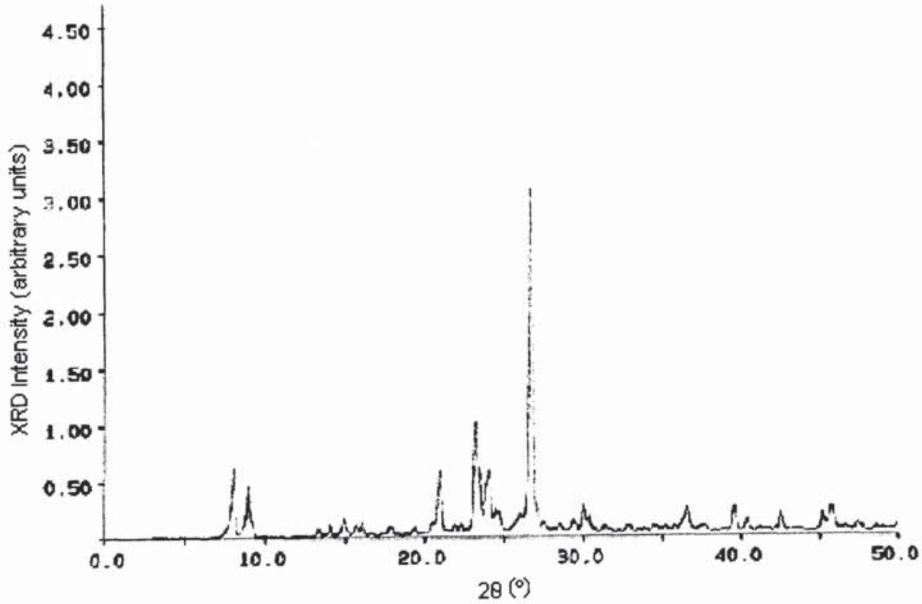

Figure 4.9 XRD pattern for the synthesized silicalite-1 powder (Sample: SIL4)

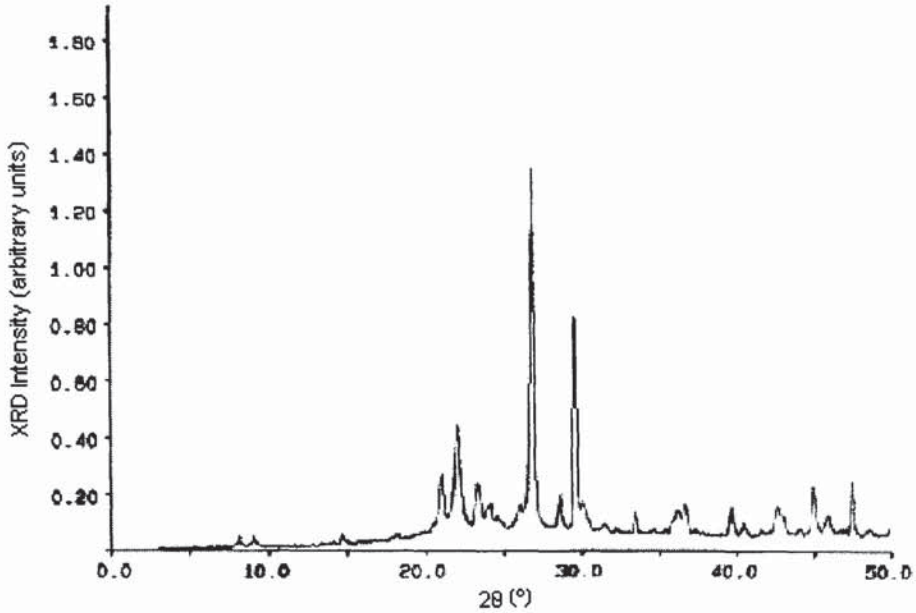

Figure 4.10 XRD pattern for the synthesized silicalite-1 powder (Sample: SIL9)

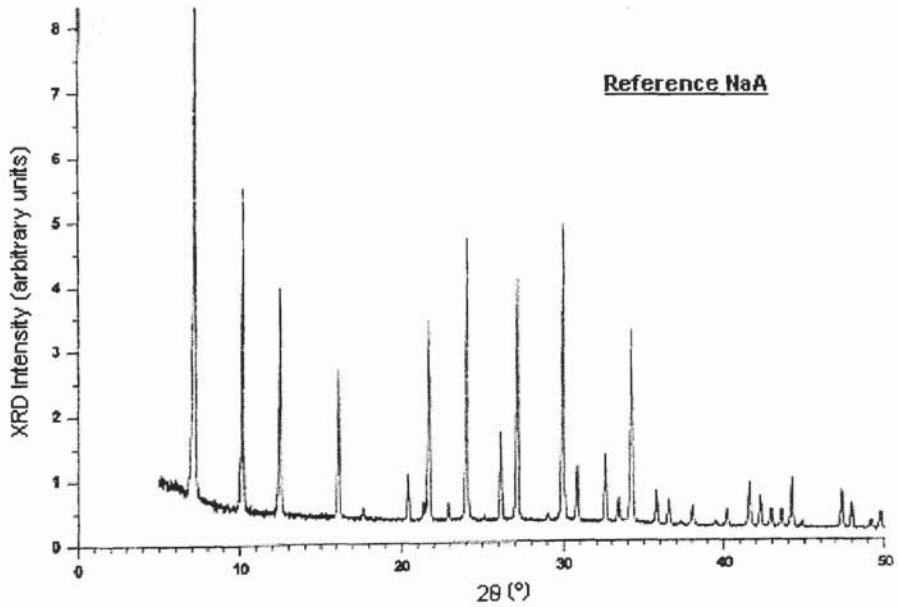

Figure 4.11 Reference XRD pattern for NaA (148)

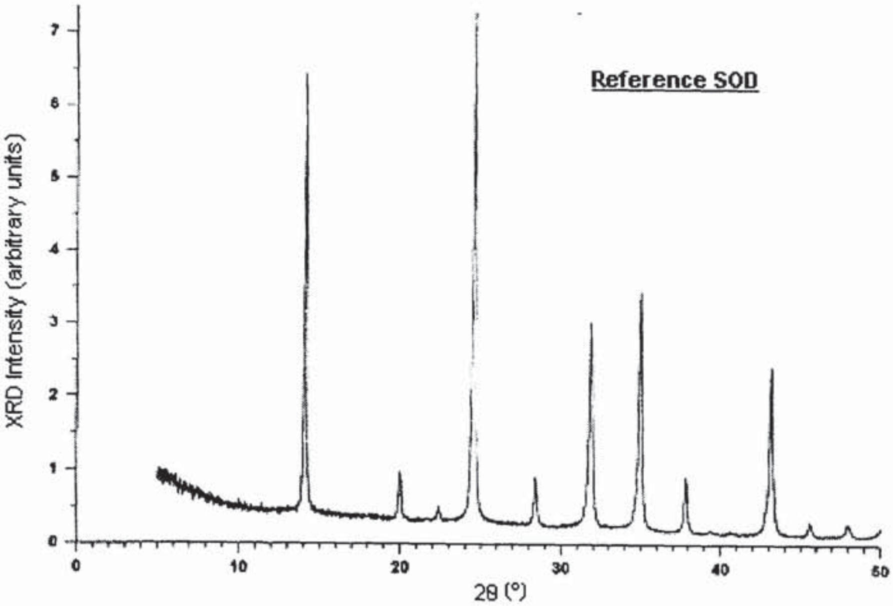

Figure 4.12 Reference XRD pattern for SOD (148)

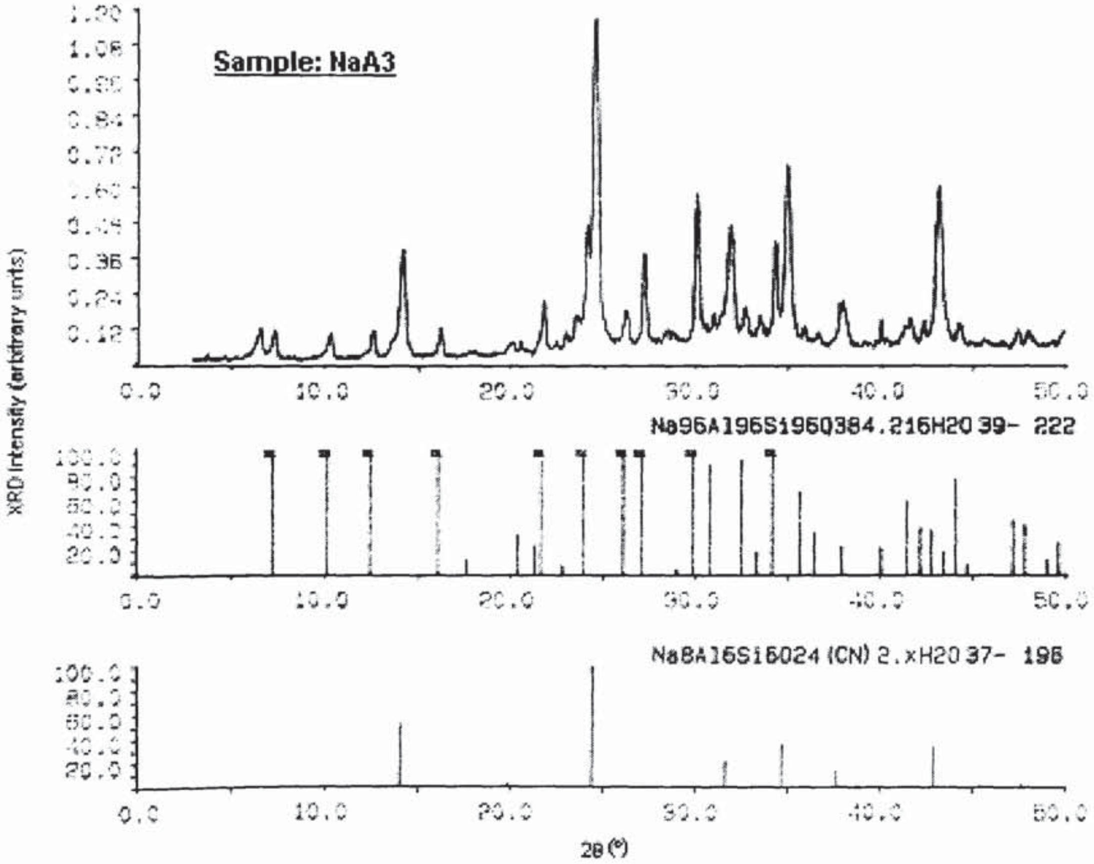

Figure 4.13 XRD pattern for the synthesized NaA powder (Sample: NaA3)

4.2.4 Thermogravimetric Analyses (TGA)

A crucial step in membrane formation that utilizes templating molecules in its preparation is the complete removal of such template molecules from the membranes structural pores as this maximizes the potential for permeation and separation purposes. Thermogravimetric analysis was carried out both in air and nitrogen to determine the ideal calcination temperature using a PerkinElmer Thermogravimetric Analyzer (Pyris 1 TGA). The thermogravimetric analysis (TGA) curves show the resultant absolute weight losses observed with increasing temperature while the derivative of the thermogravimetric analysis (DTGA) curves indicate the rates of weight loss with increasing temperature. All experiments were conducted under a nitrogen/air flow of 50 ml/min, STP with the samples heated at 5°C/min to 900°C.

4.2.4.1 Silicalite-1

Figure 4.14 shows the TGA and the resultant derivative (DTGA) curves obtained for the silicalite-1 sample. The results in figure 4.14 show that the rate of weight loss for the silicalite-1 under both nitrogen and air begins at approximately 360°C which corresponds to the start of the template removal and proceeds until about 500°C through to 700°C after which no further losses in the absolute weight occur. From the TGA curves it can be concluded the outgassing of the calcined silicalite-1 samples prior to obtaining N_2 adsorption isotherms can be carried out successfully at the maximum temperature (350°C) of the NOVA 1200 gas sorption equipment.

4.2.4.2 NaA

For the NaA sample the DTGA results in figure 4.15 show that upon heating the sample to 900°C both under nitrogen and air it is seen there are three significant weight loss events. The first main loss occurs approximately between 30 to 100°C and is attributed to the removal of loosely bound water molecules mainly on the surface of the zeolite. The second main loss occurs approximately between 200-500°C and peaks at approximately 380°C. This loss is attributed to the removal of the strongly adsorbed water molecules form within the cages of the zeolite NaA. The final main loss occurs approximately between 500-650°C and peeks at approximately 580°C.

This loss may be attributed to the dehydration of the sodium cations and possibly destruction of any defect silanol (Si-OH) groups found within the zeolite cages. From the analysis of the NaA samples it is concluded that outgassing of the NaA will prove to be difficult and the resultant N_2 adsorption isotherms obtained will not be accurate. This is attributed to the NaA strongly retaining significant quantities of water even at the maximum outgassing temperature (350°C) of the NOVA 1200 gas sorption equipment.

4.2.4.3 Carbon-graphite

Figures 4.16a and 4.16b show the TGA and the resultant derivative (DTGA) curves obtained for the carbon-graphite material. For the blank, non-oxidized carbon-graphite it was noticed that the weight loss under both nitrogen and air (Figures 4.16a and 4.16b) begins at approximately 600°C. The rate of weight loss continues steadily under nitrogen up to 900°C (Figure 4.16a) resulting in approximately 2.5% overall weight loss. For the analysis under air (Figure 4.16b) the sample experiences a large overall absolute weight loss of approximately 97% which ends at a temperature of 810°C after which no further losses occurred. With the oxidized blank carbon-graphite sample the rate of weight loss under nitrogen and air starts at approximately 150°C and 550°C respectively (Figures 4.16a and 4.16b). Once again for the analysis under nitrogen the rate of weight loss continued steadily up to 900°C resulting in overall weight loss of about 5.5% while in the analysis under air there is a large overall weight loss of about 95% which ends at 790°C after which no further loss occurred.

This indicates that for the calcination (removal of the templating agent or water) of the silicalite-1/carbon-graphite and NaA/carbon-graphite composite membranes the use of air should be avoided as it leads to almost complete decomposition of the carbon-graphite material. From the TGA results it was concluded that the calcination of the zeolite/carbon-graphite composite membranes should be conducted at 700°C under nitrogen to ensure complete template and sufficient water removal from the silicalite-1 pores and NaA cages respectively and also to minimise the decomposition of the carbon-graphite material.

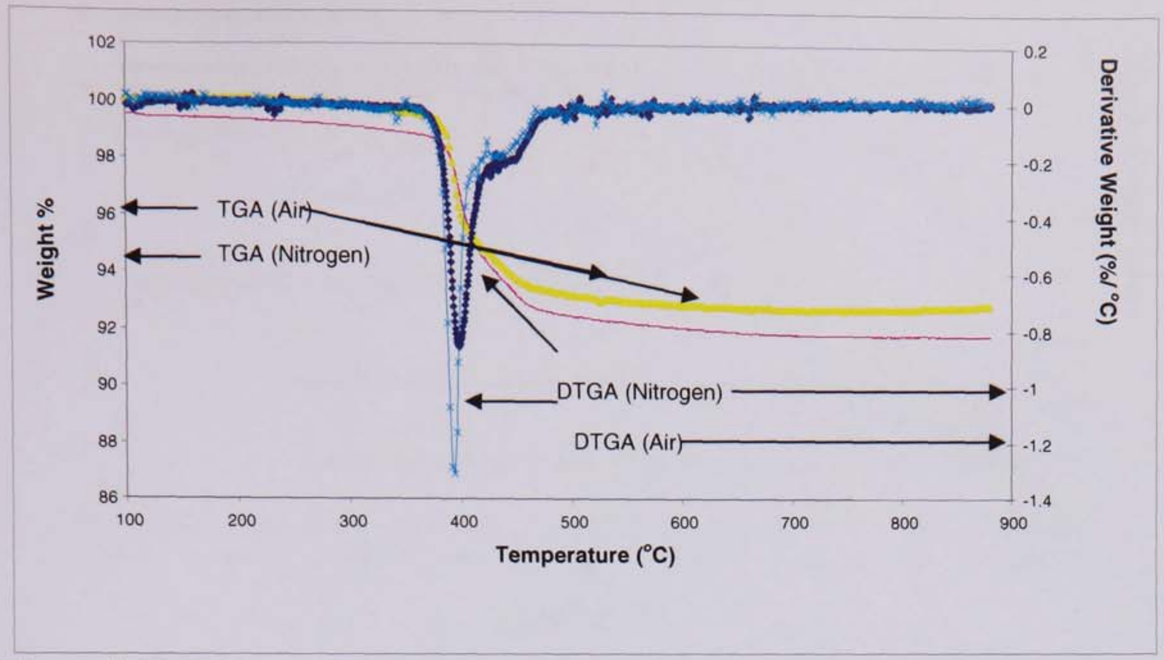

Figure 4.14 TGA and DTGA analysis of silicalite-1 powder carried out under nitrogen and air.

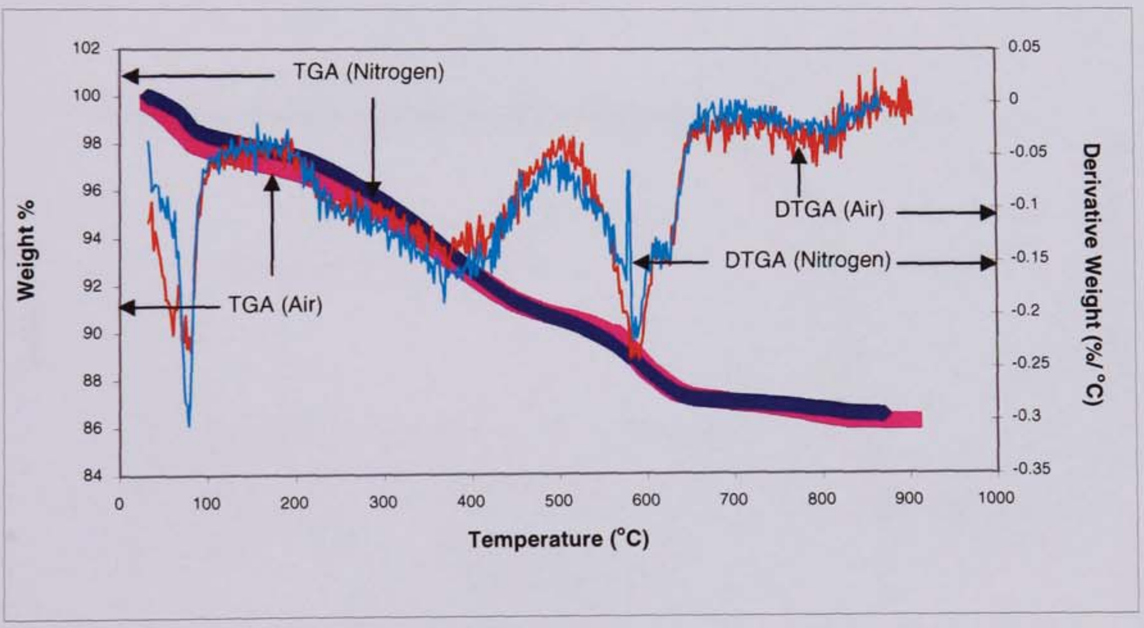

Figure 4.15 TGA and DTGA analysis of NaA powder carried out under nitrogen and air.

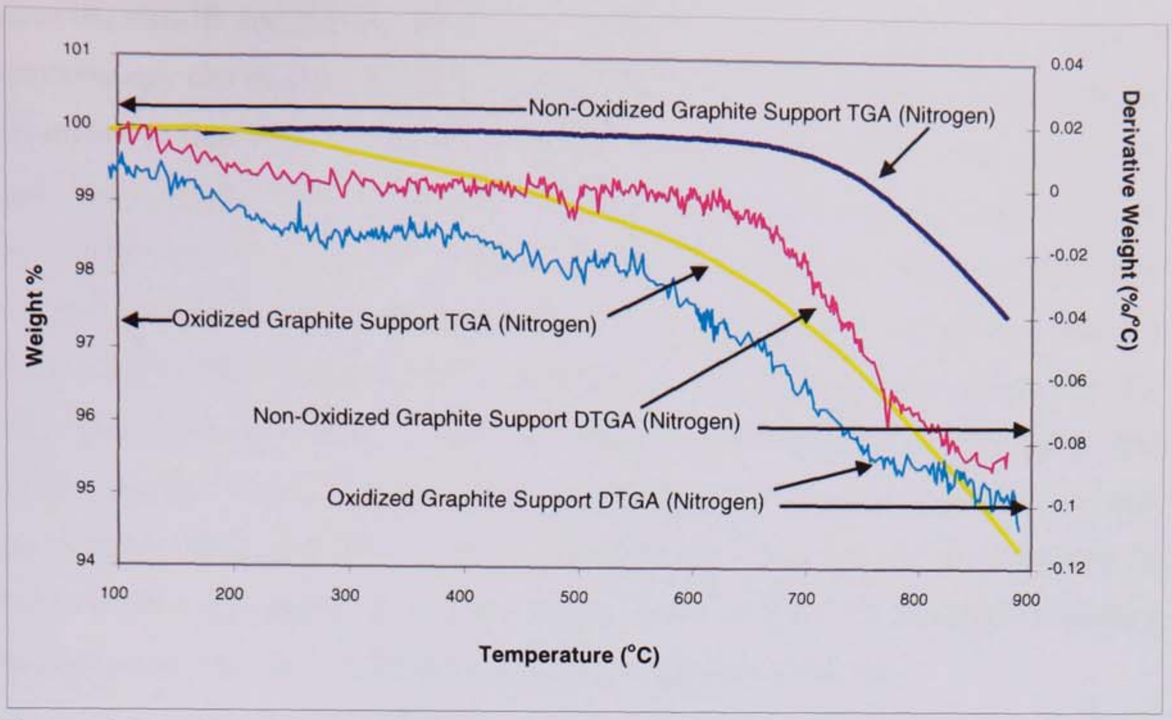

Figure 4.16a TGA and DTGA analysis of oxidized and non-oxidized carbon-graphite materials carried out under nitrogen.

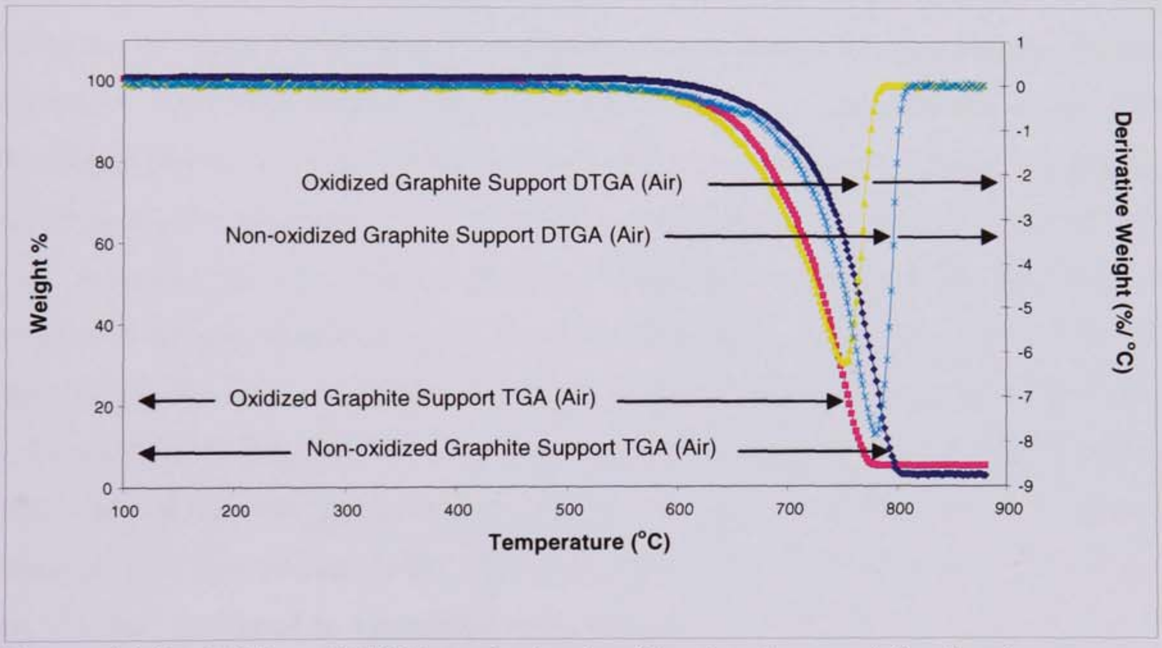

Figure 4.16b TGA and DTGA analysis of oxidized and non-oxidized carbon-graphite materials carried out under air.

4.2.5 Fourier Transform Infrared (FTIR) investigations

Infrared (IR) radiation is electromagnetic radiation that encompasses all the wavelengths between the visible and microwave regions of the electromagnetic spectrum. The IR region can also be subdivided into three smaller regions known as near-IR, mid-IR and far-IR, the ranges of which are shown in figure 4.17. Infrared spectroscopy can be used to characterize zeolites by their functional group vibrations. As shown in figure 4.17 vibrations of different building units of the zeolite framework give rise to typical bands in the mid and far infrared regions, cations vibrations in the far infrared region and hydroxyl groups vibrations in the near regions. In this work Fourier transform infrared measurements of the samples were performed using a Perkin Elmer FTIR spectrum RX-1 spectrometer. The samples were mixed with dry KBr and pressed in a die at 12 tons for 3 minutes under vacuum to form a pellet. The FTIR spectra of the samples were recorded in air at room temperature and atmospheric pressure using a range of 350-4400 cm^{-1}. The samples were scanned 25 times at a spectral resolution of 4 cm^{-1} with a 2 cm^{-1} interval. All spectrums including background scans were recorded between the ranges 350-4400 cm^{-1}.

Figures 4.18 and 4.19 show the results of the FTIR investigations for Silicalite-1 and NaA samples respectively. For the silicalite-1 samples It is seen from figure 4.18 that in the far IR region (400-600 cm^{-1}), the spectrum of silicalite-1 is characterised by two structural vibrational bands. The first band at 448 cm^{-1} corresponds to an Si-O bending found in many polymorphs of SiO_2 and a second band at 548 cm^{-1}, indicative of the silicalite-1 structure, is not present in amorphous silica. The origin of the 548 cm^{-1} band has not been defined, but it is thought to be related to the stretching of structural silicate double ring units in the silicalite-1 framework.(149,150). The spectrum, also shows a characteristic band in the OH stretching region at 3447 cm^{-1} corresponding to terminal Si-OH groups (151). Form figure 4.19 for the NaA samples it is seen that the absorption bands at 558 and 463 cm^{-1} are attributed to Si-O or Al-O bonds and double-4-rings (D4R) vibrations respectively (152) and those between 665 to 734 cm^{-1} attributed to symmetric stretches of the LTA framework and that at 995 cm-1 attributed to asymmetric stretches of the LTA framework (153,154). Of the remaining bands the band at 3436 cm^{-1} is characteristic of O–H group stretching and the bands at 1647 and 1453 cm^{-1} are characteristic of the H_2O substructure bending (155).

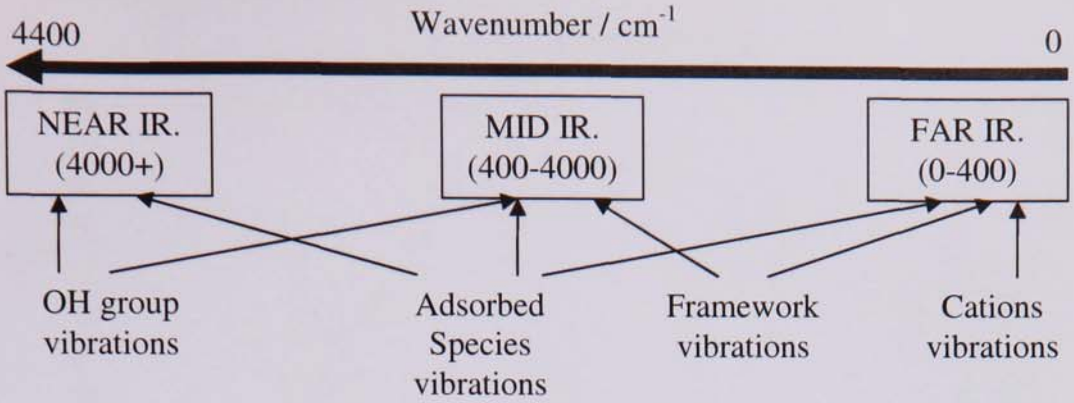

Figure 4.17 The Infrared spectrum regions

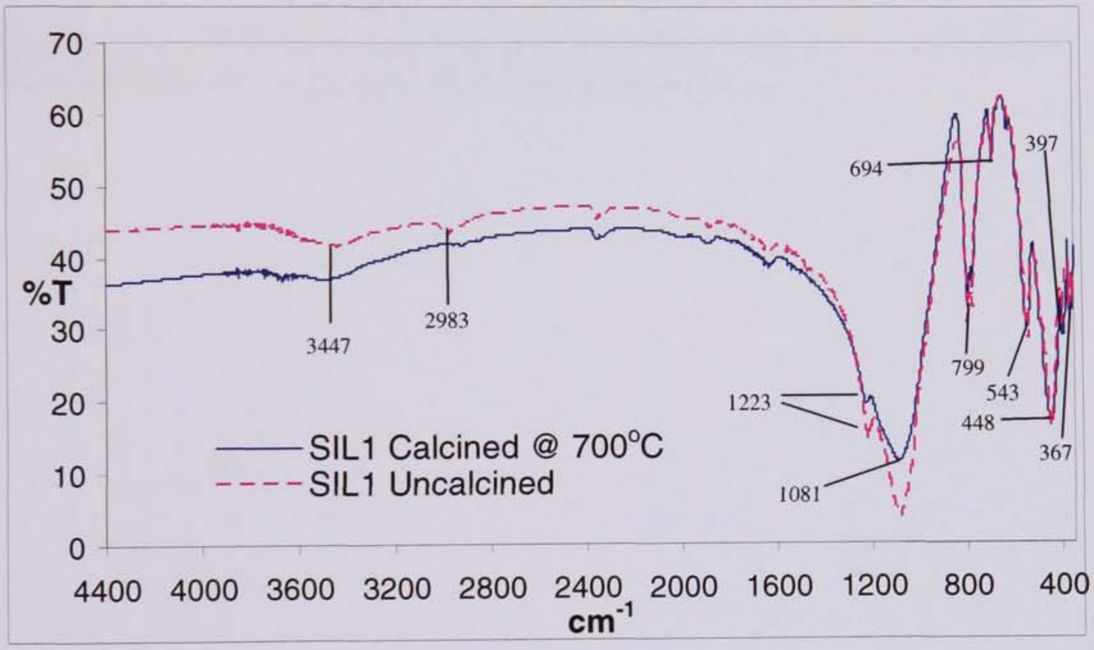

Figure 4.18 FTIR spectrum of powder taken from sample SIL1. Experiment conducted at room temperature and atmospheric pressure.

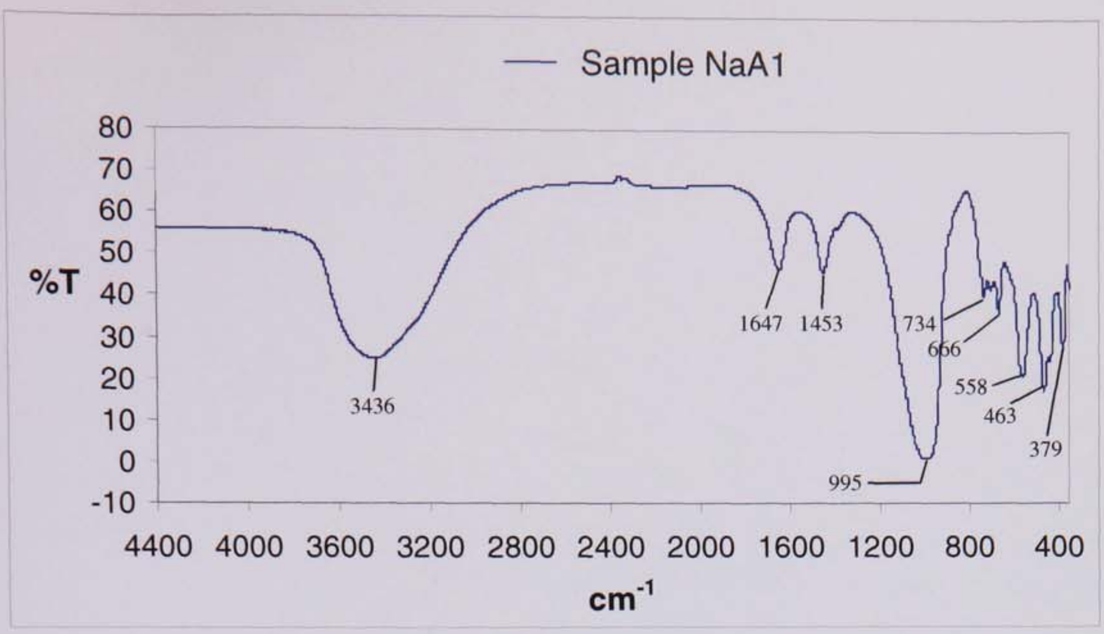

Figure 4.19 FTIR spectrum of powder taken from sample NaA1. Experiment conducted at room temperature and atmospheric pressure.

Chapter 5: Permeation Studies of Hydrocarbon Separation Through Composite Membranes

Chapter 5: Permeation Studies of Hydrocarbon Separation Through Composite Membranes

5.0 Gas permeation experiments

The selectivity and performance of the synthesized silicalite-1/carbon-graphite, NaA/carbon-graphite composite membranes and blank carbon-graphite membranes, were investigated for light hydrocarbon gas separation. A purpose built gas permeation rig (see figure 5.1) was used to evaluate the performance of the synthesised composite membranes using pure, binary and ternary gas (methane, ethane and propane) mixtures with varying feed compositions. The membrane permeation cell module is made up of two stainless steel discs with dimensions of 114 mm diameter by 30 mm thick (see figure 5.2a). The composite membranes were placed inside the membrane module and positioned between two circular plates and sealed using viton o-rings (see figures 5.2b and 5.2c). The feed gases into the membrane module consisted of pure grade methane, ethane and propane (98% minimum purity) obtained from BOC. These gases were introduced into the feed side of the membrane module and controlled by mass flow controllers and flowed across the membrane at a total flow rate of 100 cm^3/min (single pass). Gases that permeate through the membrane are swept away in a constant nitrogen sweep set to 100 cm^3/min. The permeate stream was continually analysed by a Varian CP-4900 Micro-GC equipped with a thermal conductivity detector and two columns (PPQ column and MolSieve 5A column). The pressure on both the feed and permeate side of the membrane module was kept constant at 1atm.

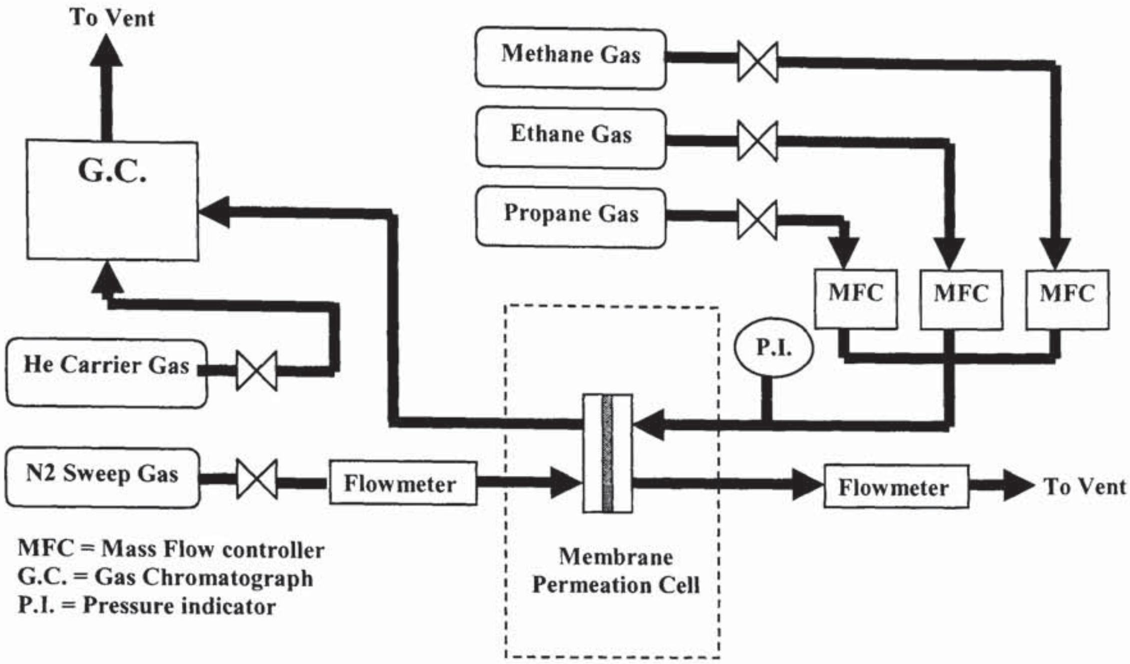

Figure 5.1 Diagram of gas permeation apparatus rig.

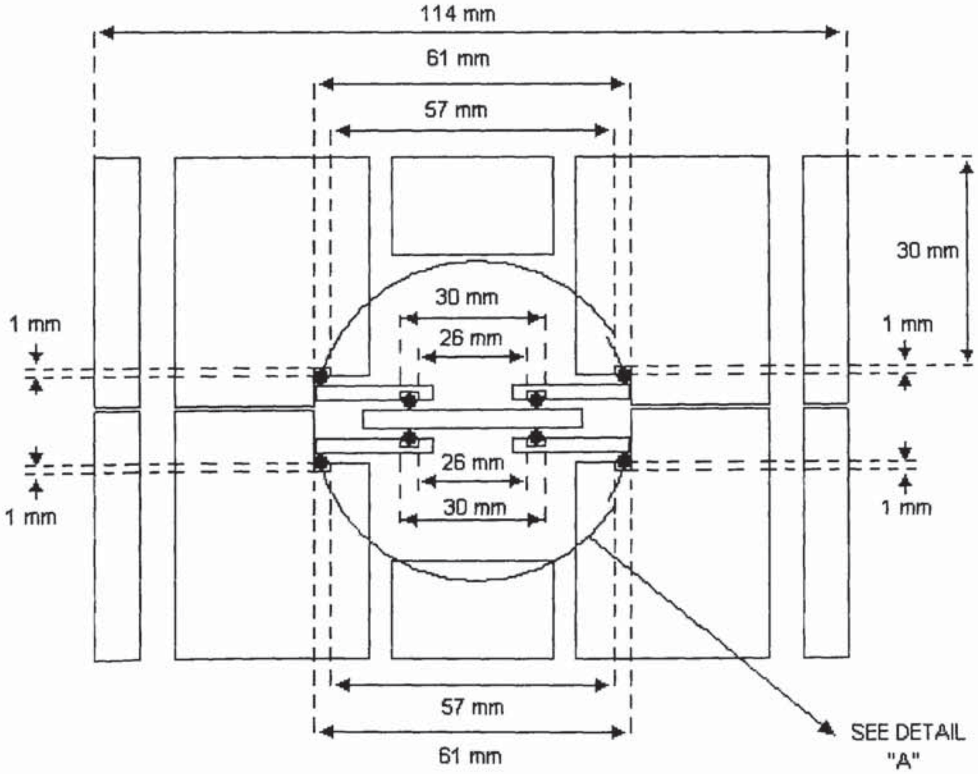

Figure 5.2a Dimensions of membrane module components.

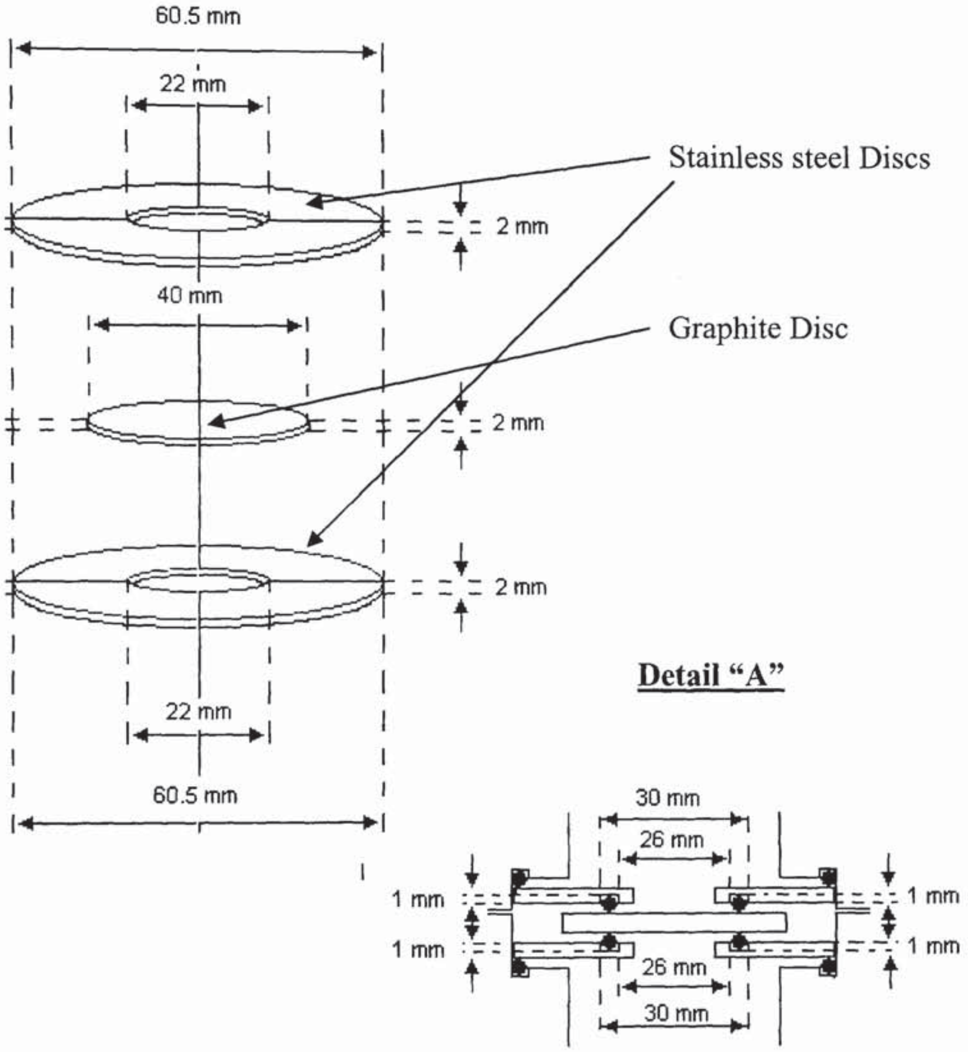

Figure 5.2b Internal configuration of membrane module.

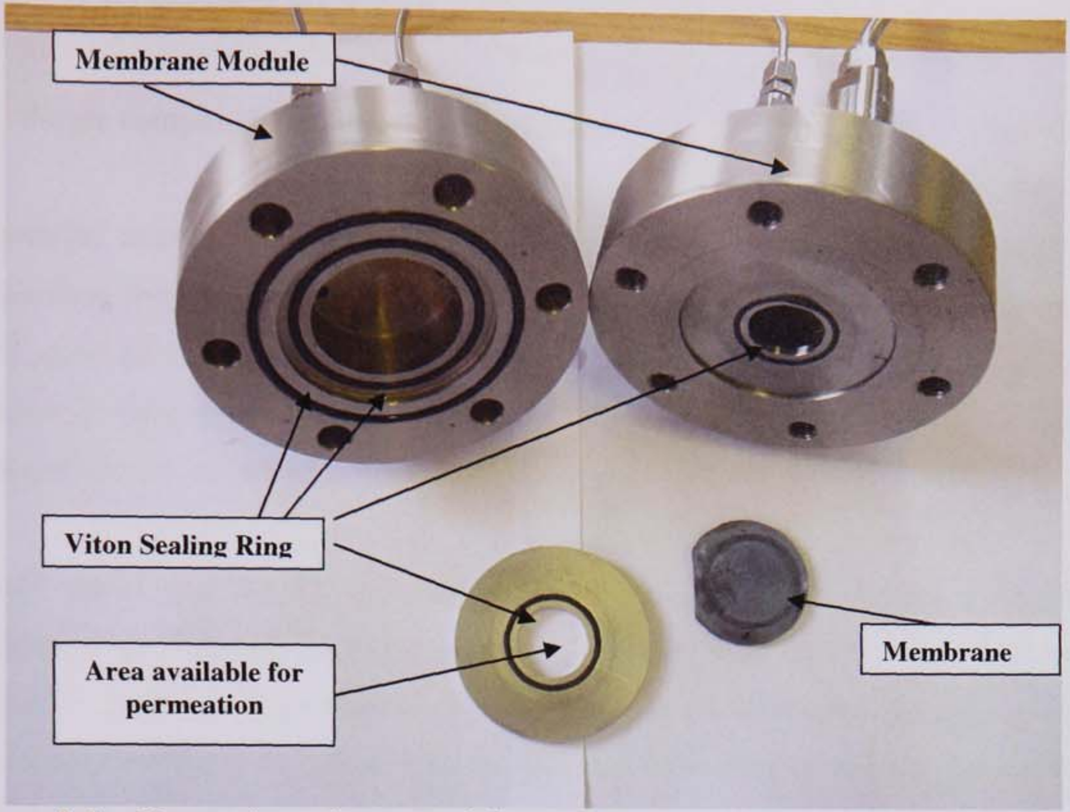

Figure 5.2c Photo of membrane module components.

The membranes separation selectivity, $\alpha_{A/B}$, for a binary mixture A and B was defined as:

$$\alpha_{A/B} = \frac{(y_A / y_B)_{permeate}}{(y_A / y_B)_{feed}} \qquad 5.1$$

y_A and y_B are the molar fractions of components "A" and "B" in the feed or permeate. This parameter $\alpha_{A/B}$ indicates the selectivity behaviour and relative performance of the membranes in separating fluid mixtures. If $\alpha_{A/B} = 1$ this corresponds to no separation for both components in the mixture. A value of less than one ($\alpha_{A/B} < 1$) indicates there is a rejection towards component "A" such that component "A's" concentration with respect to "B" in permeate is lower than that in the feed. For values greater than 1 ($\alpha_{A/B} > 1$) there is a separation towards component "A" indicating that it has a higher concentration with respect to component "B" in permeate compared to the feed. Whereas the ideal separation selectivity ($\alpha^*_{A/B}$) of the membranes towards mixtures is defined as the ratios of the pure single component fluxes:

$$\alpha^{*}_{A/B} = (\text{Pure flux})_A / (\text{Pure flux})_B \qquad 5.2$$

5.1 Single component gas permeation studies

Permeation experiments were carried out to test the integrity and performance of the synthesized membranes. Single gas permeances of methane, ethane and propane at 20°C were measured on both the silicalite-1/carbon-graphite, NaA/carbon-graphite composite membranes and calcined blank carbon-graphite membranes. The results obtained are shown in figure 5.3.

It was noted that for all the composite and blank carbon-graphite membranes considered the order of single gas permeances followed the general trend methane > ethane > propane. This was to be expected, as it highlights the strengths of interactions between the adsorbents surfaces and adsorbate molecules coupled with both diffusional and size entropy effects (106,156).

For the silicalite-1 composite membranes no data is reported for SIL1 as whilst sealing the membrane to the permeation module the module was accidentally dropped and thus the membrane cracked. For the remaining silicalite-1 composite membranes it was observed that the composite membranes synthesised from the 4 h oxidized carbon-graphite (SIL2 and SIL3) had lower fluxes at steady state for all three alkanes compared to the 24 h oxidized (SIL4, SIL5 and SIL6) and non-oxidized (SIL7, SIL8 and SIL9) carbon-graphite composites. It is seen from figure 5.3 that SIL2 had a methane flux 6.5 times higher than the ethane flux and 21.4 times higher than the propane flux. Whilst SIL3 had a methane flux 6.5 times higher than the ethane flux and 24.9 times higher than the propane flux.

For the 24 hr oxidized carbon-graphite composite membranes the methane fluxes were found to be 5.1, 3.7 and 2.4 times higher than ethane and 13.9, 10.9 and 3.6 times higher than propane for SIL4, SIL5 and SIL6 respectively. Whilst the non-oxidized carbon-graphite composites membranes SIL7, SIL78 and SIL9 showed methane fluxes 3.9, 3.2 and 1.7 times higher than that of ethane and 8.8, 6.3 and 2.9 times higher than propane fluxes respectively .

For the NaA composite membranes the methane fluxes were found to be 2.3, 2.6 and 3.1 times higher than ethane fluxes and 3.3, 4.1 and 5.9 times higher than propane fluxes respectively for NaA1, NaA2 and NaA3.

It was interesting to note that SIL6 which required two hydrothermal synthesis to obtain a continuous layer of silicalite-1 had comparable low ratios of single component fluxes as seen for the NaA composite membranes which also required two hydrothermal synthesis and also exhibited low single component flux ratios.

For the blank carbon-graphites it was found that BCGN1 had a methane flux 6.3 times higher than that of ethane and 18.8 times higher than propane while the oxidised blank (BCGO1) show a similar but slightly lower fluxes with a methane flux 5.4 times that of ethane and 15.5 times that of propane. These ratios of the single component fluxes indicate the ability of the membrane to perform separations and in general the larger the ratio between fluxes the better the separation performance of the membrane.

The permeation fluxes obtained for both blank carbon-graphite membranes with and without surface oxidation (BCGN1 and BCGO1) gave rise to the highest single gas permeances measured for all the membrane samples. This was to be expected highlighting the much larger pore widths (1.94 nm) of the carbon-graphite samples determined from the Horvarth-Kawazoe (HK) method seen earlier in chapter 4. These larger pore widths would tend to result in higher fluxes of the single gases. This was found to be true for the smaller methane single component fluxes but not in the cases of the larger ethane and propane single component fluxes, which showed only slight differences from those obtained from the composite membranes. A plausible explanation for this is that due to the slit shape geometry and larger size of the pores the interactions between carbon-graphite surfaces and methane molecules are much weaker compared to that with the pore surfaces of silicalite-1 or NaA (which have a comparable pore dimensions to the three alkanes molecules). On the other hand the strength of interaction between the ethane/propane molecules and carbon-graphite surfaces is almost similar to that for the silicalite-1 or NaA pore surfaces thus resulting in comparable ethane and propane fluxes.

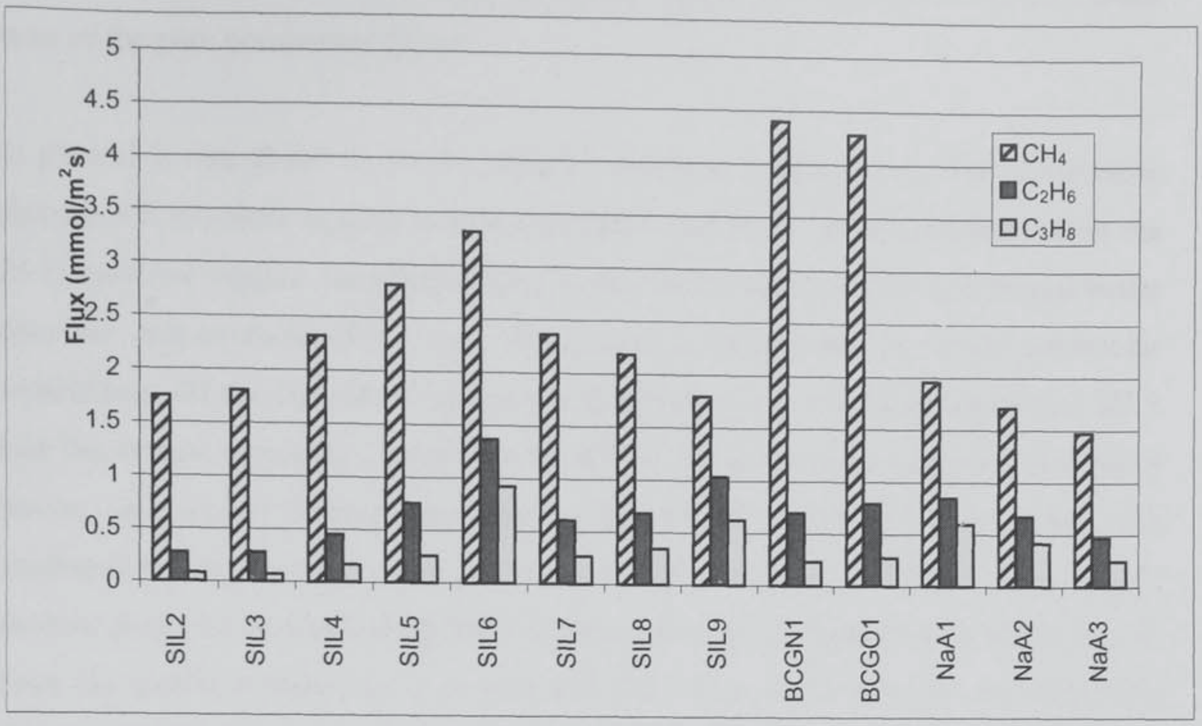

Figure 5.3 Pure single gas permeate fluxes of methane, ethane and propane through silicalite-1/carbon-graphite, NaA/carbon-graphite composite membranes and blank carbon-graphite membranes.

5.2 Binary gas mixture permeation

The separation properties of the membranes towards binary gas mixtures of CH_4/C_2H_6, CH_4/C_3H_8 and C_2H_6/C_3H_8 were investigated at 20°C. For all experiments the binary feed total flow rate was kept at 100 cm^3/min STP with the feed gas compositions varied. The steady state permeation fluxes for the gases in the binary mixture were noted to be much lower than their respective pure single component fluxes shown in Figure 5.3. From Table 5.1 it is seen that for all membranes the selectivity for methane/propane is far better than those seen either for methane/ethane or ethane/propane mixtures. In general the separation selectivities show there is separation towards component "A" in the mixture (the lighter component).

For all the membranes investigated the selectivities observed for methane/propane mixtures were better than those of methane/ethane and ethane/propane mixtures. It was also interesting to see that the ideal selectivity calculated based on the ratios of single component fluxes was in reasonably good agreement to the actual calculated selectivities of the membranes (Table 5.1). With the slight discrepancies being owed to the fact that in binary mixture permeation adsorbate-adsorbate interactions between different species occur and the significance of this is not represented by the simple ratio of the pure component fluxes.

In general it was observed for the silicalite-1/carbon-graphite composite membranes that the 4 h oxidized support membranes (SIL2 and SIL3) performed better than the 24 h oxidized support membranes (SIL4 and SIL5) which in turn performed better than the non-oxidized (SIL7 and SIL8) support membranes in binary equimolar separations. Of the silicalite-1 composite membranes it is seen that membrane SIL9 had the lowest separation behaviour of all the membranes investigated with SIL6 having the second lowest separation selectivity. This behaviour for SIL9 was attributed to the presence of large cracks within the silicalite-1 layer, as is clearly evident from the corresponding SEM micrograph seen in appendix A. While for the NaA composite membranes it is seen that they have the lowest set of separation selectivities of all the membranes investigated with the exceptions of SIL9 and SIL6. It was interesting to see that the blank carbon-graphite membranes have the highest overall permeate fluxes compared to any of the composite membranes. A consequence of this was lower separation selectivities, which were comparable to that of the 24 h oxidized support membranes (SIL4 and SIL5).

5.2.1 Influence of feed composition ratio on binary gas mixture permeation

Furthermore the effect of varying the feed composition ratio on the membranes separation properties was investigated. The feed mixture composition was varied by volume % ratio of 1:9 and 9:1. The separation selectivities for the binary components at varying feed composition are shown in Table 5.2.

For the composite membranes and the blank carbon-graphite membranes it was found that for binary mixtures of CH_4/C_2H_6, CH_4/C_3H_8 regardless of the feed composition the separation selectivities, indicate a preferential separation towards the lighter component in the feed. The magnitude of the separation selectivity of the lighter components is found to depend on the feed gas composition ratio. The only exception to this behaviour was seen with the NaA composite membrane (NaA1) for a binary mixture of CH_4/C_2H_6 at a feed composition of 9:1, which shows a preferential separation towards the propane (the heavier component in the mixture).

For the binary C_2H_6/C_3H_8 mixtures at a feed composition of 1:9 it is seen that all the membranes investigated show a preferential separation towards the lighter component in the feed mixture. But when the feed composition is changed to 9:1 (i.e. higher concentration of the lighter species (ethane) in the mixture) it was observed (Table 5.2) that membranes SIL2 to SIL4 show a separation towards the lighter ethane whereas the remaining composite membranes all show a preferential separation toward the heavier propane. For the blank carbon-graphite membranes (BCGN1 and BGCO1) it is seen for the binary ethane/propane mixture at a 9:1 feed composition ratio that the resulting separation selectivities were approximately 1 indicating no separation of the feed mixture.

It was interesting also to see that the silicalite-1composite membranes (with the exceptions of SIL6 and SIL9) overall performed better in separations of binary mixtures than compared to that of the NaA composite membranes. For the blank carbon-graphite membranes it was seen that the oxidized and calcined sample (BCGO1) had the lower separation selectivity behaviour compared to the non-oxidized calcined sample.

The results of this work differ to the findings in previous work where silicalite-1 membranes show preferential separation selectivity behaviour towards the heavier component in the mixture regardless of feed concentrations or temperature used (21,33,34). Bakker et al. (21) reported that mixture separation selectivities do not reflect the single-component permeance ratio and observed that besides molecular sieving and differences in diffusivities, difference in the adsorption strengths is a key factor in determining the separation selectivity. It was concluded that the greater the difference in adsorption strengths between the components in the mixture the greater the separation selectivity of the components. The concentration of the strongly adsorbing component was also found to be significant. A plausible explanation as to the differences with this work lies primarily with the underlying support used in the membrane preparation. In other works using supported zeolite membranes the supports have been meso/macroporous and thus have insignificant or no influence on the separation properties of the membrane and separation is only governed by the zeolite layer. In this work the carbon-graphite (support) is microporous and thus is a membrane itself and is able to influence the separation behaviour. For our composite membranes this results in a two-stage separation process, one through the silicalite-1 layer and the second through the carbon-graphite layer. Separation through the silicalite-1 layer would result in the expected mixture separation with separation selectivity towards the larger component in the mixture. The reason being, as discussed earlier, the silicalite-1 has pore dimensions which are comparable to that of all three alkane molecules and thus transport through the silicalite-1 is via single file diffusion and thus the strongly adsorbing component in the mixture is preferentially separated (Figure 5.4a). This is only valid for a defect free silicalite-1 layer and if significant inter-crystalline micro/mesoporous cracks were present the mass transport would occur through these cracks with the strongly adsorbing component being adsorbed into the zeolite as the gas mixture passes through the cracks. This would leave the weakly adsorbing component to be preferentially separated (Figure 5.4b). For the carbon-graphite layer a similar behaviour as discussed for the crystalline micro/mesoporous cracks would be seen due to its larger micro-pore size. This would result in weakly adsorbing molecules being able to overtake the larger strongly adsorbing molecules and thus separation would be a function of the differences in diffusivities and adsorption strengths (Figure 5.4c). In this case the lighter component would have the lowest adsorption strength coupled with the highest diffusivity (156) thus resulting in the greatest mobility and separation selectivity through the carbon-graphite layer.

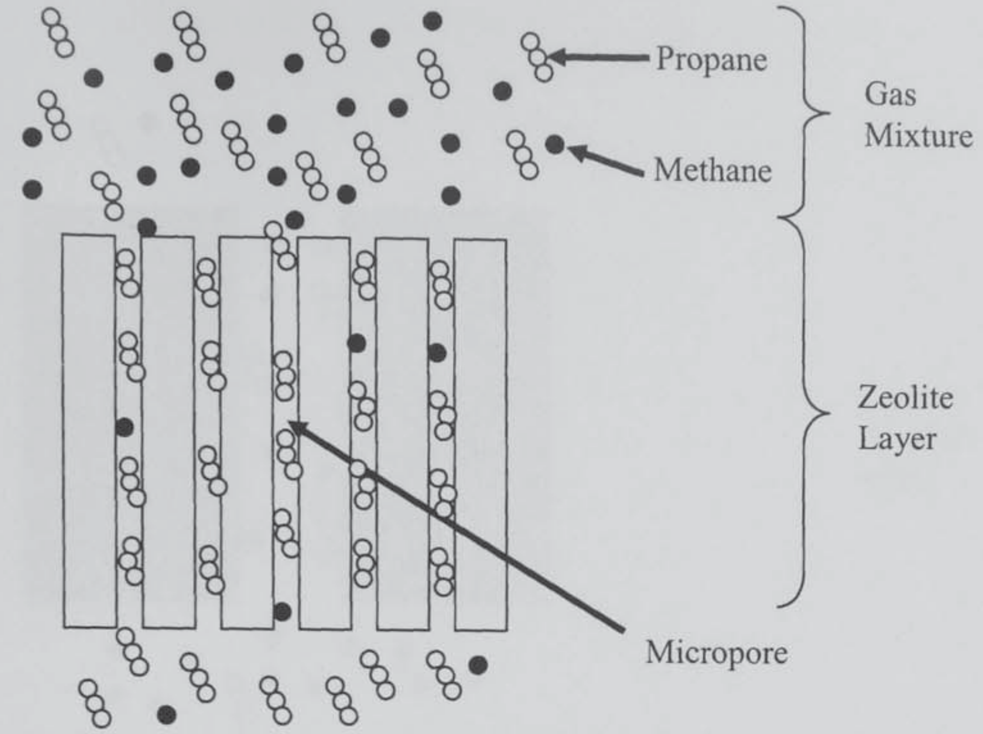

Figure 5.4a Separation through a defect free silicalite-1 layer

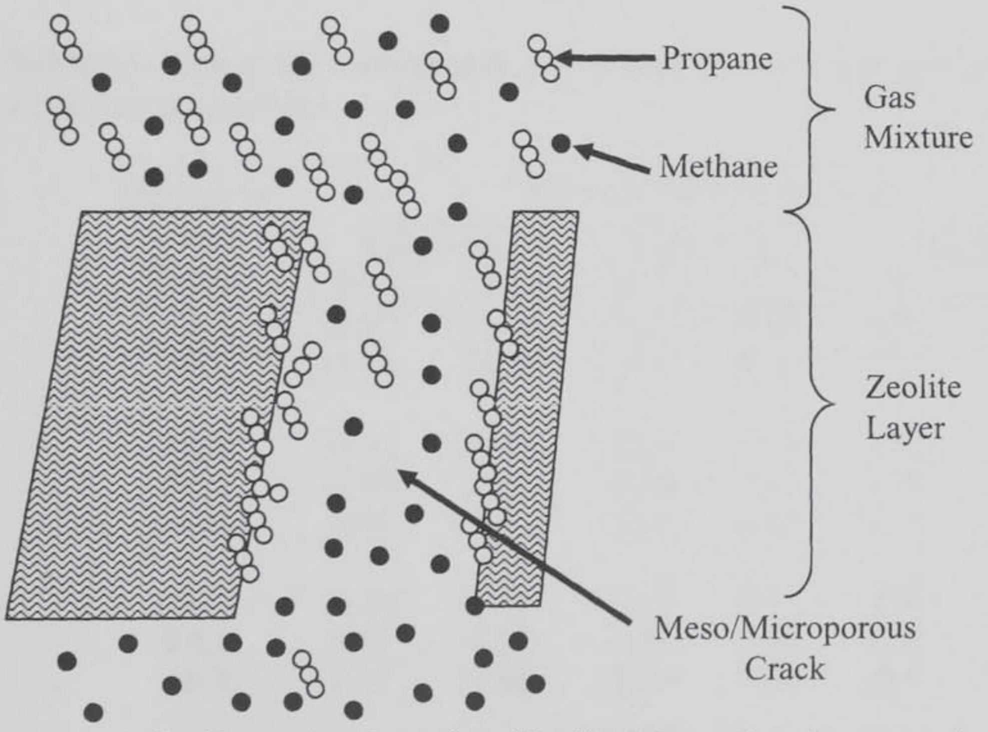

Figure 5.4b Separation through a silicalite-1 layer showing a meso/microporous crack

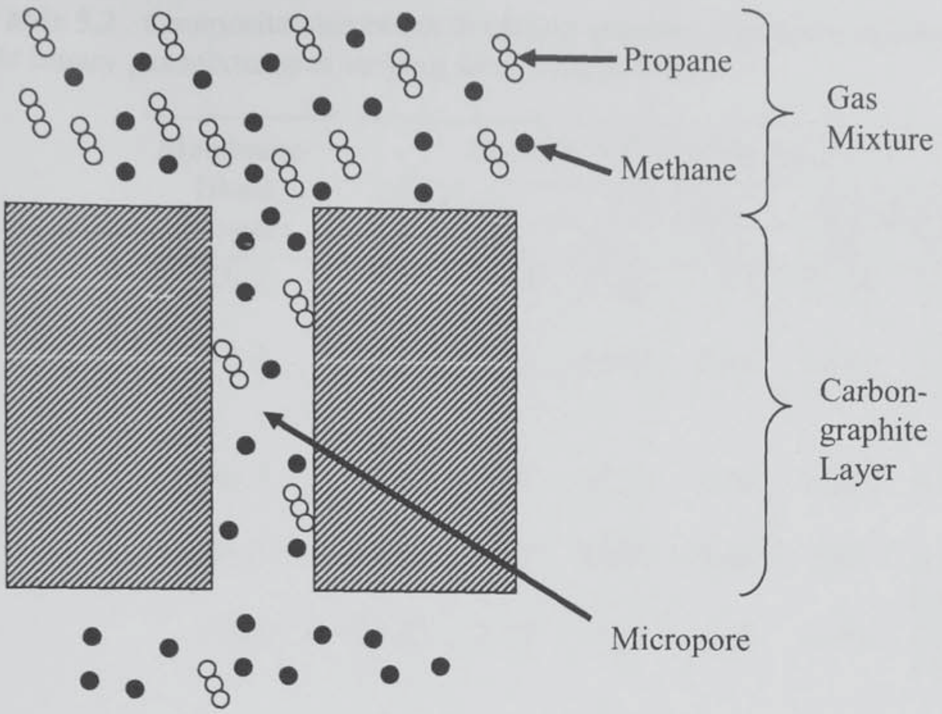

Figure 5.4c Separation through a carbon-graphite layer showing micropore slit

Table 5.1 Composite membrane & carbon-graphite separation selectivities at 20°C for binary gas mixtures

Membrane/ Blank Support	Separation Selectivity ($\alpha_{A/B}$)					
	CH_4/C_3H_8		CH_4/C_2H_6		C_2H_6/C_3H_8	
	1:1[a]	1:1[b]	1:1[a]	1:1[b]	1:1[a]	1:1[b]
SIL2	22.27	21.41	5.86	6.47	3.69	3.31
SIL3	19.56	24.85	5.91	6.46	3.61	3.85
SIL4	15.53	13.94	4.98	5.11	3.04	2.73
SIL5	11.94	10.91	4.36	3.71	2.79	2.94
SIL6	5.99	3.60	3.02	2.43	1.94	1.48
SIL7	11.04	8.81	4.12	3.87	2.66	2.28
SIL8	9.36	6.35	3.71	3.20	2.52	1.98
SIL9	1.37	2.88	1.14	1.74	0.90	1.66
BCGN1	16.51	18.79	4.87	6.30	3.02	2.98
BCGO1	13.23	15.52	4.77	5.41	2.90	2.87
NaA1	4.82	3.27	2.91	2.30	1.62	1.42
NaA2	7.62	4.11	3.70	2.55	2.00	1.61
NaA3	8.96	5.87	3.95	3.10	2.18	1.89

[a] Selectivity based on mixed binary gas component permeation fluxes

[b] Ideal selectivity based on single component permeation fluxes

Table 5.2 Composite membrane & carbon-graphite separation selectivities at 20°C for binary gas mixtures at varying feed compositions

Membrane/ Blank Support	Separation Selectivity ($\alpha_{A/B}$)[a]					
	CH_4/C_3H_8		CH_4/C_2H_6		C_2H_6/C_3H_8	
	1:9	9:1	1:9	9:1	1:9	9:1
SIL2	67.26	7.14	17.30	1.95	11.36	1.43
SIL3	70.32	7.57	17.74	1.97	11.83	1.50
SIL4	54.49	6.17	15.55	1.76	10.06	1.26
SIL5	41.89	4.57	13.01	1.48	7.90	0.96 1.04[b]
SIL6	20.10	2.29	9.62	1.26	5.60	0.72 1.38[b]
SIL7	40.07	4.20	14.65	1.60	7.49	0.79 1.27[b]
SIL8	35.95	3.10	13.97	1.34	7.90	0.80 1.25[b]
SIL9	23.08	1.76	13.37	1.17	6.75	0.48 2.08[b]
BCGN1	52.406	4.35	15.10	1.64	8.63	1.04
BGCO1	43.61	3.76	14.37	1.59	8.23	0.99
NaA1	17.10	1.29	9.78	0.88 1.14[b]	5.78	0.47 2.14[b]
NaA2	22.24	2.44	10.47	1.35	5.73	0.72 1.40[b]
NaA3	25.29	2.95	10.96	1.46	6.14	0.78 1.28[b]

[a] $\alpha_{A/B}$ Selectivity of component A over component B in binary gas mixture.

[b] $\alpha_{B/A}$ Selectivity of component B over component A in binary gas mixture.

5.3 Ternary gas mixture permeation

The separation selectivity and effectiveness of the membranes were also investigated for ternary gas mixtures of methane, ethane and propane at 20°C. The total feed flow rate was again kept at 100 cm^3/min STP with the feed gas composition varied and set to four different volume % ratios of 8:1:1, 1:8:1, 1:1:8 and 1:1:1 (CH_4:C_2H_6:C_3H_8). The observed separation selectivities for the composite membranes and blank carbon-graphite are shown in Table 5.3.

It was observed that regardless of the feed compositions all the membranes in general have preferential separation selectivity towards methane. With the exception of SIL9 at a feed composition ratio of 8:1:1, which showed a rejection towards methane and preferential separation selectivity towards the ethane and propane. It was interesting to see again that the separation selectivity towards methane is highest with the 4h oxidized carbon-graphite membranes (SIL2 and SIL3). In general the order of the membranes separation selectivities followed that as seen earlier for the binary mixtures.

For all the membranes investigated it is also seen there is a small but noticeable separation selectivity towards ethane in the ternary gas mixtures especially at a low ethane and methane feed gas ratio (1:1:8). Once again as seen earlier for the binary mixtures the magnitude of separation selectivity is dependant on the feed mixtures composition ratio such that the highest separation selectivities for the methane are seen when the concentrations of the smaller components (methane and ethane) are low (feed mixture composition ratio of 1:1:8). And with the lowest separation selectivities occurring when methane's concentration is high (feed mixture composition ratio of 8:1:1).

The two blank carbon-graphite membranes (BGCN1 and BCGO1) showed similar separation behaviours towards the ternary mixtures as seen from their separation selectivities with values comparable to that found for SIL4 and SIL5.

Table 5.3 Composite membrane & carbon-graphite separation selectivities at 20°C for ternary gas mixtures at varying feed compositions

Membrane	Membrane Separation Selectivity(α)											
	CH_4/ (C_2H_6+C_3H_8)				C_2H_6/ (CH_4+ C_3H_8)				C_3H_8/ (CH_4+C_2H_6)			
	Feed gas composition ratio (CH_4:C_2H_6:C_3H_8)											
	1:1:1	1:8:1	1:1:8	8:1:1	1:1:1	1:8:1	1:1:8	8:1:1	1:1:1	1:8:1	1:1:8	8:1:1
SIL2	9.34	17.43	29.96	3.08	0.32	0.11	1.48	0.56	0.08	0.27	0.02	0.15
SIL3	9.55	19.10	34.24	3.08	0.31	0.11	1.29	0.56	0.08	0.24	0.02	0.15
SIL4	8.07	15.58	25.45	2.87	0.36	0.13	1.52	0.60	0.10	0.30	0.03	0.17
SIL5	6.40	13.46	21.28	2.43	0.42	0.14	1.51	0.64	0.14	0.42	0.05	0.25
SIL6	4.00	9.12	12.79	1.63	0.57	0.18	1.81	0.85	0.25	0.71	0.08	0.45
SIL7	6.07	14.73	21.99	2.22	0.44	0.12	1.43	0.69	0.15	0.46	0.05	0.28
SIL8	5.51	12.30	18.82	2.08	0.47	0.15	1.58	0.72	0.17	0.52	0.05	0.31
SIL9	1.67	9.88	10.03	0.75	0.68	0.14	2.51	1.45	0.83	1.26	0.09	1.13
BCGN1	7.71	14.94	24.64	2.46	0.36	0.13	1.38	0.63	0.12	0.39	0.04	0.25
BCGO1	7.36	13.90	23.49	2.33	0.37	0.13	1.41	0.66	0.13	0.42	0.04	0.27
NaA1	3.66	8.66	10.88	1.09	0.56	0.17	2.04	1.15	0.31	1.07	0.09	0.72
NaA2	5.15	10.12	14.45	1.81	0.46	0.17	1.70	0.78	0.21	0.67	0.07	0.39
NaA3	5.50	10.41	15.23	1.99	0.45	0.17	1.66	0.73	0.18	0.61	0.07	0.34

5.4 Influence of temperature on gas permeation

In order to investigate the influence of temperature on the composite membranes the 4 h oxidised carbon-graphite membranes (SIL2 and SIL3) were chosen as they had the highest selectivity behaviour of all the silicalite-1 composite membranes. For The NaA composite membranes all three membranes were used for the experiments. The separation selectivity and permeation properties of the chosen composite membranes were investigated for pure and binary gas mixtures. The permeation experiments were repeated at temperatures of 60°C and 100°C. The temperature increase was achieved by inserting the membrane module into a hot oil bath, with the temperature monitored by inserting a thermocouple between the membrane module compartments.

5.4.1 Temperature influence on single gas permeation

Figures 5.5a and 5.5b show the influence of temperature on the pure gas permeation measured for SIL2 and SIL3. It is seen for SIL2 that there is a decrease in the ethane flux with increasing temperature but for the methane and propane this was not the case. The methanes flux is seen to find a minimum at 60°C then increase at 100°C, however for the propane it is seen at 60°C there is no propane detected by the G.C. and on increasing the temperature to 100°C we once again find a propane flux but at a level lower than that found at 20°C. For SIL3 It is seen that with increasing temperature there is a decrease in the fluxes of both methane and ethane. Propane, however, was observed to decrease at 60°C then increase at 100°C although not to the level found at 20°C. This strange behaviour was initially observed by Bernal et al. (35) for light alkane permeances through a silicalite-1 membrane and the results obtained confirm their observations. At low temperatures the occupancy in the pores is high due to adsorption, and this lead to an increase in the permeate flux with increasing temperature and consequently a maximum is reached. Any further increase in temperature at this stage leads to reduction in pore occupancy with an accompanying decrease in permeate flux. As the temperature is increased further the high adsorption strength of propane becomes negligible and the permeate flux is now driven by the increase in molecular diffusivity through the micropores. This increase in propane diffusivity due to increasing temperature was observed in simulation work and will be confirmed in chapter 7. For the NaA composite membranes it is seen from figures 5.6a,b and c that with increasing temperatures all three membranes show a general increase in the fluxes of all three alkanes.

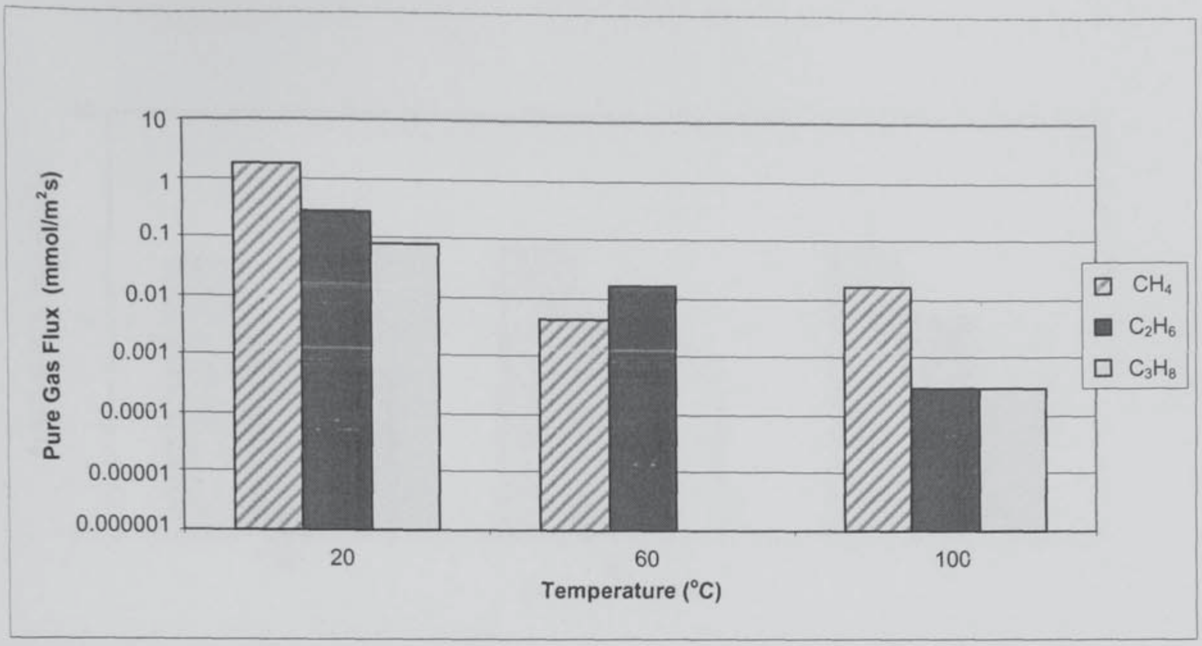

Figure 5.5a Pure single gas permeation fluxes at different temperatures for silicalite-1 composite (SIL2).

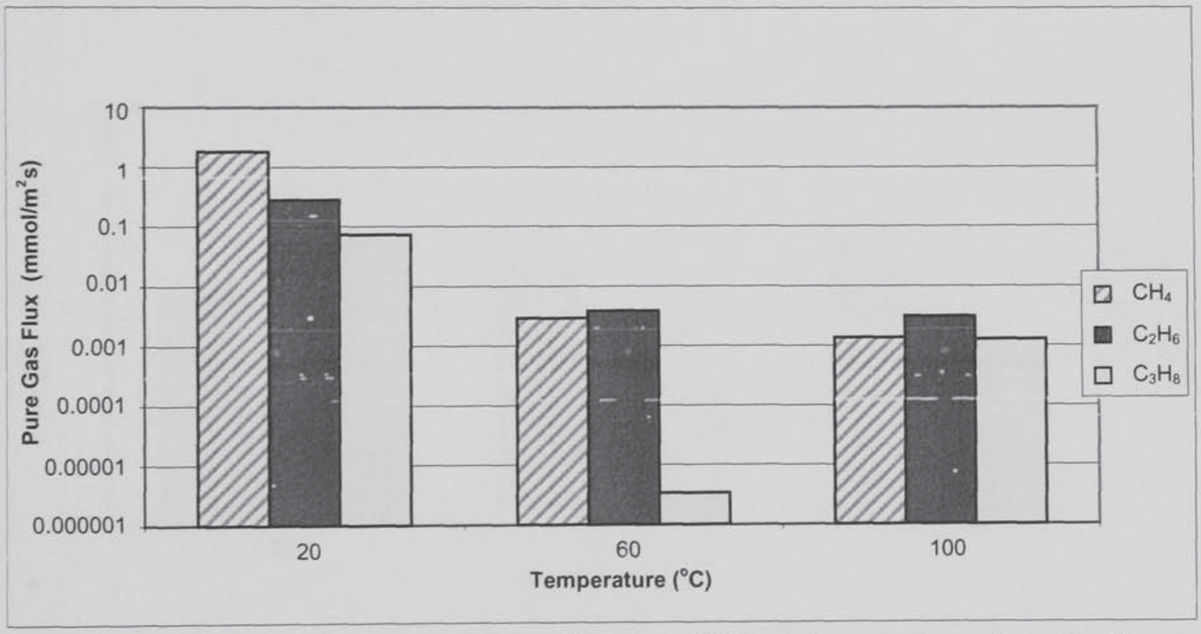

Figure 5.5b Pure single gas permeation fluxes at different temperatures for silicalite-1 composite (SIL3).

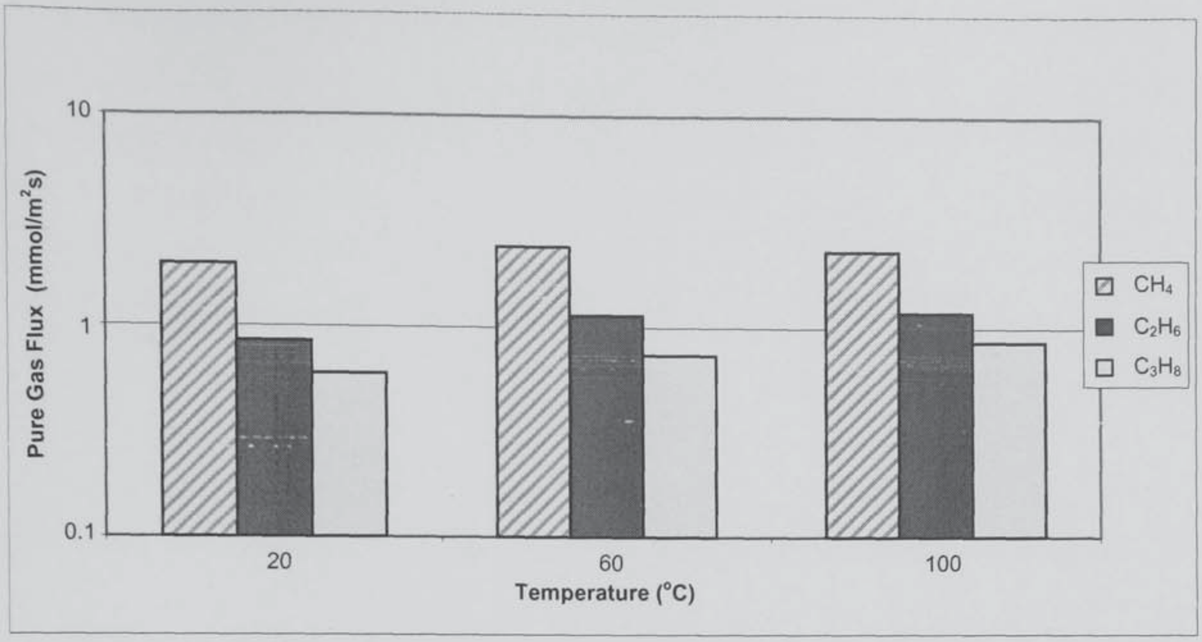

Figure 5.6a Pure single gas permeation fluxes at different temperatures for NaA composite (NaA1).

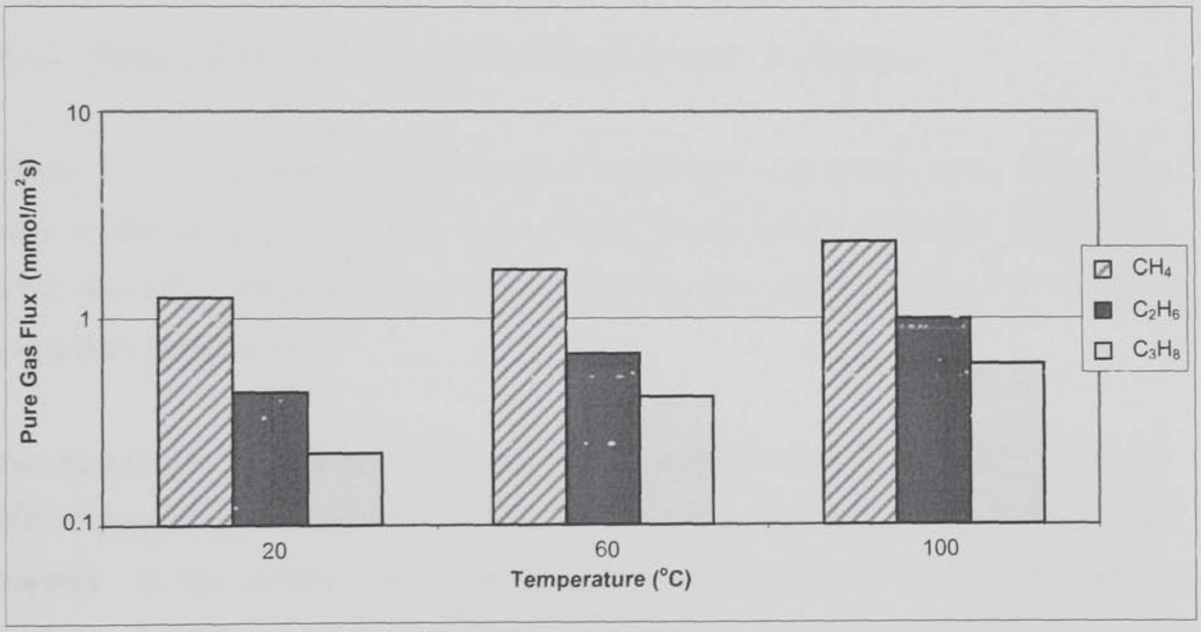

Figure 5.6b Pure single gas permeation fluxes at different temperatures for NaA composite (NaA2).

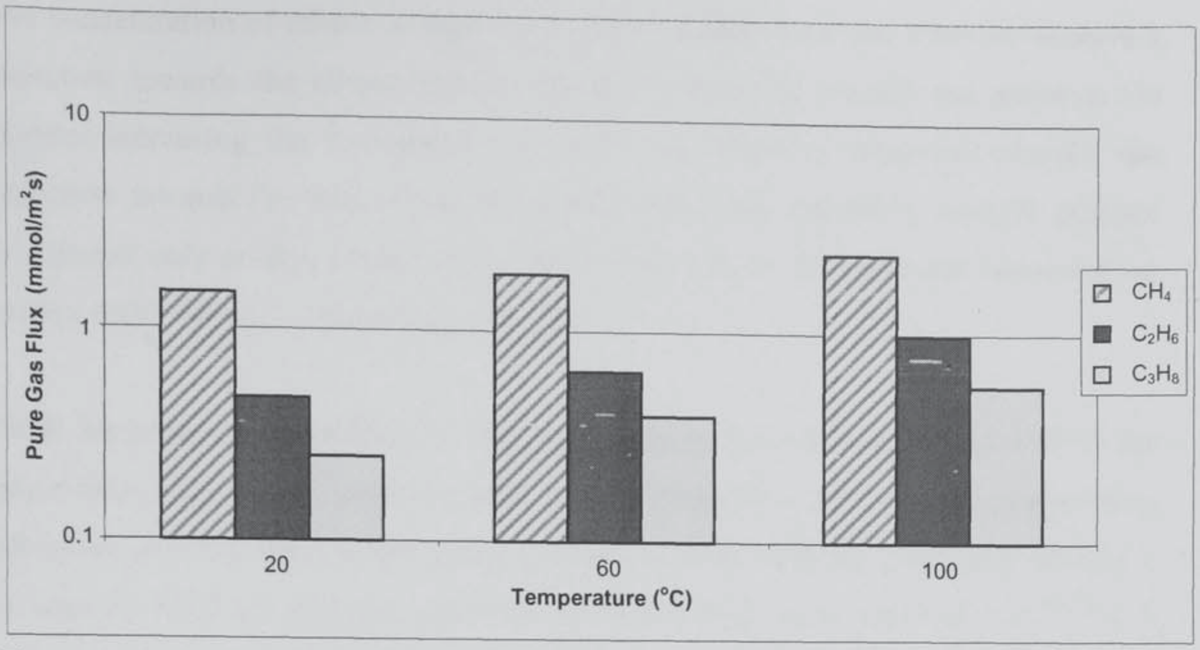

Figure 5.6c Pure single gas permeation fluxes at different temperatures for NaA composite (NaA3).

5.4.2 Temperature influence on binary gas mixture permeation

Tables 5.4a to 5.5b show the influence of temperature and binary feed composition ratio on the measured separation selectivity of the silicalite-1 composite membranes SIL2 and SIL3. Whereas Tables 5.6 to 5.8 show the results obtained for the NaA composite membranes.

For the silicalite-1 composite membranes it was noticed that for the binary mixtures at 20°C the membrane separation selectivity is towards the lighter component in the mixture. As the temperature is increased it is observed that for methane/propane mixtures there is a separation towards propane. This effect is more significant For SIL3 and occurs at feed composition ratios of 1:1 and 1:9 (Table 5.4b) for a temperature of 60°C and at 100°C occurs at all three compositions investigated (Table 5.4b). In comparison to SIL2 the separation selectivity towards propane only occurs at 60°C at feed composition ratios of 1:1 and 1:9 (Table 5.5b).

For ethane/propane mixture a similar behaviour for both SIL2 and SIL3 is seen with separation selectivity towards ethane at 20°C for all composition ratios investigated. But at 60°C we only see a separation selectivity towards ethane when the concentration of ethane is low (ratios of 1:9 and 1:1, Tables 5.4a and 5.5a) and when the concentration of ethane is high (ratio of 9:1, Tables 5.4a and 5.5a) we observe a rejection towards the ethane and a separation selectivity towards the propane. On further increasing the temperature to 100°C the effect is enhanced whereby the rejection towards the ethane and consequent separation selectivity towards propane occurs not only at high ethane concentrations but also at the equimolar concentration (ratios of 9:1 and 1:1, Tables 5.4a and 5.5a).

With methane/ethane mixture it was interesting to note that at 60°C for SIL3 the separation selectivities were towards ethane irrespective of the feed composition. However at 100°C the selectivity changes back towards methane. A similar behaviour is seen for SIL2 but with the selectivity towards ethane only occurring at 60°C for a composition ratio of 1:1 (Table 5.5a) with the remaining two composition ratios showing a lower selectivity towards methane than that seen at 20°C. Surprisingly on increasing the temperature to 100°C it is seen the selectivity towards methane has greatly increased for SIL2 than compared to SIL3 were only a slight difference to that observed at 20°C is seen. It is also interesting to note for GD3 that for the binary methane/ethane mixture when the methanes feed concentration is high (ratio of 9:1, Table 5.4a) and temperature is high 100°C there is little separation of the mixture as indicated by the separation selectivity values of 1.01 and 0.99 for methane and ethane respectively.

For the NaA composite membranes it was seen all three membranes showed similar separation behaviours. For the binary methane/propane mixtures it was seen that all three membranes show separation selectivity towards the methane regardless of feed composition ratio. The influence of increasing the temperature on all three membranes resulted a noticeable decrease in the separation selectivity towards the methane.

Whereas for binary methane/ethane and ethane/propane mixtures a similar behaviour as seen for the binary methane/propane mixtures is observed but only at feed composition ratios of 1:9 and 1:1 (Tables 5.6a, 5.7a and 5.8a) with the general trend of decreasing separation selectivity towards the lighter component with increasing temperature. But when the lighter components feed concentration is high (ratio of 9:1, Tables 5.6a, 5.7a and 5.8a) it is seen there is a rejection towards the lighter component with a separation selectivity towards the heavier component in the binary mixture. It is also seen the selectivity towards the heavier component increases noticeably with increasing temperature.

Table 5.4a SIL3 separation selectivities for lighter component in binary gas mixture at different temperatures

Temp (°C)	Separation Selectivity ($\alpha_{A/B}$)								
	CH_4/C_3H_8			CH_4/C_2H_6			C_2H_6/C_3H_8		
	1:9	1:1	9:1	1:9	1:1	9:1	1:9	1:1	9:1
20	70.32	19.56	7.57	17.74	5.91	1.97	11.83	3.61	1.50
60	2.26	0.36	0.003	0.05	0.006	0.0006	10.35	1.19	0.12
100	0.47	0.07	0.01	26.82	6.32	1.01	1.76	0.20	0.03

Table 5.4b Corresponding SIL3 separation selectivities for heavier component in binary gas mixture at different temperatures

Temp (°C)	Separation Selectivity ($\alpha_{B/A}$)								
	C_3H_8/ CH_4			C_2H_6/ CH_4			C_3H_8/ C_2H_6		
	9:1	1:1	1:9	9:1	1:1	1:9	9:1	1:1	1:9
20	0.01	0.05	0.13	0.06	0.17	0.51	0.08	0.28	0.67
60	0.44	2.77	353.46	19.44	162.20	1707.68	0.10	0.84	8.47
100	2.13	14.40	89.95	0.04	0.16	0.99	0.57	4.94	37.73

Table 5.5a SIL2 separation selectivities for lighter component in binary gas mixture at different temperatures

Temp (°C)	Separation Selectivity ($\alpha_{A/B}$)								
	CH_4/C_3H_8			CH_4/C_2H_6			C_2H_6/C_3H_8		
	1:9	1:1	9:1	1:9	1:1	9:1	1:9	1:1	9:1
20	67.26	22.27	7.14	17.30	5.86	1.95	11.36	3.69	1.43
60	3.49	0.43	0.74	7.70	0.12	2.19	8.65	15.34	0.77
100	159.03	23.91	6.84	199.82	45.69	12.25	2.54	0.49	0.06

Table 5.5b Corresponding SIL2 separation selectivities for heavier component in binary gas mixture at different temperatures

Temp (°C)	Separation Selectivity ($\alpha_{B/A}$)								
	C_3H_8/ CH_4			C_2H_6/ CH_4			C_3H_8/ C_2H_6		
	9:1	1:1	1:9	9:1	1:1	1:9	9:1	1:1	1:9
20	0.01	0.04	0.14	0.06	0.17	0.51	0.09	0.27	0.70
60	0.29	2.35	1.35	0.13	8.50	0.46	0.12	0.07	1.30
100	0.01	0.04	0.15	0.01	0.02	0.08	0.39	2.05	16.16

Table 5.6a Membrane (NaA1) separation selectivities for lighter component in binary gas mixture at different temperatures

Temp (°C)	Separation Selectivity ($\alpha_{A/B}$)								
	CH_4/C_3H_8			CH_4/C_2H_6			C_2H_6/C_3H_8		
	1:9	1:1	9:1	1:9	1:1	9:1	1:9	1:1	9:1
20	17.10	4.82	1.29	9.78	2.91	0.87	5.78	1.62	0.47
60	16.21	4.60	1.26	9.52	2.82	0.86	5.58	1.61	0.47
100	15.75	4.52	1.26	9.39	2.75	0.82	5.62	1.61	0.46

Table 5.6b Membrane (NaA1) separation selectivities for heavier component in binary gas mixture at different temperatures

Temp (°C)	Separation Selectivity ($\alpha_{B/A}$)								
	C_3H_8/ CH_4			C_2H_6/ CH_4			C_3H_8/ C_2H_6		
	9:1	1:1	1:9	9:1	1:1	1:9	9:1	1:1	1:9
20	0.06	0.21	0.77	0.10	0.34	1.14	0.17	0.62	2.14
60	0.06	0.22	0.79	0.11	0.35	1.16	0.18	0.62	2.12
100	0.06	0.22	0.79	0.11	0.36	1.21	0.18	0.62	2.16

Table 5.7a Membrane (NaA2) separation selectivities for lighter component in binary gas mixture at different temperatures

Temp (°C)	Separation Selectivity ($\alpha_{A/B}$)								
	CH_4/C_3H_8			CH_4/C_2H_6			C_2H_6/C_3H_8		
	1:9	1:1	9:1	1:9	1:1	9:1	1:9	1:1	9:1
20	22.24	7.62	2.44	10.47	3.70	1.35	5.73	2.00	0.71
60	18.51	6.31	2.09	9.54	3.32	1.20	5.18	1.84	0.66
100	16.52	5.65	1.85	8.63	3.08	1.12	5.11	1.82	0.64

Table 5.7b Membrane (NaA2) separation selectivities for heavier component in binary gas mixture at different temperatures

Temp (°C)	Separation Selectivity ($\alpha_{B/A}$)								
	C_3H_8/ CH_4			C_2H_6/ CH_4			C_3H_8/ C_2H_6		
	9:1	1:1	1:9	9:1	1:1	1:9	9:1	1:1	1:9
20	0.04	0.13	0.41	0.10	0.27	0.74	0.17	0.50	1.40
60	0.05	0.16	0.48	0.10	0.30	0.84	0.19	0.54	1.51
100	0.06	0.18	0.54	0.12	0.32	0.89	0.20	0.55	1.56

Table 5.8a Membrane (NaA3) separation selectivities for lighter component in binary gas mixture at different temperatures

Temp (°C)	Separation Selectivity ($\alpha_{A/B}$)								
	CH_4/C_3H_8			CH_4/C_2H_6			C_2H_6/C_3H_8		
	1:9	1:1	9:1	1:9	1:1	9:1	1:9	1:1	9:1
20	25.29	8.96	2.95	10.96	3.95	1.46	6.14	2.18	0.78
60	23.74	6.74	1.78	9.54	3.32	1.20	5.54	1.97	0.70
100	16.99	5.96	1.96	8.71	3.14	1.15	5.06	1.84	0.66

Table 5.8b Membrane (NaA3) separation selectivities for heavier component in binary gas mixture at different temperatures

Temp (°C)	Separation Selectivity ($\alpha_{B/A}$)								
	C_3H_8/ CH_4			C_2H_6/ CH_4			C_3H_8/ C_2H_6		
	9:1	1:1	1:9	9:1	1:1	1:9	9:1	1:1	1:9
20	0.04	0.11	0.34	0.09	0.25	0.68	0.16	0.46	1.28
60	0.04	0.15	0.56	0.10	0.30	0.84	0.18	0.51	1.43
100	0.06	0.17	0.51	0.11	0.32	0.87	0.20	0.54	1.51

Chapter 6: Atomistic Simulation Studies of Hydrocarbon Adsorption in Zeolites

Chapter 6: Atomistic Simulation Studies of Hydrocarbon Adsorption in Zeolites

6.0 Introduction

The molecular sieving properties of zeolites are not only owed to their uniform pore sizes but also to the adsorption of molecules within their pores. To better understand this behaviour a clear picture of the microscopic mechanism of mass transport through zeolites is needed. The knowledge of where a particular molecule in a mixture prefers to adsorb and the magnitude of adsorption both within the bulk zeolite channels and on the surface of the zeolite can be used to explain experimental results and determine how a mixture should be separated.

In the first part of this chapter atomistic simulations using the code METADISE have been conducted to obtain information on the microscopic behaviour of linear alkanes (methane, ethane and propane) within the bulk pores of the siliceous zeolites: Linde Type A, Mordenite and Silicalite-1. Preferential sites of adsorption and corresponding adsorption energies have been determined.

In the second part of this chapter the code METADISE has been used to generate and determine the most stable crystal surface configurations for silicalite-1 and Na-mordenite zeolites. Following this surface adsorption studies using the three alkanes (methane, ethane and propane) were conducted to determine both surface adsorption energies and preferential sites of surface adsorption.

6.1 Bulk zeolite simulations

In this work the alkane adsorbate molecules have been represented by a combination of an all atomistic potential (AAP) and a modified united atom potential (UAP) model while the zeolite lattice framework is represented with an all atomistic potential model as outlined in chapter 3. Throughout the simulations the zeolite lattice framework and the adsorbates were allowed to remain flexible. All simulations were performed at a temperature of 0 K in a single unit cell of the zeolite. The unit cell has periodicity in all three dimensions to simulate an infinite crystal.

6.1.1 Linde Type A (LTA)

The LTA model (See figure 6.1) has a cubic structure with space group Fm3c and unit cell a =b=c of 23.69Å. The structure is made up of linked truncated octahedral array of sodalite units joined together by double four-rings (D4R) via oxygen bridges. This results in the formation of α-cages with an eight-membered oxygen ring windows (Beagley and Titiloye (157)).

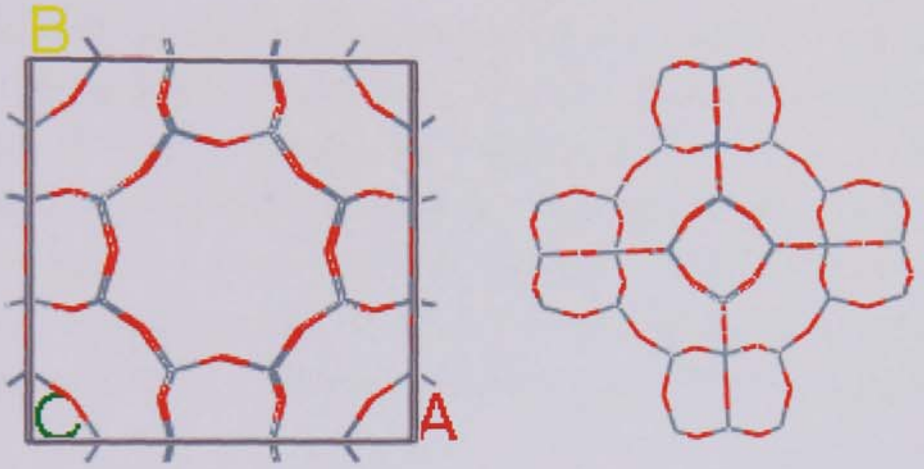

(a) **(b)**

Figure 6.1 LTA structure (a) single α - cage showing 8-ring window, (b) single β - cage with D4Rs showing 6-ring windows.

6.1.1.1 Adsorption of pure components methane, ethane & propane in LTA

Molecules were placed at different starting positions in and around the α-cages. Starting positions in the β-cages where ignored because the cage is inaccessible to all three alkane molecules considered. In all cases considered, the sorbed molecules drift towards two different favourable sites; inside the α-cage just off the centre of the 8-ring window (figures 6.2 & 6.3 (a,b)) and off the centre of the silicon atom connecting the 8-, 6-, and 4-ring windows in the α-cage (figures 6.2 & 6.3 (c,d)).

It was noted that the predicted sorption sites and energies were in line with previous calculated and experimental work. This was as expected in particular when considering molecules adsorbed at 0 K and at very low molecular loadings. It was also observed that at low molecular loading, there is no real difference in the results from using the two different sets of potentials. One main drawback noticed in using the all atomistic potentials (AAP) is the inability to handle effectively the effect of loadings. On the other hand, the modified united atom potentials (UAP) was found to be very effective for studying the effect of loadings per cavity or per unit cell. The calculated heats of adsorption for methane, ethane and propane in LTA at 0 K using both sets of potentials is shown in figure 6.4 and compared with the experimental results of Triebe et al. (158), Parsonage and Stroud (159), and Ruthven et al. (160). The adsorption enthalpies calculated with UAP for low loading is slightly lower than that obtained with AAP. However, both set of potential models are reasonably in good agreement with the experimentally determined heats of sorption. It is worth noting that the experimental results were carried out at higher temperatures with full compositional variations and extra framework cations while in this work only the siliceous form is modelled. Looking at the calculated enthalpies of adsorption for these molecules using both set of potentials, it can be seen that they are in remarkable agreement with available experimental data which suggest the level of approximation introduced in the model composition is adequate for such levels of concentrations.

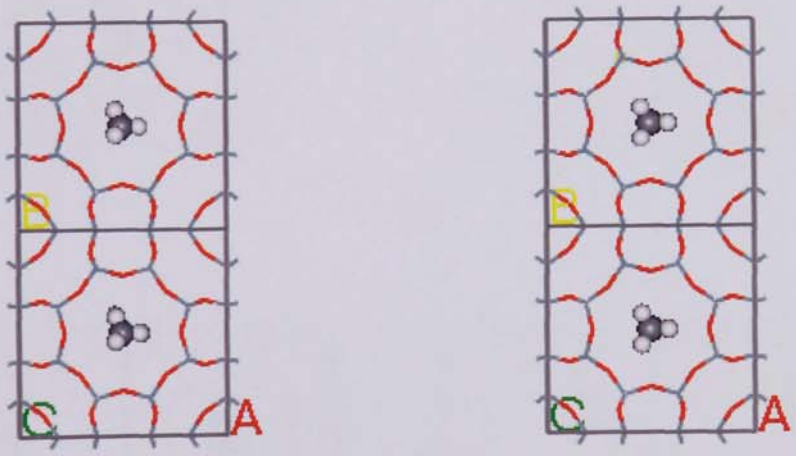

(a) **(b)**

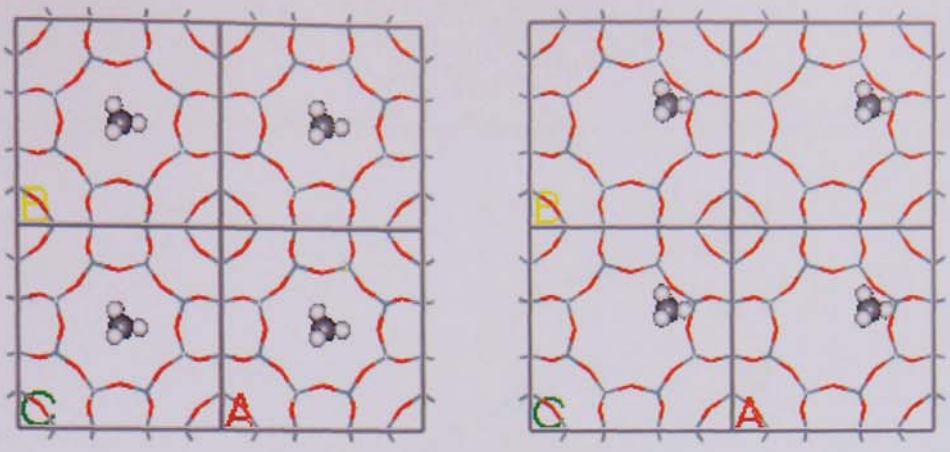

(c) (d)

Figure 6.2 Methane in LTA (a&c before energy minimization; b&d preferred sorption site after minimization)

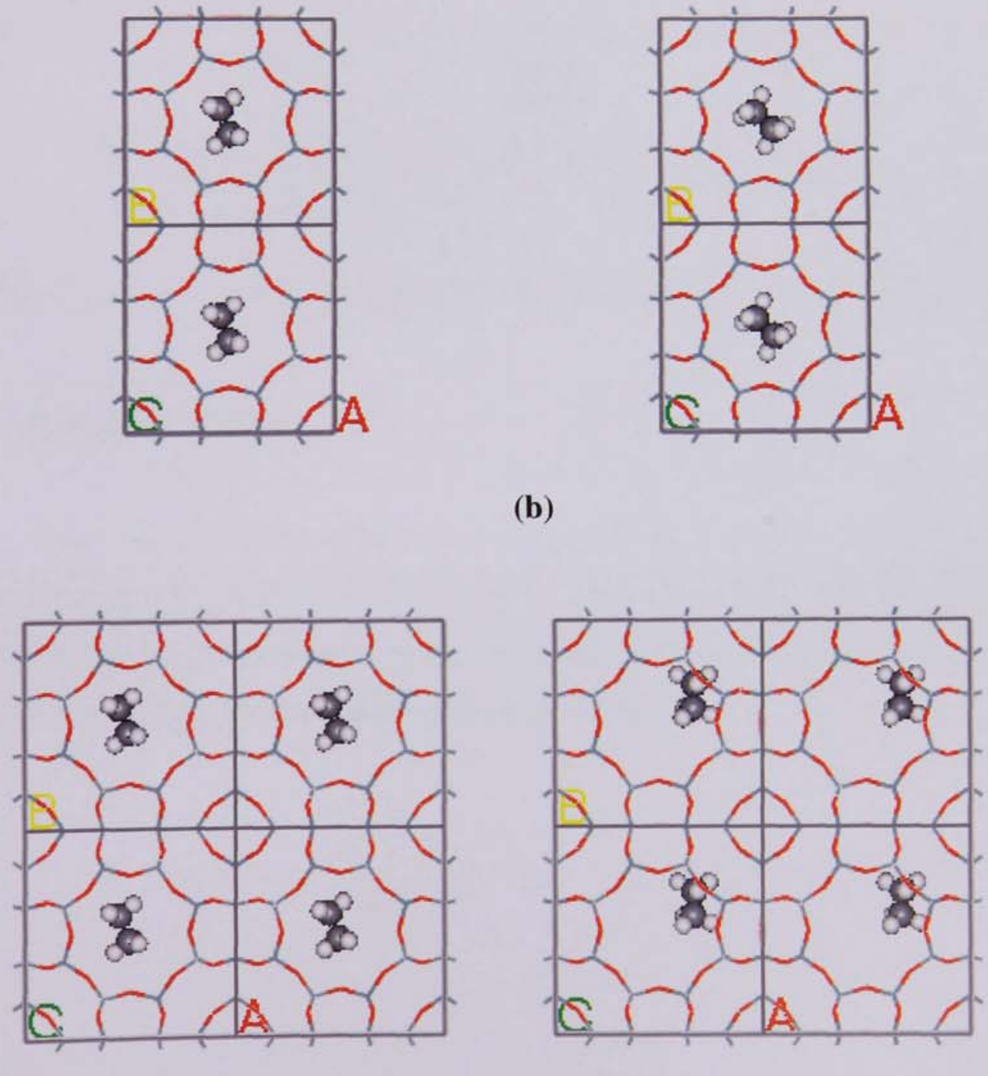

(a) (b)

(c) (d)

Figure 6.3 Ethane in LTA (a&c before energy minimization; b&d preferred sorption site after minimization.

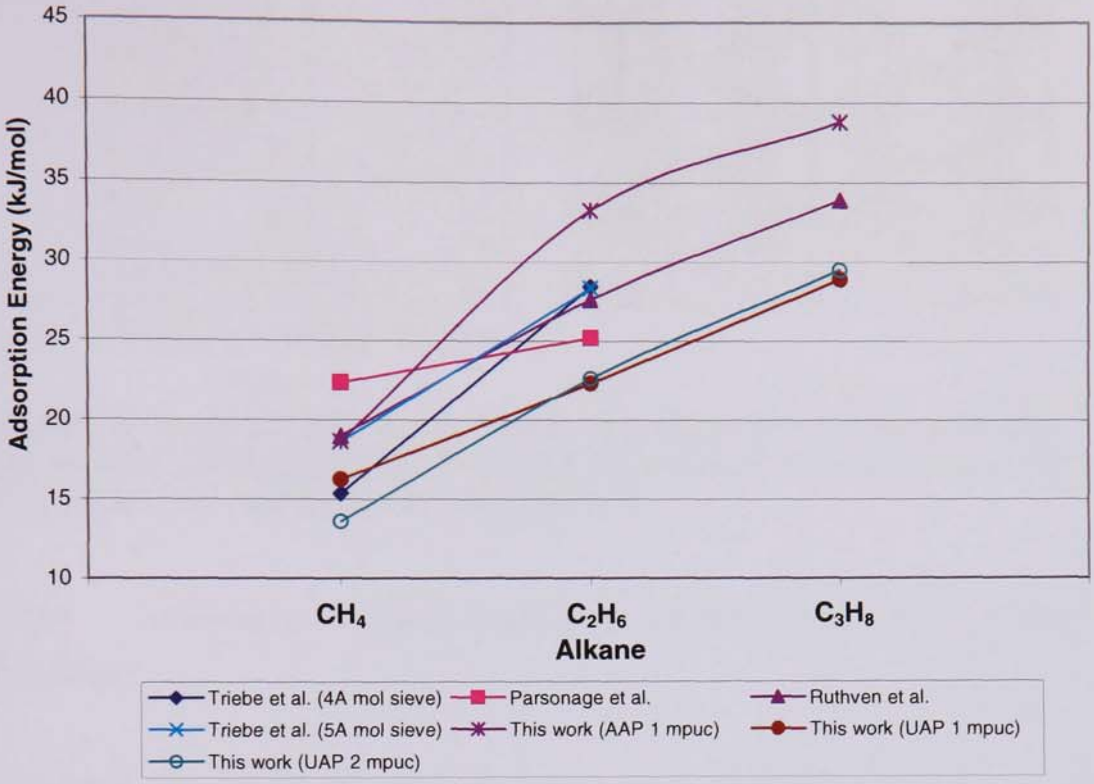

Figure 6.4 Calculated and Experimental adsorption energies of n-alkanes in LTA

6.1.2 Mordenite (MOR)

The mordenite model (see figure 6.5) has an orthorhombic structure with space group Cmcm and unit cell a = 18.11 Å , b = 20.53 Å , and c = 7.53 Å . The channel system is 2-dimensional and comprises of both 12-ring and 8-ring straight channels, which are interconnected via parallel elliptical 8-ring channels.

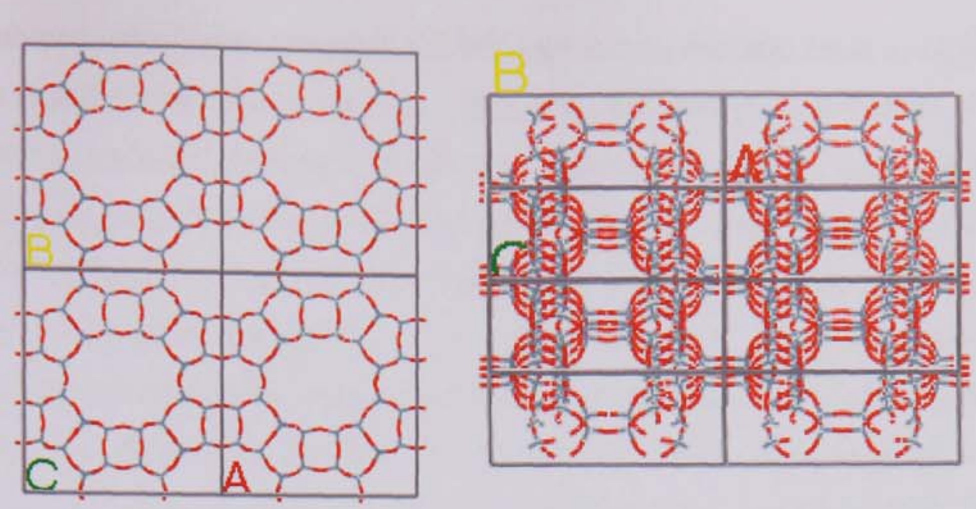

(a) **(b)**

Figure 6.5 Mordenite structure (a) Straight linear Channels (12-ring & 8-ring) viewed along [001] (C-axis), (b) Parallel Elliptical Channels (8-ring) viewed along [010] (B-axis) & tilted approx 20 degrees from axis.

6.1.2.1 Adsorption of pure components methane, ethane & propane in Mordenite

The mordenite zeolite has three channel systems, which are accessible to sorbed molecules. These are the straight 12-ring channels with dimensions of 6.7 x 7.0 (Å), the straight 8-ring channels with dimensions of 2.9 x 5.7 (Å), and the "side pocket" elliptical 8-ring channels, which interconnect the two linear channels with dimensions of about 3.4 x 4.8 (Å).

Of the three channel systems the methane molecule is small enough to gain access into all, but the larger ethane and propane molecules are restricted only to the straight 12-ring channel (161). In all cases considered the sorbed molecules tend to drift in the 12-ring channel towards the entrance of the parallel elliptical 8-ring channels (see figures 6.6 & 6.7), and most often molecules were found to prefer being located just off the centre of the 12-ring channel and closer to the wall of the smaller 8-ring channels. The centre of the parallel elliptical 8-ring "side pockets" channels was found to be another favourable site but only for methane molecules. Figure 6.8 compares the calculated enthalpies of adsorption with previous theoretical and experimental work. Notwithstanding the siliceous model used in the present studies the predicted energies are broadly in line with experimental values.

The combined united atom potentials (UAP) used at zero loadings seem to agree well with the experimental data of Ma et al. (162). Also the adsorption enthalpies derived from the all atomistic potentials (AAP) for methane and propane agree well with experimentally observed values. The average calculated sorption energies of 23.874 and 36.083 kJ/mol for CH_4 and C_3H_8 respectively using AAP agrees well with the experimental values of Webster et al. (161) and Triebe et al. (158). It is interesting, however, that the calculated energies for ethane from the 2 sets of potentials differs by a wide margin (Figure 6.8). A reason for this may be attributed to the orientation of the ethane molecule affecting the adsorption enthalpy (i.e. configurational energy effects). It was noticed that the UAP was able to handle configuration energy effect far better than the AAP. This reinforces the argument of choosing the UAP model over the AAP in this type of simulation.

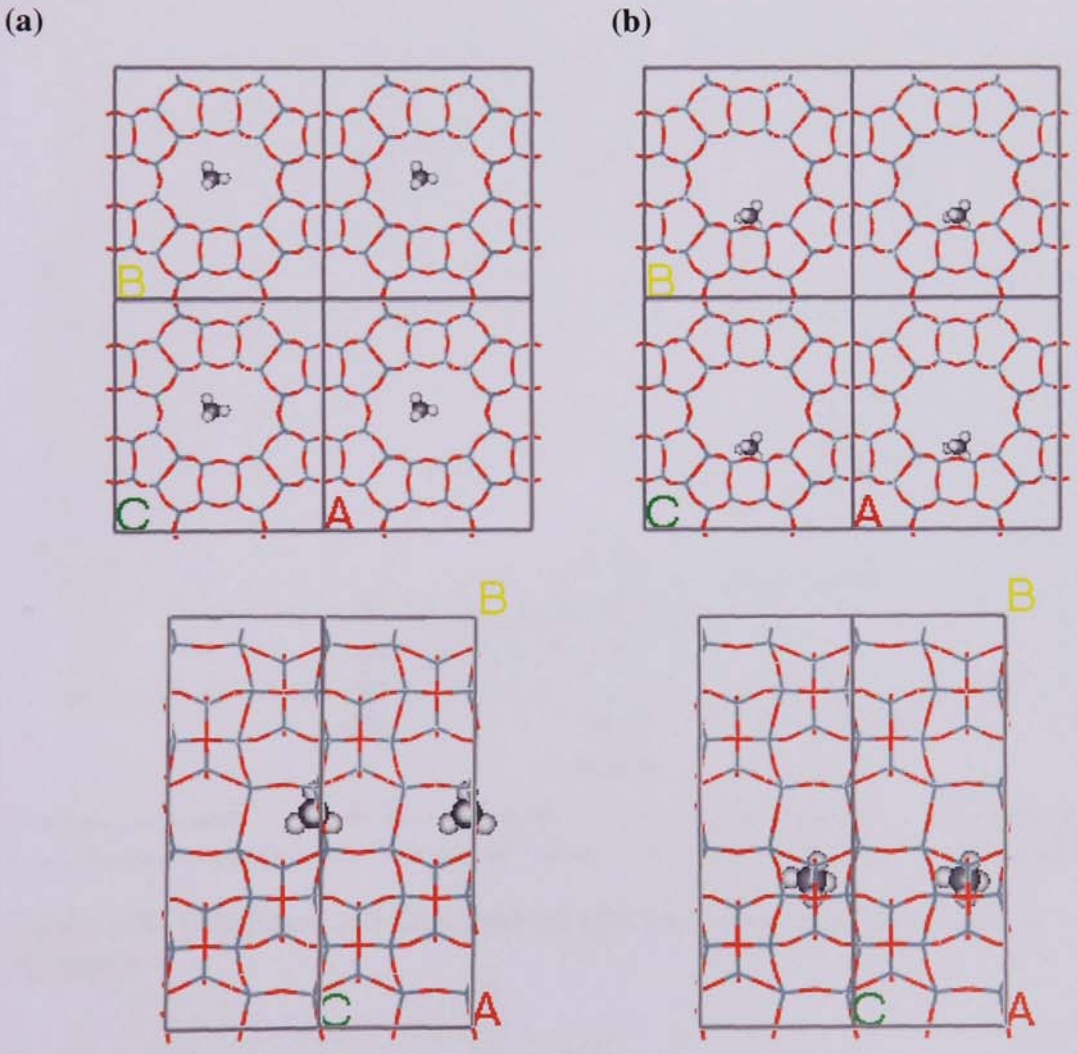

Figure 6.6 Methane molecule in Mordenite 12-ring channel; (a) before minimization (b) after minimization. Top: view down C-axis [001], Bottom: view down A-axis [100]

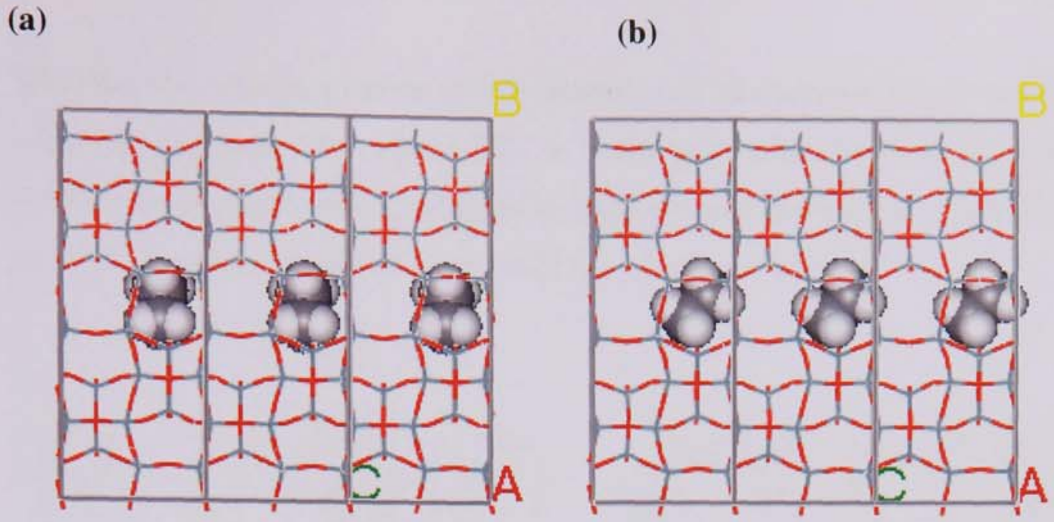

Figure 6.7 Ethane molecules in Mordenite 12-ring channel viewed down A-axis [100]; (a) before (b) after minimization

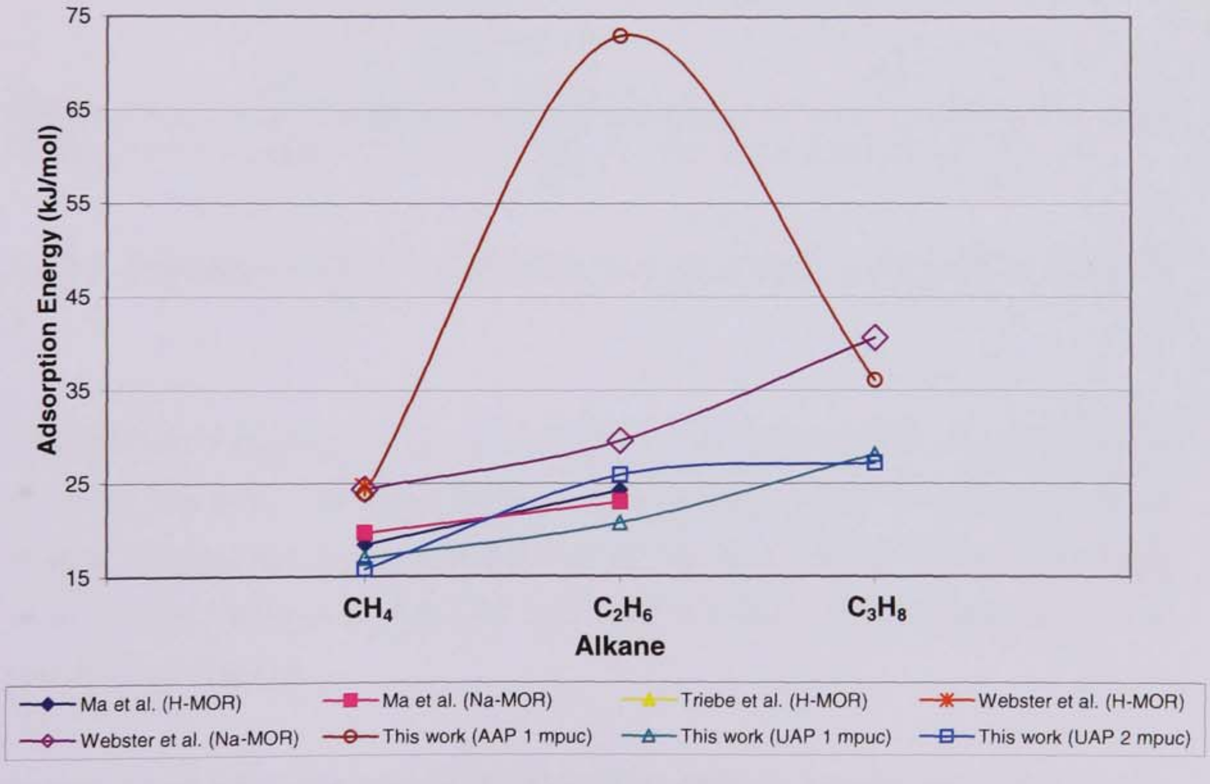

Figure 6.8 Calculated and Experimental adsorption energies of n-alkanes in Mordenite

6.1.3 Silicalite-1

The silicalite structure consists of a combination of 10 membered rings of straight and sinusoidal channels (See figure 6.9). It is the pure siliceous form of iso-structural ZSM-5 zeolite series with orthorhombic structure and space group Pnma having unit cell dimensions a = 20.076 Å , b = 19.926 Å , and c = 13.401 Å .

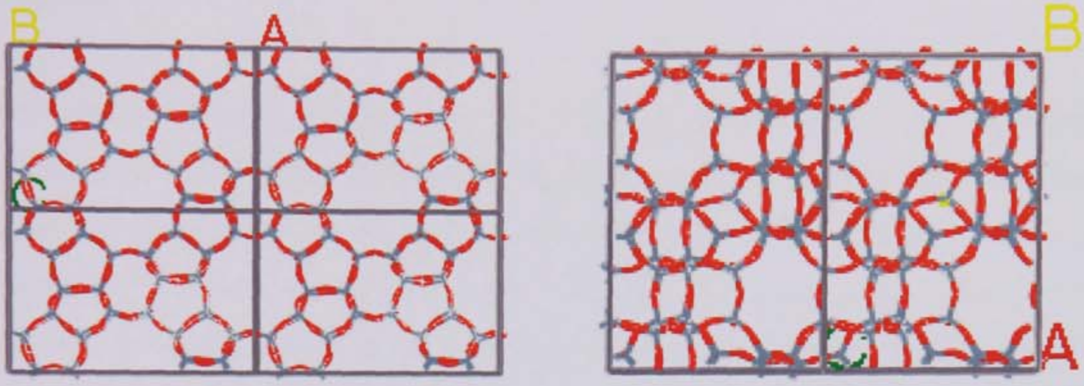

(a) (b)

Figure 6.9 Silicalite-1 structure (a) Straight Channels (10-rings) viewed down [010] (B-axis), (b) Sinusoidal Channels (10-rings) viewed down [100] (A-axis).

6.1.3.1 Adsorption of pure components methane, ethane & propane in Silicalite-1

The Silicalite-1 topology produces a combination of intersecting linear and sinusoidal channels. The sorbed molecules thus have a choice of locations to occupy namely the straight 10-ring channels with dimensions of 5.4 x 5.6 (Å), the sinusoidal 10-ring channels with dimensions of 5.1 x 5.2 (Å), and the channel intersection between the two 10-rings channels.

In previous work carried out by Titiloye et al. (84) the channel intersections were determined to be the most preferred sites for sorption and the chances of sorbed molecules occupying the straight channels was higher than that of sinusoidal channels. Nascimento (85) concluded that linear alkanes (C1-C4) showed an equal probability of being found in both the straight and the sinusoidal channels. The results obtained from using the all atom potentials (AAP) agree well with previous works (Figure 6.10). The calculated enthalpies of adsorption for methane and ethane (AAP) agree with the works of Vlugt et al. (163), Hufton and Danner (164) and Nijhuis et al. (165). However, the calculated enthalpy for propane is 9 kJ/mol higher than the corresponding experimental data. The calculated sorption energies using the united atom potential (UAP) for methane and propane also agree with the experimental results except for the ethane that gave a lower adsorption energy. A similar trend was noticed even when the number of molecules per unit cell was increased.

The findings in this work also show that there are three preferred sites of adsorption for methane and ethane molecules. Firstly at the centre of the double 10-ring straight channel windows, secondly being located in the channel intersections but closer to the channel walls and finally the centre of the double 10-ring sinusoidal windows. It was observed that there is a preference for the channel intersections over the straight and sinusoidal channels. However, for propane the observed behaviour was different having a strong preference for being located first in the straight channels followed by the channel intersections with the least preference for the sinusoidal channels. As can be seen from Figures 6.11 and 6.12, propane molecules favour the straight channels over the channel intersections; this is reflected by the movement of the molecule from the channel intersection into the straight channels after minimization. The propane molecule only tend to find a minimum energy site in the centre of the sinusoidal 10-ring window if it was placed at this centre initially prior to minimisation (Figure 6.13) which indicates this site is a local minima. This view is supported by the fact that the molecule did not move from the channel intersections into the sinusoidal channels during any of simulations carried out. Infact the molecule tend to either preferentially move out of the channel intersections into the straight channels as discussed above or remain in the channel intersections but closer to the channel wall.

The current work confirms some of the earlier work of Titiloye et al. (84) and that of Nascimento (85) for methane and ethane in silicalite. In general, smaller molecules appear to reside in the channel intersection but with large molecules such as propane, it was noticed that the straight channel is preferred to either the sinusoidal or channel intersections.

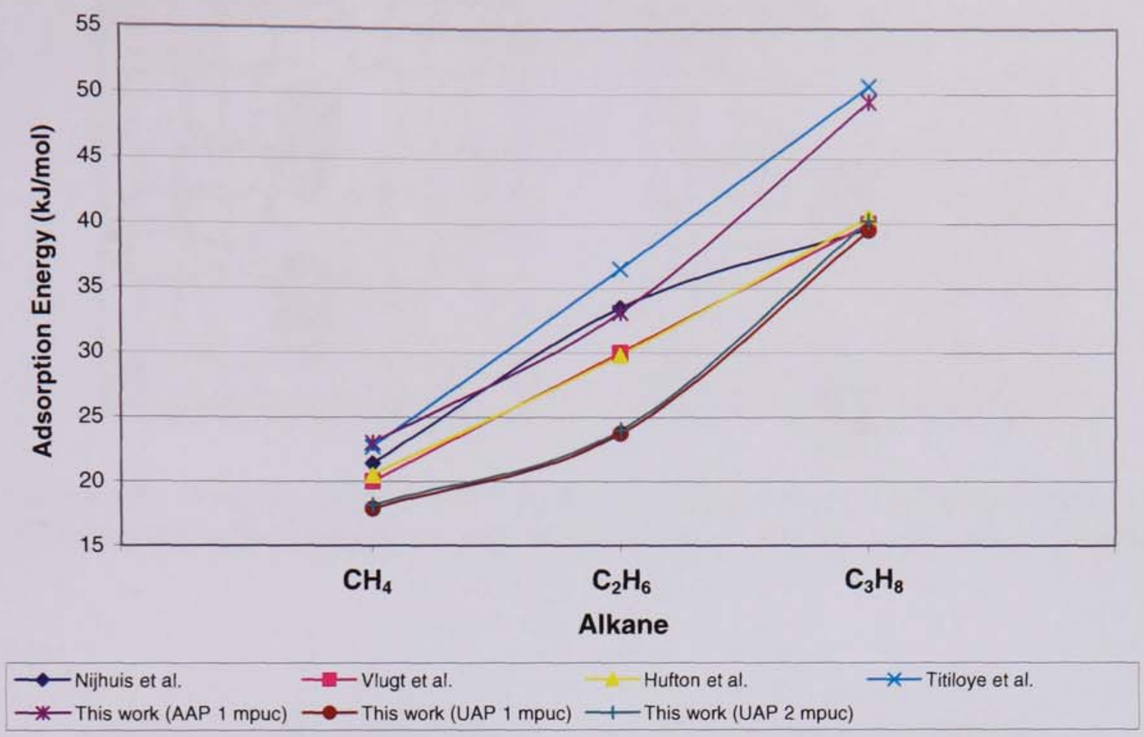

Figure 6.10 Calculated and Experimental heats of adsorption of n-alkanes in Silicalite

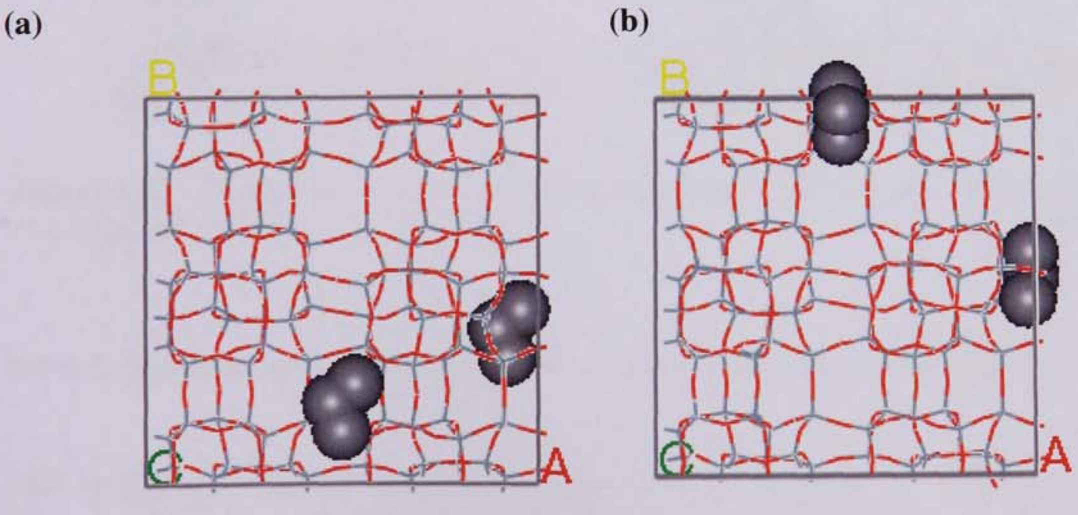

Figure 6.11 Propane molecules in Silicalite channels viewed down C-axis [001]; (a) before minimization in both straight and sinusoidal channel (b) after minimization in the straight channels

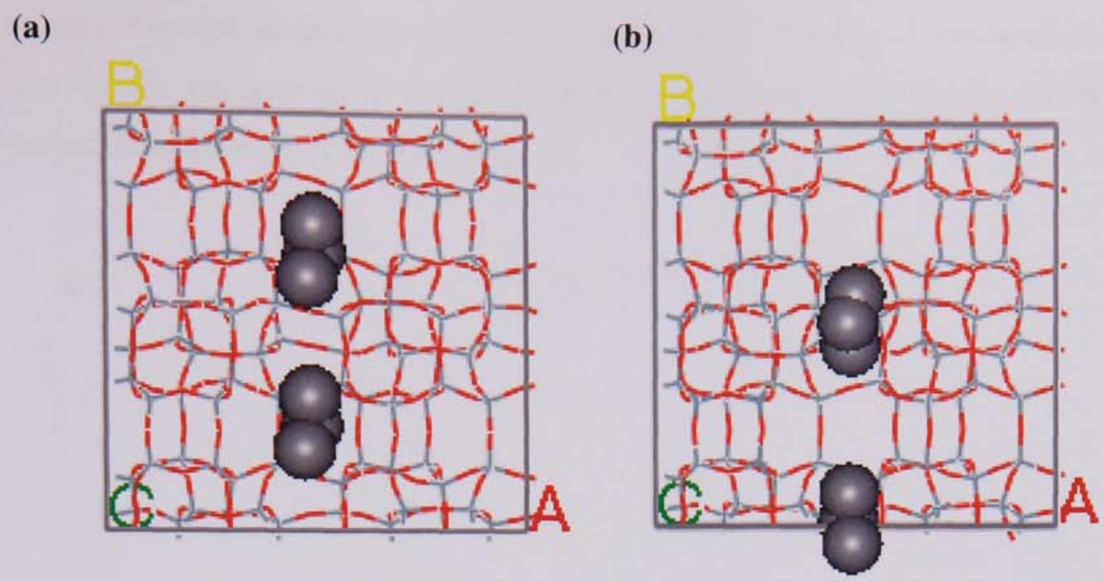

Figure 6.12 Propane molecules in Silicalite channels viewed down C-axis [001]; (a) before minimization channel intersection (b) after minimization in the straight channels

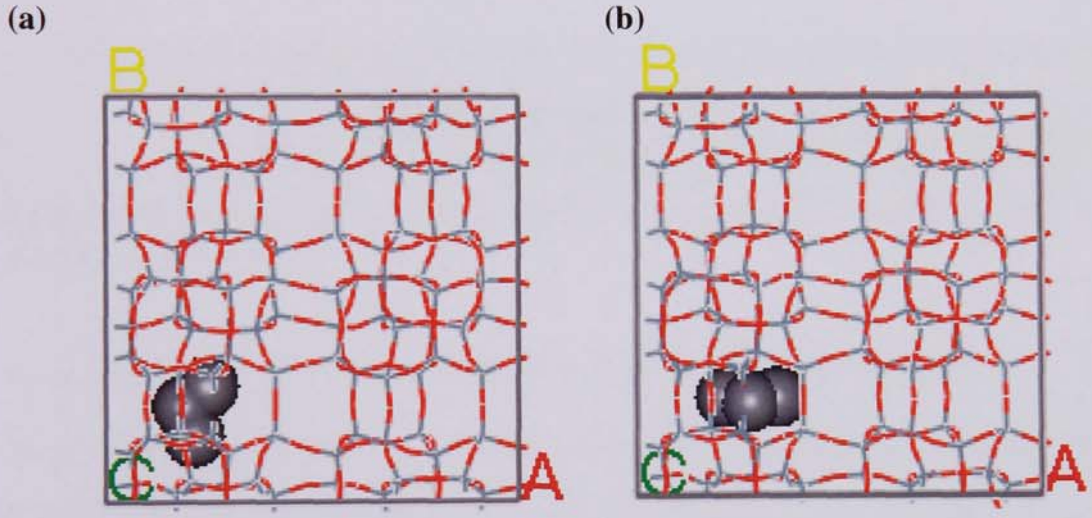

Figure 6.13 Propane molecules in Silicalite sinusoidal channels viewed down C-axis [001]; (a) before (b) after minimization.

6.1.3.2 Influence of temperature and loading on Silicalite-1 adsorption energies

Due to the relevance of silicalite-1 membranes in separating hydrocarbon fluids, molecular dynamic simulations were used to study the effect of temperature and loading on calculated enthalpies. The final minimised configurations from the static runs were used as starting inputs in the molecular dynamics runs and using only the united atom potentials. Typical observed changes in energies for ethane and propane between 0 and 350 K are shown in Figure 6.14. The calculated average sorption energies for each molecule remain fairly constant as the loading is increased per unit cell. As the temperature is increased the heats of adsorption increases slightly but remain constant with increase loading.

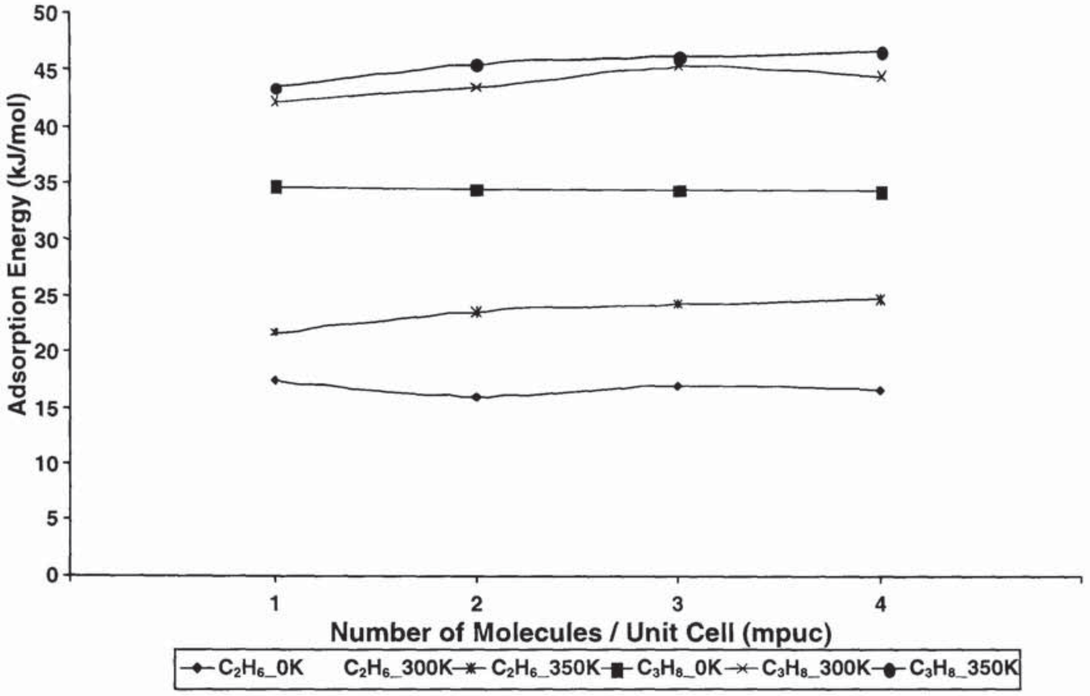

Figure 6.14 Calculated heats of adsorption of ethane and propane in Silicalite-1 at different temperatures.

6.1.4 Adsorption of mixed components in LTA, MOR and Silicalite-1

Static simulations of binary (1:1) and ternary (1:1:1) mixtures of methane ethane and propane were also investigated on the purely siliceous forms of the three zeolites LTA, mordenite and silicalite. The calculated enthalpies of adsorption for the various binary and ternary mixtures are shown in Table 6.1. The siliceous LTA zeolite has the lowest enthalpies of adsorption for both binary and ternary mixtures (Table 6.1). This is followed by mordenite and silicalite-1. It was observed that the highest enthalpies of adsorption for binary components are for mixtures, which contain ethane and propane. Unlike the static simulations of single components there is competition from molecules for adsorption sites. It is therefore difficult to state which locations are preferred by each of the components in the mixtures from the static simulations. The enthalpies clearly suggest there is a preference for binary mixtures of methane and ethane over other mixtures. In addition, separation of ethane and propane mixtures would prove to be problematic even when compared to ternary component mixtures.

This problem is better investigated using both static and dynamic simulations, as this would give a clearer picture of favourable sites of adsorption, locations and activities of the various components in the mixtures. The diffusion coefficients for the individual species in a given binary or ternary mixture would also make it easier to determine the diffusional path and identify which of the components in the mixtures are preferentially adsorbed. (This is the focus of the work in chapter 7)

Table 6.1 Calculated heats of adsorption for binary and ternary mixtures (kJ/mol)

Zeolite	**Mixture Adsorption Energies (kJ/mol)**			
	CH_4:C_2H_6:C_3H_8 (1:1:1)	**CH_4:C_2H_6 (1:1)**	**CH_4:C_3H_8 (1:1)**	**C_2H_6:C_3H_8 (1:1)**
LTA (0 K)	18.807	15.611	20.850	22.590
MOR (0 K)	22.316	17.008	25.523	27.580
Silicalite-1 (0 K)	23.285	20.240	27.180	28.070

6.2 Zeolite surface simulations

6.2.1 Methodology

Relaxed silicalite-1 and Na-mordenite structures were generated using the METADISE code. Following this different surface cuts (codes) were obtained for each zeolite with the general orientations (miller indices): {100}, {001}, {010} and {101}. The approach of Tasker (Chapter 3) was employed to generate only charge neutral and non-dipolar surface configurations for each chosen miller index. Since the aluminated zeolite structures have a lower symmetry compared to purely siliceous zeolite structures, several cleavage planes for each miller index are possible. This results in a large number of possible surface termination configurations, where the surface energy of each termination configuration needs to be determined to obtain the most stable surface configuration. For this reason only four low miller indices were chosen for each zeolite with the zeolite structure modelled by a single crystallographic unit cell. Since the synthesis of zeolites is typically carried out in an aqueous environment the influence of both hydroxylated and non-hydroxylated termination configurations were investigated. For each miller index investigated the surface energies reported are only for those termination configurations which minimised successfully.

6.2.2 Silicalite-1 surface generation

For the {001} surface 16 possible termination configurations were generated of which only two were found to be stable and thus minimise successfully. Similarly for the {010} surface out of a possible 24 termination configurations only two were found to minimise successfully whilst for the {101} surface out of a possible 10 termination configurations only one was found to minimise.

Tables 6.2a and 6.2b show the resultant calculated surface energies for each silicalite-1 miller index investigated (hydroxylated and non-hydroxylated). It is seen in general that the non-hydroxylated surfaces have the lowest surface energies compared to that of the hydroxylated surfaces which have the largest surface energies. Of the miller indices investigated it was seen that the {010} index has the lowest surface energies for both the hydroxylated and non-hydroxylated surface configurations. The largest surface energies for the hydroxylated surfaces correspond to {001} miller index whereas for the non-hydroxylated surfaces the largest surface energies correspond to the {101}.

The resultant silicalite-1 surface configurations and surface maps for each miller index are depicted in Figures 6.15 to 6.30. The surface configuration figures show the predicted atom positions and bonding present whereas the surface maps give a clear indication of the predicted surface morphology present (i.e. channel structures, apertures and trenches).

Table 6.2a Pure (Non-hydroxylated) silicalite-1 surface energies before and after energy minimization (relaxation).

Pure (Non-Hydroxylated) Surface			
		Unrelaxed	Relaxed
Miller	Code	Surface Energy (J/m^2)	
0 0 1	226	6.136	1.894
	466	6.136	1.894
0 1 0	113	3.258	1.532
	353	3.258	1.532
1 0 1	419	5.367	2.174

Table 6.2b Hydroxylated silicalite-1 surface energies before and after energy minimization (relaxation).

		Hydroxylated Surface	
		Unrelaxed	Relaxed
Miller	Code	Surface Energy (J/m^2)	
0 0 1	266	7.467	3.372
	466	6.136	2.717
0 1 0	113	3.258	2.010
	353	3.258	2.010
1 0 1	419	5.366	2.532

6.2.2.1 Silicalite-1 {001} surface

Figures 6.15 to 6.20 show the generated stable surfaces of the {001} silicalite-1 surface. It was interesting to note that for the two stable {001} surface configurations (codes 266 and 466) that non-hydroxylated surface energies following energy minimization (relaxation) were equal but for the hydroxylated surfaces it was seen that the surface energies following relaxation and prior to relaxation were quite different. A possible reason for this observed difference in surface energies maybe due to the number of surface hydroxyl groups present. From figures 6.16 and 6.19 it can be seen that code266 has 20 surface hydroxyl groups whereas code466 has only 16 surface hydroxyl groups per unit surface area. From Table 6.2b it can be seen that the surface with the greater number of hydroxyl groups had a higher surface energy. It was also found that the hydroxylated surfaces consisted of both partial and full six membered ring (6MR) and five membered ring (5MR) terminations (figure 6.16c and 6.19c). But for the non-hydroxylated surfaces as seen in figures 6.15c and 6.18c it was found that during energy minimization (EM) partial reconstruction of the surfaces occurred resulting in the formations of four membered rings (4MR).

From the surface maps of the {001} hydroxylated surfaces generated (figures 6.17 and 6.20) it can be seen in general for both surfaces (codes 266 and 466) that there are distinct morphological features present. The half exposed straight channels, sinusoidal channels and channel intersections are all seen and represented as trenches running parallel to the surface. Due to the nature of the {001} surface configurations generated adsorbate molecules will be permitted from the surface into the bulk zeolite structure.

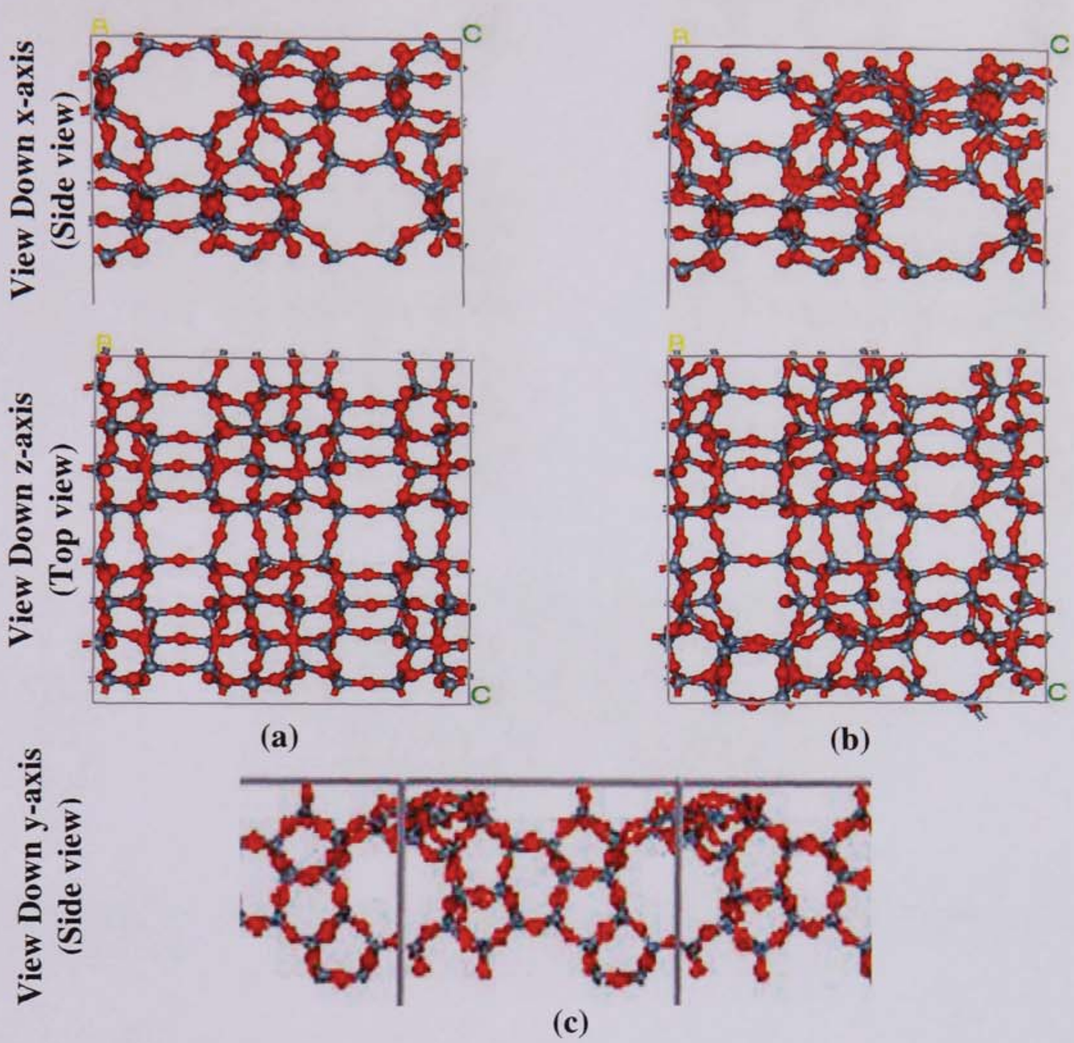

Figure 6.15 {001} Non-Hydroxylated Surface code266 Configurations (a) Before EM (b & c) After EM

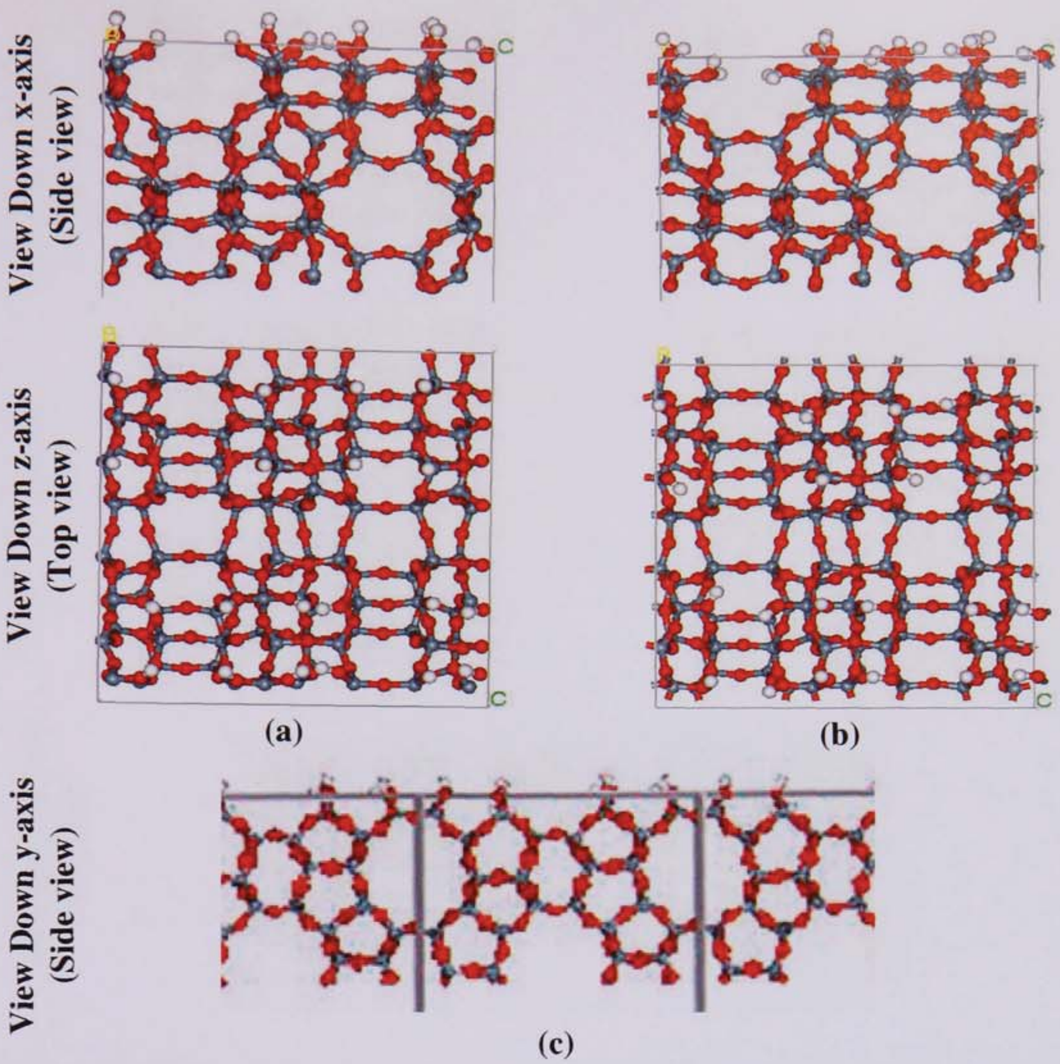

Figure 6.16 {001} Hydroxylated Surface code266 Configurations (a) Before EM (b & c) After EM

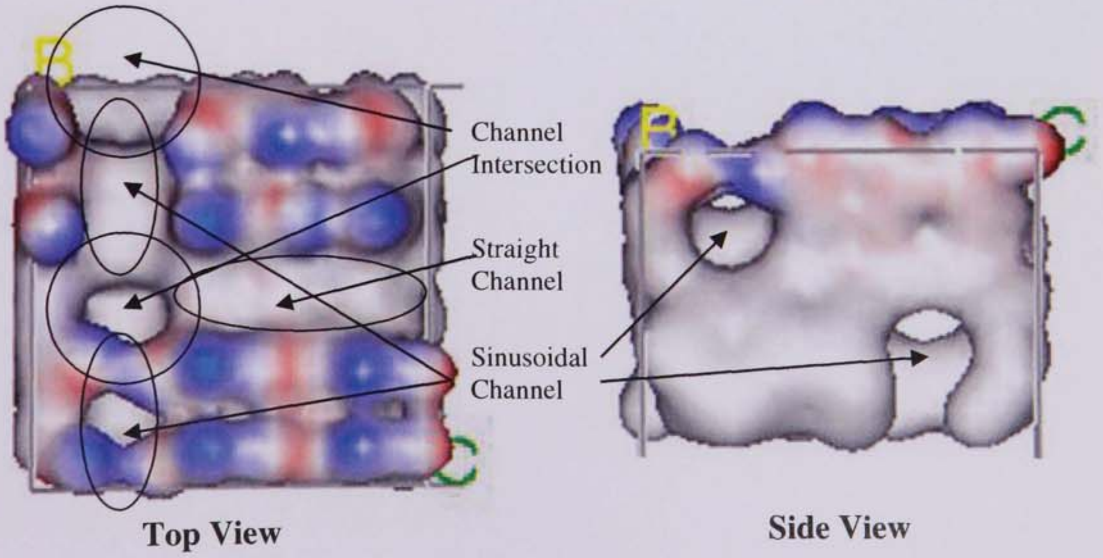

Figure 6.17 {001} Hydroxylated Surface code266 Surface Map (After EM)

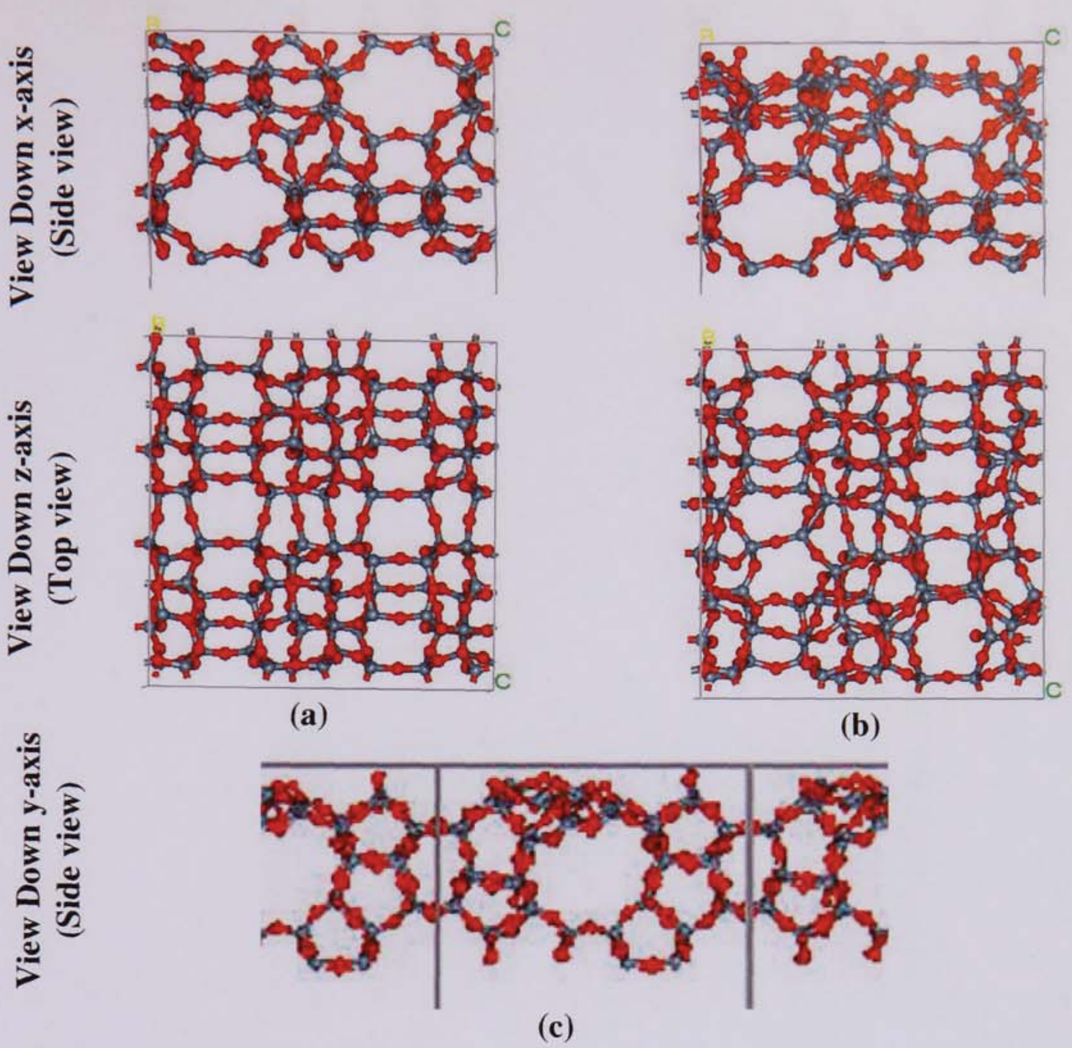

Figure 6.18 {001} Non-Hydroxylated Surface code466 Configurations (a) Before EM (b & c) After EM

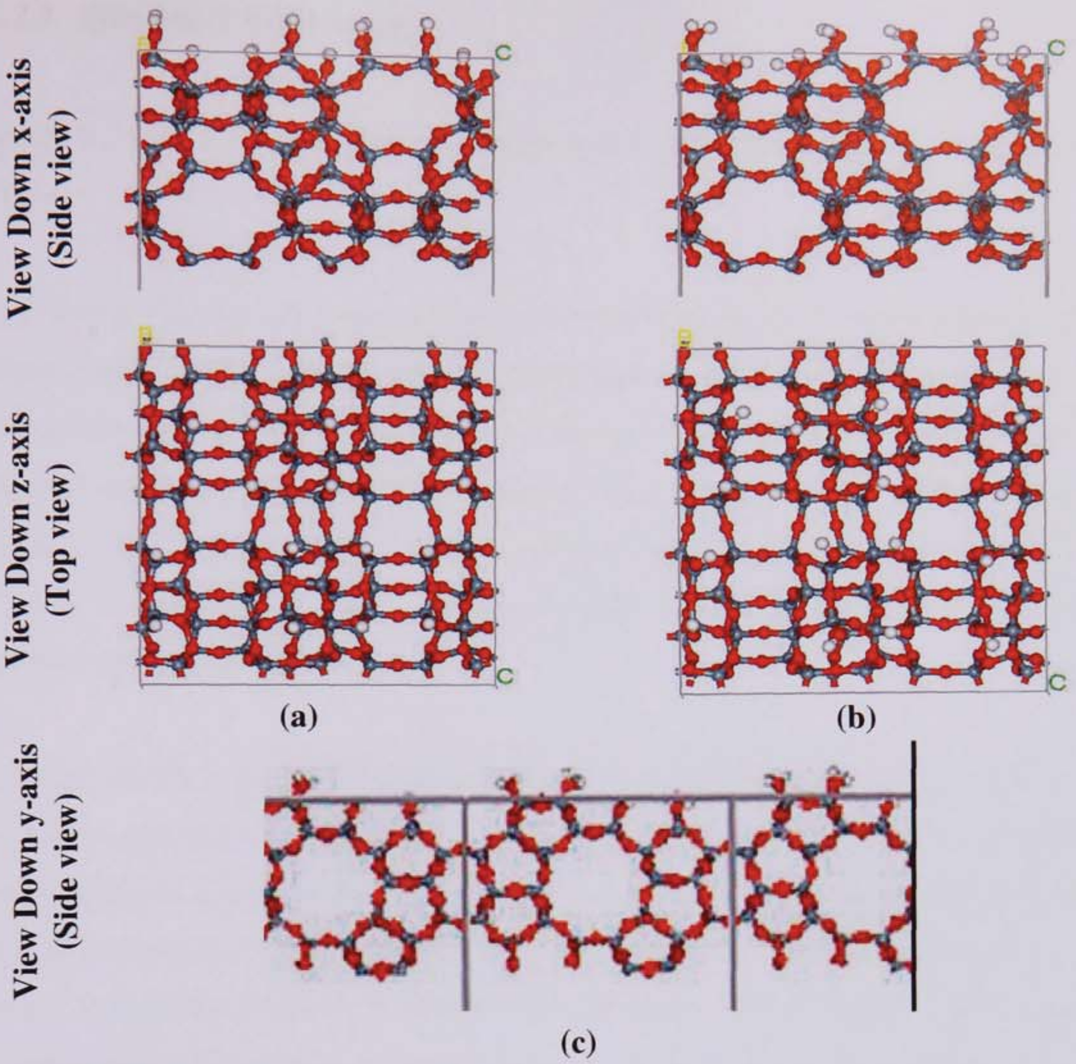

Figure 6.19 {001} Hydroxylated Surface code466 Configurations (a) Before EM (b & c) After EM

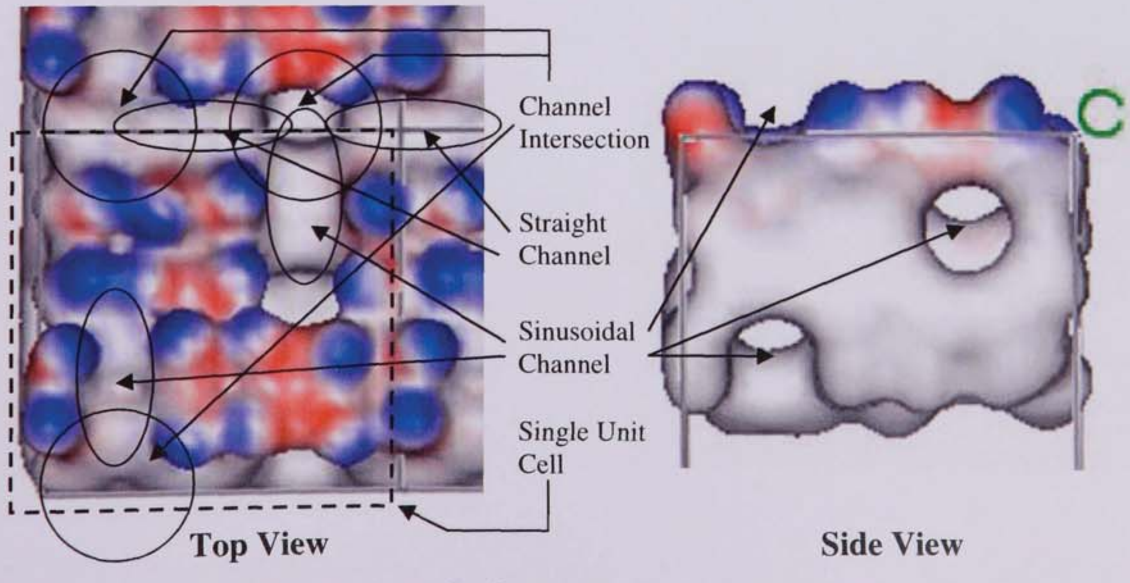

Figure 6.20 {001} Hydroxylated Surface code466 Surface Map (After EM)

6.2.2.2 Silicalite-1 {010} surface

Figures 6.21 to 6.26 show the generated stable surfaces of the {010} silicalite-1 surface.

From Tables 6.2a & 6.2b it was interesting to note that unlike the hydroxylated {001} surface configurations which had large differences in surface energies, both the {010} hydroxylated surfaces had similar surface energies. The reason for the similarity in hydroxylated surface energies maybe due to the equal number of surface hydroxyl groups present on each surface. From figures 6.22 and 6.25 it can be seen that codes 113 and 353 each have 8 surface hydroxyl groups per unit surface area thus resulting in similar surface energies.

From the surface maps of the {010} surfaces generated (figures 6.23 and 6.26) it can be seen in general for both surfaces (codes 113 and 353) that the ten-membered straight channel apertures are present. The surfaces are also seen to consist of half exposed sinusoidal channel trenches and channel intersections running parallel to the surface. Due to the presence of the straight channel apertures on the {010} surfaces adsorbate molecules will be permitted from the surface into the bulk zeolite structure with minimal resistance.

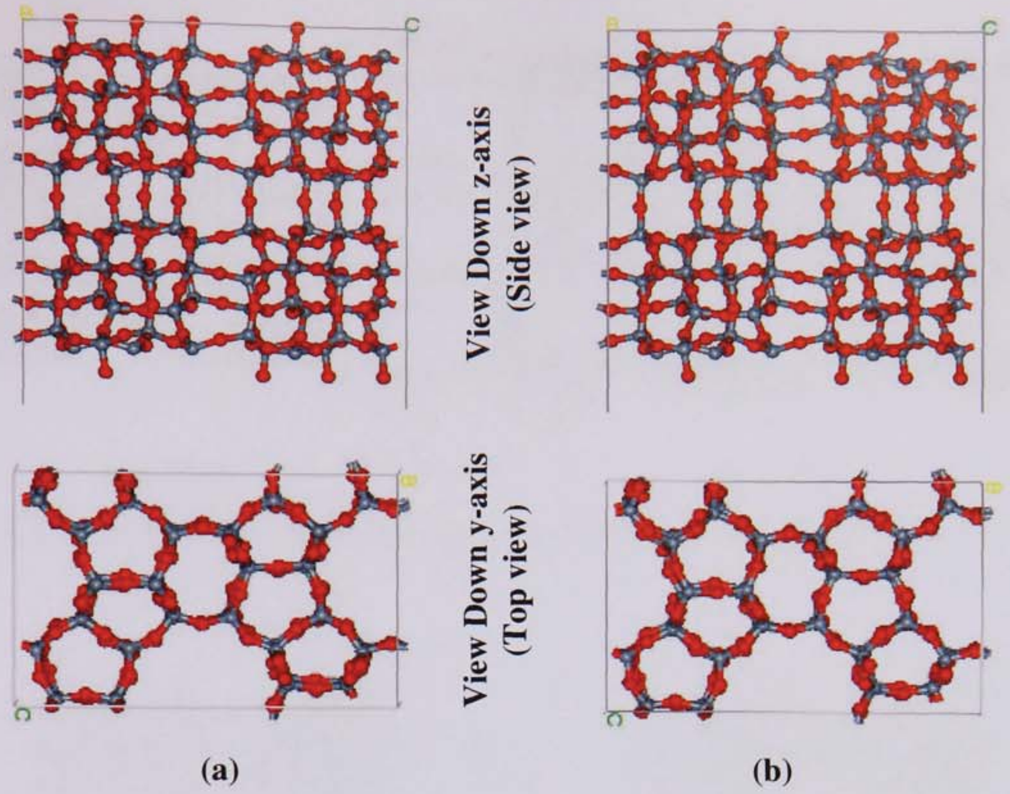

Figure 6.21 {010} Non-Hydroxylated Surface code113 Configurations (a) Before EM (b) After EM

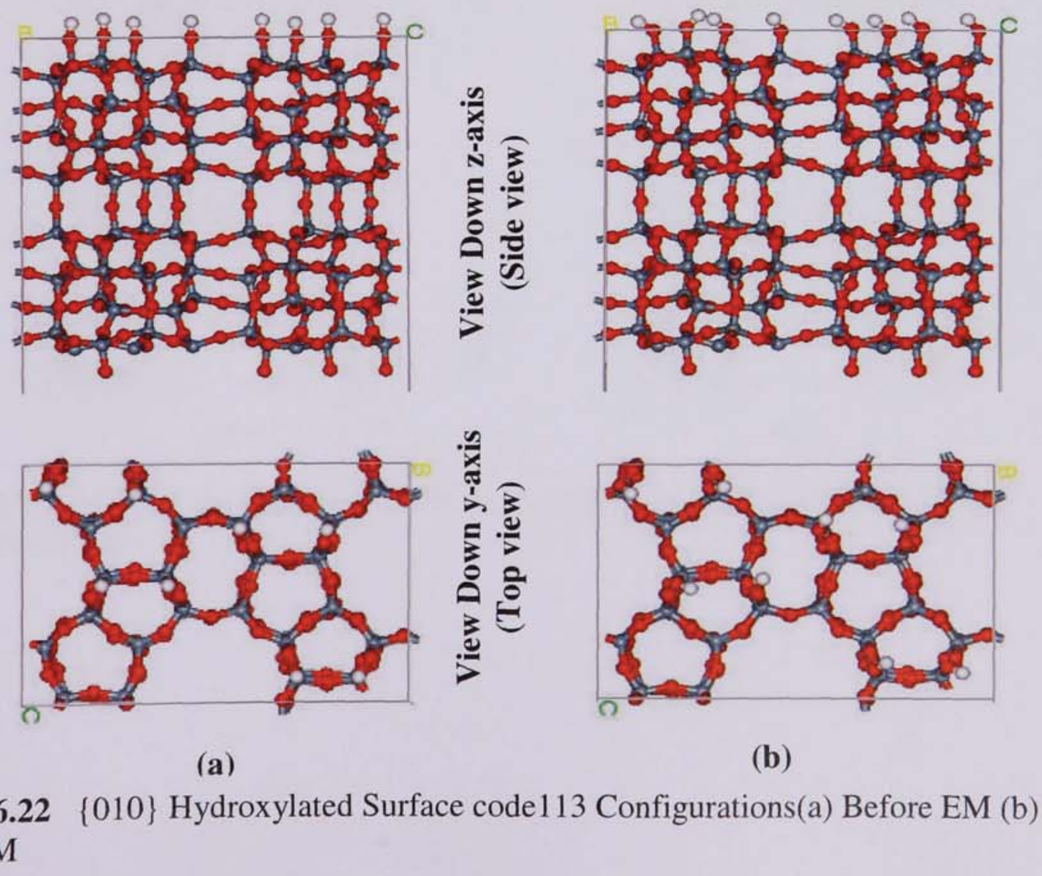

Figure 6.22 {010} Hydroxylated Surface code113 Configurations(a) Before EM (b) After EM

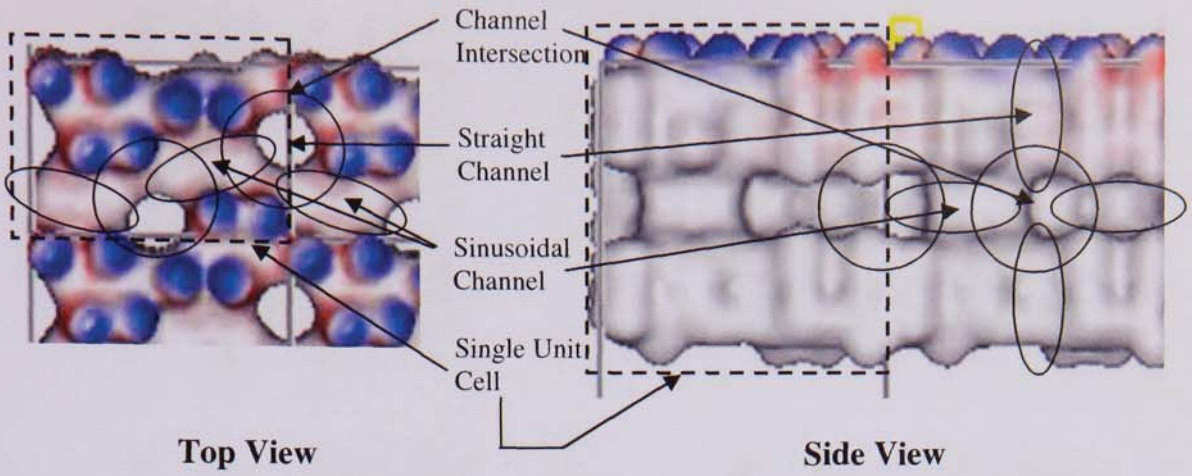

Figure 6.23 {010} Hydroxylated Surface code113 Surface Map (After EM)

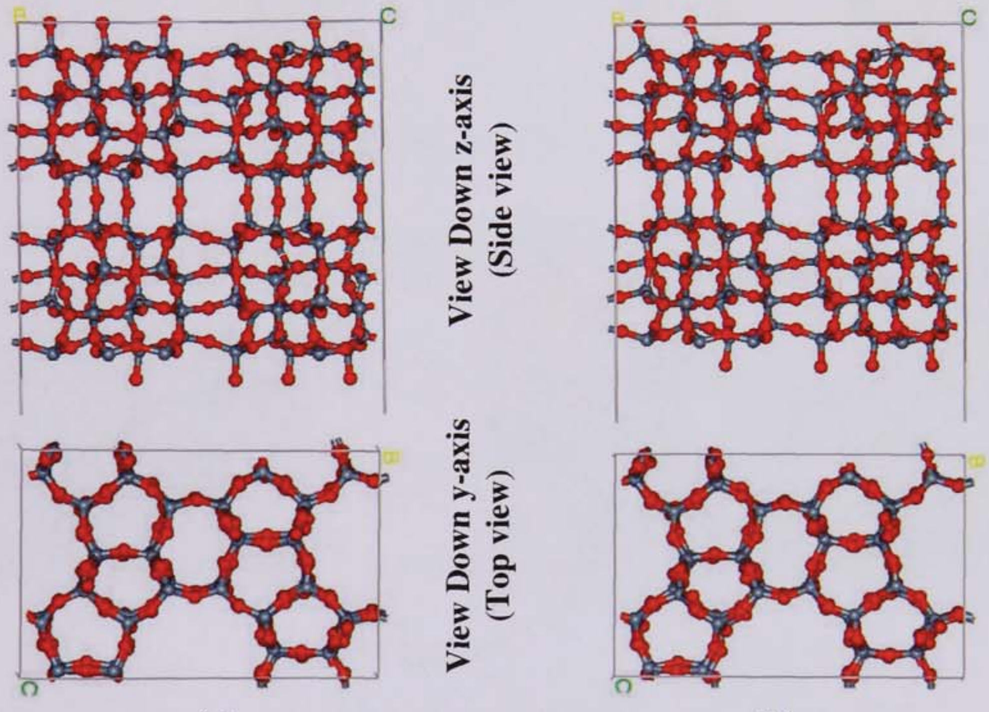

(a) **(b)**

Figure 6.24 {010} Non-Hydroxylated Surface code353 Configurations (a) Before EM (b) After EM

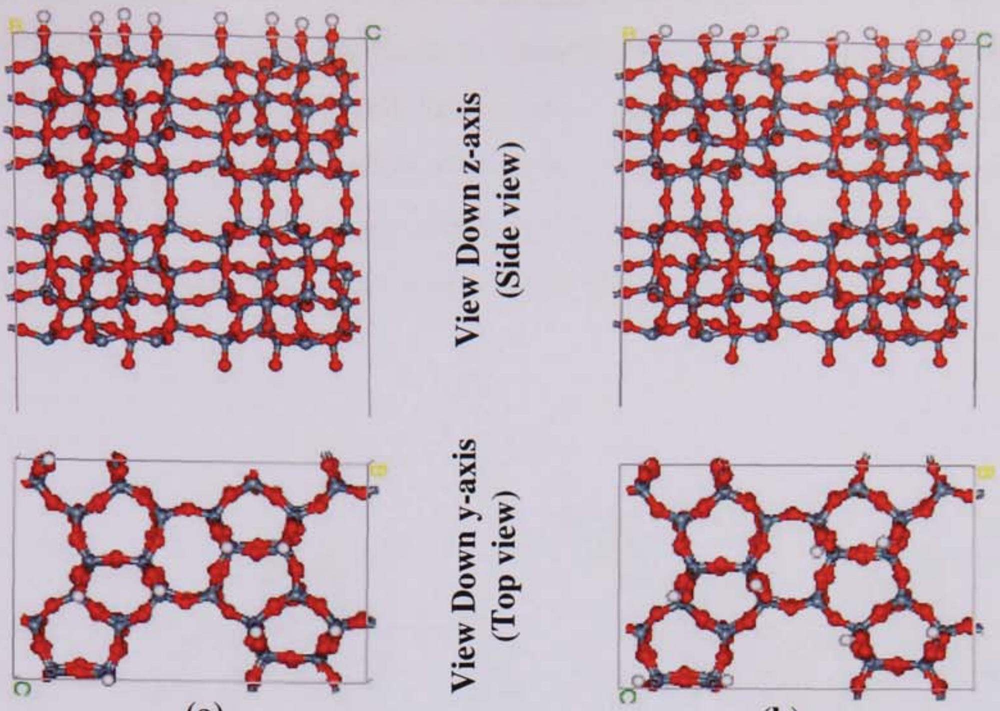

(a) (b)

Figure 6.25 {010} Hydroxylated Surface code353 Configurations (a) Before EM (b) After EM

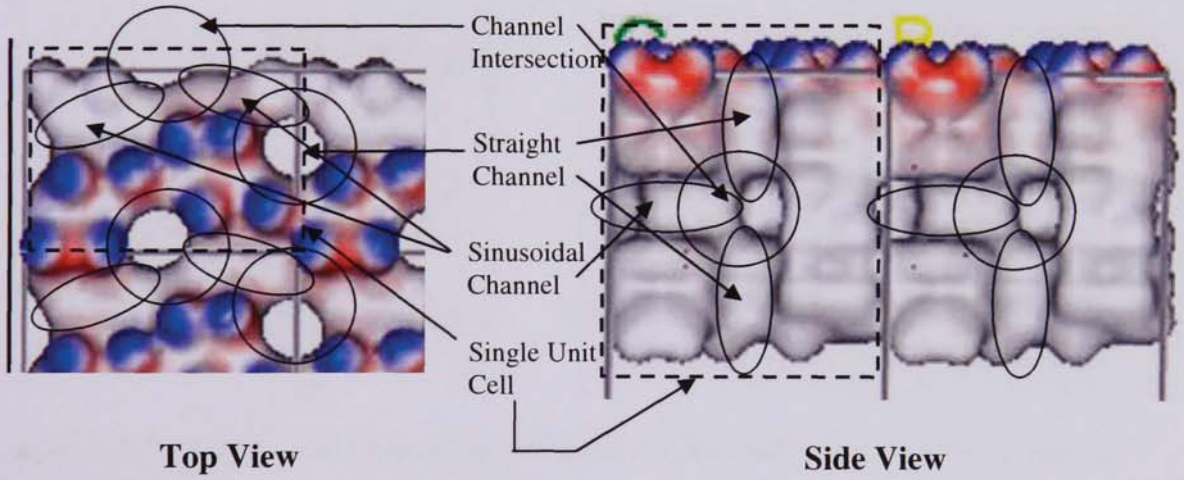

Figure 6.26 {010} Hydroxylated Surface code353 Surface Map (After EM)

6.2.2.3 Silicalite-1 {101} surface

Figures 6.27 to 6.29 show the most surface stable generated for the {101} plane. It can be seen that the {101} predicted surface terminations for both hydroxylated and non-hydroxylated consist of complete 5MRs coordinated to both a 5MR and a 6MR. From Tables 6.2a & 6.2b it is seen again that the {101} hydroxylated surface energy is much higher than that of the corresponding non-hydroxylated surface.

From the surface map of the {101} surface (figure 6.29) it can be seen that the ten-membered sinusoidal channel apertures are present. The surfaces are also seen to consist of channel intersections and half exposed sinusoidal and straight channel trenches running parallel to the surface. Due to the presence of the sinusoidal channel apertures on the {101} surface, adsorbate molecules will be permitted from the surface into the bulk zeolite structure with minimal resistance.

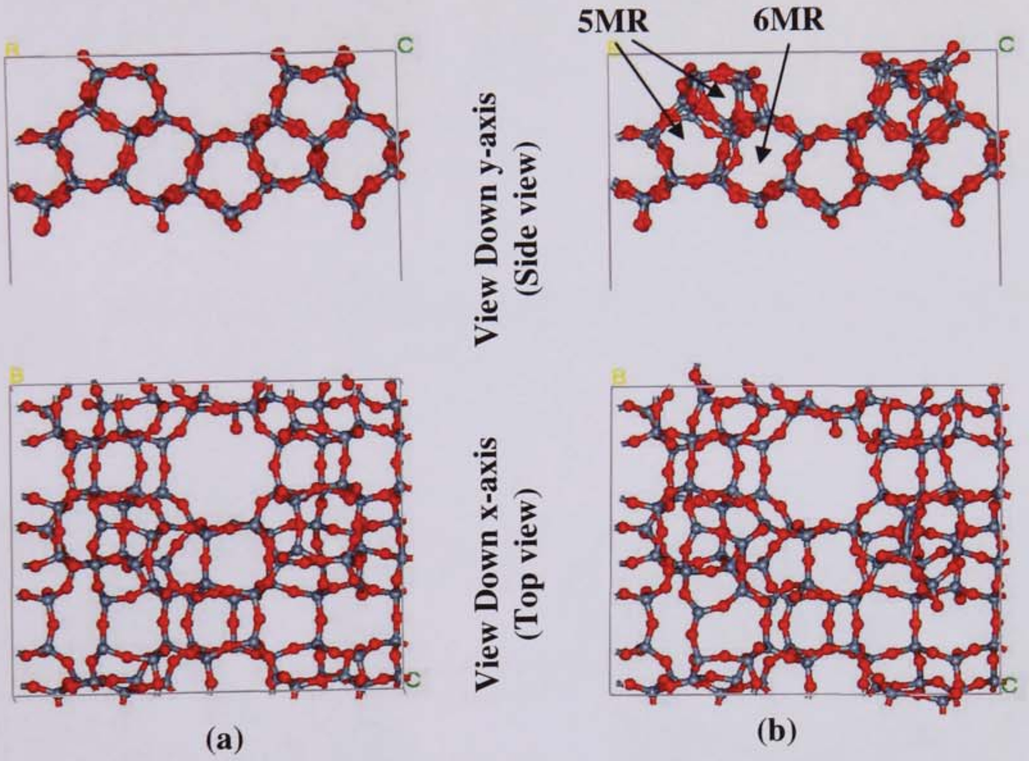

Figure 6.27 {101} Non-Hydroxylated Surface code419 Configurations (a) Before EM (b) After EM

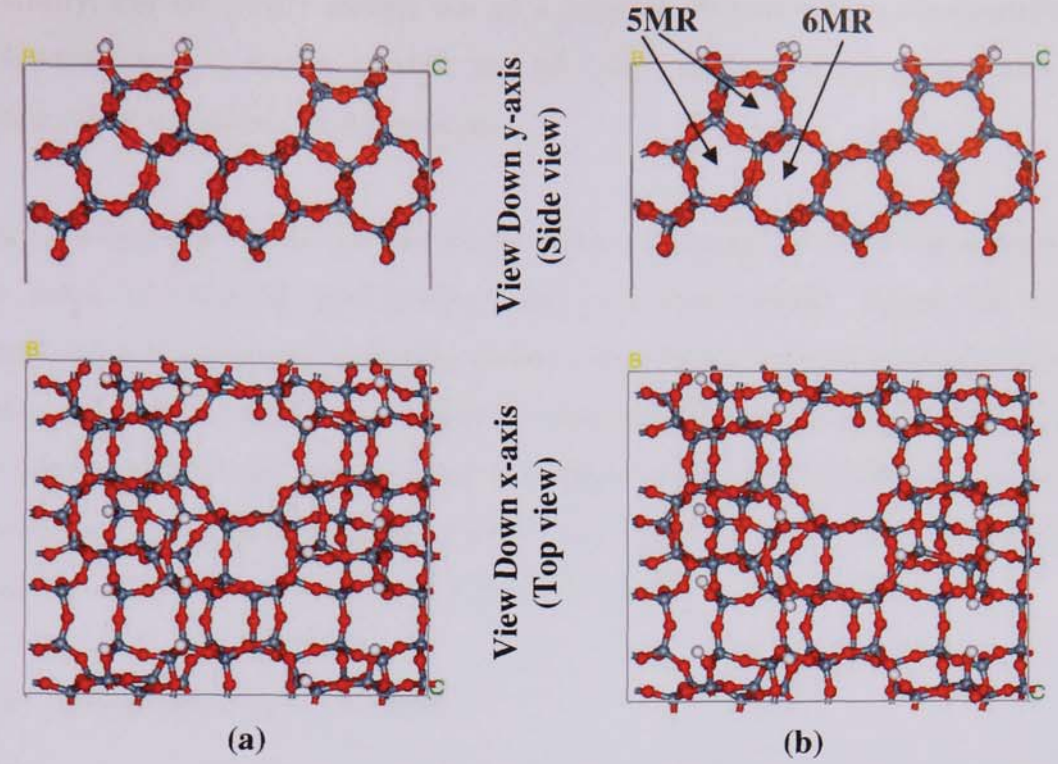

(a) (b)

Figure 6.28 {101} Hydroxylated Surface code419 Configurations (a) Before EM (b) After EM

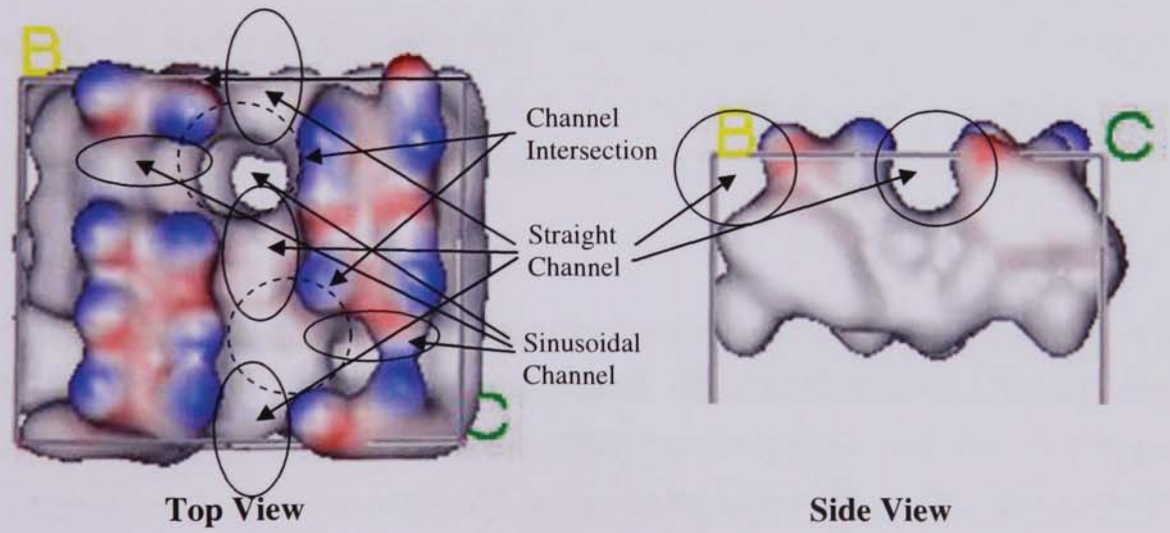

Top View **Side View**

Figure 6.29 {101} Hydroxylated Surface code419 Surface Map (After EM)

6.2.3 Na-mordenite surface generation

For the {100} surface 12 possible termination configurations were generated of which only 1 was found to stabilise and minimise successfully while for the {001} surface out of a possible 16 termination configurations only 1 was found to minimise successfully. For the {010} surface out of a possible 20 termination configurations only 4 were found to minimise while for the {101} surface only 2 were found to minimise out of a possible 10 terminations.

Tables 6.3a and 6.3b show the calculated surface energies for each Na-mordenite miller index investigated (hydroxylated and non-hydroxylated). Again the non-hydroxylated surfaces were found to have the lowest surface energies compared to the hydroxylated surfaces. Of the miller indices investigated it is interesting to see that the most stable surface for the non-hydroxylated surfaces is the {010} (code 35) while for the same corresponding hydroxylated surface we find that {010} (code 35) has the least stable surface indicated by the large surface energy.

6.2.3.1 Na-mordenite {100} surface

Figures 6.30 to 6.32 show the generated stable {100} Na-mordenite surface. It can be seen that the non-hydroxylated surface consists of five membered rings (5MR) terminations (figure 6.30). But for the hydroxylated surfaces as seen in figure 6.31b it was found that during energy minimization (EM) partial reconstruction of the surface occurred resulting in the coordination of an oxygen atom to 1 aluminium atom and to 2 silicon atom. This oxygen atom formed the union between a 2MR, 4MR and a 5MR surface termination.

From the generated surface map of the {100} hydroxylated surface (figure 6.32) it can be seen that there is a distinct trench present. This trench running parallel to the surface corresponds to the half exposed 12MR straight channels. It is also noticed that the presence of the surface hydroxyl groups on the terminations of the half exposed 8MR straight channels (The 8MR straight channels are located between the 12MR straight channels) results in the 8MR straight channel trenches not being seen on the surface map. Due to the nature of the {100} surface configurations generated adsorbate molecules will not be permitted from the surface into the bulk Na-mordenite structure.

Table 6.3a Pure (Non-hydroxylated) Na-Mordenite surface energies before and after energy minimization (relaxation).

Pure (Non-Hydroxylated) Surface			
		Unrelaxed	Relaxed
Miller	Code	Surface Energy (J/m^2)	
1 0 0	7	2.619	1.256
0 0 1	42	4.725	1.364
0 1 0	1	4.241	1.208
	35	4.875	0.992
	55	4.480	1.480
	91	4.875	1.569
1 0 1	2	4.299	1.696
	126	4.244	1.338

Table 6.3b Hydroxylated Na-Mordenite surface energies before and after energy minimization (relaxation).

Hydroxylated Surface			
		Unrelaxed	Relaxed
Miller	Code	Surface Energy (J/m^2)	
1 0 0	7	2.619	1.525
0 0 1	42	4.725	2.172
0 1 0	1	4.241	1.992
	35	4.875	4.249
	55	4.480	3.432
	91	4.875	2.491
1 0 1	2	4.299	2.344
	126	4.244	2.345

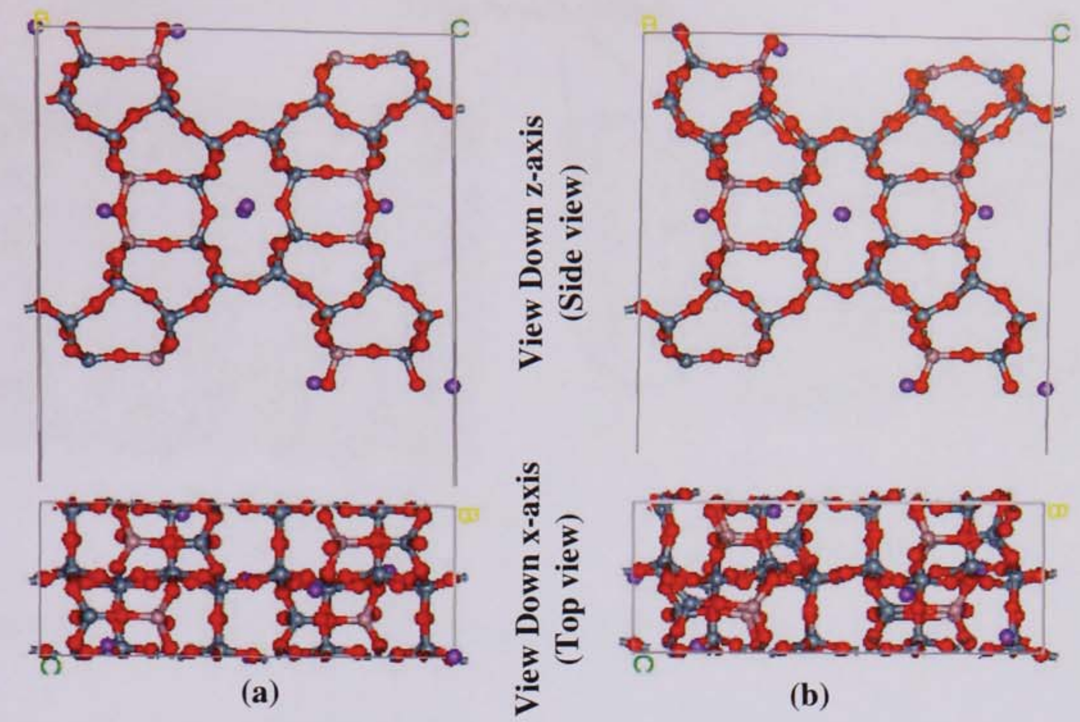

Figure 6.30 {100} Non-Hydroxylated Surface code7 Configurations (a) Before EM (b) After EM

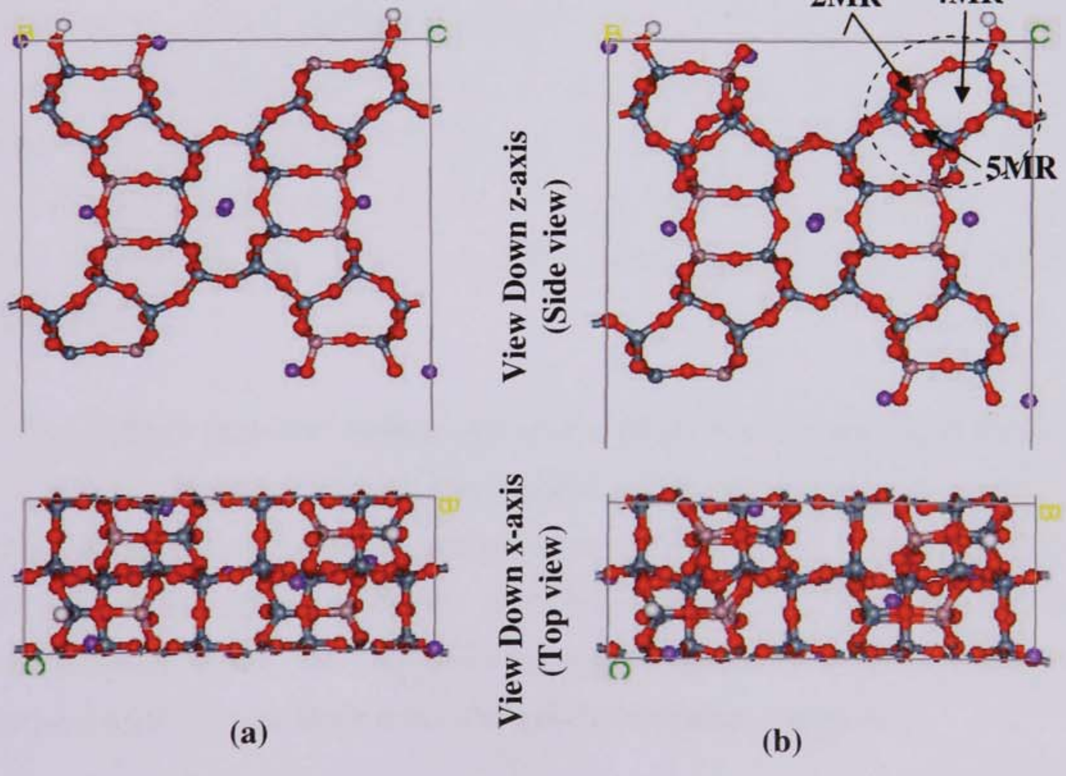

Figure 6.31 {100} Hydroxylated Surface code7 Configurations (a) Before EM (b) After EM

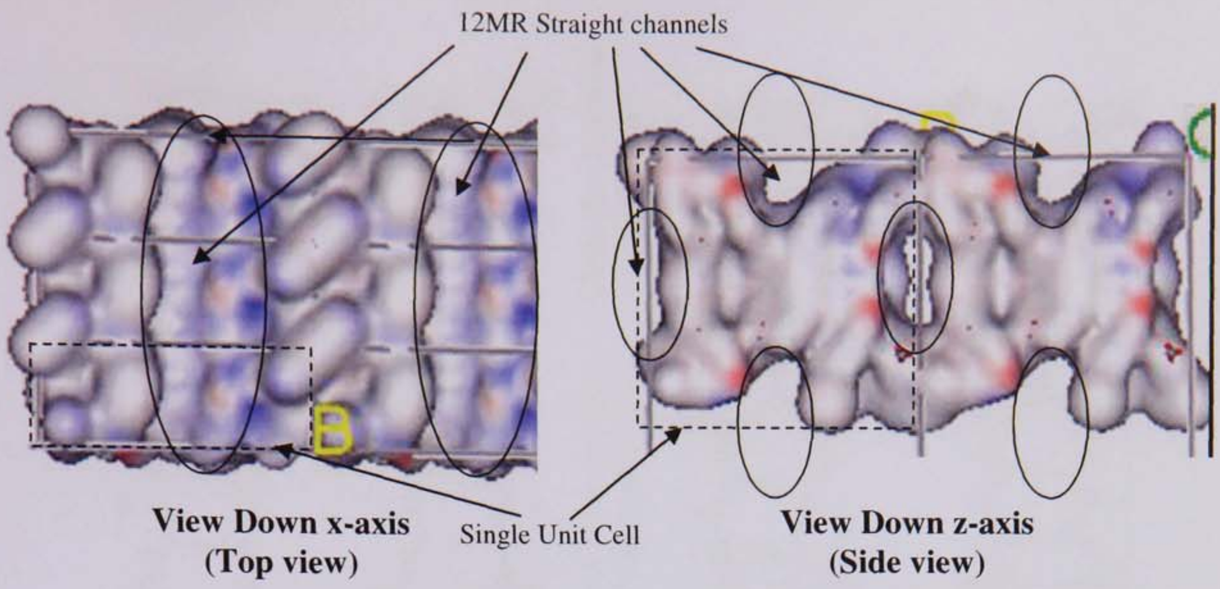

Figure 6.32 {100} Hydroxylated Surface code7 Surface Map (After EM)

6.2.3.2 Na-mordenite {001} surface

Figures 6.33 to 6.35 show the generated stable {001} Na-mordenite surface. It can be seen that both the hydroxylated and non-hydroxylated surfaces (figures 6.33 and 6.34) have undergone partial reconstruction during energy minimization. The partial combination of the 12MR straight channel entrance with the 8MR "side pocket" parallel elliptical channels results in the formation of a much larger 14 MR straight channel aperture at the surface of both hydroxylated and non-hydroxylated configurations.

From the resultant generated surface map of the {001} hydroxylated surface (figure 6.35) it can be seen that there are two distinct surface apertures present. The first aperture corresponds to the 12MR straight channel entrance and the second triangle shaped aperture corresponds to the new much larger 14MR straight channel entrance. Due to the nature of the {001} surface configuration generated adsorbate molecules will be permitted from the surface into the bulk Na-mordenite structure.

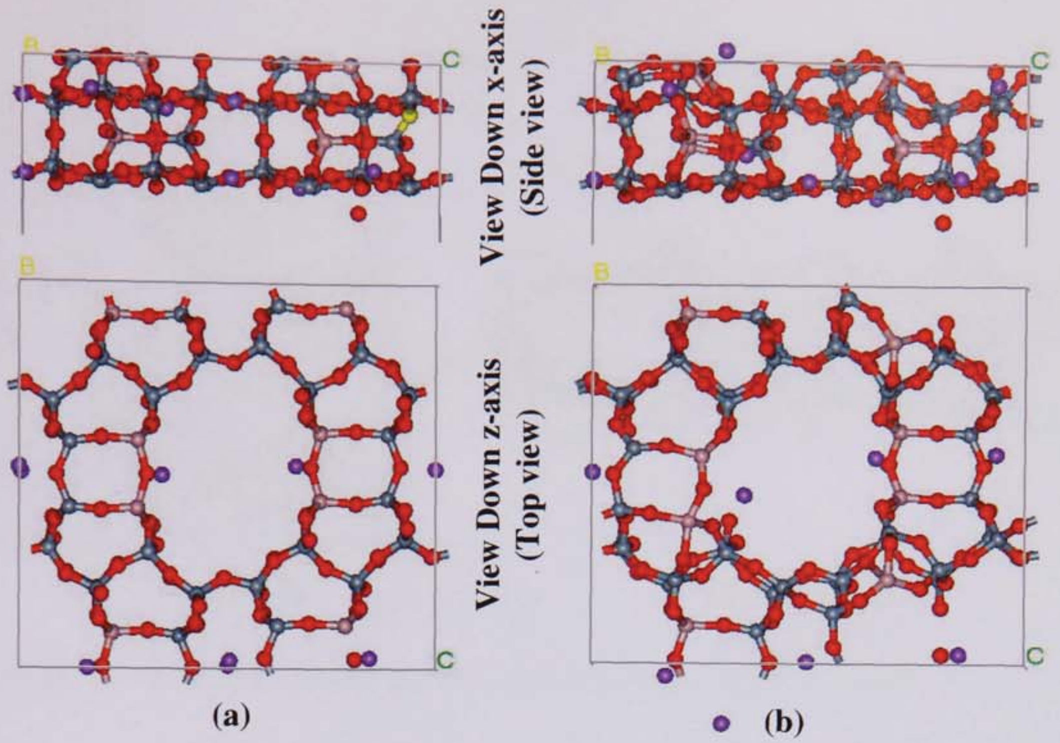

(a) (b)

Figure 6.33 {001} Non-Hydroxylated Surface code42 Configurations (a) Before EM (b) After EM

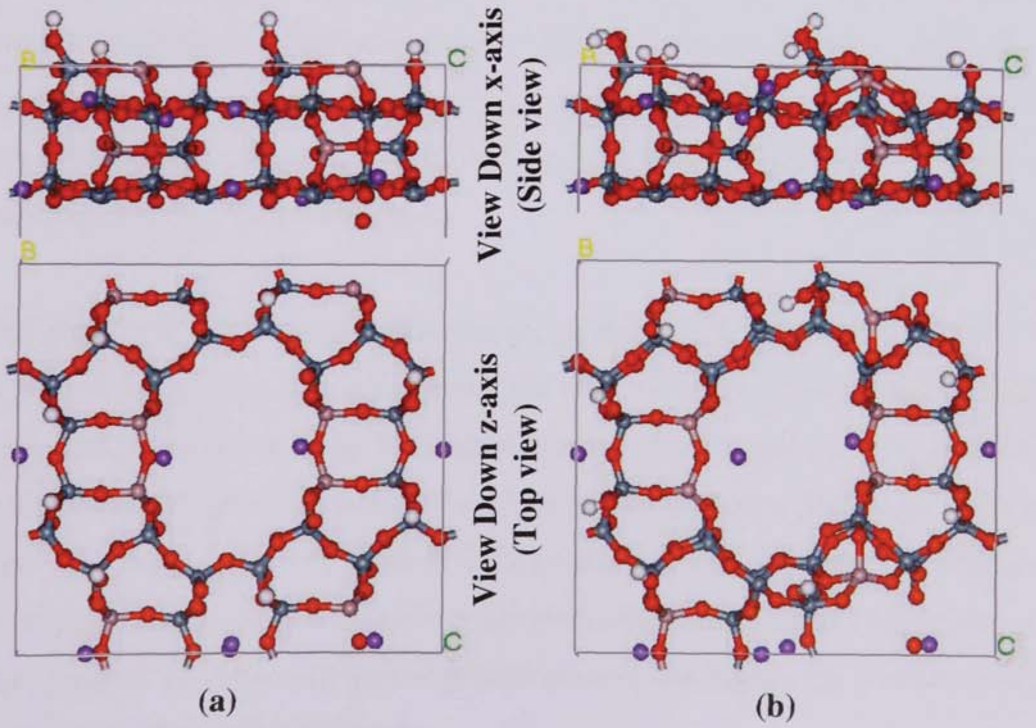

(a) (b)

Figure 6.34 {001} Hydroxylated Surface code42 Configurations (a) Before EM (b) After EM

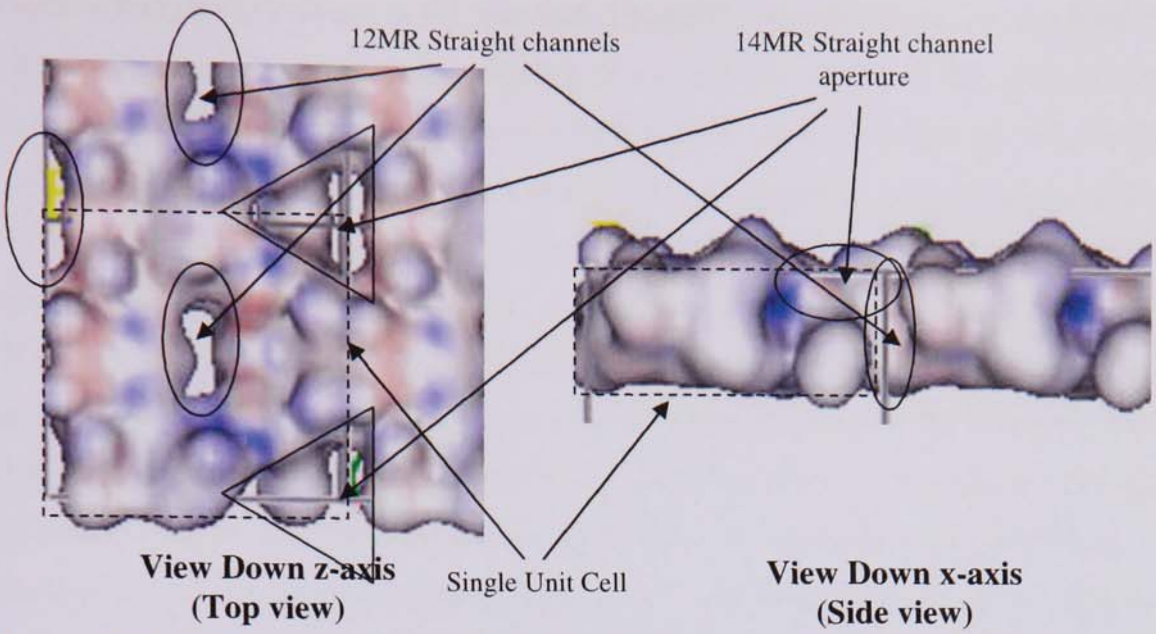

Figure 6.35 {001} Hydroxylated Surface code42 Surface Map (After EM)

6.2.3.3 Na-mordenite {010} surface

Figures 6.36 to 6.47 show the 4 generated stable {101} Na-mordenite surfaces. In general it was found that the non-hydroxylated surfaces had the greatest surface reconstructions compared to the hydroxylated surfaces. The reconstruction of the non-hydroxylated surfaces resulted in the formation of surfaces composed of 2, 3, 4 and 5MR units. While the minimal reconstruction of the hydroxylated surfaces resulted in surfaces composed of 3, 4 and 5MR units.

From Tables 6.3a & 6.3b it was interesting to see that the non-hydroxylated surface code 35 had the lowest surface energy hence the most stable of all four configurations generated. On hydroxylation code 35 became the least stable surface. The reason for this is code 35 has the greatest number of surface hydroxyl groups present (8 hydroxyl groups per unit surface area) of all four {010} surface configurations generated and thus the largest surface energy. This observation reinforces the earlier finding that the higher the number of surface hydroxyl groups present the higher the surface energy and the less stable the surface becomes.

From the resultant generated surface maps of the {010} hydroxylated surfaces (figures 6.38, 6.41, 6.44 and 6.47). For code 1 it can be seen that there are two distinct surface trenches present running parallel to the surface (figure 6.38). The deeper trench corresponds to the half exposed 12MR straight channel and the second trench corresponds to the smaller half exposed 8MR straight channel. The presence of the “side pocket” elliptical 8MR channels is not seen due to the positioning of the sodium cation which occupies the entrance into the “side pocket” channels. Due to the nature of code 1’s surface configuration adsorbate molecules will not be permitted from the surface into the bulk Na-mordenite structure. For code 35 (figure 6.41) it can be seen that there are three distinct surface features present. The first two correspond to 12MR and 8MR straight channel trenches running parallel to the surface. The third feature corresponds to the presence of the “side pocket” elliptical 8MR channel apertures following the length of both the 12MR and 8MR channel trenches. Due to the nature of code 35’s surface configuration adsorbate molecules will be permitted from the surface into the bulk Na-mordenite structure. For code 55 (figure 6.44) it can be seen that there is only one distinct surface feature present which corresponds to the presence of the “side pocket” elliptical 8MR channel apertures. Due to the nature of code 55’s surface configuration adsorbate molecules will be permitted from the surface into the bulk Na-mordenite structure. For code 91 (figure 6.47) it can be seen that there is again only one distinct surface feature present corresponding to the presence of deep 12MR straight channel trenches running parallel to the surface. Once again due to the positioning of the sodium cations in the centres of the “side pocket” elliptical 8MR channel entrances code 91’s surface configuration will not permit adsorbate molecules from the surface into the bulk Na-mordenite structure.

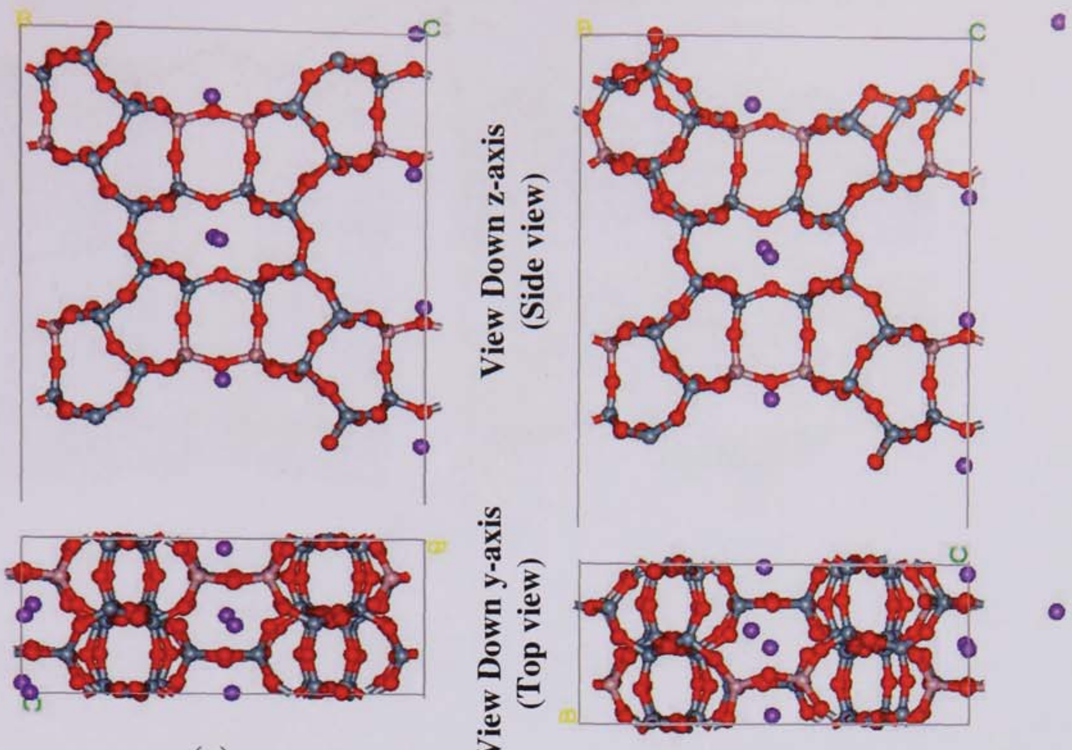

(a) (b)

Figure 6.36 {010} Non-Hydroxylated Surface code1 Configurations (a) Before EM (b) After EM

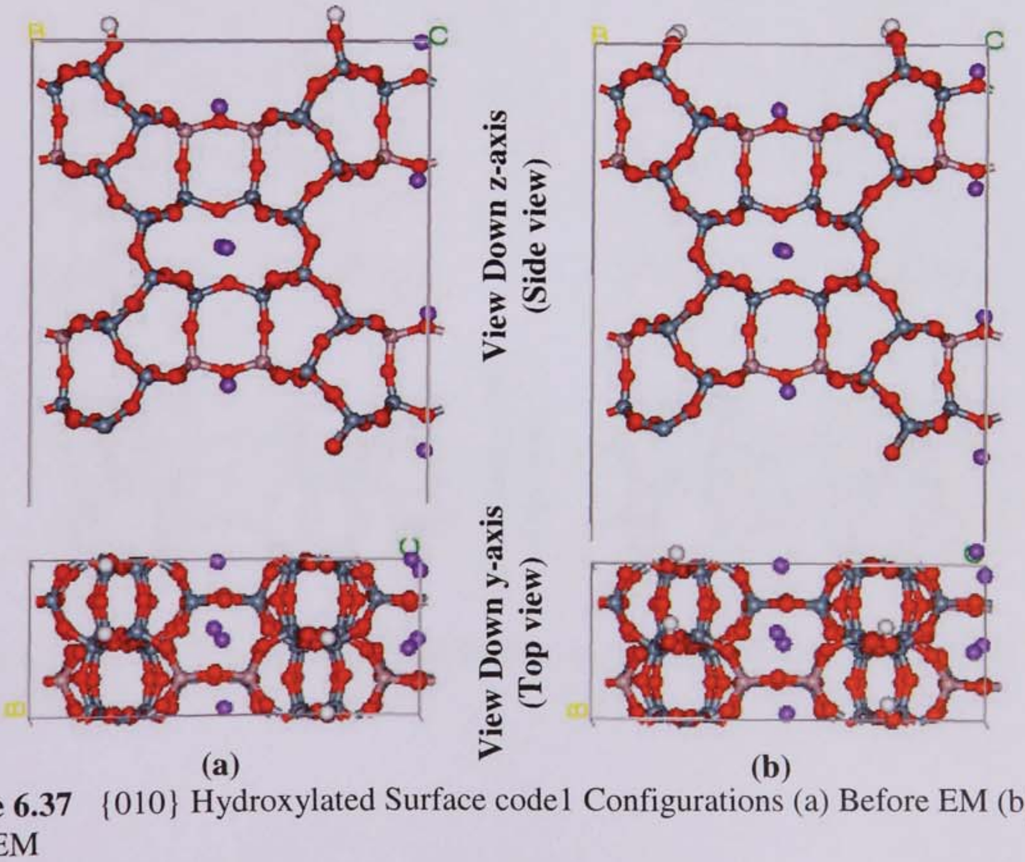

(a) (b)

Figure 6.37 {010} Hydroxylated Surface code1 Configurations (a) Before EM (b) After EM

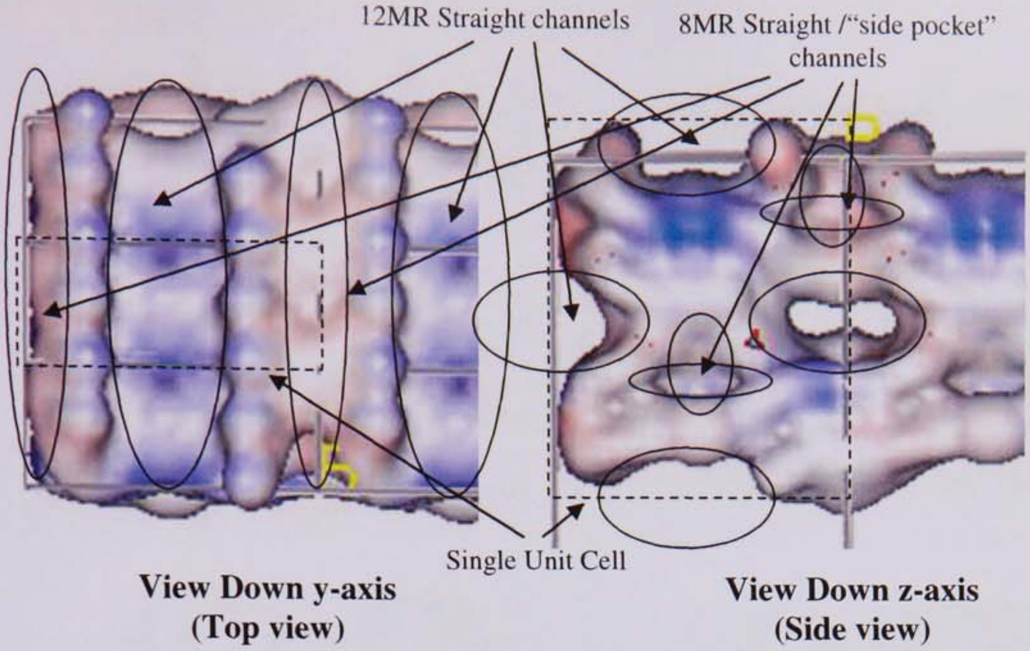

Figure 6.38 {010} Hydroxylated Surface code1 Surface Map (After EM)

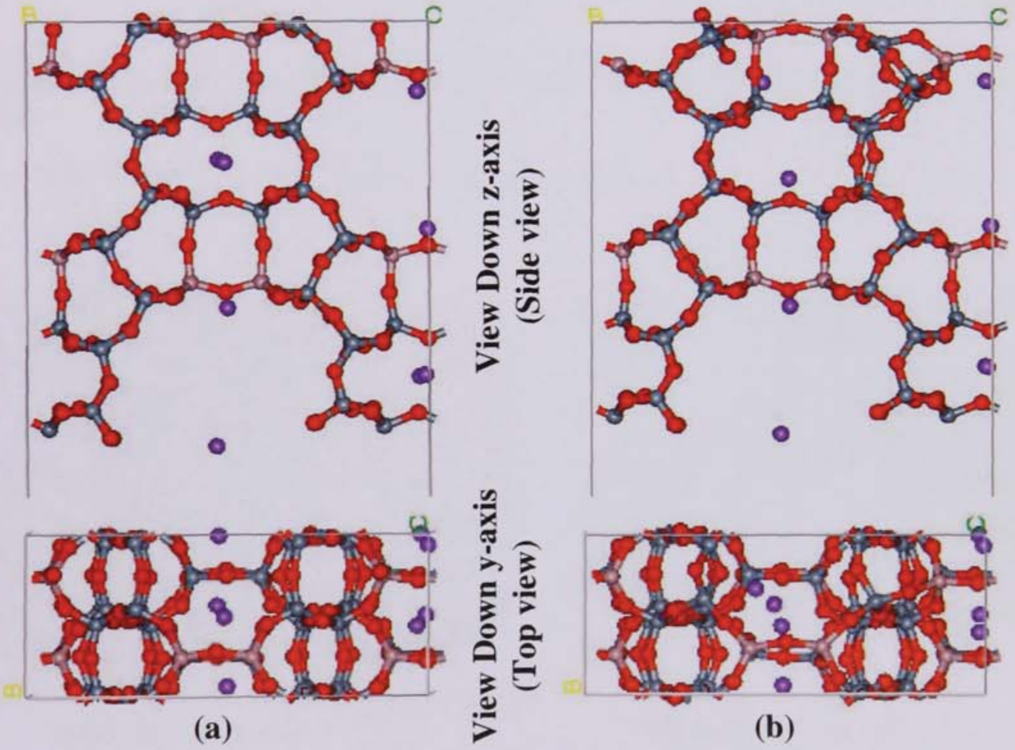

(a) (b)

Figure 6.39 {010} Non-Hydroxylated Surface code35 Configurations (a) Before EM (b) After EM

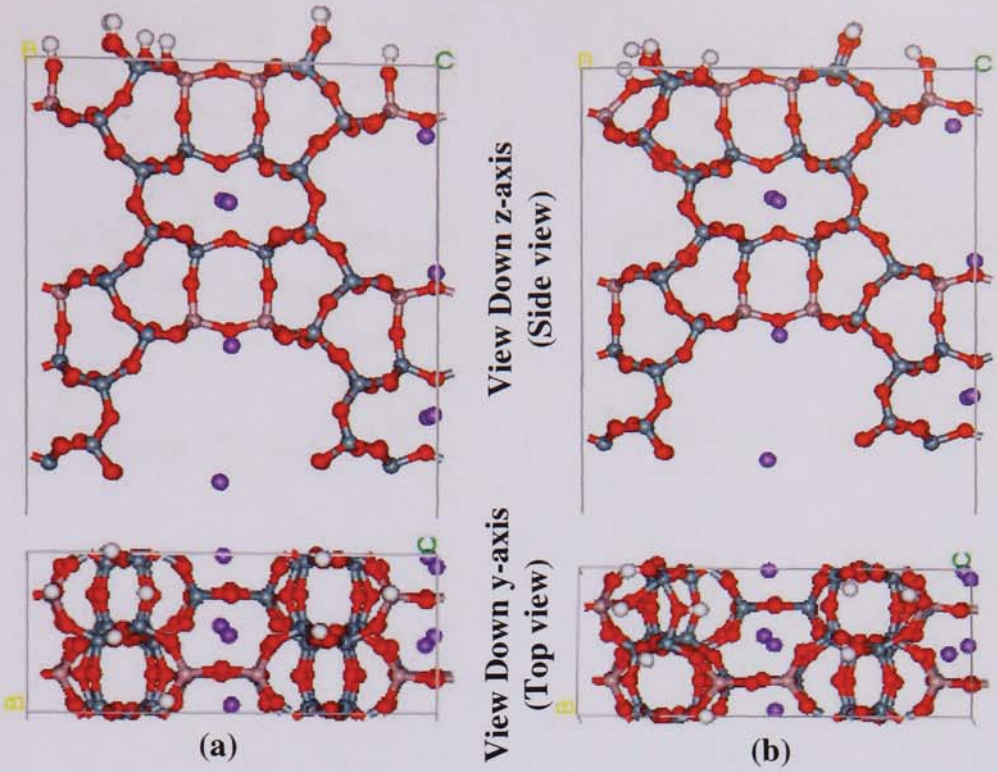

Figure 6.40 {010} Hydroxylated Surface code35 Configurations (a) Before EM (b) After EM

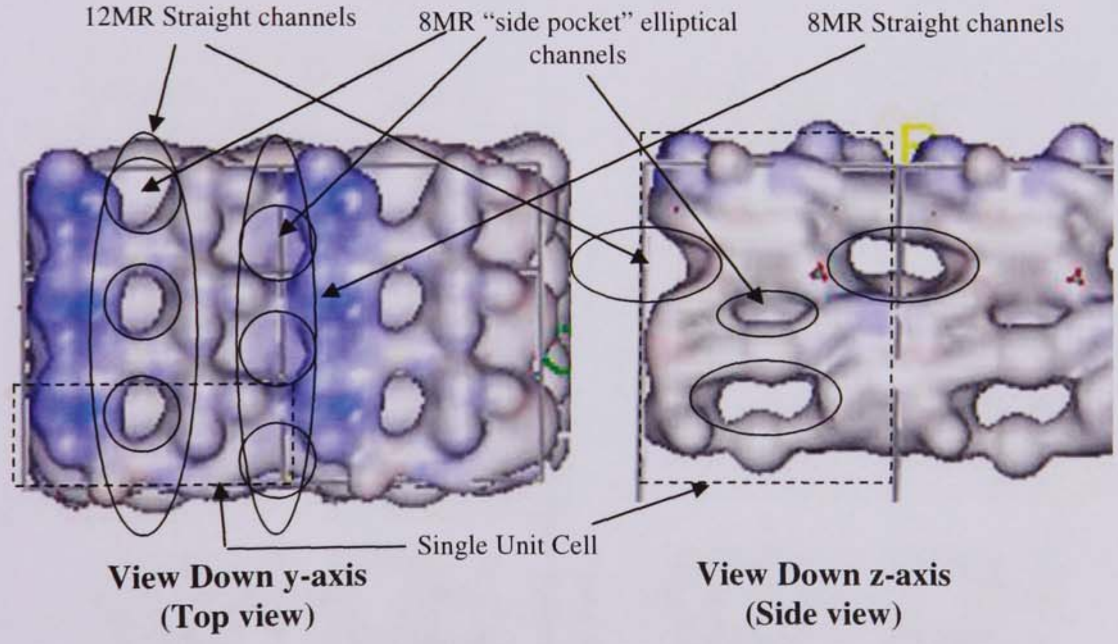

Figure 6.41 {010} Hydroxylated Surface code35 Surface Map (After EM)

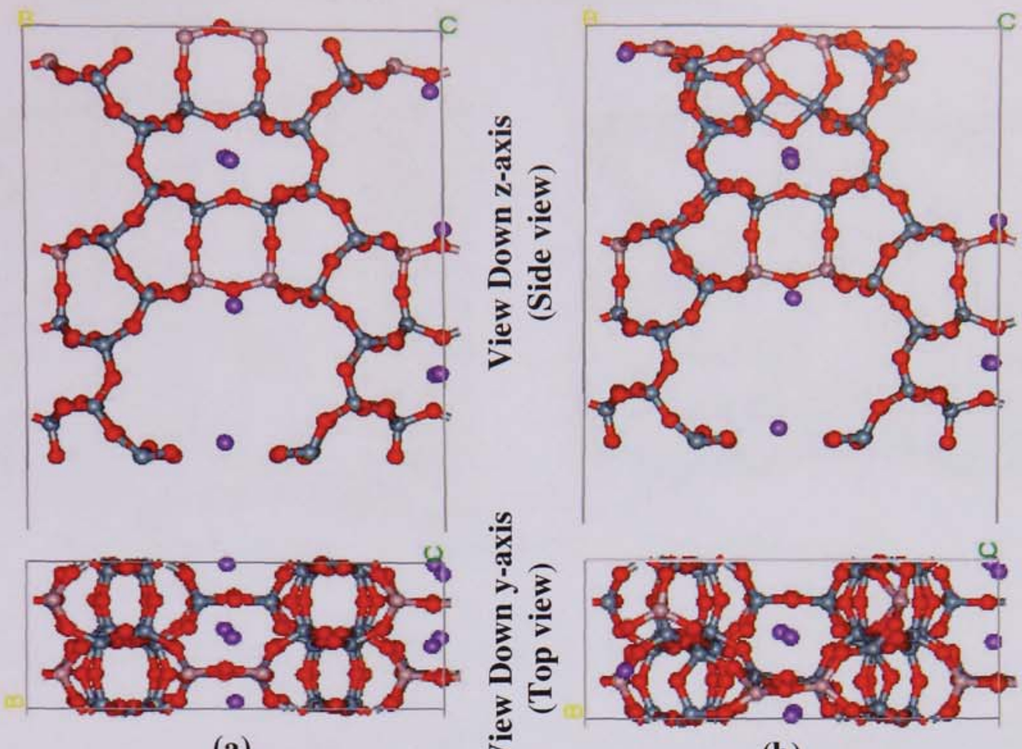

(a) (b)

Figure 6.42 {010} Non-Hydroxylated Surface code55 Configurations (a) Before EM (b) After EM

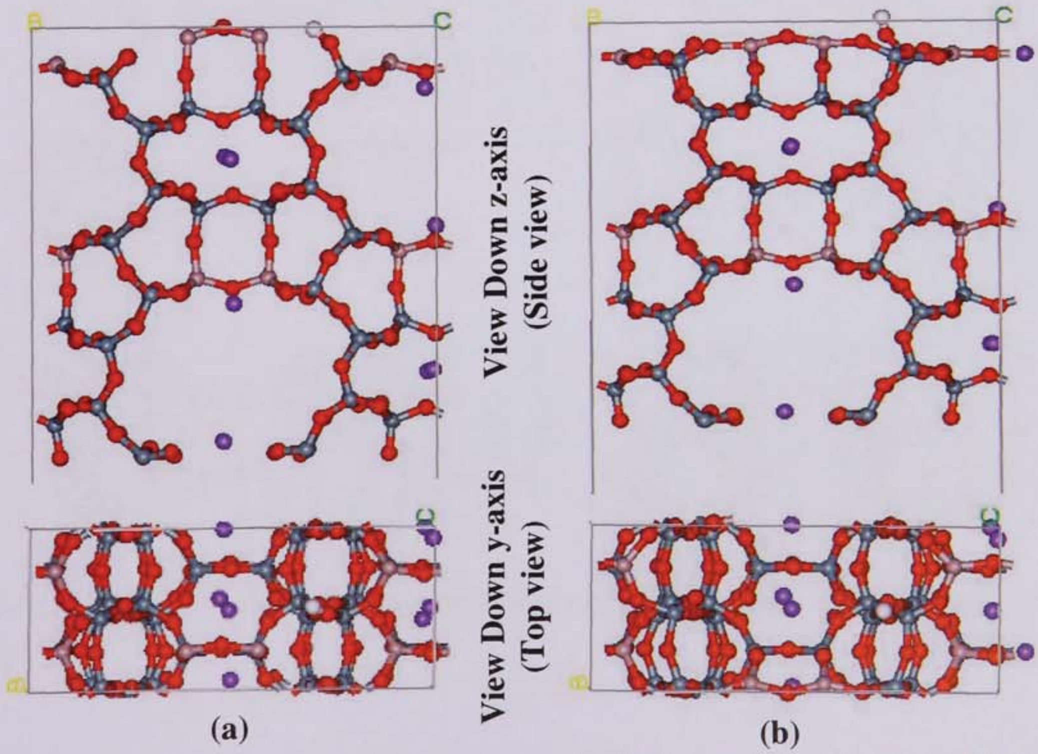

(a) (b)

Figure 6.43 {010} Hydroxylated Surface code55 Configurations (a) Before EM (b) After EM

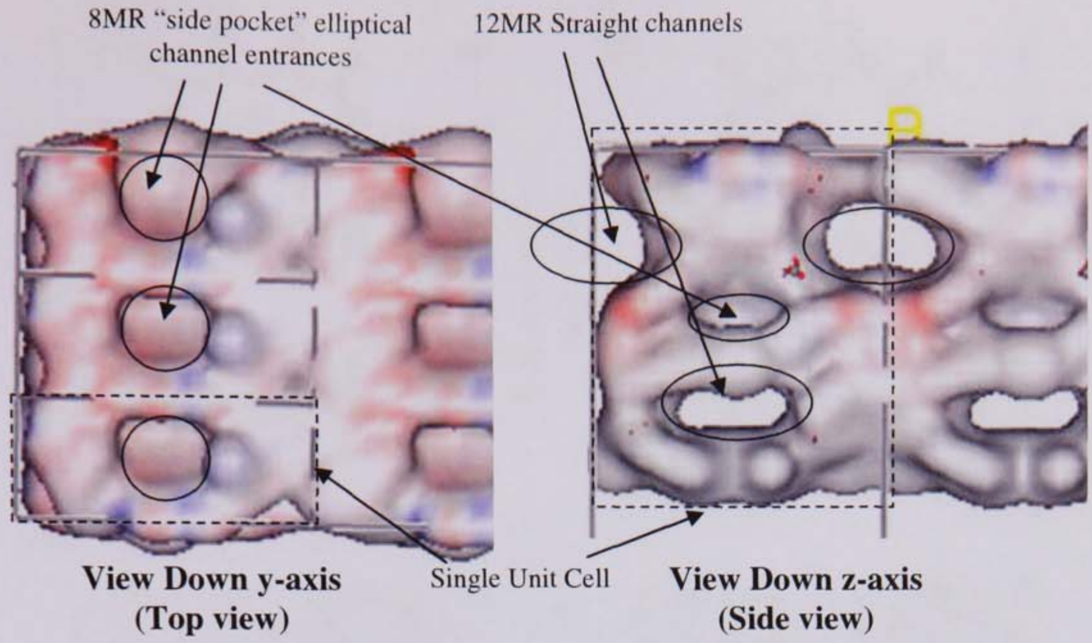

Figure 6.44 {010} Hydroxylated Surface code55 Surface Map (After EM)

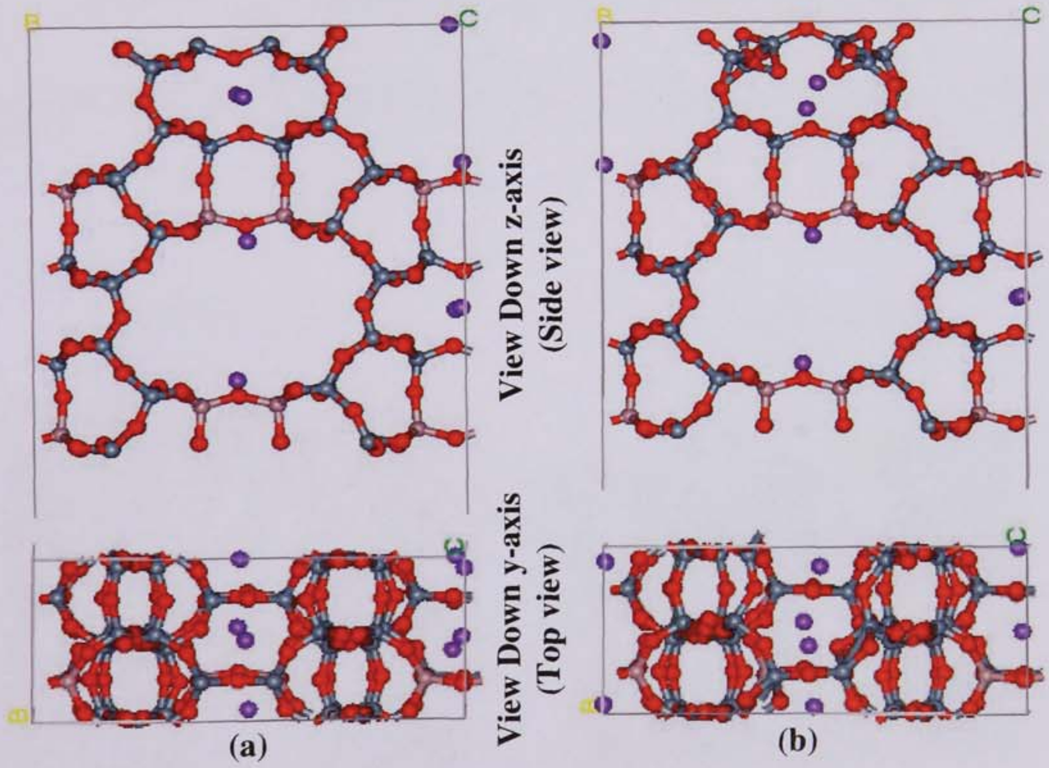

(a) (b)

Figure 6.45 {010} Non-Hydroxylated Surface code91 Configurations (a) Before EM (b) After EM

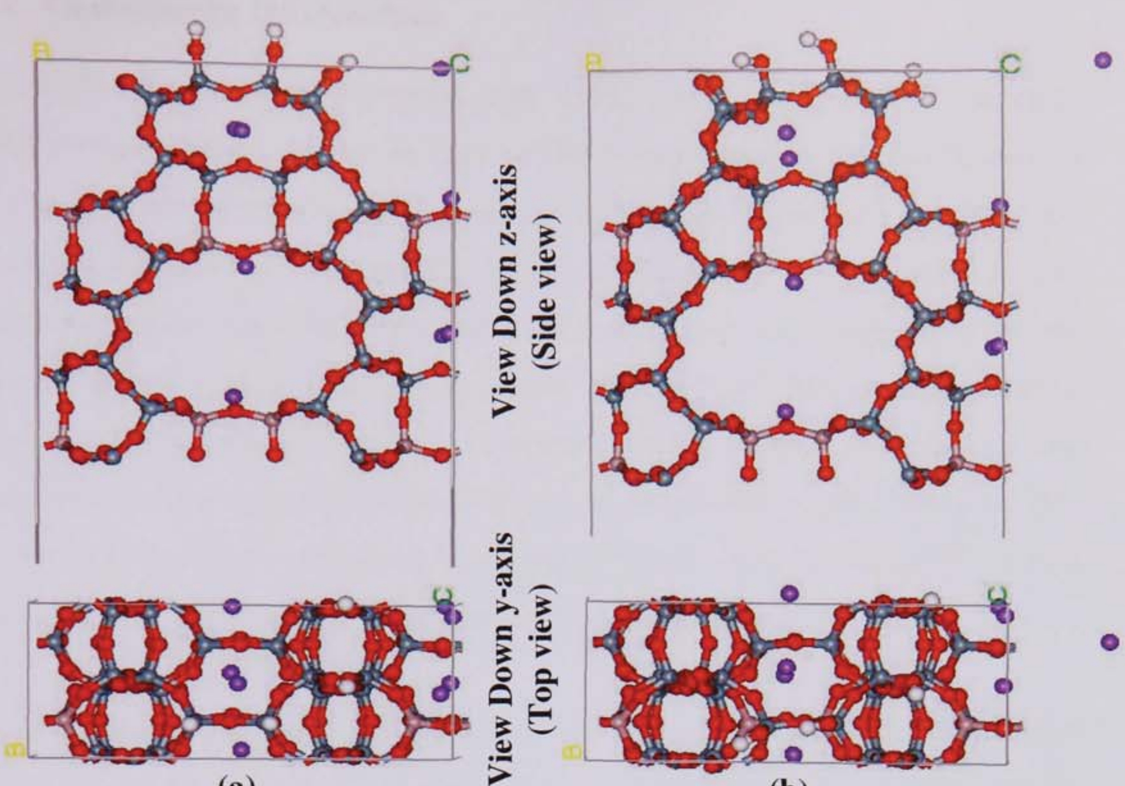

(a) (b)

Figure 6.46 {010} Hydroxylated Surface code91 Configurations (a) Before EM (b) After EM

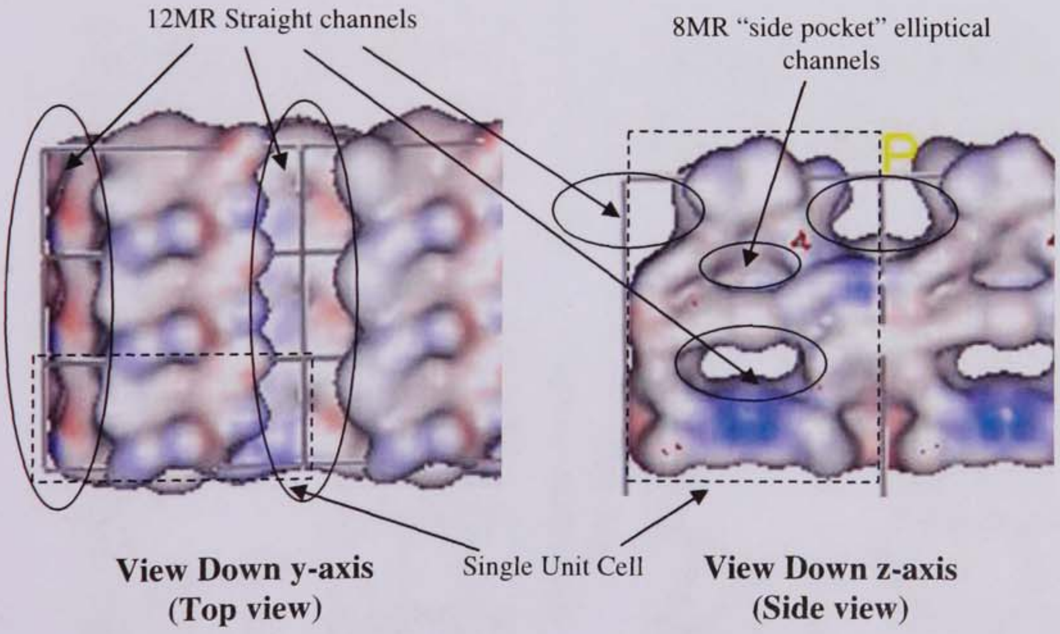

Figure 6.47 {010} Hydroxylated Surface code91 Surface Map (After EM)

6.2.3.4 Na-mordenite {101} surface

Figures 6.48 to 6.53 show the generated stable {101} Na-mordenite surfaces. It can be seen that both generated surfaces are very similar in nature and the only differences is due to the positions of the vacancies at the surfaces. From Tables 6.3a & 6.3b it was interesting to note that the two generated surface configurations (code 2 and code 126) both hydroxylated and non-hydroxylated prior to relaxation had comparable surface energies. Following relaxation it was found that the non-hydroxylated surface energies had noticeable differences compared to the surface energies of the hydroxylated surface configurations which had almost similar surface energies. The reason for this similarity is again due to the equal number of surface hydroxyl groups per unit surface area (12 surface hydroxyl groups for both codes).

From the resultant generated surface maps of the {101} hydroxylated surfaces (figures 6.50 and 6.53) it can be seen that there are distinct surface apertures present. These apertures correspond to the 12MR straight channel entrances. Due to the nature of the {101} surface configuration generated adsorbate molecules will be permitted from the surface into the bulk Na-mordenite structure with minimal resistance.

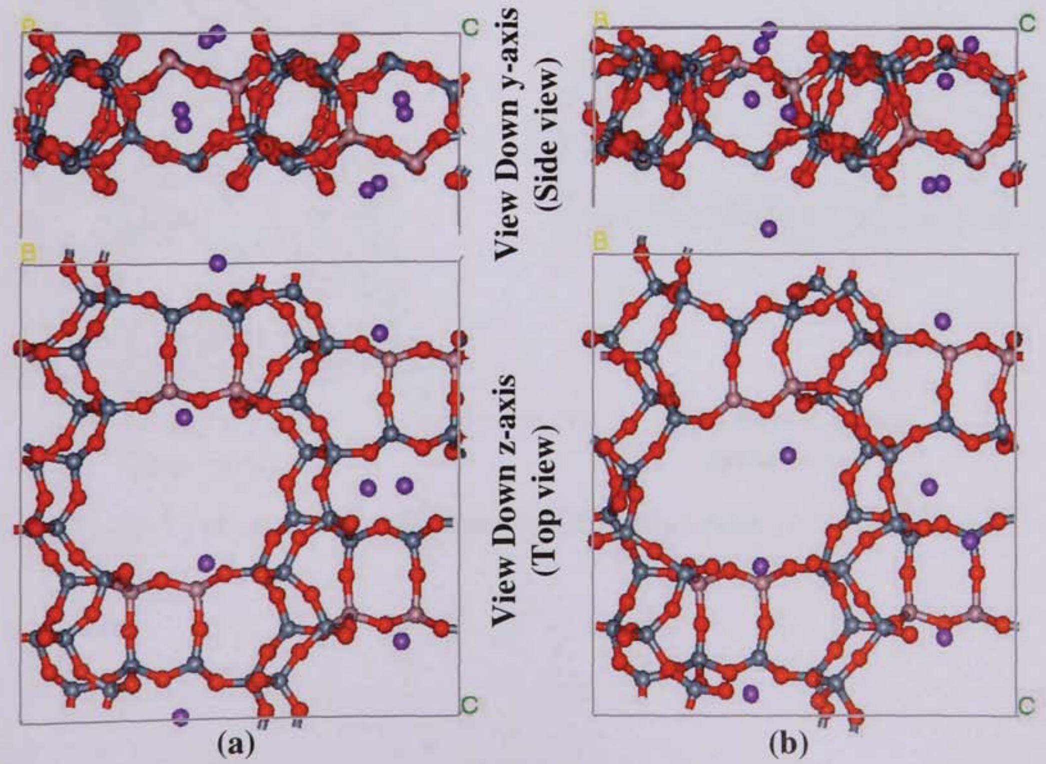

(a) (b)

Figure 6.48 {101} Non-Hydroxylated Surface code2 Configurations (a) Before EM (b) After EM

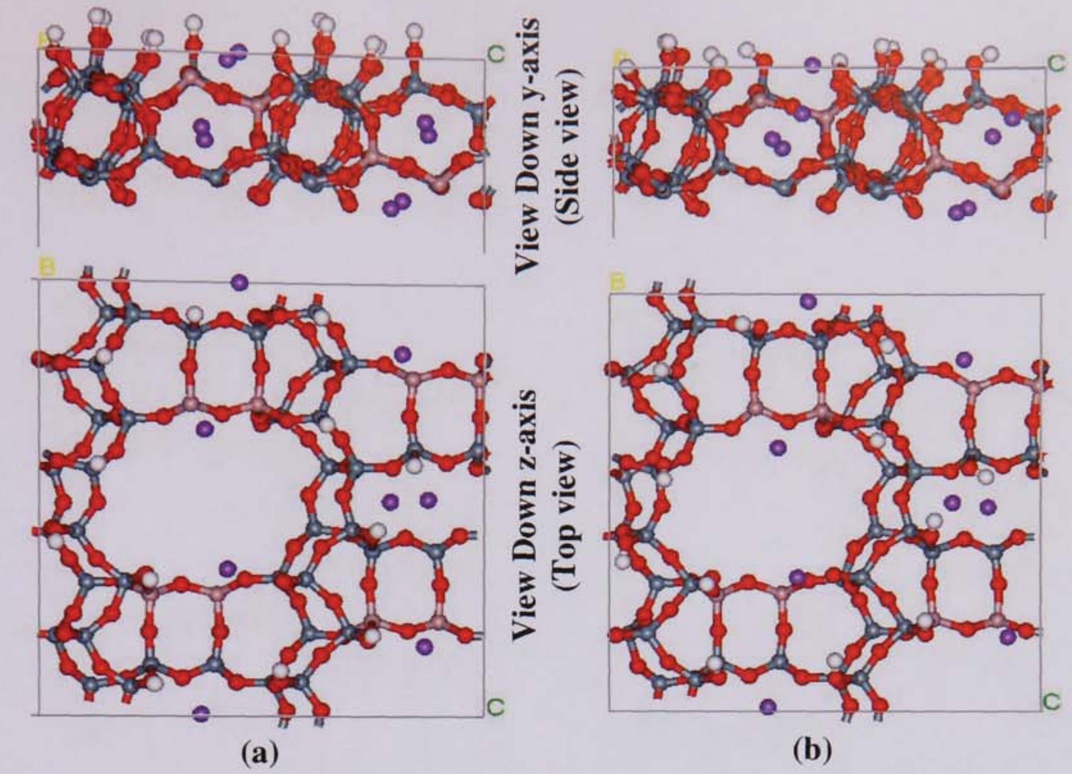

Figure 6.49 {101} Hydroxylated Surface code2 Configurations (a) Before EM (b) After EM

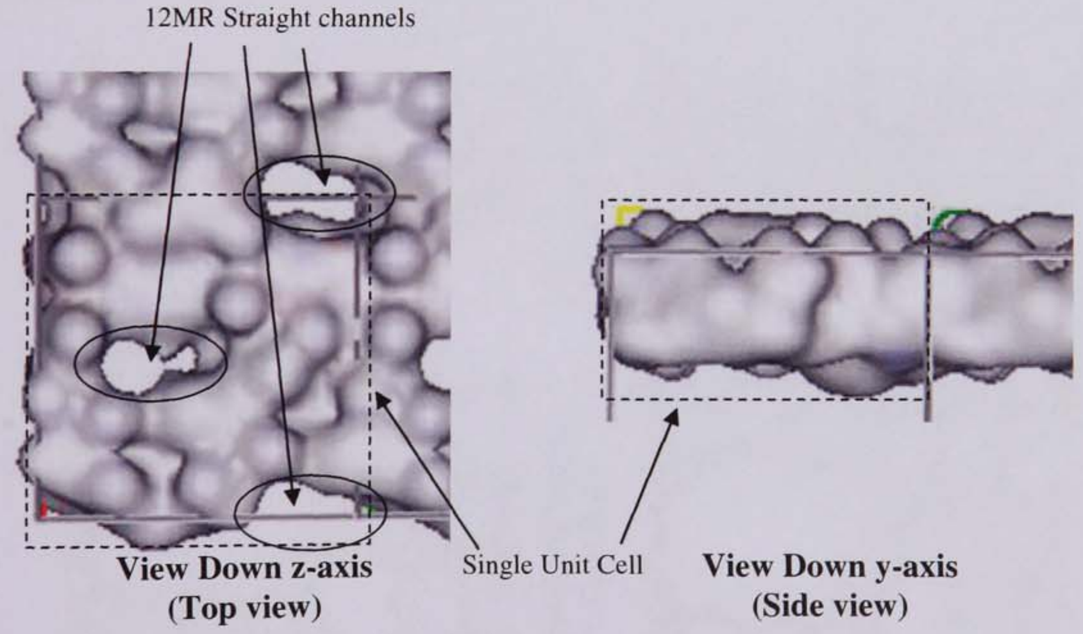

Figure 6.50 {101} Hydroxylated Surface code2 Surface Map (After EM)

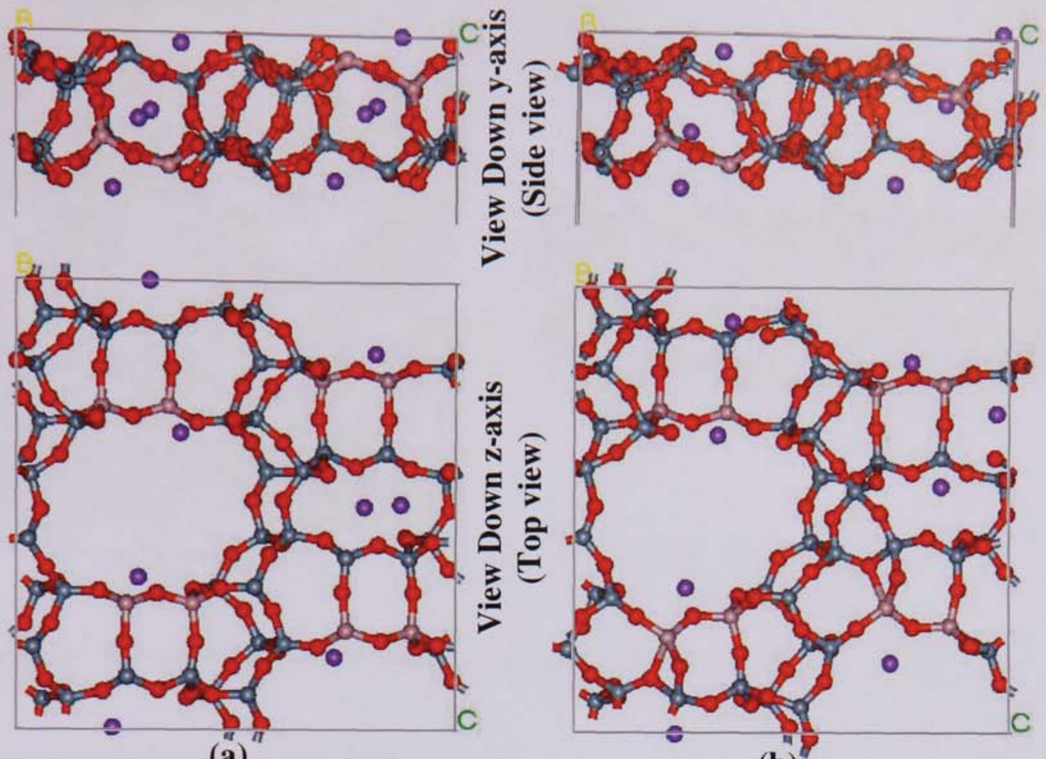

(a) (b)

Figure 6.51 {101} Non-Hydroxylated Surface code126 Configurations (a) Before EM (b) After EM

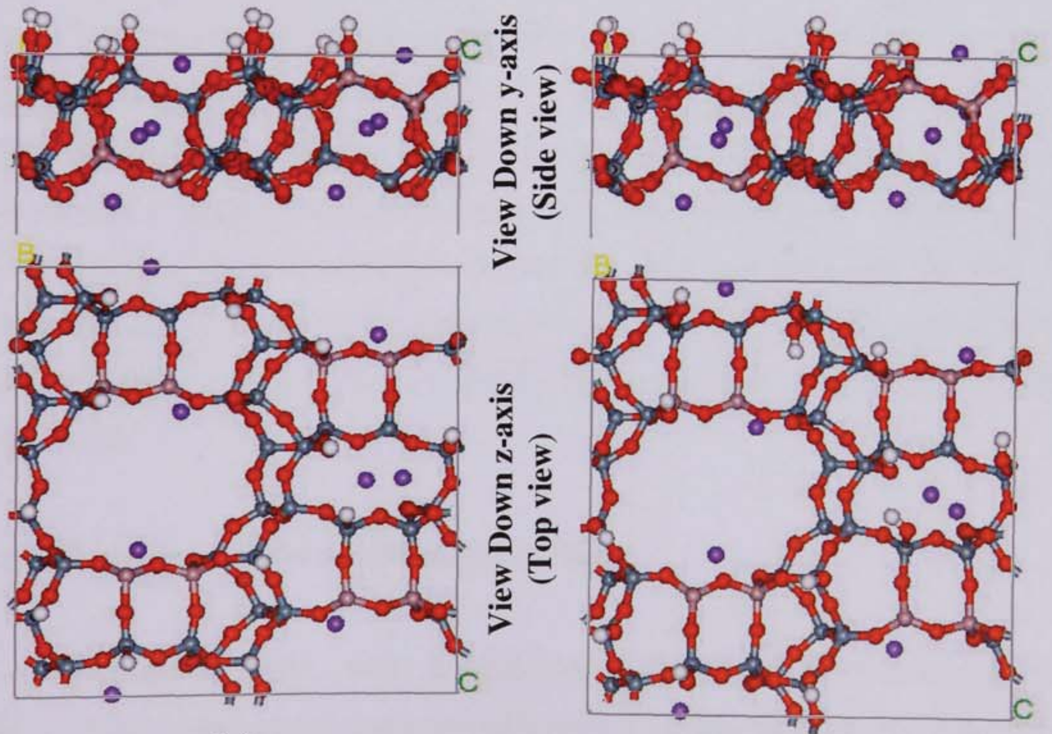

(a) (b)

Figure 6.52 {101} Hydroxylated Surface code126 Configurations (a) Before EM (b) After EM

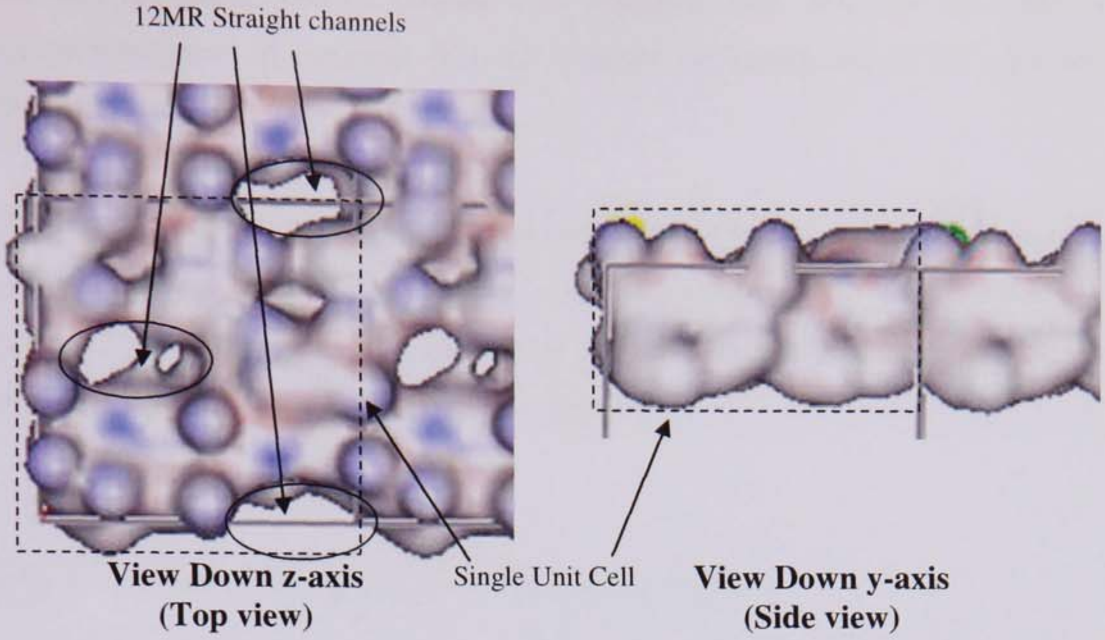

Figure 6.53 {101} Hydroxylated Surface code126 Surface Map (After EM)

6.2.4 Surface adsorption investigations

The generated stable zeolite surface configurations which permitted adsorbate molecules from the surface of the zeolite into the bulk zeolite channels were used further for surface adsorption investigations. A single 1 x 1 surface repeat unit cell of the given zeolite was divided into nine equal surface sections, to the centre of each surface section a single adsorbate molecule was introduced at an arbitrary height above the zeolite surface. This method ensured the whole surface of the unit cell was investigated as fully as possible for adsorption sites. Following this relaxation of both the zeolite surface and adsorbate molecule was conducted to determine surface adsorption sites.

6.2.4.1 Adsorption studies on silicalite-1 surfaces

For each miller index ({001}, {010} & {101}) the surface cut with the lowest surface energies for both hydroxylated and non-hydroxylated surface terminations was chosen for surface adsorption investigations. Of the three silicalite-1 surface configurations (both hydroxylated and non-hydroxylated) investigated for surface adsorption it was found that the silicalite-1 surface with the lowest surface energies (miller {010} code 113 both hydroxylated and non-hydroxylated) appeared to readily adsorb all four adsorbates (Methane, ethane, propane and water) studied. Whereas the other two silicalite-1 surfaces investigated showed virtually no adsorption of the adsorbates investigated.

Of the miller {010} hydroxylated and non-hydroxylated surface configurations investigated it was found that the hydroxylated surface (surface with silanol groups) appeared to have the greatest number of different surface adsorption sites than compared to that of the non-hydroxylated surface.

6.2.4.1.1 Methane adsorption on {010} silicalite-1 surface

Figure 6.54 shows four distinct methane adsorption sites found on the hydroxylated {010} code 113 surface of silicalite-1 and also one adsorption site found on the non-hydroxylated surface, whilst Table 6.4 shows the corresponding adsorption energies. It was found that in general for the hydroxylated surface when the methane molecule was located in a close proximity to a surface silanol (Si-OH) group (figures 6.54a and 6.54d) it had the strongest adsorption energies of -239.13 and -241.41 kJ/mol. But when it was located over the centre of a pentasil ring (5MR) (figure 6.54b) away from any surface silanol groups it had the weakest adsorption energy of -12.933 kJ/mol.

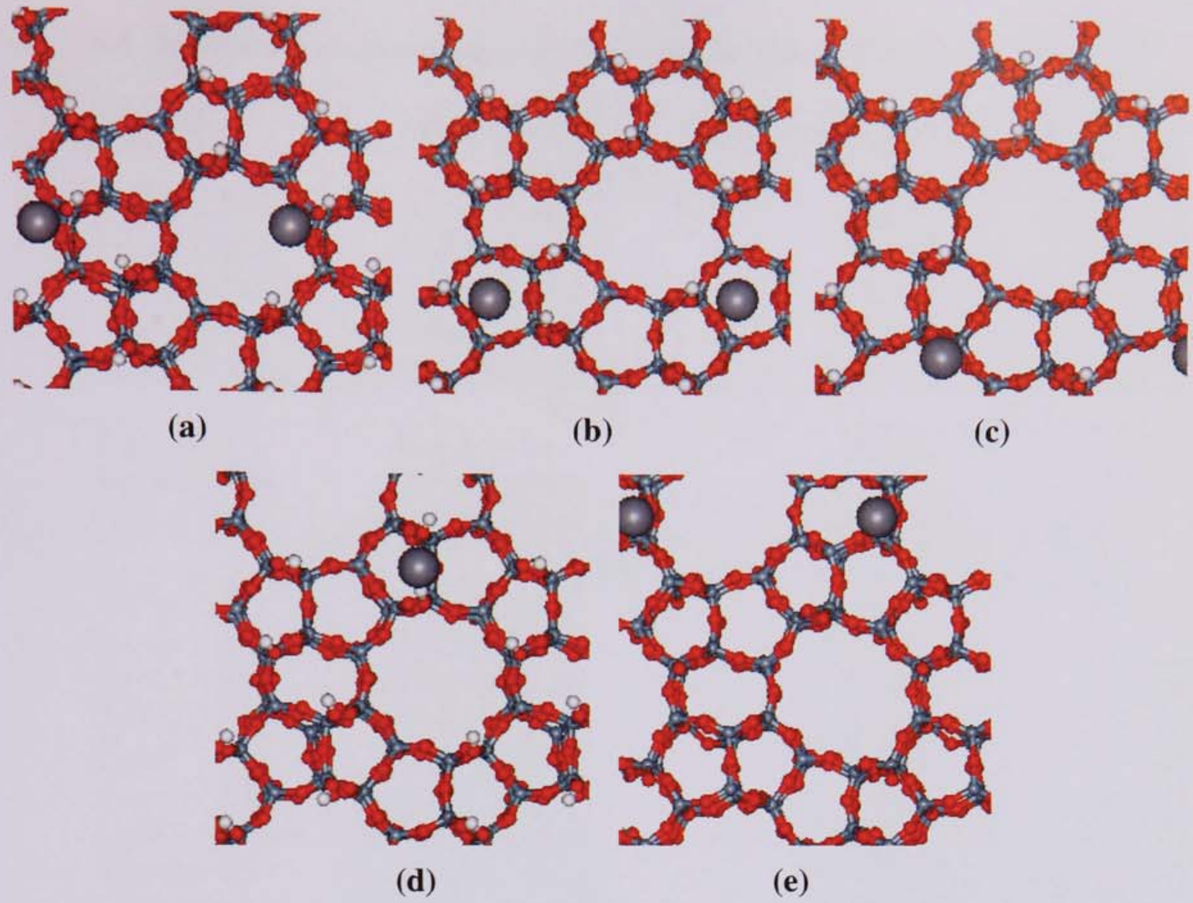

Figure 6.54 Adsorption of methane on the {010} code 113 silicalite-1 surface (a) hydroxylated (OH) surface over straight channel entrance close to Si-OH group connecting 10MR, 5MR & 6MR; (b) OH surface over 5MR close to oxygen connecting two 5MRs; (c) OH surface over straight channel entrance close to Si atom connecting 10MR, 5MR & 6MR; (d) OH surface over centre of oxygen atom connecting two 5MRs; (e) Non-OH surface over Si atom connecting 10MR, 5MR & 6MR.

Table 6.4 Hydrocarbon adsorption energies at the silicalite-1 {010} code 113 surface

Location	Surface type	Adsorption energy / kJ mol^{-1}
	Methane	
Figure 6.54a	Hydroxylated	-241.41
Figure 6.54b	Hydroxylated	-12.933
Figure 6.54c	Hydroxylated	-20.312
Figure 6.54d	Hydroxylated	-239.13
Figure 6.54e	Non-hydroxylated	+319.63
	Ethane	
Figure 6.55a	Hydroxylated	-238.61
Figure 6.55b	Hydroxylated	-25.051
Figure 6.55c	Non-hydroxylated	+314.339
	Propane	
Figure 6.56a	Hydroxylated	-36.431
Figure 6.56b	Hydroxylated	-35.967
Figure 6.56c	Hydroxylated	-23.805
Figure 6.56d	Hydroxylated	-25.49
Figure 6.56e	Hydroxylated	-227.04
Figure 6.56f	Hydroxylated	-57.183
Figure 6.56g	Non-hydroxylated	+392.149
Figure 6.56h	Non-hydroxylated	+302.657
Figure 6.56i	Non-hydroxylated	+282.764

6.2.4.1.2 Ethane adsorption on {010} silicalite-1 surface

Figure 6.55 shows the distinct ethane adsorption sites found on both the hydroxylated and non-hydroxylated external {010} surface of silicalite-1, whilst Table 6.4 shows the corresponding adsorption energies. For the ethane molecule it was found that for the hydroxylated surface there were two sites of adsorption, firstly over the centre of a 5MR which yielded the strongest adsorption energy of -238.61 kJ/mol. While the second site over the straight channel entrance close to Si atom connecting 10MR, 5MR & 6MR gave the lowest adsorption energy of 25.051 kJ/mol. Once again for the non-hydroxylated surface only one adsorption site was found located over the centre of 5MR, which gave an adsorption energy of +314.339 kJ/mol (endothermic adsorption) indicating that the non-hydroxylated surface is an unfavourable adsorption surface for the ethane molecule.

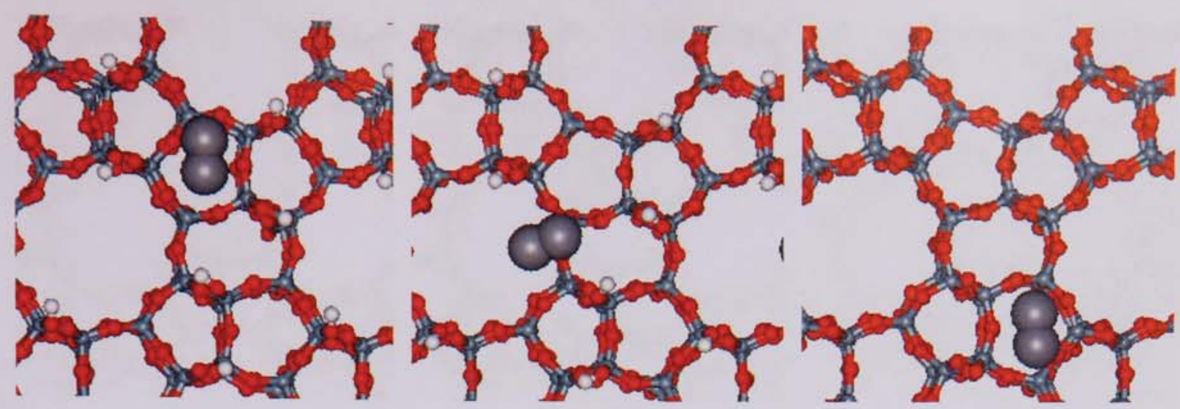

(a) (b) (c)

Figure 6.55 Adsorption of ethane on the {010} silicalite-1 surface (a) hydroxylated (OH) surface over centre of 5MR; (b) OH surface over straight channel entrance close to Si atom connecting 10MR, 5MR & 6MR; (c) Non-OH surface over centre of 5MR.

6.2.4.1.3 Propane adsorption on {010} silicalite-1 surface

Figure 6.56 shows the propane adsorption sites found on both the hydroxylated and non-hydroxylated {010} surface of silicalite-1, while Table 6.4 shows the corresponding adsorption energies. It was found that in general that for the hydroxylated surface the propane molecule tended to only adsorb above the 5MRs away from any surface silanol groups with corresponding adsorption energies ranging from -23.805 to -36.431 kJ/mol. It was also interesting to see that the propane molecule had the strongest adsorption energies when it was adsorbed directly from the surface into the straight channel pores (figures 6.56e and 6.56f) this resulted in adsorption energies of -57.183 to -227.04 kJ/mol. Similar sites of adsorption were again found for the adsorption of propane onto the non-hydroxylated {010} silicalite-1 surface. The large positive corresponding adsorption energies again showed endothermic adsorption indicating that adsorption onto the non-hydroxylated surface is an unfavourable process.

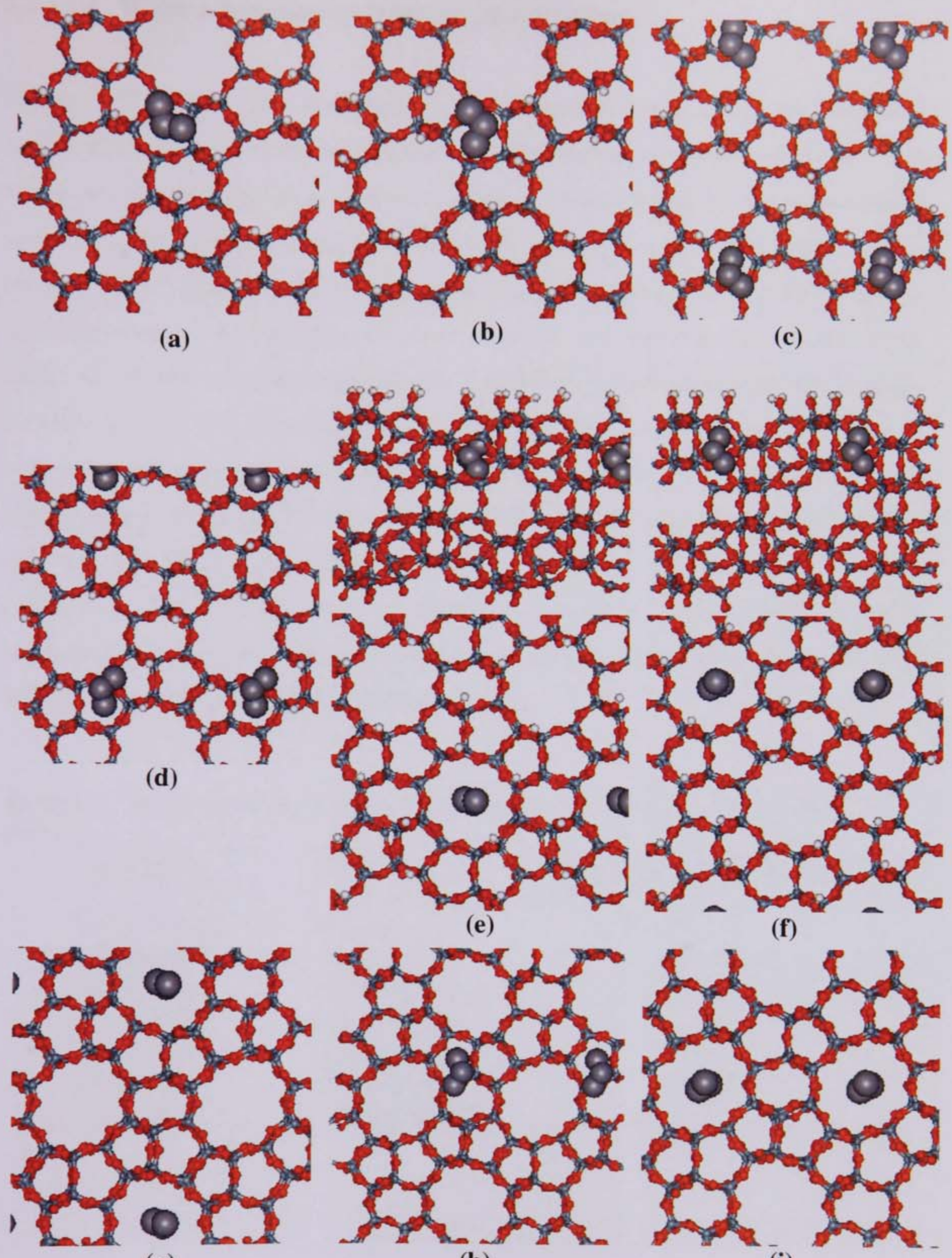

Figure 6.56 Adsorption of propane on the {010} silicalite-1 surface (a, b, c & d) hydroxylated (OH) surface adsorption over a 5MR; (e & f) OH surface adsorption into 10MR straight channel pore; (g & i) Non-OH surface adsorption into 10MR straight channel pore; (h) Non-OH surface adsorption over a 5MR.

6.2.4.1.4 Water adsorption on {010} silicalite-1 surface

Figure 6.57 shows the molecular water adsorption sites found on both the hydroxylated and non-hydroxylated external {010} surface of silicalite-1, while Table 6.5 shows the corresponding adsorption energies. It was found for the hydroxylated surface that the water molecule tends to adsorb strongly over a 5MR bonded to three silanol groups (figure 6.57f) resulting in an adsorption energy of -524.06 kJ/mol. It was interesting to see that when the water molecule was adsorbed over another 5MR which only had two silanol groups (figure 6.57d) the corresponding adsorption energy (-113.63 kJ/mol) was approximately 4.5 times lower. The lowest adsorption energy was found when the water molecule was over a straight channel entrance close to a silanol group connecting 10MR, 5MR & 6MRs. For the non-hydroxylated surface only one adsorption site was found (figure 6.57g) for the water molecule over the centre of a 5MR. The corresponding adsorption energy of +330.943 kJ/mol showed endothermic adsorption, which indicates that adsorption of water onto the non-hydroxylated surface is an unfavourable process.

Table 6.5 Molecular water adsorption energies at the silicalite-1 {010} code 113 surface

Location	Surface type	Adsorption energy / kJ mol^{-1}
	Water	
Figure 6.57a	Hydroxylated	-331.76
Figure 6.57b	Hydroxylated	-104.86
Figure 6.57c	Hydroxylated	-99.348
Figure 6.57d	Hydroxylated	-113.63
Figure 6.57e	Hydroxylated	-335.14
Figure 6.57f	Hydroxylated	-524.06
Figure 6.57g	Non-hydroxylated	+330.943

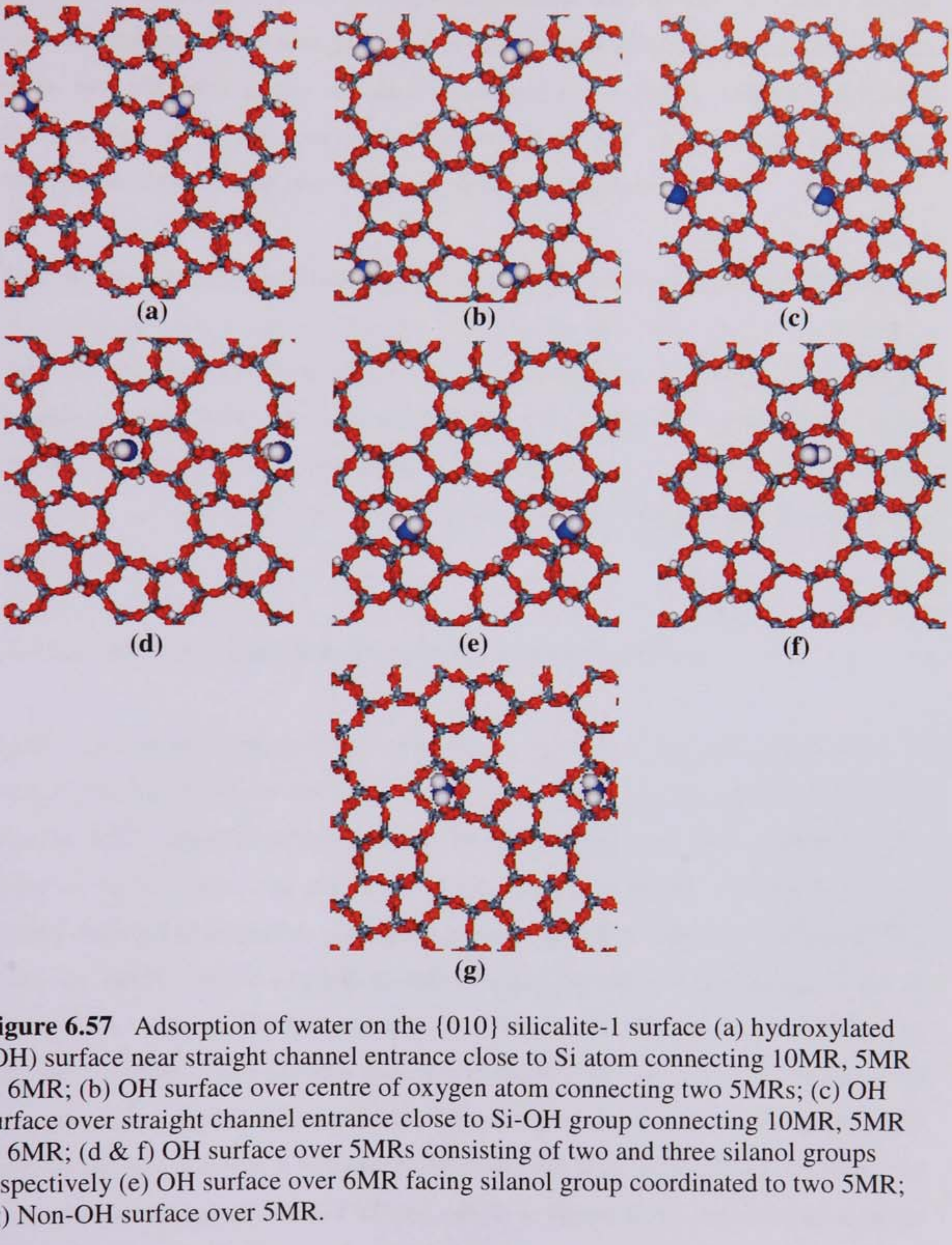

Figure 6.57 Adsorption of water on the {010} silicalite-1 surface (a) hydroxylated (OH) surface near straight channel entrance close to Si atom connecting 10MR, 5MR & 6MR; (b) OH surface over centre of oxygen atom connecting two 5MRs; (c) OH surface over straight channel entrance close to Si-OH group connecting 10MR, 5MR & 6MR; (d & f) OH surface over 5MRs consisting of two and three silanol groups respectively (e) OH surface over 6MR facing silanol group coordinated to two 5MR; (g) Non-OH surface over 5MR.

6.2.4.2 Adsorption studies on Na-mordenite surfaces

For the Na-mordenite only the surface configuration with the lowest surface energy from each miller index which permitted adsorbate molecules from the surface of the zeolite into the bulk zeolite channels was chosen for further surface adsorption investigations. A similar procedure for obtaining the zeolite surface/adsorbate configuration as described previously for silicalite-1 was used.

The following (both hydroxylated and non-hydroxylated) Na-mordenite surfaces with corresponding surface cuts were chosen: {010} (code 35), {101} (code 126) & {001} (code 42). Of the three Na-mordenite surface configurations investigated for surface adsorption it was found that only the {010} code 35 surface configuration readily adsorbed all four adsorbates (Methane, ethane, propane and water) studied. Whereas both {001} code 42 and {101} code 126 showed no adsorption of the adsorbates investigated.

6.2.4.2.1 Methane adsorption on {010} Na-mordenite surface

Figure 6.58 shows three methane adsorption sites found for the {010} code 35 surface. For the hydroxylated surface only one adsorption site was found on the external {010} code 35 surface with an adsorption energy of -29.612 kJ/mol. From figure 6.58a it is seen that the methane molecule is adsorbed over the edge of a parallel elliptical 8MR near to a Si-OH group coordinated to one 5MR and two 8MRs, which are directly above a 12MR straight channel. For the non-hydroxylated surface the methane molecule was found to adsorb at two distinct adsorption sites. Both sites had similar surface characteristics and corresponded to the adsorption of methane over the centre of a parallel elliptical 8MR. The differences lay with the immediate sub surface configuration which in figure 6.58b consisted of an 8MR straight channel with an adsorption energy of -46.437 kJ/mol, while in figure 6.58c consisted of a larger 12MR straight channel with an adsorption energy of -11.214 kJ/mol.

Table 6.6 Hydrocarbon adsorption energies at the Na-mordenite {010} code 35 surface

Location	Surface type	Adsorption energy / kJ mol^{-1}
	Methane	
Figure 6.58a	Hydroxylated	-29.612
Figure 6.58b	Non-hydroxylated	-46.437
Figure 6.58c	Non-hydroxylated	-11.214
	Ethane	
Figure 6.59a	Hydroxylated	-149.84
Figure 6.59a	Non-hydroxylated	+148.247
Figure 6.59a	Non-hydroxylated	-16.722
Figure 6.59a	Non-hydroxylated	-29.475
	Propane	
Figure 6.60a	Hydroxylated	-160.72
Figure 6.60b	Hydroxylated	-11.967
Figure 6.60c	Hydroxylated	-158.7
Figure 6.60d	Hydroxylated	+58.572
Figure 6.60e	Hydroxylated	+62.001
Figure 6.60f	Hydroxylated	-65.593
Figure 6.60g	Non-hydroxylated	+137.499
Figure 6.60h	Non-hydroxylated	-15.092
Figure 6.60i	Non-hydroxylated	-21.386

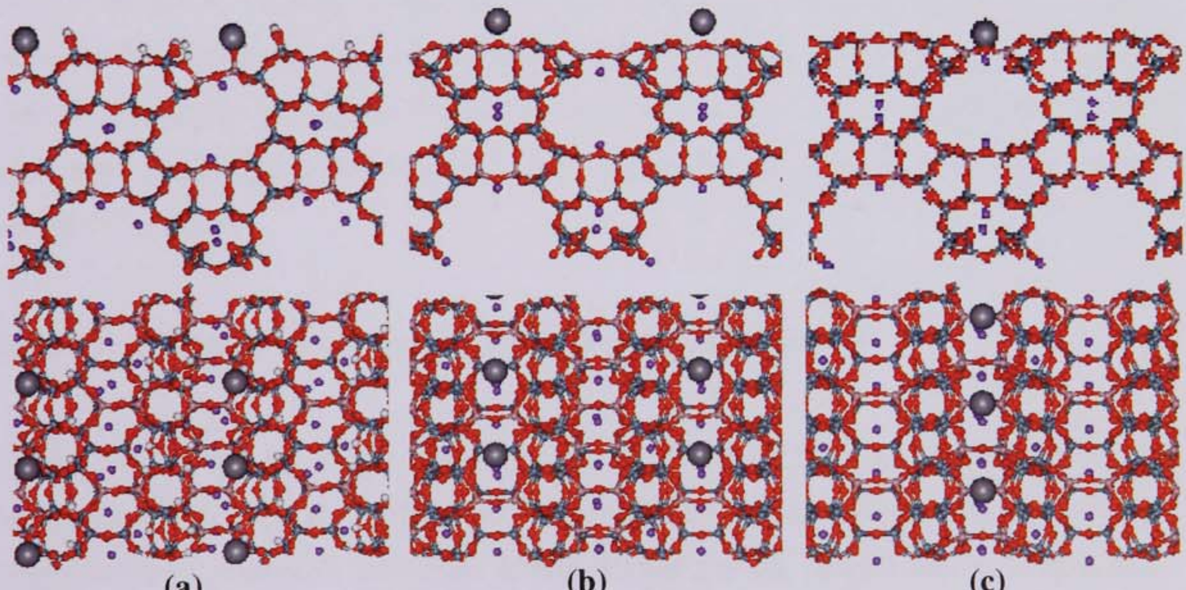

(a) (b) (c)

Figure 6.58 Adsorption of methane on the {010} code 35 Na-mordenite surface (a) hydroxylated (OH) surface edge of parallel elliptical 8MR directly above 12MR straight channel near Si-OH group coordinated to one 5MR and two 8MR; (b) Non-OH surface over centre of parallel elliptical 8MR directly above 8MR straight channel; (c) Non-OH surface over centre of parallel elliptical 8MR directly above 12MR straight channels.

6.2.4.2.2 Ethane adsorption on {010} Na-mordenite surface

Figure 6.59 shows the four ethane adsorption sites found on both the hydroxylated and non-hydroxylated {010} surface of Na-mordenite, whilst Table 6.6 shows the corresponding adsorption energies. For the ethane molecule it was found there was only one adsorption site for the hydroxylated surface, which corresponded to the ethane being located over an Al-OH group connecting a 5MR with two 8MRs, which sat directly above a subsurface 12MR straight channel. The resulting strong adsorption energy of -149.84 kJ/mol indicates that this is a favourable adsorption site. For the non-hydroxylated surface two distinct adsorption sites were found of which one site was found to have two different adsorption energies. From figures 6.59b and 6.59c it can be seen that in each case the ethane is located over the centre of a parallel elliptical 8MR sat directly above a 12MR straight channel with corresponding adsorption energies of +148.247 and -16.722 kJ/mol. The reason for the difference is attributed to breakage of an Al-O-Si bond forming the parallel elliptical 8MR as seen in figure 6.59b which results in an unfavourable large positive adsorption energy. This bond breakage is not seen in figure 6.59c as a result a low negative adsorption energy is found for the ethane. The second adsorption site for the non-hydroxylated surface corresponds to the adsorption of ethane into the centre of a parallel elliptical 8MR pore, which sits directly above 8MR straight channel resulting in an adsorption energy of -29.475 kJ/mol.

6.2.4.2.3 Propane adsorption on {010} Na-mordenite surface

Figure 6.60 shows the propane adsorption sites found on both the hydroxylated and non-hydroxylated {010} surface of Na-mordenite, while Table 6.6 shows the corresponding adsorption energies. It was found for the hydroxylated surface the propane molecule tended to adsorb at two distinct adsorption sites. The first site corresponded to the propane being adsorbed at the centre of a parallel elliptical 8MR directly above 12MR straight channel (figures 6.60a,c,d & 6.60e). From Table 6.6 it was interesting to see that the propane molecule had four different adsorption energies when adsorbed at this site the reason for the differences is unclear and may well be due to the different orientations of the propane molecule at the site. The second site for the hydroxylated surface corresponds to the propane molecule being located inside the centre of a parallel elliptical 8MR pore sitting directly above an 8MR straight channel (figures 6.60b & 6.60f). Once again it is seen that this site gives two different adsorption energies of -11.967 and -65.593 kJ/mol, with the differences being attributed to the different orientations of the propane molecule within the pore. For the non-hydroxylated surface again two distinct adsorption sites were found. The first site corresponds to the adsorption of propane over the centre of a parallel elliptical 8MR sat directly above an 8MR straight channel. The second site which corresponds to the adsorption of propane over the centre of a parallel elliptical 8MR directly above 12MR straight channel was found to have two different adsorption energies. The reason for this difference as seen in figures 6.60g and 6.60i is attributed to the orientation of the propane molecule. When the propane is orientated forming a V shape parallel to the surface a large unfavourable positive adsorption energy of +137.499 kJ/mol is seen but when the propane is on its side parallel to the surface a favourable negative adsorption energy of -21.386 kJ/mol is found.

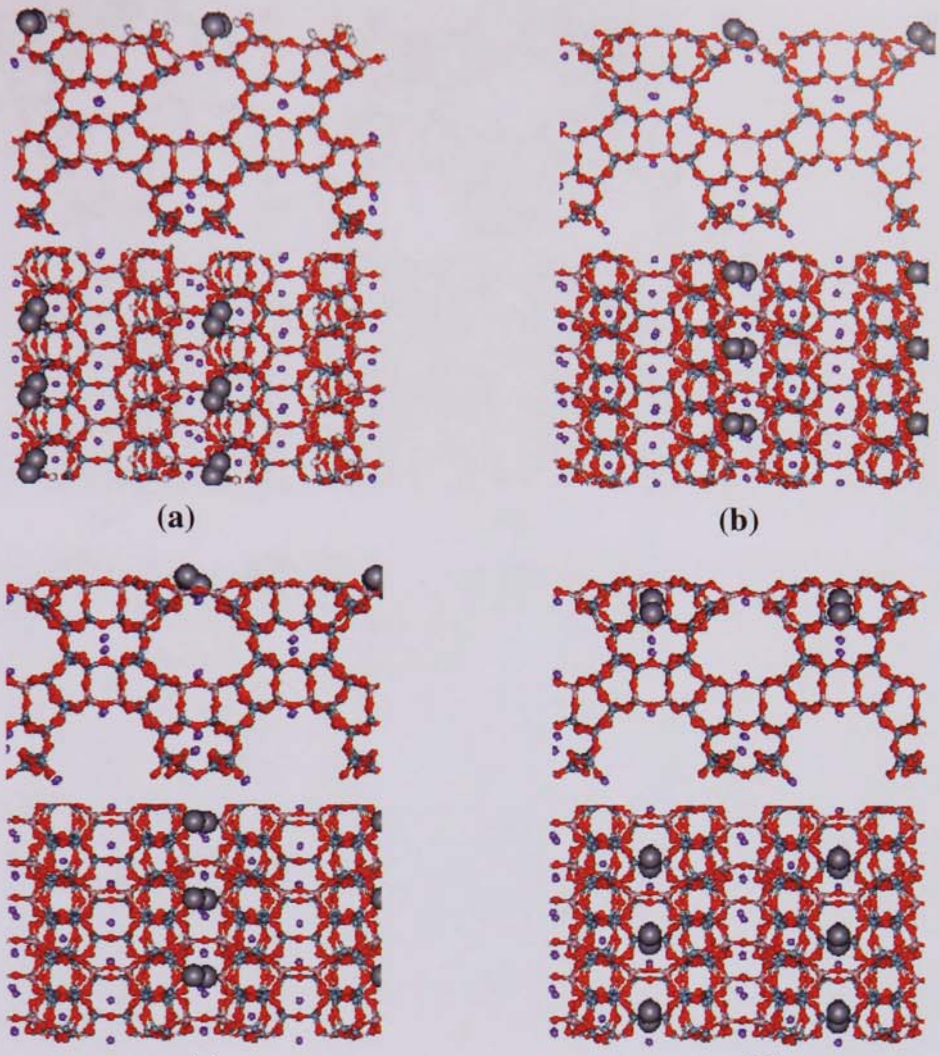
(a) (b) (c) (d)

Figure 6.59 Adsorption of ethane on the {010} code 35 Na-mordenite surface (a) hydroxylated (OH) surface over Al-OH group connecting a 5MR with two 8MR directly above 12MR straight channel; (b) Non-OH surface over centre of parallel elliptical 8MR directly above 12MR straight channel; (c) Non-OH surface over centre of parallel elliptical 8MR directly above 12MR straight channel; (d) Non-OH surface Inside centre of parallel elliptical 8MR pore directly above 8MR straight channel.

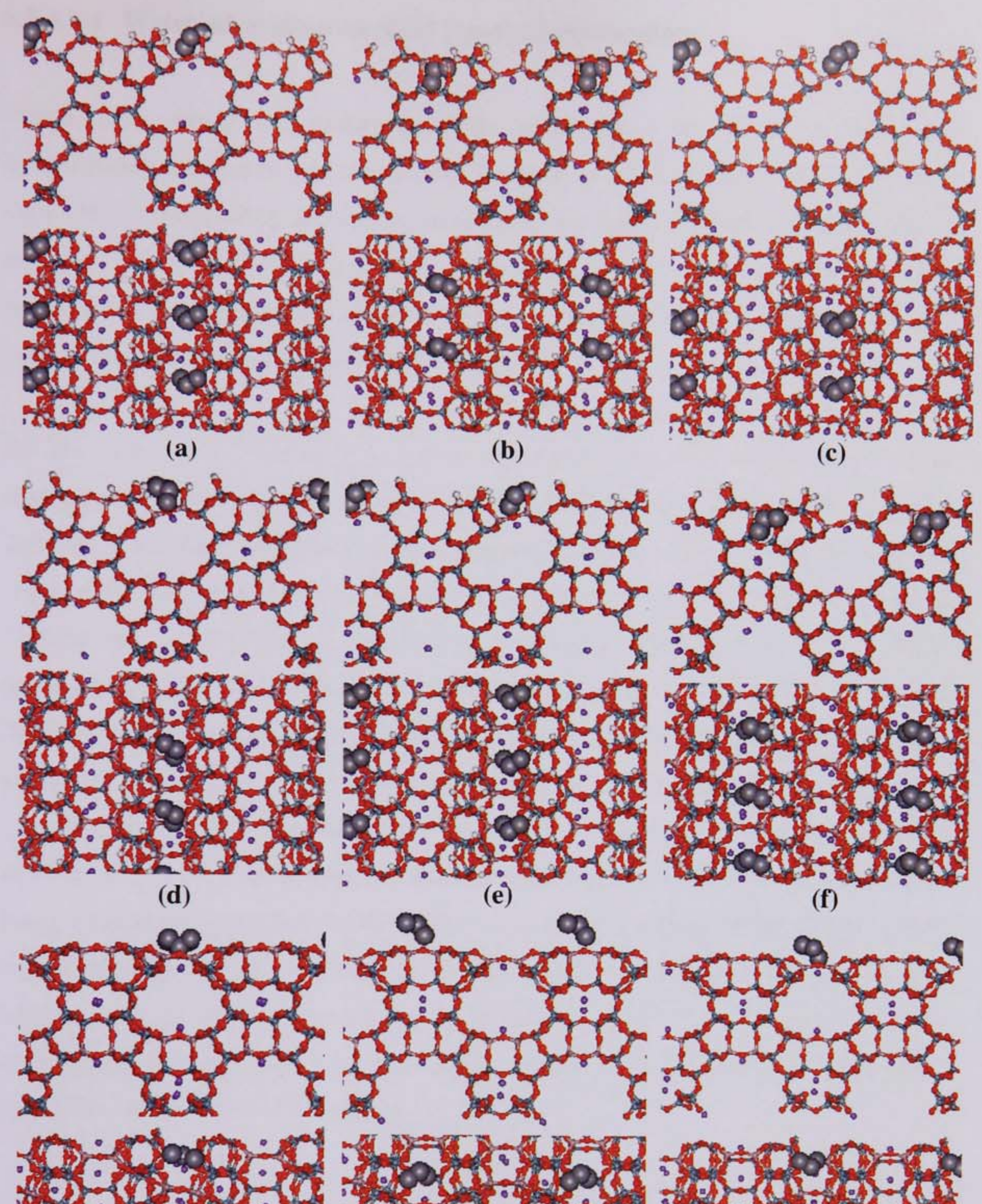

Figure 6.60 Adsorption of propane on the {010} code 35 Na-mordenite surface (a,c,d,e,) hydroxylated (OH) surface at the centre of a parallel elliptical 8MR directly above 12MR straight channel; (b & f) OH surface inside and centre of parallel elliptical 8MR pore directly above 8MR straight channel; (g & i) Non-OH surface over parallel elliptical 8MR directly above 12MR straight channel; (h) Non-OH surface over centre of parallel elliptical 8MR directly above 8MR straight channel.

6.2.4.2.4 Water adsorption on {010} Na-mordenite surface

Figure 6.61 shows the molecular water adsorption sites found on both the hydroxylated and non-hydroxylated {010} surface of Na-mordenite, while Table 6.7 shows the corresponding adsorption energies. It was found for both the hydroxylated and non-hydroxylated surfaces that the water molecule tends to adsorb more strongly and at many more locations compared to that of the hydrocarbons investigated with large favourable exothermic adsorption energies.

For the hydroxylated surface five distinct adsorption sites were determined for the adsorption of water (figures 6.61a to 6.61g). Of these adsorption sites the largest adsorption energies corresponds to the adsorption of water above a 5MR, close to a Si atom of Si-OH group (figures 6.61f & 6.61g) with resulting adsorption energies of -251.88 and -250.98 kJ/mol. The lowest adsorption energy for the hydroxylated surface correspond to the water molecule being located over the middle of a 8MR and 5MRs sat directly above a 12MR straight channel (figure 6.61d) with an adsorption energy of -203.91 kJ/mol. For the non-hydroxylated surface eight distinct adsorption sites were determined (figures 6.61h to 6.61o) all of which had favourable exothermic adsorption energies. The largest adsorption energy corresponds to the water molecule being located over a Si atom coordinated to one 8MR and two 5MRs (figure 6.61o) with a resultant adsorption energy of -266.98 kJ/mol. The lowest adsorption energy corresponded to the water molecule being above a 5MR but close to a Si atom coordinated to one 8MR and two 5MRs (figure 6.61i) with a corresponding adsorption energy of -51.897 kJ/mol.

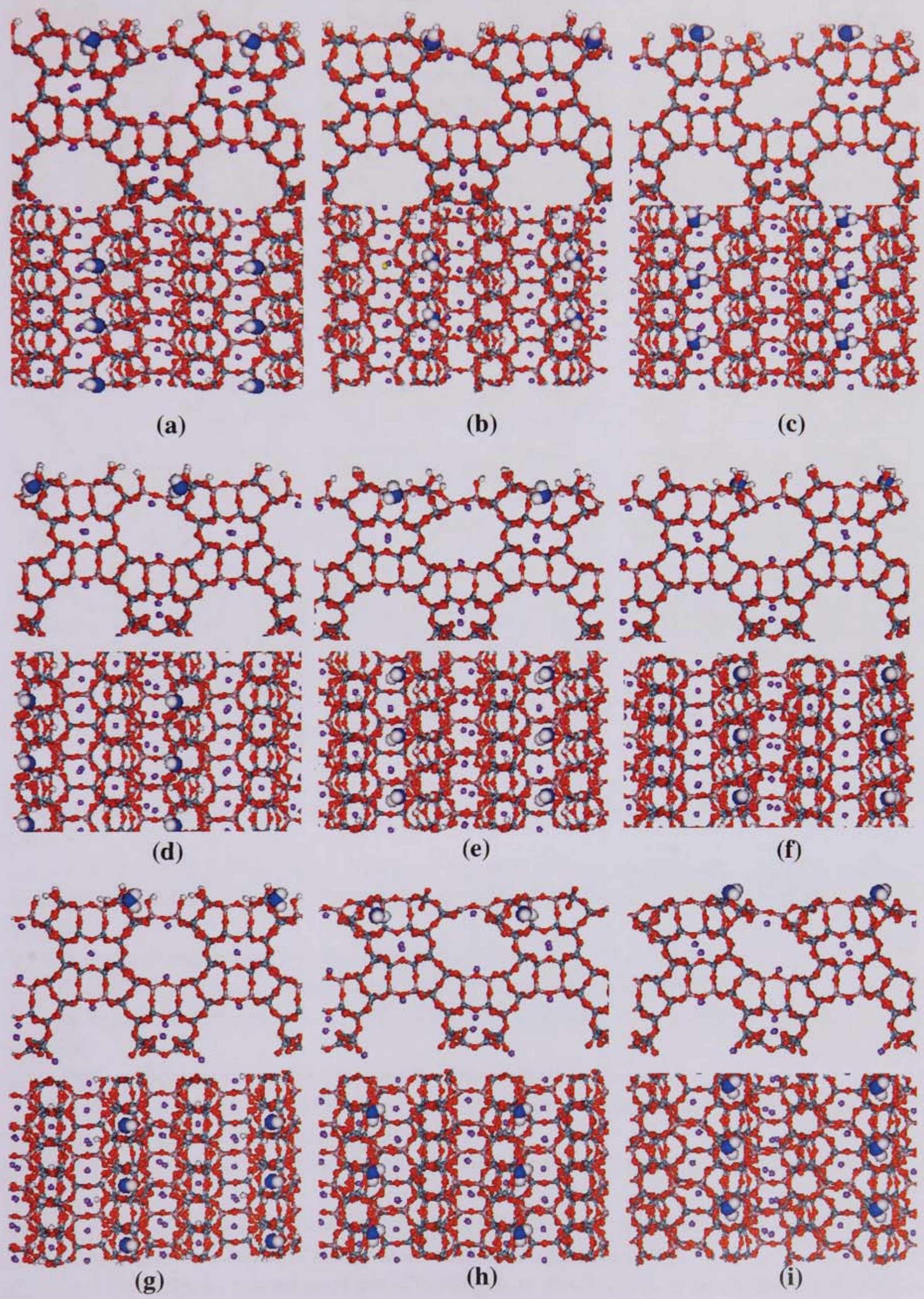

(a) (b) (c)

(d) (e) (f)

(g) (h) (i)

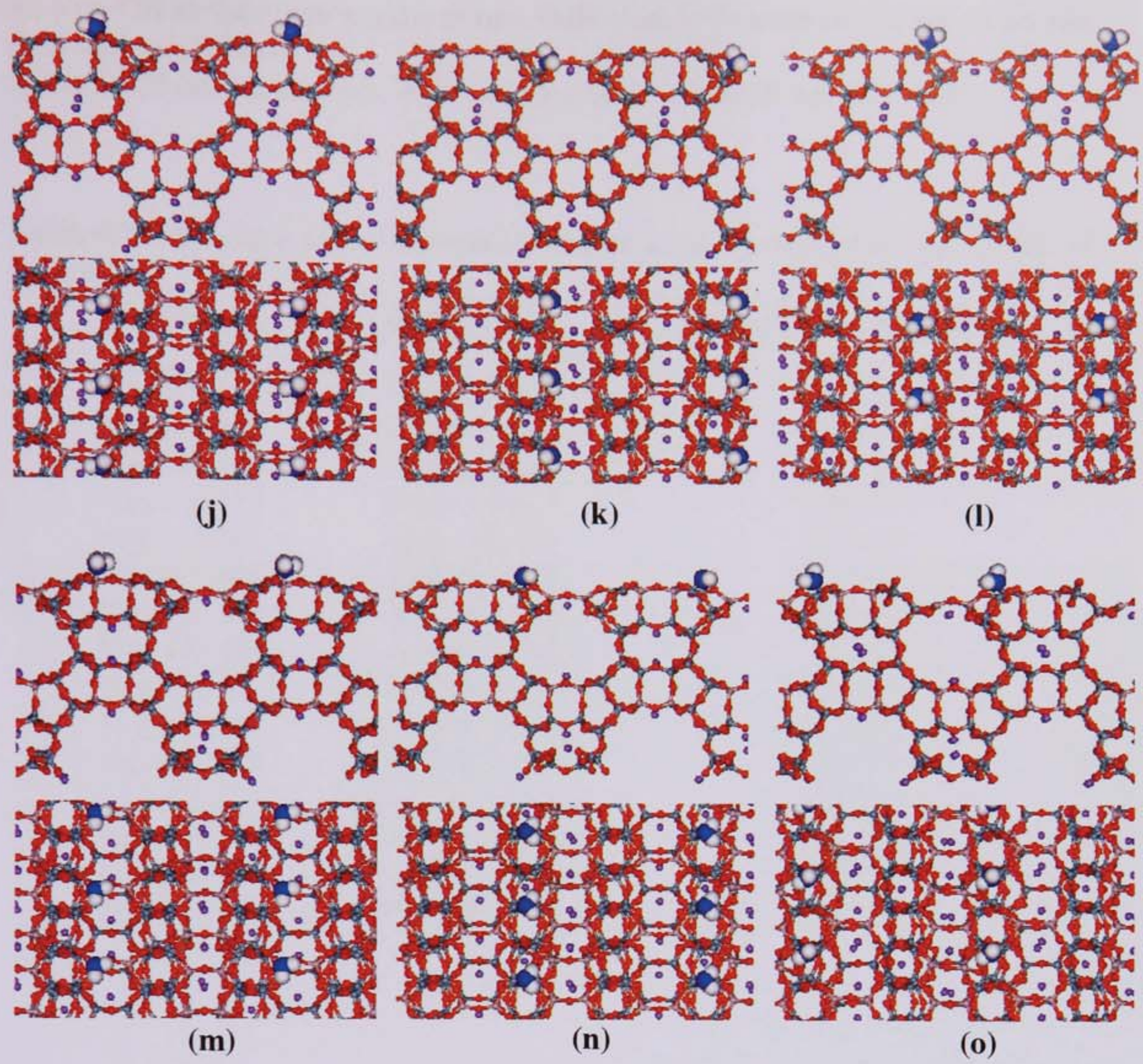
(j) (k) (l)
(m) (n) (o)

Figure 6.61 Adsorption of molecular water on the {010} code 35 Na-mordenite surface:

(a,e) hydroxylated (OH) surface Inside of parallel elliptical 8MR pore close to wall by Al atom connected to two 8MR and one 5MR, directly above 8MR straight channel.

(b) OH surface above Si atom coordinated to two 5MR and one 8MR.

(c) OH surface above Al atom coordinated to two 8MR and one 5MR.

(d) OH surface middle of & over 8MR and 5MRs, directly above 12MR straight channel.

(f, g) OH surface above 5MR, close to Si atom of Si-OH group.

(h) Non-OH surface in side 8MR close to Si atom coordinated to one 8MR and two 5MR, directly above 8MR straight channel.

(i) Non-OH surface above 5MR but close to Si atom coordinated to one 8MR and two 5MR.

(j) Non-OH surface over edge of parallel elliptical 8MR close to Al atom coordinated to one 5MR and two 8MR, directly above 8MR straight channel.

(k) Non-OH surface over edge of parallel elliptical 8MR close to Si atom coordinated to one 8MR and two 5MR, directly above 12MR straight channel.

(l) Non-OH surface directly above Si atom coordinated to one 8MR and two 5MR.

(m) Non-OH surface directly above Al atom coordinated to one 5MR and two 8MR.

(n) Non-OH surface over middle of two 5MR close to Si atom coordinated with one 8MR and two 5MR.
(o) Non-OH surface above Si atom coordinated to one 8MR and two 5MR.

Table 6.7 Molecular water adsorption energies at the Na-mordenite {010} code 35 surface

Location	Surface type	Adsorption energy / kJ mol^{-1}
	Water	
Figure 6.61a	Hydroxylated	-244.74
Figure 6.61b	Hydroxylated	-243.77
Figure 6.61c	Hydroxylated	-207.5
Figure 6.61d	Hydroxylated	-203.91
Figure 6.61e	Hydroxylated	-244.65
Figure 6.61f	Hydroxylated	-251.88
Figure 6.61g	Hydroxylated	-250.98
Figure 6.61h	Non-hydroxylated	-243.73
Figure 6.61i	Non-hydroxylated	-51.897
Figure 6.61j	Non-hydroxylated	-128.87
Figure 6.61k	Non-hydroxylated	-76.658
Figure 6.61l	Non-hydroxylated	-102.94
Figure 6.61m	Non-hydroxylated	-92.596
Figure 6.61n	Non-hydroxylated	-139.97
Figure 6.61o	Non-hydroxylated	-266.98

Chapter 7: Molecular Dynamic Simulation Investigations of Hydrocarbon Adsorption and Diffusion in Silicalite-1

Chapter 7: Molecular Dynamic Simulation Investigations of Hydrocarbon Adsorption and Diffusion in Silicalite-1

7.0 Methodology and simulation details

Molecular dynamic simulations technique has been used in this study with simulations carried out using the DLPoly code developed by Forrester and Smith (126). The silicalite-1 model used is the purely siliceous end member of the iso-structural ZSM-5 series with orthorhombic Pnma space group containing 288 atoms and unit cell dimensions, a=20.076 Å, b=19.926 Å and c=13.401 Å. The silicalite-1 topology consists of a combination of intersecting linear and zigzag (sinusoidal) channels to which access is gained via 10-membered ring windows.

A modified version of united atom potential was used in the simulations to represent the alkane adsorbate molecules whereas the silicalite-1 lattice framework was represented with an all atomistic potential model (chapter 3).

The zeolite lattice framework and the adsorbates were allowed to remain flexible throughout the simulations. All simulations were performed in the microcanonical (NVE) ensemble carried out at a pressure of 1 bar and temperatures of 300 K and 400 K in a single silicalite-1 unit cell. The maximum saturation loadings in molecules per unit cell (mpuc) determined from dual-site Langmuir pure component isotherms at 300 K are 19, 15 and 12 mpuc for methane, ethane and propane respectively at pressures greater than 1000 bars (166). At 1 bar the dual-site Langmuir pure component isotherms predicts loadings of 0.05, 1 and 5 mpuc for methane, ethane and propane respectively. Thus it was chosen to simulate loadings of up to 8-12 mpuc of each component. An energy minimized structure of sorbed molecule-zeolite lattice configuration, obtained from static simulation runs were used as the starting configurations in the molecular dynamic runs (chapter 6).

For all simulation a time step of 0.5 fs was employed, as this was sufficiently small enough to ensure good energy conservation. Periodic boundary conditions were applied in the simulation cell with a non-bonded interaction cutoff set at 6.5 Å. The system was initially allowed to equilibrate for the first 1000 steps and following this, simulations of 1 ns were performed and the trajectories saved every 1000 steps for further analysis.

7.1 Results and discussion

The diffusion coefficients were obtained from linear regression of the mean square displacements (MSD) plots of the alkane molecules with the use of the 3-D Einstein equation (Chapter 3). Figures 7.1 to 7.3 show the MSD plots at 300 K of methane, ethane and propane respectively at various loadings in molecules per unit cell (mpuc) in silicalite-1.

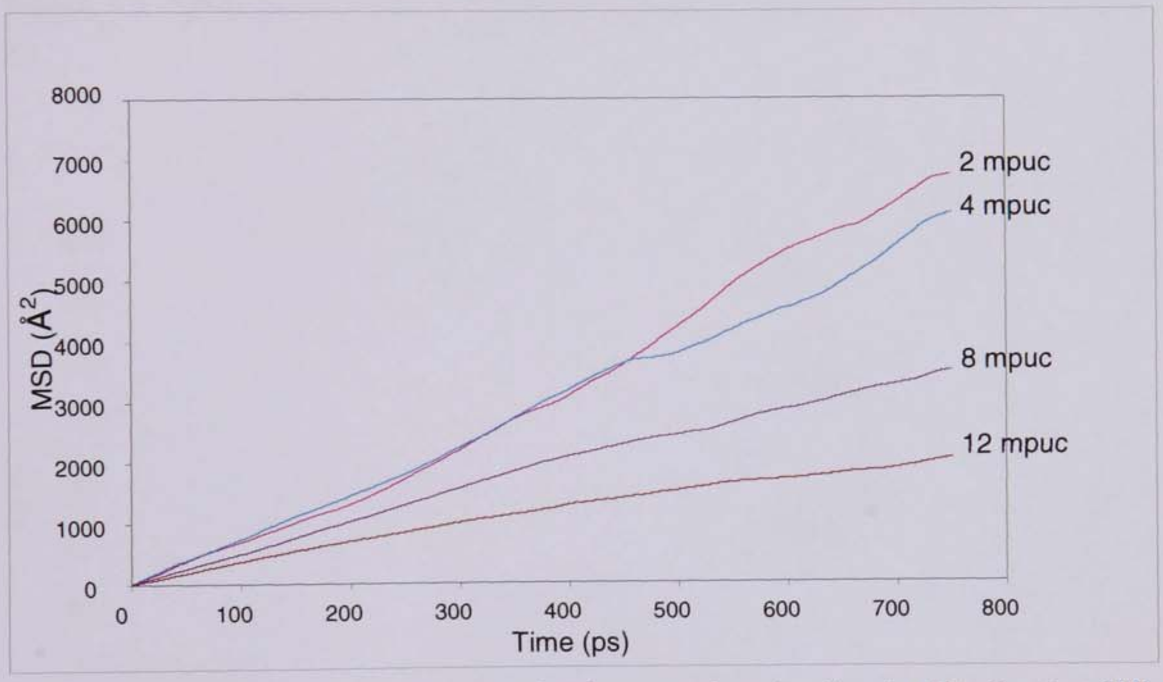

Figure 7.1 MSD plots of methane molecules at various loading in silicalite-1 at 300 K

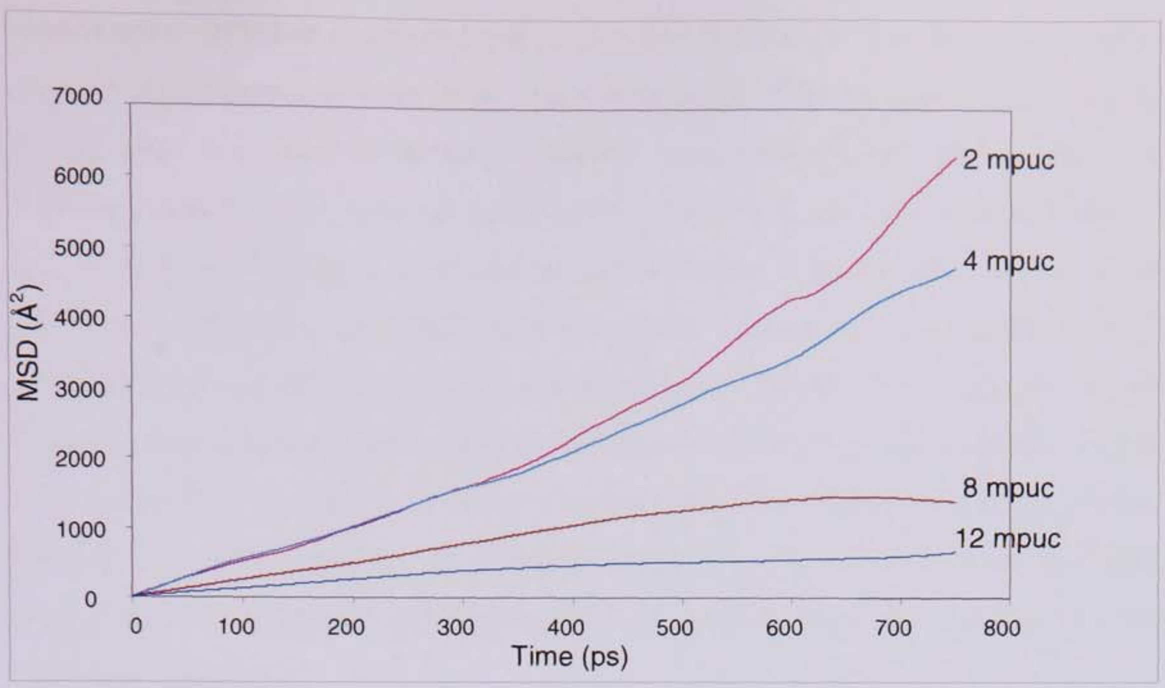

Figure 7.2 MSD plots of ethane molecules at various loadings in silicalite-1 at 300 K

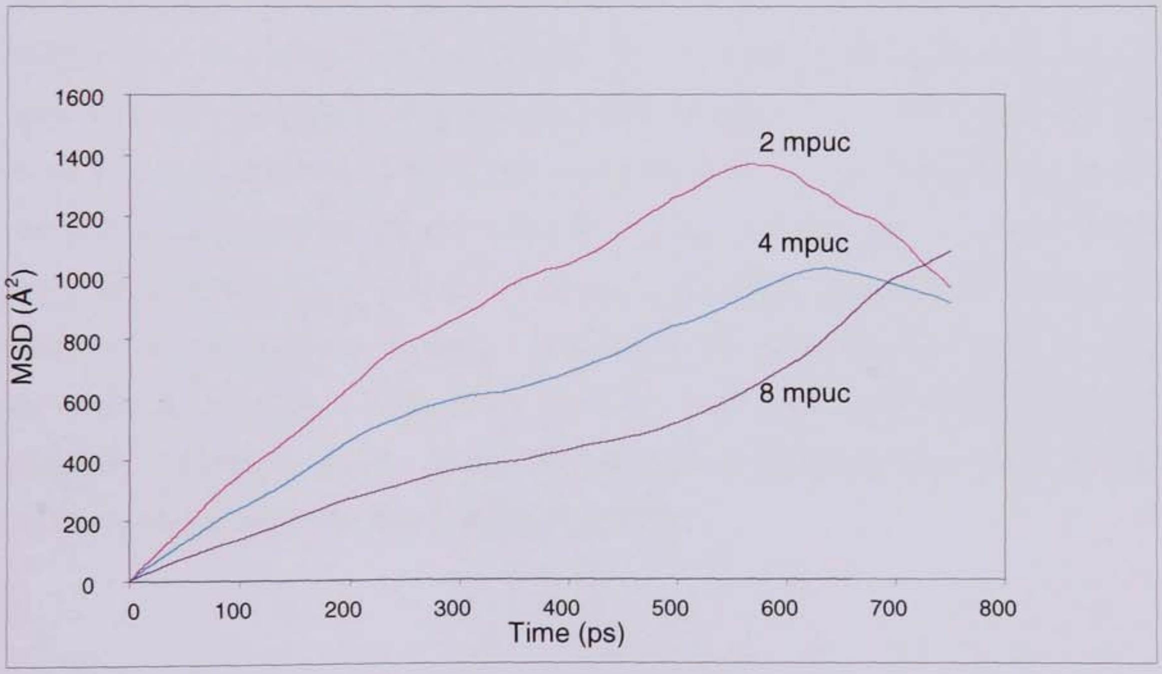

Figure 7.3 MSD plots of propane molecules at various loadings in silicalite-1 at 300 K

7.1.1 Pure components diffusion

The calculated self-diffusion coefficients for methane molecules at 300 K for loadings of 4, 8 and 12 molecules per unit cell (mpuc) are 12.14 x 10^{-9}, 9.05 x 10^{-9} and 5.25 x 10^{-9} m^2/s respectively (Table 7.1). These values are in good agreement with reported experimental diffusion coefficients of 13.0 x 10^{-9}, 9.50 x 10^{-9} and 6.0 x 10^{-9} m^2/sec respectively obtained by Caro et al. (167) from PFG-NMR measurements. They are also in good agreement with those obtained from previous MD simulations using different potential force field and criteria (95,168,169). It can be seen from Table 7.1 that as methane loading is increased at (300 K) there is an overall decrease in the diffusion coefficients. Thus with each successive increase in loading there is less available space for the fast moving methane molecules hence the movement becomes hindered. Apparently, a similar trend of decrease in diffusion coefficients with loading was observed also at 400 K. In general as the simulation temperature was increased there is an overall increase in diffusion coefficients for the methane molecules suggesting the influence of temperature on zeolite framework flexibility and molecular diffusivity.

For ethane and propane molecules, the calculated self-diffusion coefficients are also shown in Table 7.1 These are in agreement with the experimental measurements obtained by Caro et al. (167) at 300 K. The calculated values are also in good agreement with simulation work of Dumont and Bougeard (169) and comparable with the results of Nowak et al. (168). It was noted that just as in methane there is a general decrease in diffusion coefficients with increasing loadings, and on increasing the temperature to 400 K, the diffusion coefficients increases in general but retaining the trend of decreasing with loadings. Comparing the relative diffusivities of these molecules, it was observed that methane diffuses faster than ethane and propane in the channels irrespective of the loading and temperature. Similarly ethane was noted to diffuse faster in the channels compared to propane.

Table 7.1 Self-diffusion coefficients of pure alkanes in silicalite-1

LOADING (mpuc)		Self-diffusion coefficients / 10^{-9} m^2/s				
		Temperature (K)				
		300	400	300		
		This Work		Expt* (167)	MD (168,169)	MD (95)
CH_4	2	12.35	25.24	-	6.2	11.1
	4	12.14	26.07	13	16	8.5
	8	9.05	9.33	9.5	-	5.1
	12	5.25	8.96	6	-	2.7
C_2H_6	2	9.31	13.38	5	4.7	-
	4	8.87	9.67	4	5.9	-
	8	4.31	6.75	2.5	-	-
	12	2.19	3.05	1.0	-	-
C_3H_8	2	4.66	8.33	4	4.1	-
	4	3.15	2.73	2.9	1.9	-
	8	1.95	2.43	0.6	-	-

* Values extrapolated from graph

7.1.2 Binary and ternary components diffusion

The diffusion profiles of three binary mixtures and one ternary mixture for these alkanes (methane, ethane and propane) in silicalite-1 were also investigated and the resultant self-diffusion coefficients for each component in the mixtures calculated. A 1:1 binary mixture of methane/propane, methane/ethane and ethane/propane were simulated in the silicalite-1 channels and the resultant self-diffusion coefficients for the mixture components are shown in Figure 7.4.

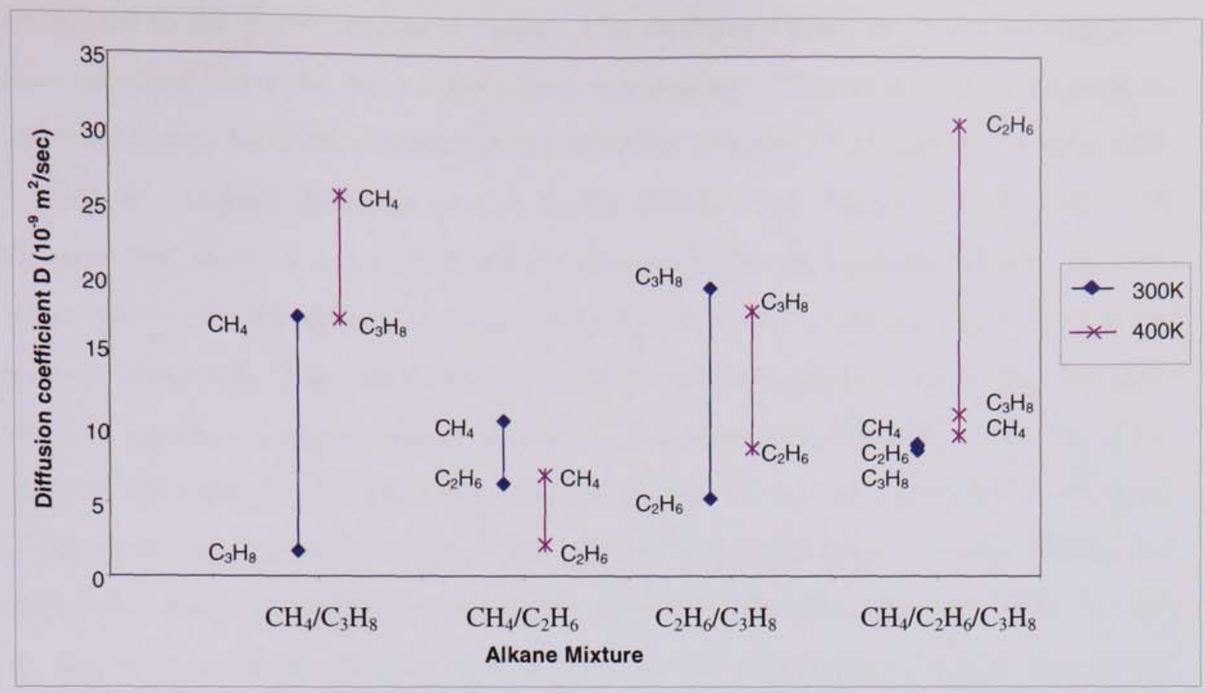

Figure 7.4 Self-diffusion coefficients of binary and ternary alkane mixtures at 300 K and 400 K in silicalite-1 at loadings of 1 mpuc each.

7.1.2.1 Binary mixtures of methane/propane

Comparing these values with their respective pure component self-diffusion coefficients (at similar loadings) indicates that for methane/propane mixture at 300 K the methane's diffusion coefficients increases while propane's decreases suggesting that methane diffuses faster than propane in the channel probably due to competitive adsorption occurring between them. Figure 7.5a shows the density profile plots obtained at 300 K for methane/propane mixture where both molecules are preferentially located in both the side and middle straight/intersection channels indicating that the molecules are interacting with each other and thus competing for diffusional pathways. These density profile plots are valuable in determining the focal points of sorbate and diffusion activities. These plots are particularly useful for identifying competitive adsorption and preferred diffusional pathways for components in the channels. The channels are identified on the plot as 'middle' or 'side' straight/intersection channels. In each unit cell along the z-axis, the main straight channel is flanked on each side by the sinusoidal channels. This main channel is referred to as the 'middle' straight/intersection channels, and following the sinusoidal channel is the 'side' straight/intersection channels. At 400 K (Figure 7.4), it is noted that there is a considerable increase in the propane molecules diffusion coefficients compared to the pure component values. The methane values were almost similar to that obtained from the pure component simulations. The competitive adsorption effect observed from the z-density plots at 300 K (Figure 7.5a.) appears to have little impact on propane diffusion at the higher temperature. Krishna et al. (102,170) showed that there is a coupling effect between diffusing species, which can slow down faster moving species (in this case methane) and accelerate the slow moving partner (propane). The results shown confirm this observation such that the slow moving species propane was observed to accelerate considerably while methane species diffusion coefficients was almost similar to that obtained from the pure component simulations. The reason for this could be attributed to preferred sorption pathways taken by methane as seen on the density profile plots in Figure 7.5b. At 400 K, the methane in the mixture now prefers to stay and diffuse through the middle straight/intersection channels while the propane species now occupies both the middle and the side straight/intersection channels. This reduces the chances of collisions and competition between the two species at 400 K compared to 300 K.

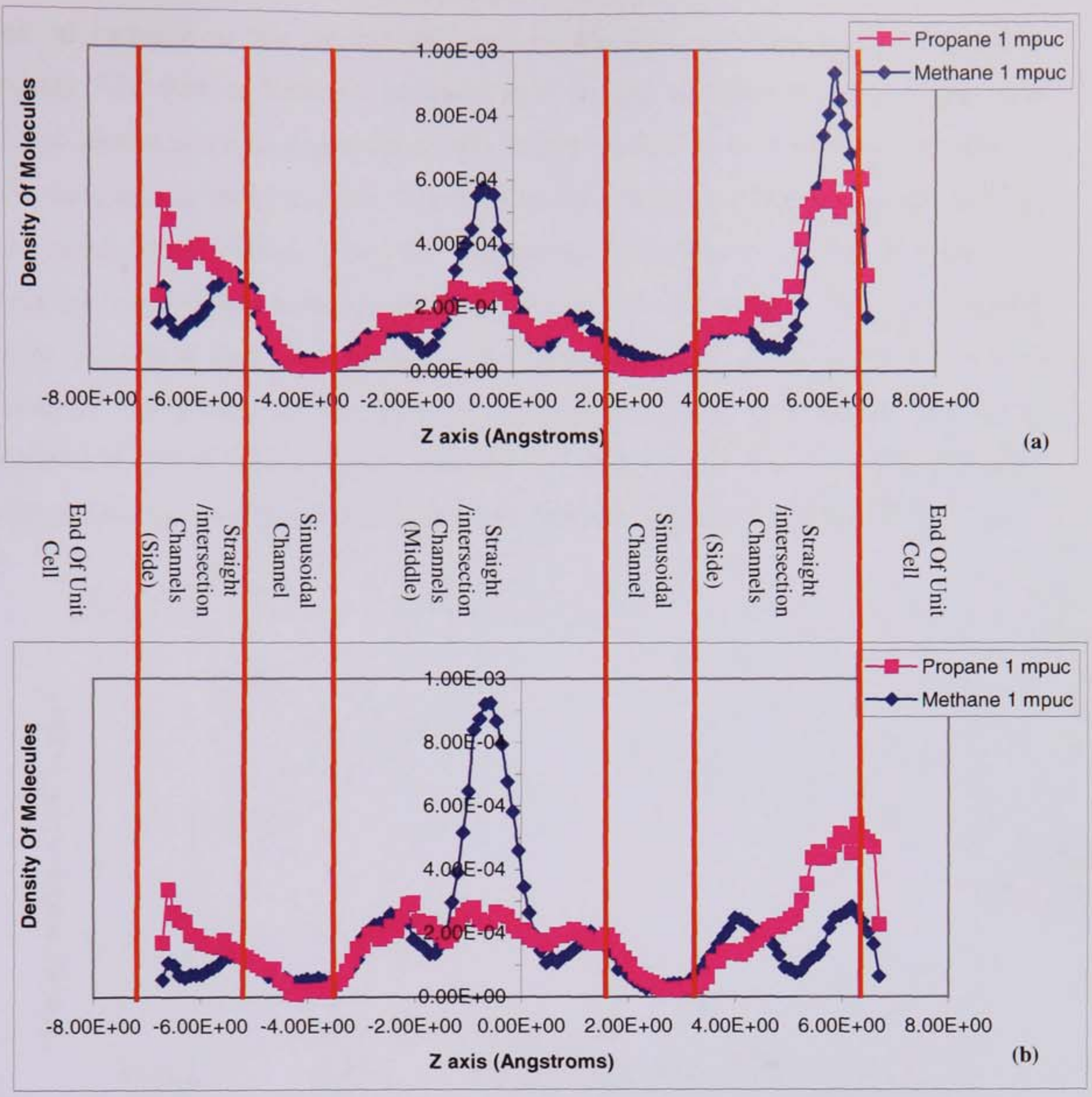

Figure 7.5 The z-density population plots for binary mixture of methane/propane (1:1) in silicalite-1 at (a) 300 K (b) 400 K.

7.1.2.1.1 Influence of loading on binary methane/propane mixtures

Furthermore the effect of increase loadings on diffusion behaviour of the component species in the mixture was investigated. The binary mixture now consists of loadings of up to five molecules per unit cell for each species in the mixture in equal ratio. The overall effect of loading on the calculated diffusion coefficients is shown in Figure 7.6 at both temperatures.

For the methane components in the mixture at low loadings (1-2 mpuc) there is a general increase in the overall diffusion coefficients with increasing temperature (Figure 7.6). But as loadings increases (3-5 mpuc) the diffusion coefficients now remain almost constant especially at 400 K. The overall trend at both temperatures is that the methane molecules diffusion coefficients decrease with increasing loadings. An interesting situation occurs for the propane component at 300 K where the diffusion coefficients were observed to remain constant across the entire loading range. At 400 K there is a change in the behaviour of the propane molecules with diffusion coefficients at low loadings (1-2 mpuc) being much higher than those obtained at 300 K, and at higher loadings (3-5 mpuc) the diffusion coefficients drop with increasing loadings to almost the same order as simulated at 300 K (Figure 7.6).

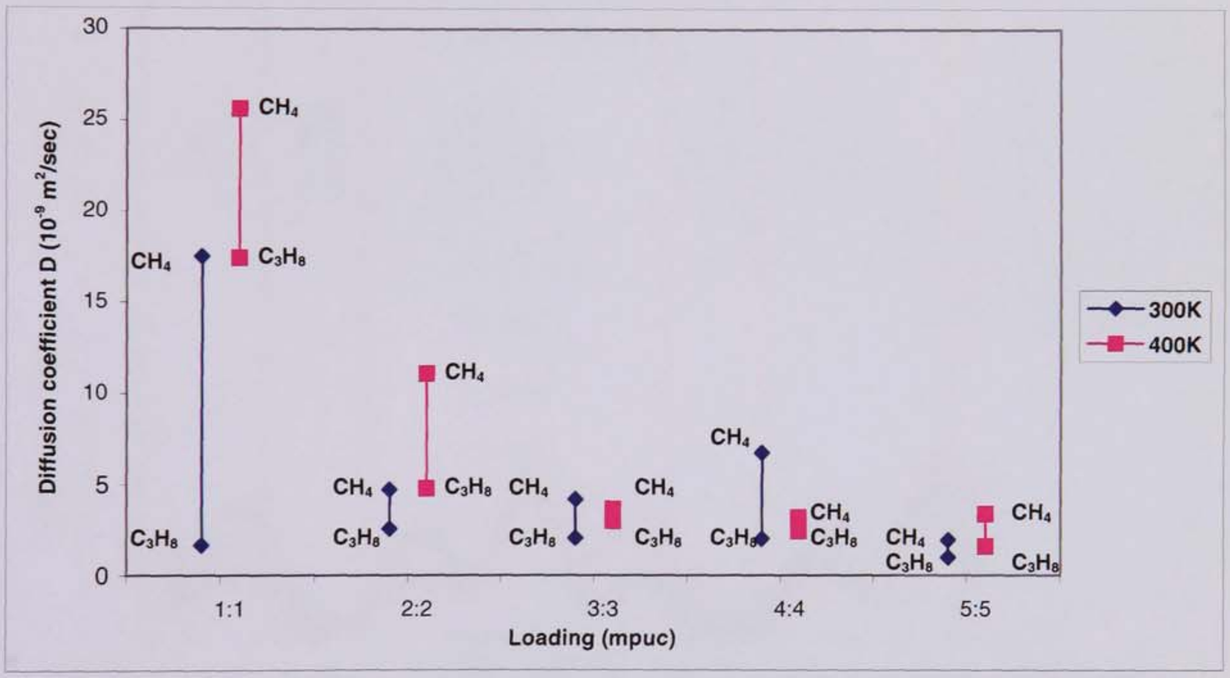

Figure 7.6 Self-diffusion coefficients of binary methane/propane mixtures at 300 K and 400 K in silicalite-1 at various loadings.

It is interesting to note from the z-density graphs (loading 3:3 mpuc) at 300 K (Figure 7.7a) that, methane molecules are still preferentially active in the middle straight channel but this time with an increased diffusional activity at the entrance to the right sinusoidal channel, which is a vital link between the middle and right side straight/channel intersection. While the propane molecules in the mixture were noted to have similar diffusional behaviour in both the middle and side straight/intersection channels and were seen taking preference over methane molecules in the side straight/intersection channels. As the temperature is increased for the 3:3 loading (400 K), the diffusional activities of the two components in the mixture appear to be similar in both the middle and side straight/intersection channels thereby resulting in similar diffusivities as shown in Figure 7.6.

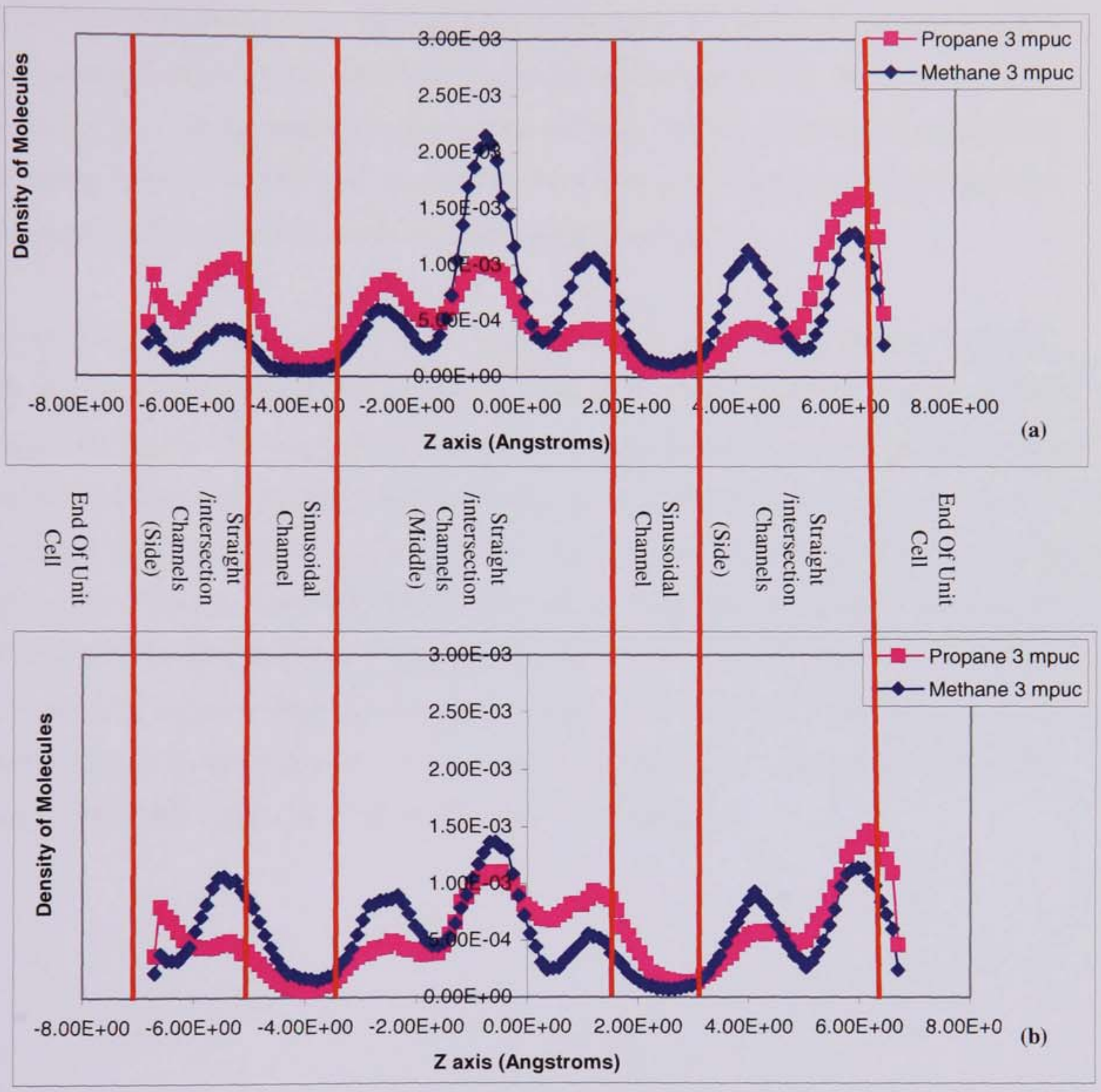

Figure 7.7 The z-density population plots for binary mixture of methane/propane (3:3) in silicalite-1 at (a) 300 K (b) 400 K.

On increasing the mixture ratio to 5:5 mpuc at 300 K (Figure 7.8a.), both molecules were observed to have varying distribution across the middle and side straight/intersection channels. In the middle straight/intersection channels the two species appear to have equal distributions, with propane diffusing out through the right side channel intersection and methane diffusing through the left side channel. At 400 K (Figure 7.8b) propane molecules are now seen to displace the methane in the middle straight channel with methane now occupying the two intersection channels leading to the sinusoidal channels.

Overall in the mixture at low loadings the methane molecules have the higher diffusion coefficients compared to propane irrespective of simulated temperatures and as loading is increased the calculated diffusion coefficients for the two species begin to converge. This appears to be due to the influence of the coupling effect between diffusing species, which tends to slow down the faster moving species (in this case methane) and accelerate the slow moving partner (propane).

As increasing temperature results in an increase in kinetic energy for the molecules the possibilities of propane molecules being able to move about much more rapidly increases but as the loading is increased the movement becomes hindered and localized mainly to the straight/intersection channel. This view is supported with the evidence that the propane molecule has very limited diffusional activity in the sinusoidal channels even with increased loadings. This is not the case for the smaller methane molecules, which have higher diffusional activity in the sinusoidal channels compared to propane with increasing loadings. As a result methane molecules are able to move from channel to channel with little hindrance and therefore have the higher diffusion coefficients across the entire loading range.

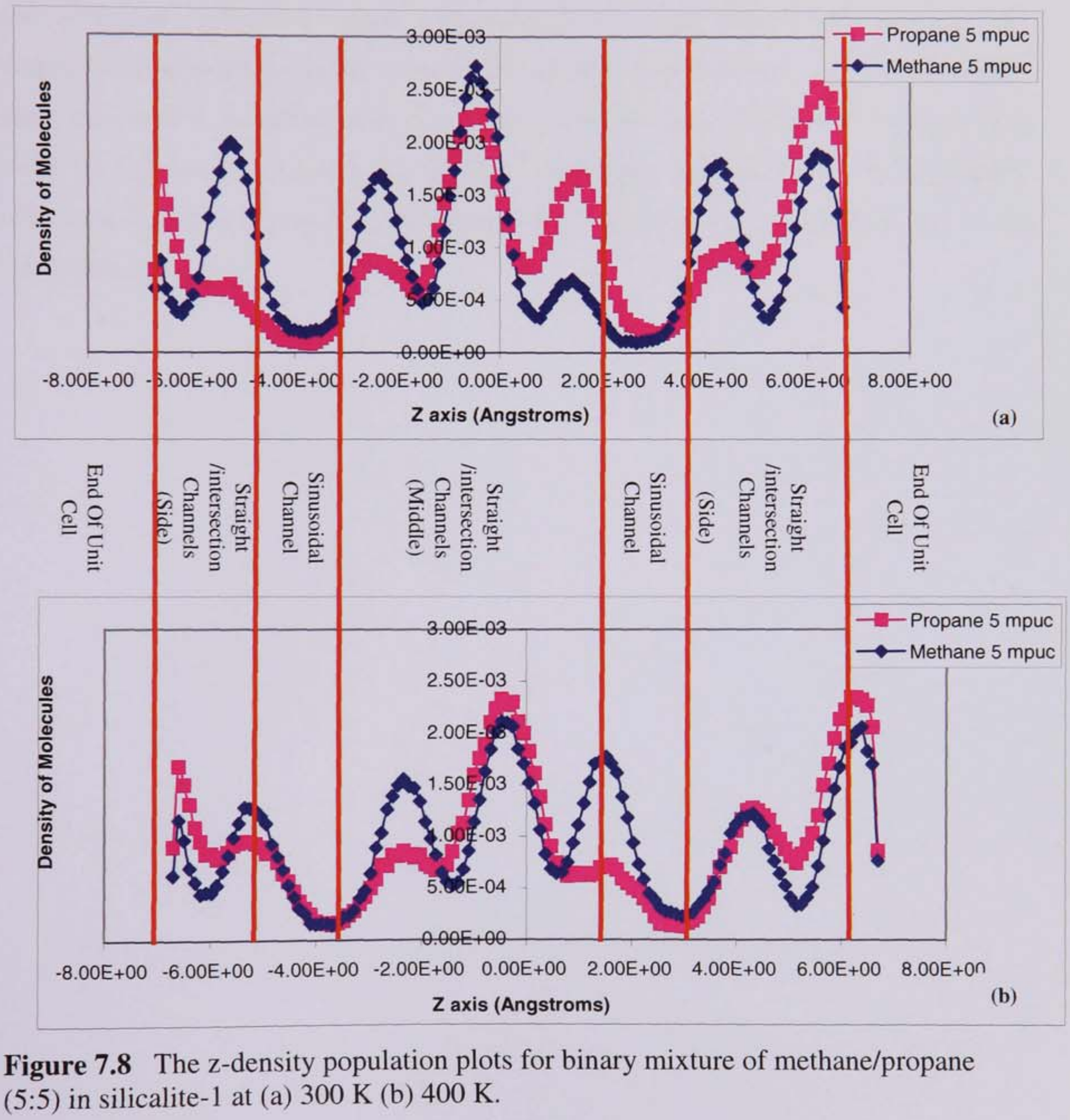

Figure 7.8 The z-density population plots for binary mixture of methane/propane (5:5) in silicalite-1 at (a) 300 K (b) 400 K.

7.1.2.2 Binary mixtures of methane/ethane

For the binary mixture of methane/ethane (1:1), it was observed that the diffusion coefficients of the components in the mixture at 300 K and 400 K are much smaller than values obtained for their respective pure component simulations (Table 7.1 and Figure 7.4). The z-density profiles for the species (Figure 7.9) at a mixture ratio of 1:1 shows that the methane molecule has a higher preference for the straight channel compared to ethane as indicated by the dominant peaks in both the middle and side straight/intersection channels. The presence of the ethane molecule in the same channel appears to hinder the fast diffusing methane thus explaining the reduction in the diffusion coefficient when compared to the pure component values. This competitive adsorption was observed in the simulation trajectories showing the ethane molecule unable to diffuse and exit freely using the same channel as methane, but uses the sinusoidal channels instead thus explaining why there is a much higher diffusional activity in the sinusoidal channels for ethane compared to methane at both temperatures.

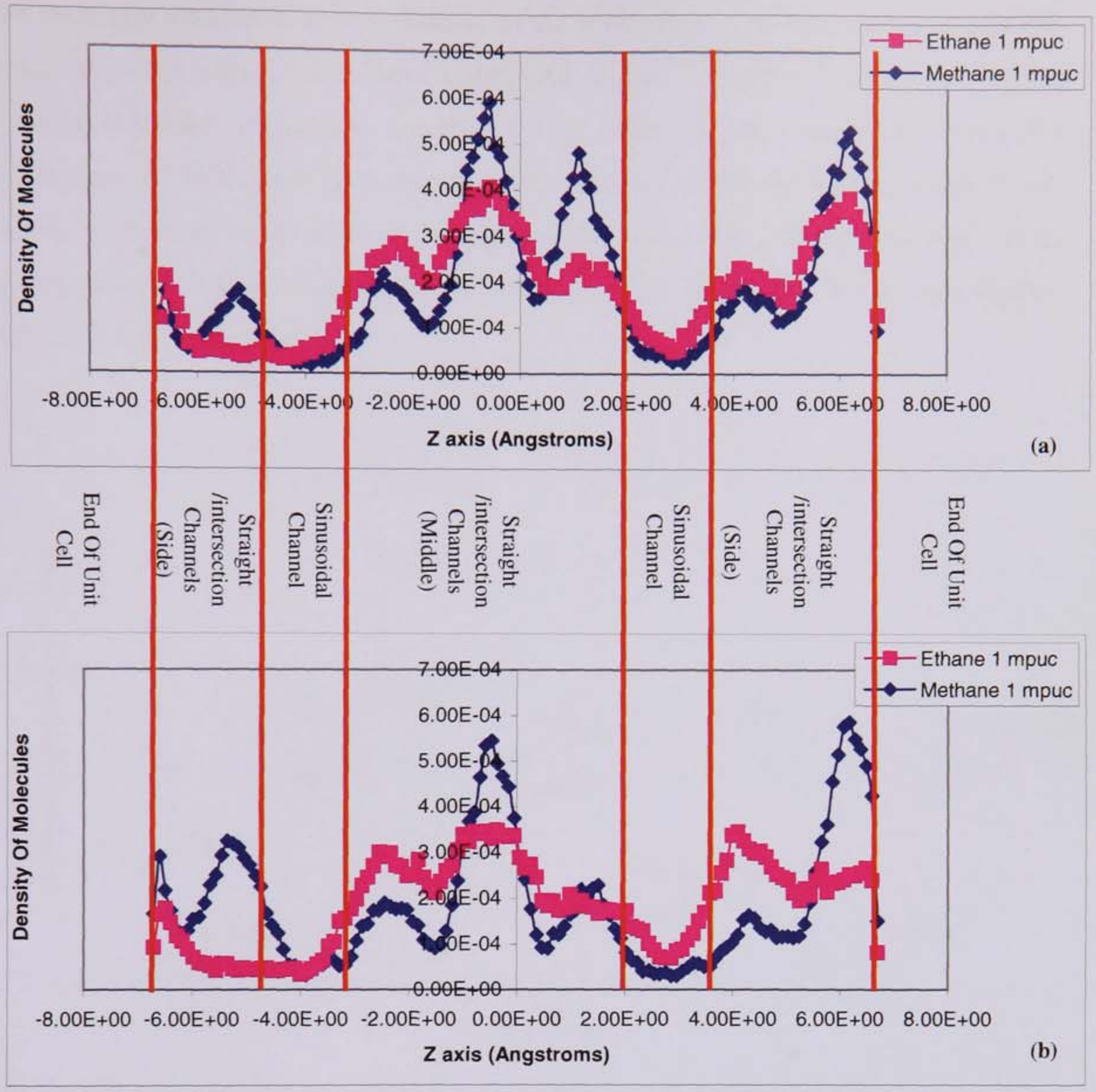

Figure 7.9 The z-density population plots for binary mixture of methane/ethane (1:1) in silicalite-1 at (a) 300 K (b) 400 K.

7.1.2.2.1 Influence of loading on binary methane/ethane mixtures

The effect of molecular loadings on the diffusional behaviour between methane and ethane components in the mixture was further investigated. The binary mixture once again consists of loadings of up to five molecules per unit cell for each species in the mixture in equal ratio. The overall effect of loading on the calculated diffusion coefficients is shown in Figure 7.10. It was noted that the diffusion coefficients increase with loadings at 300 K (1:1–2:2) with the methane components having the higher diffusional coefficients, but on increasing the loadings (3:3–4:4) we see a sudden decrease in the diffusional coefficients of both molecules in the mixture but interestingly we also observe a reversal in the preference of diffusional behaviour this time with the ethane molecules having the higher diffusion coefficients. As the loading is further increased to a ratio of 5:5 we noticed again a second reversal in the preference of diffusional behaviour with the methane molecules diffusing faster than ethane molecules in the mixture. A similar observation was noted for the simulations carried out at 400 K except that the reversal in the diffusional behaviour appears earlier at lower loadings.

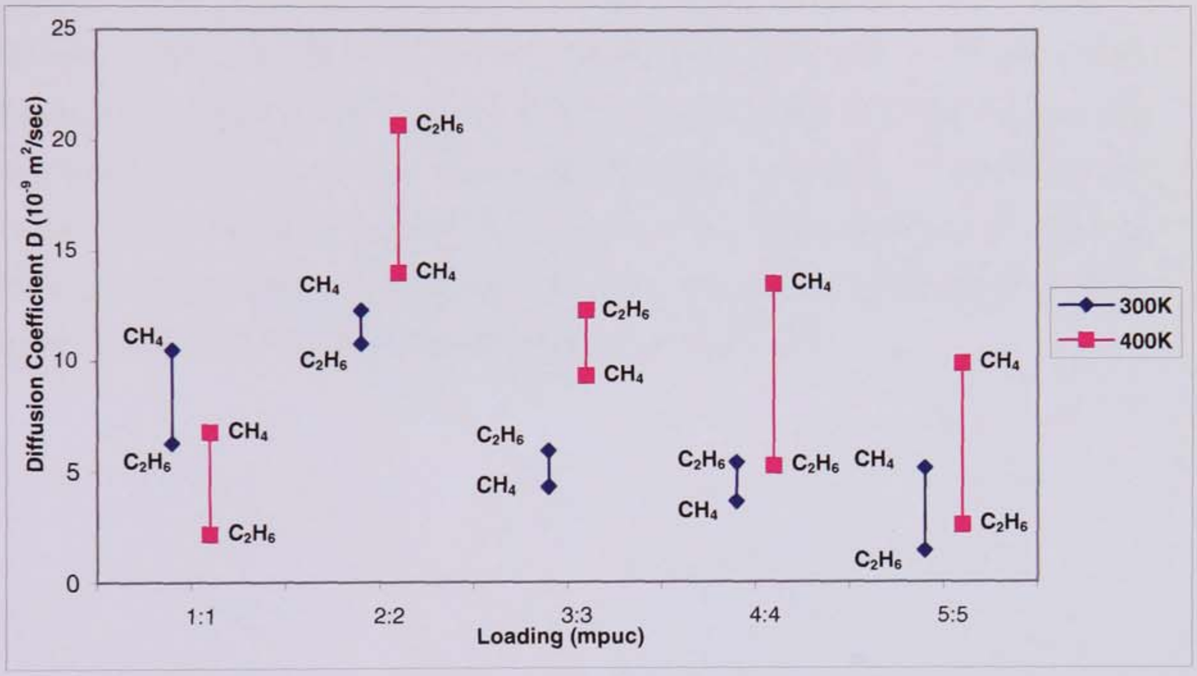

Figure 7.10 Self-diffusion coefficients of binary methane/ethane mixtures at 300 K and 400 K in silicalite-1 at various loadings.

A plausible explanation for this diffusional behaviour reversal between the molecules at both temperatures might be due to the size of the two components in the mixture. The two components are small enough in size to move freely within the channels with little hindrance between each other especially at low loadings (1:1-2:2) and thus the size entropy effect dominates resulting in the methane molecules having higher diffusion coefficients. As the loading is increased, the coupling effect between diffusing species appears to come into play and dominates at intermediate loadings of 3:3-4:4, which results in the first reversal in the diffusional behaviour. On increasing the loading to 5:5 near to saturation loadings, the adsorption sites and pathways in the silicalite-1 channels are more easily filled up with the smaller methane molecules as they are able to pack more efficiently compared to larger ethane molecules. This behaviour is attributed to the size entropy effect. At this loading the coupling effect is no longer dominant but instead the size entropy effect dominates and thus we see the second observed diffusional behaviour reversal.

Figures 7.11 and 7.12 show this loading effect on diffusional behaviour of the mixtures. At 300 K at loading of 3:3 (Figure 7.11a), the ethane activity in the middle straight/intersection channels is noticeably increased when compared to the simulations carried out at 1:1 (Figure 7.9) and this is the point where we observed a reversal in the diffusion behaviour with the ethane components having higher diffusion coefficients. However, methane is still present but largely in the side straight channels as indicated by the large peak (Figure 7.11a). At 400 K, both molecules now have a similar distribution especially in the side straight/intersection channels (Figure 7.11b). On increasing the loading to 5:5 mpuc, the methane molecules as discussed above are now diffusing through and filling up the channel thereby resulting in a higher diffusion coefficient compared to ethane (Figure 7.12).

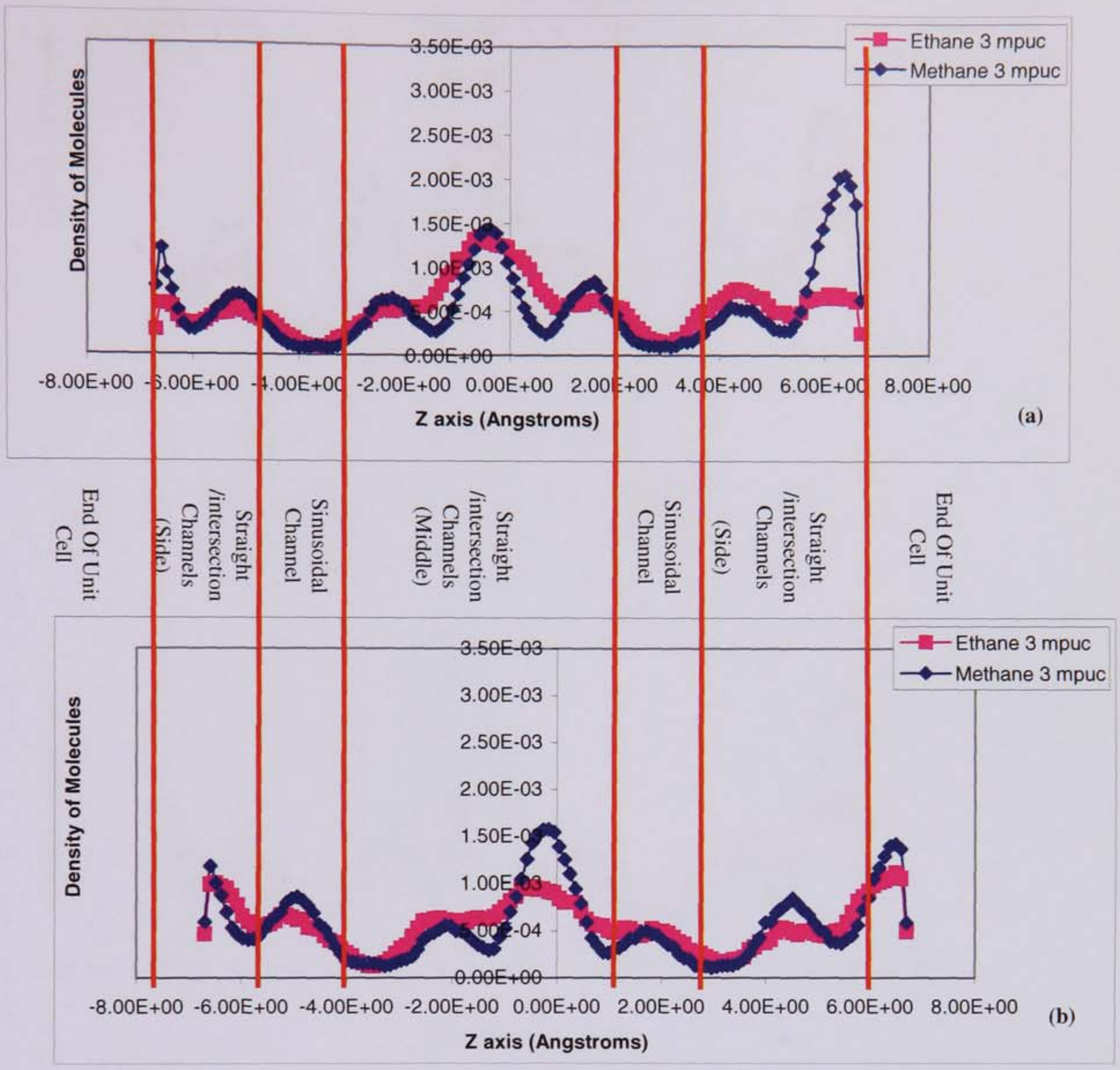

Figure 7.11 The z-density population plots for binary mixture of methane/ethane (3:3) in silicalite-1 at (a) 300 K (b) 400 K.

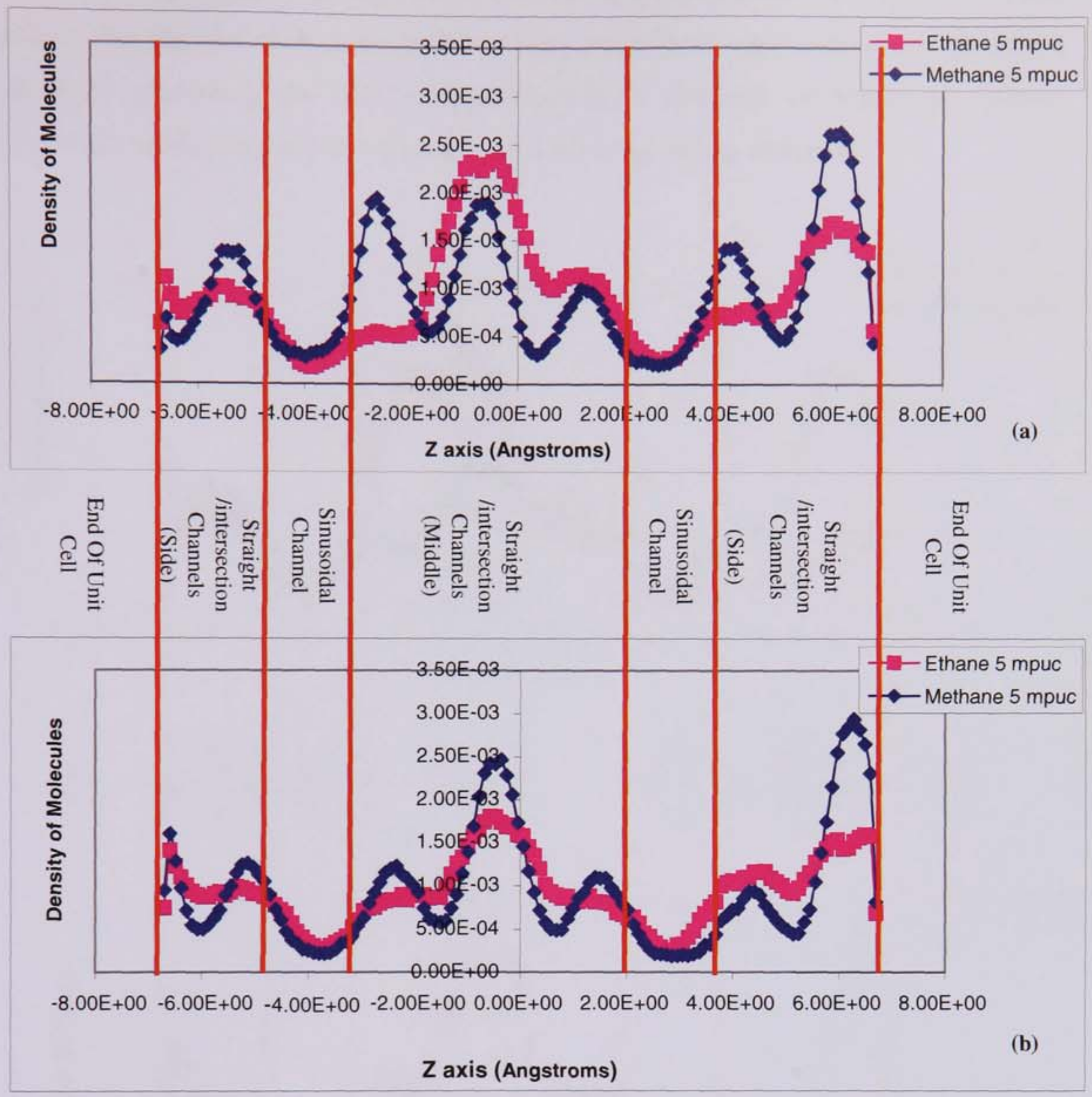

Figure 7.12 The z-density population plots for binary mixture of methane/ethane (5:5) in silicalite-1 at (a) 300 K (b) 400 K.

7.1.2.3 Binary mixtures of ethane/propane

The calculated results for the binary mixture of ethane/propane at loadings of 1:1 are shown in Figure 7.4. At the simulated temperatures propane molecule was observed to have the higher diffusion coefficients in the mixture. The diffusion coefficients for ethane in the mixture are much lower than that observed for pure ethane simulations, while the calculated values for propane in the mixture is much higher than that observed for the pure propane simulations. This observed behaviour agrees with the coupling effect explanation suggested by Krishna et al. (102,104,170) . The corresponding z-density plots at 300 K and 400 K at loadings of 1:1 (Figure 7.13) also shows that the two molecules prefer to keep away from each other with the ethane molecule preferring the side straight/intersection channels compared to propane molecule residing mainly in the middle straight/intersection channels.

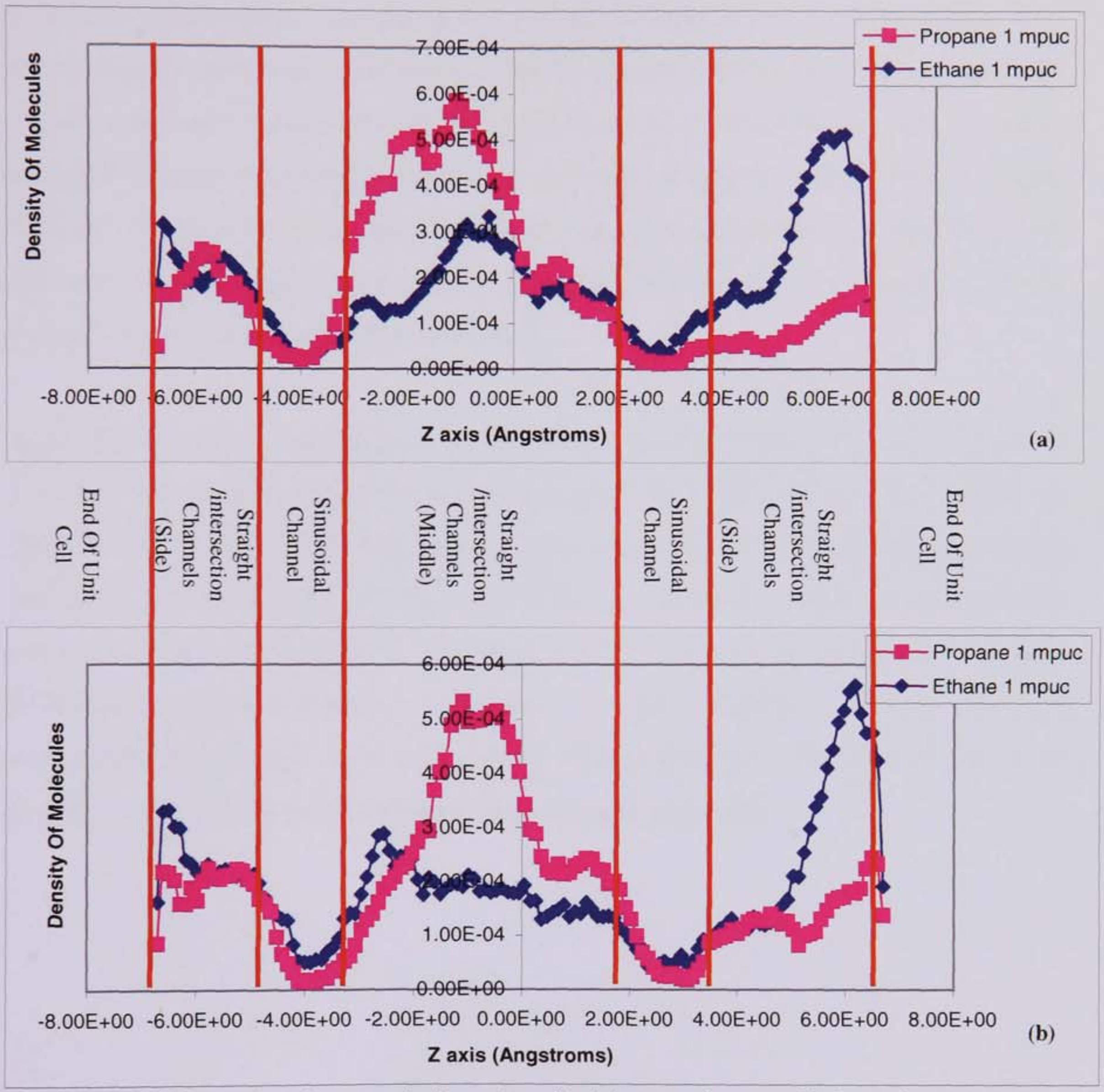

Figure 7.13 The z-density population plots for binary mixture of ethane/propane (1:1) in silicalite-1 at (a) 300 K (b) 400 K.

7.1.2.3.1 Influence of loading on binary ethane/propane mixtures

The overall effect of loading on the calculated diffusion coefficients is shown in Figure 7.14. At 300 K the propane molecules were noted to have a higher diffusional coefficients compared to the ethane molecules up to a loading of 4:4 mpuc with an overall decrease in the diffusion coefficients with increasing loadings. At these loadings the diffusion behaviour of the mixture appears to be governed by the propane molecules as it is strongly adsorbed (due to its higher adsorption energy compared to that of ethane) and coupled with its large size is able to block the ethane molecules passage. This is evident from the z-density graphs (Figure 7.15a) showing propane molecules preferentially occupying the middle straight /channel intersections. This site occupancy behaviour is not seen at 400 K (Figure 7.15b) instead the propane and ethane components have almost identical distributions in both the side and the middle straight/intersections channels and this is reflected in both molecules having similar diffusion coefficients which are much lower than those obtained at 300 K. At the highest molecular loading (5:5) the ethane molecules were noted to diffuse faster than propane in the mixture at both temperatures.

Again this reversal in the diffusional preference could be attributed to the fact that at or near to saturation loadings the adsorption pathways in the silicalite-1 channels are more easily filled up with the smaller ethane molecules than the larger propane molecules, as they are able to pack more efficiently within the channel. Looking at the z-density graphs at a loading of 5:5 (Figure 7.16) it can be seen that there is a higher diffusional activity of ethane molecules in the sinusoidal channels at both temperatures resulting in easy passage for ethane molecules diffusing to and from straight channels with little hindrance from propane molecules.

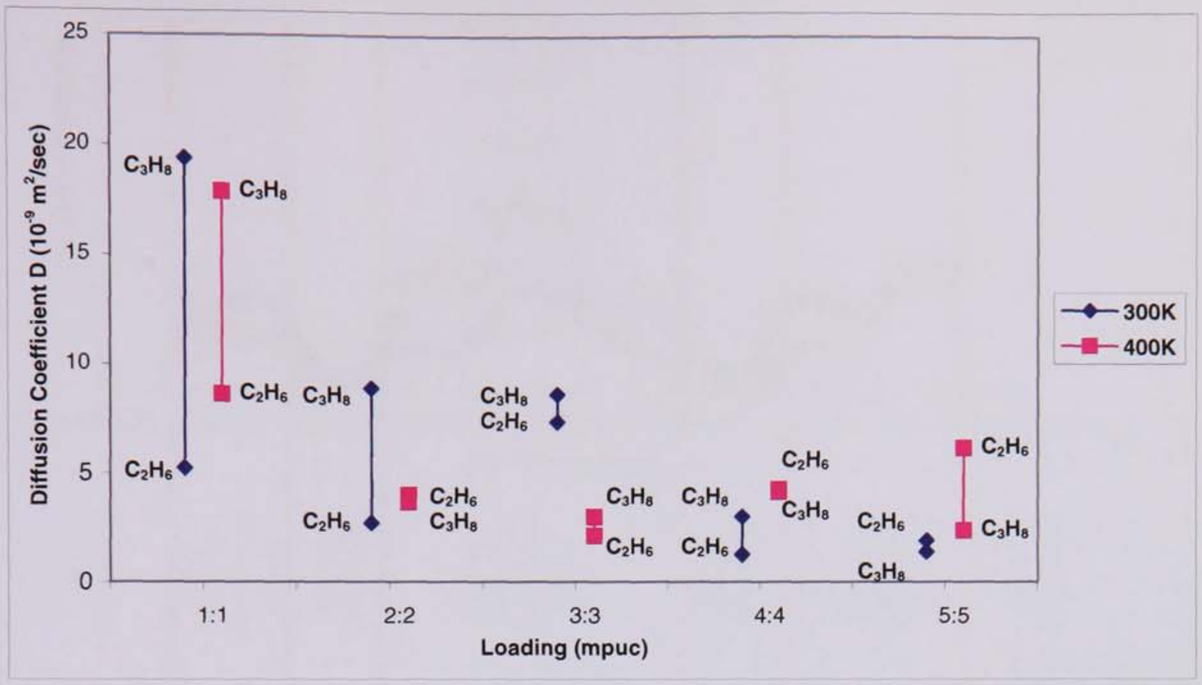

Figure 7.14 Self-diffusion coefficients of binary ethane/propane mixtures at 300 K and 400 K in silicalite-1 at various loadings.

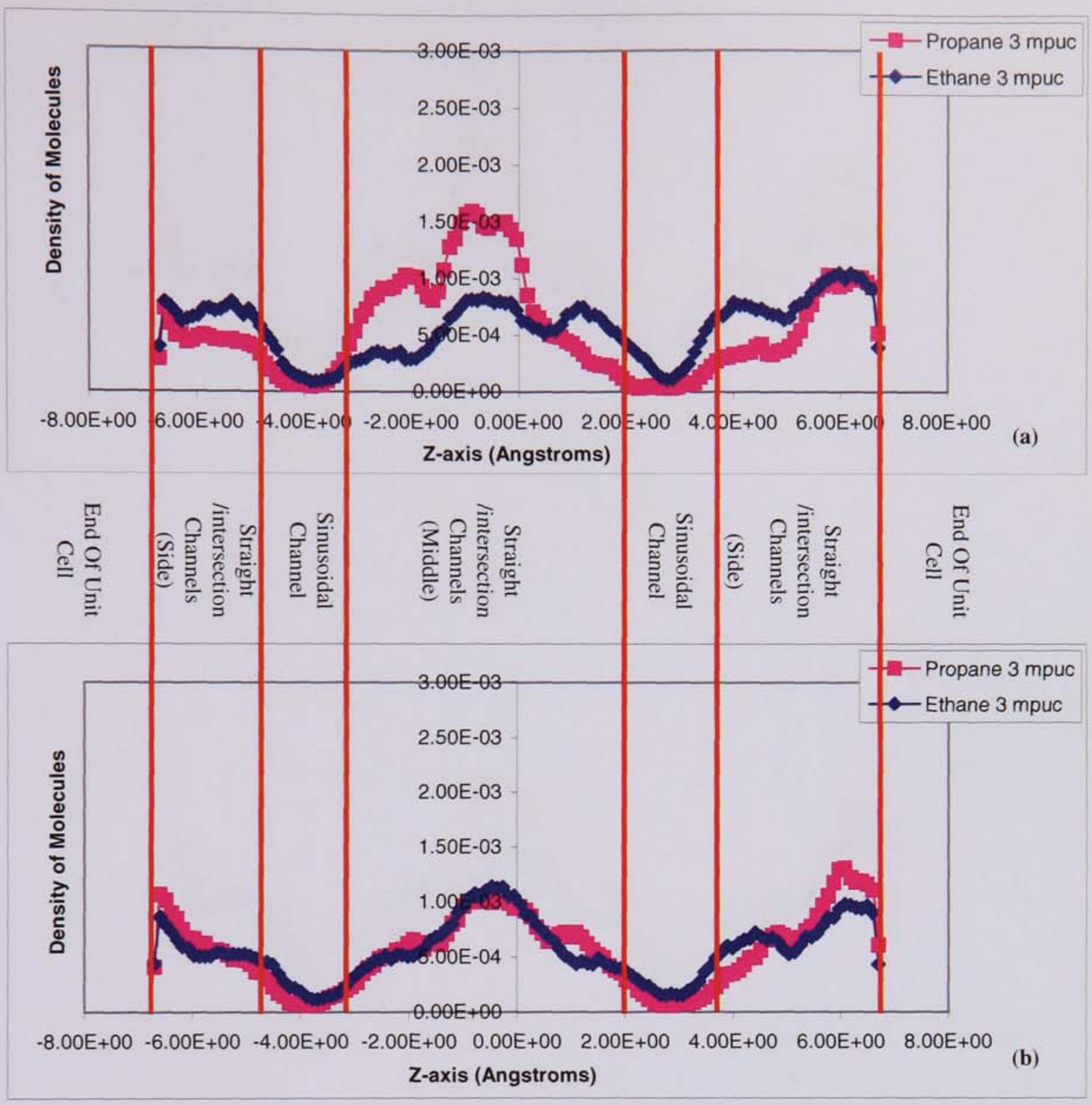

Figure 7.15 The z-density population plots for binary mixture of ethane/propane (3:3) in silicalite-1 at (a) 300 K (b) 400 K.

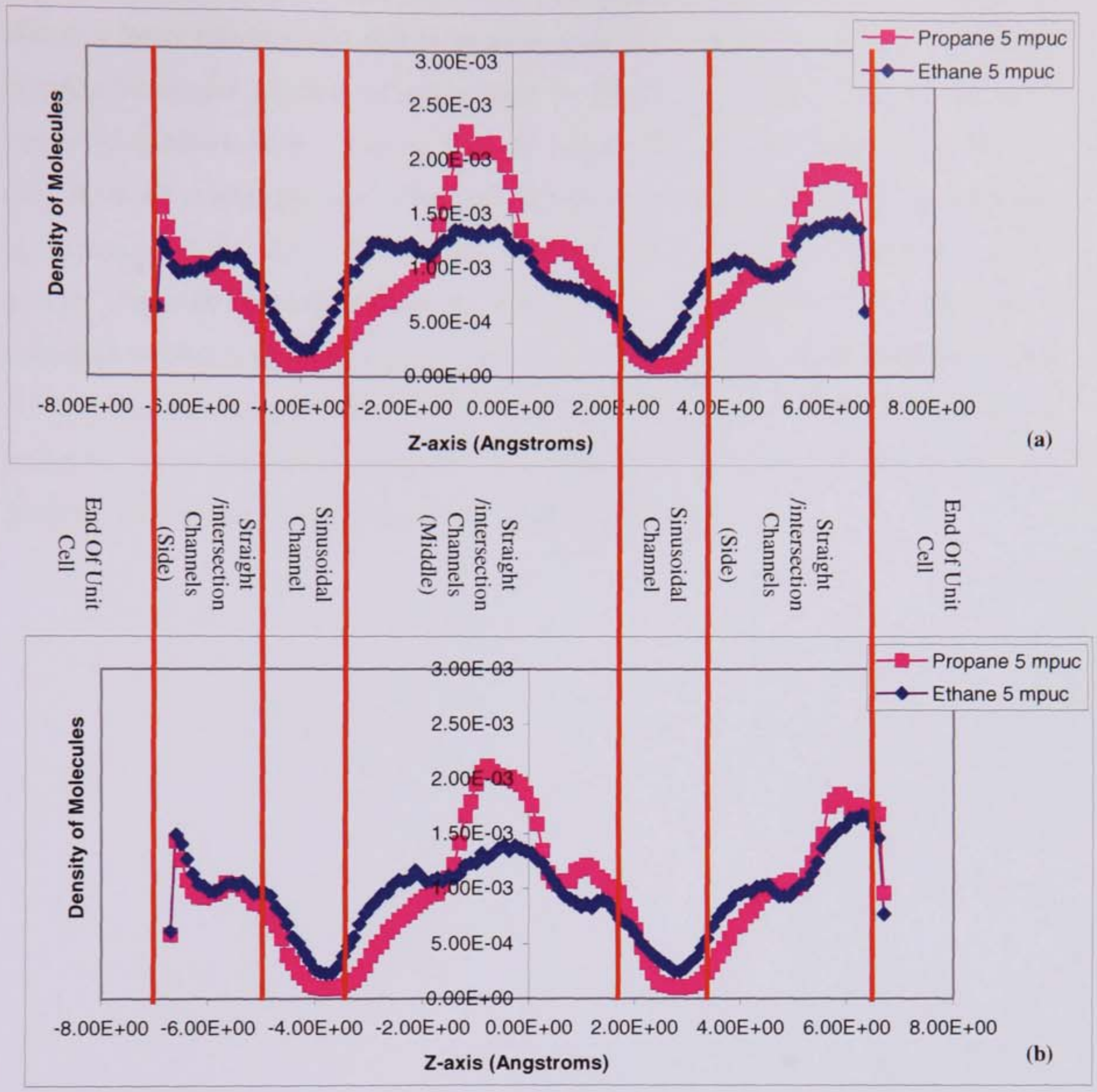

Figure 7.16 The z-density population plots for binary mixture of ethane/propane (5:5) in silicalite-1 at (a) 300 K (b) 400 K.

7.1.2.4 Ternary mixture of methane/ethane/propane

Finally the simulation of a ternary mixture of methane, ethane and propane at a loading of 1:1:1 mpuc was carried out. The calculated self-diffusion coefficients for each of the components in the mixture are shown in Figure 7.4. One striking feature observed in the calculation was the similarities in the calculated diffusion coefficient values for the three components at 300 K. However, at 400 K the order of diffusion coefficients is such that ethane molecule has the highest diffusion coefficients. From the z-density profile plots (Figure 7.17) we observed that all the three molecules are now competing strongly for positions in the middle straight/intersection channel and also to a lesser extent in the side straight/intersection channel. At 300 K methane and propane molecules gaining an upper hand in the middle straight channel while the ethane molecule is now diffusing into the sinusoidal channel. Propane molecule is also observed occupying one of the side straight/intersection channels. On increasing the temperature to 400 K the ethane molecule tended to move rapidly out of the middle straight/intersection channel into the side straight/intersection channel as indicated by the increased ethane peak in the right side sinusoidal channel (Figure 7.17b). This was also apparent in the simulation trajectories obtained for the ternary mixtures where the ethane molecule was able to move with little hindrance from propane and methane molecules via the sinusoidal channels.

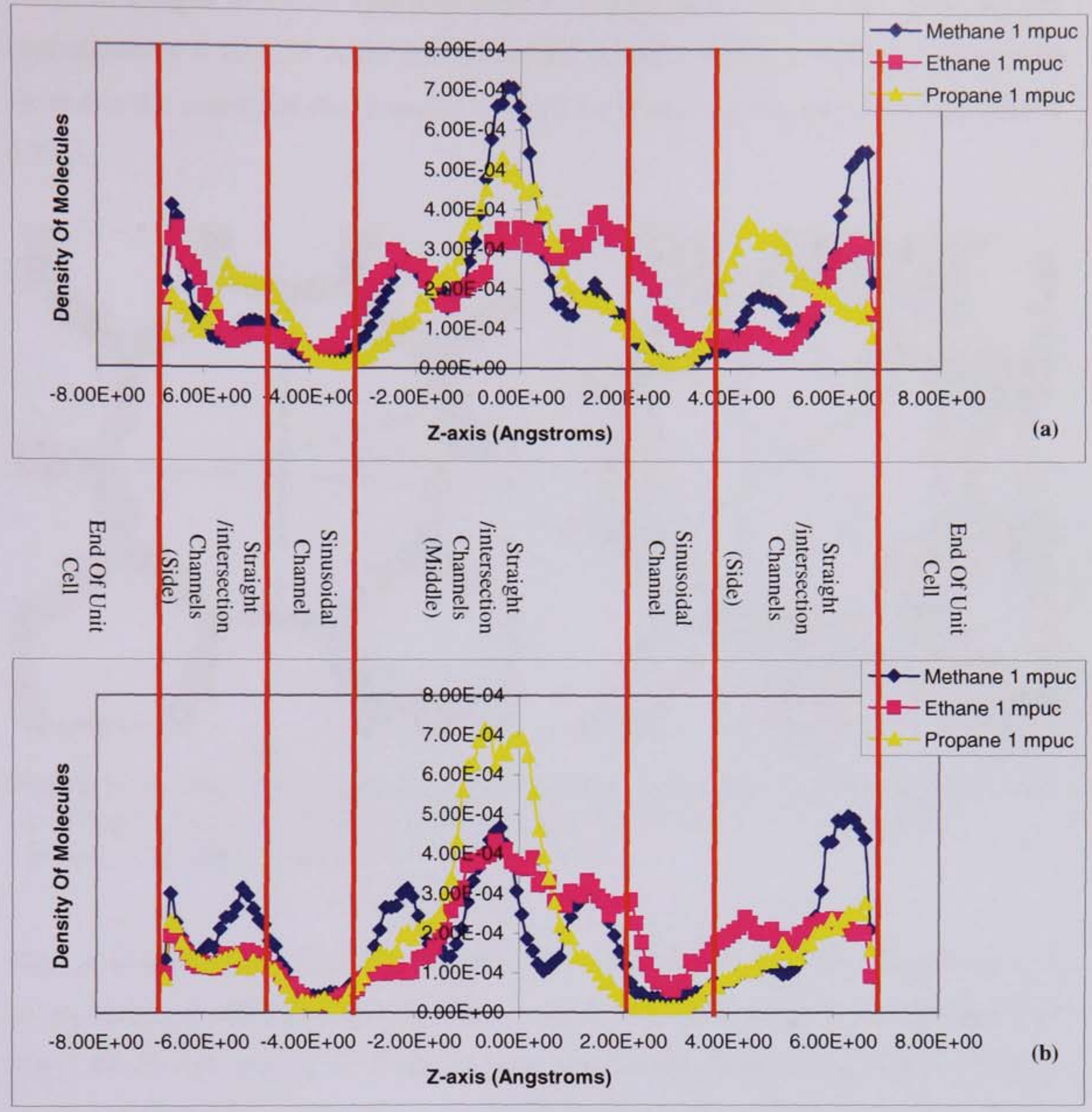

Figure 7.17 The z-density population plots for ternary mixture of methane/ethane/propane (1:1:1) in silicalite-1 at (a) 300 K (b) 400 K.

7.1.3 Radial distribution functions of pure alkanes in silicalite-1

To gain a further understanding of the behaviour of molecules within the silicalite-1 channels, atom-atom radial distribution functions (RDF) have been analysed. The RDF shows the probability density of finding an atom/particle of type ***b*** within a sphere of radius ***r*** around an atom/particle of type ***a***. In the simulations performed using the united atom (UA) CH_4, CH_3 and CH_2 groups the distances were measured from the centres of the united atom groups. It can be seen from Figure 7.18 the channels in the silicalite-1 framework have diameters from the centres of the oxygen atoms to oxygen atoms of approximately 8.11-8.85 Å for the straight channels and approximately 8.10-8.55 Å for the sinusoidal channels and if a molecule were to be located at the centres of the channels it would be found at a distance of approximately 4.25 Å.

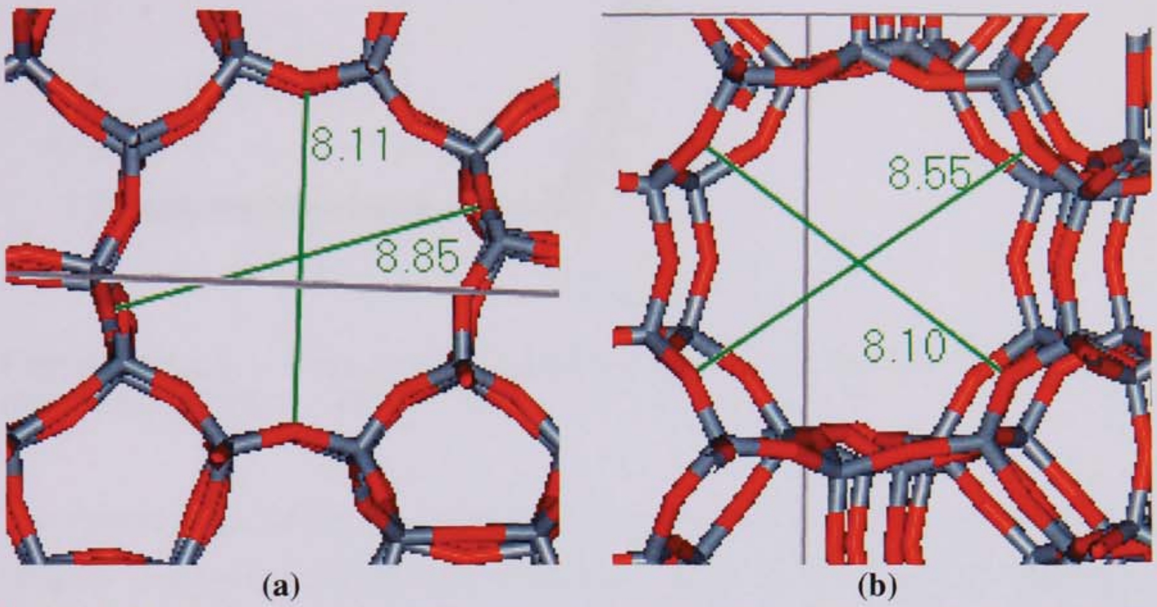

Figure 7.18 Silicalite-1 channel dimensions from centres of oxygen to oxygen atoms (a) Straight Channels (10-rings) viewed down [010] (B-axis), (b) Sinusoidal Channels (10-rings) viewed down [100] (A-axis).

The resulting graphs for the RDF's for simulations of pure components at temperatures of 300 and 400 K for UA --- lattice oxygen can be seen in Figures 7.19 and 7.20. From Figure 7.19 it can be seen that for the methane the CH4 --- O RDF shows a first dominate peak located at 4.28 Å. This value of 4.28 Å clearly indicates that the methane molecules preferentially move along and close to the centres of the channels in silicalite-1.

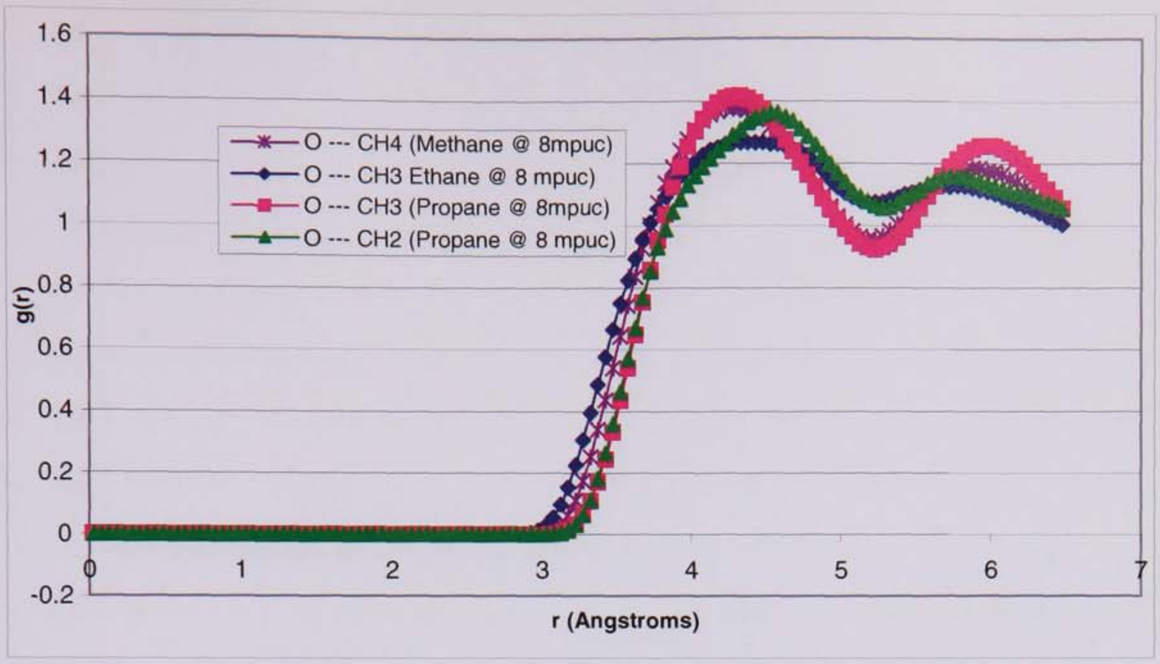

Figure 7.19 UA --- Oxygen radial distribution functions for methane, ethane, and propane in silicalite-1 at 300K.

The second peak, which is located at a distance of approximately 5.83 Å, can be assigned to oxygen atoms in other channels systems in the silicalite-1 framework. Note no other peaks are shown as the potential cut-off was set to 6.5 Å due to periodic boundary conditions. For the ethane the CH3 --- O RDF shows a plateau from 4.28-4.48 Å this once again indicates preferential movement along or close to the centres of the channels. While for the propane molecule The CH3 --- O RDF show a first dominate peak at 4.28 Å followed by a second peak at 5.98 Å whereas the CH2 --- O RDF for propane although showing a similar trend to that of the CH3 --- O has broadening of its peaks this is due to the V nature of the propane molecule. If we can envisage the two CH3 end groups laying close to and along the centres of the channels as a result the CH2 group will be closer to the inner channel wall and due to the rotation of the propane the CH2---O RDF peeks will be more broader and as a result of this the second peak will be much closer than compared with the methane or ethane. A similar trend was seen for all simulations carried out at different temperatures.

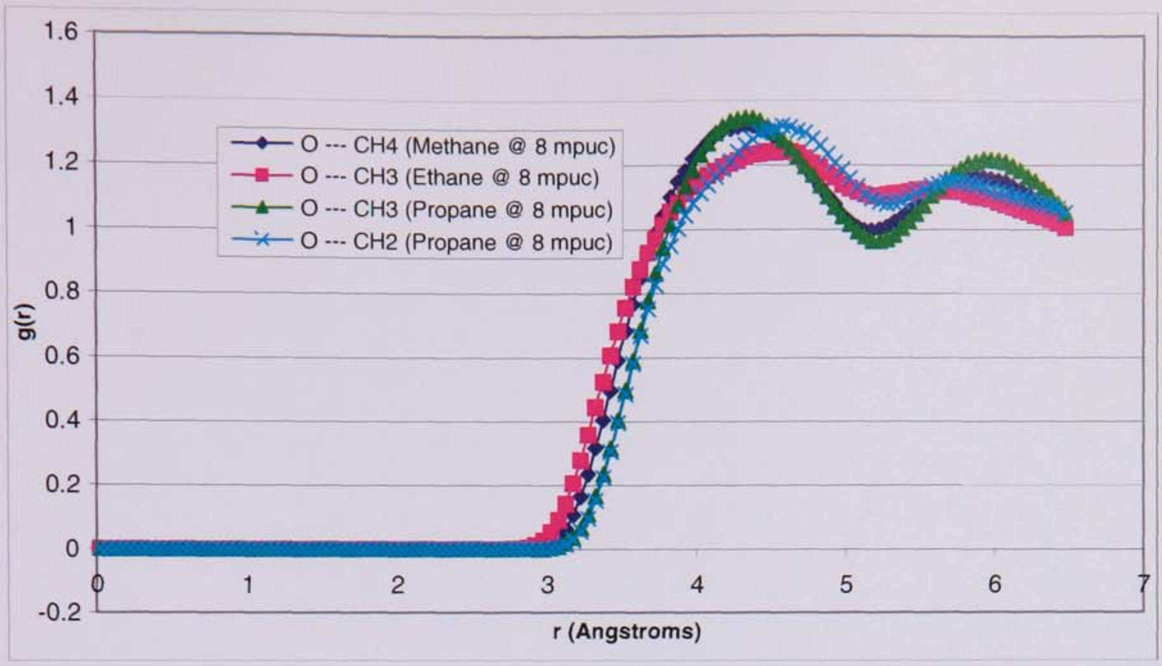

Figure 7.20 UA --- Oxygen radial distribution functions for methane, ethane, and propane in silicalite-1 at 400K.

Chapter 8: Conclusions and Recommendations for Future Work

Chapter 8: Conclusions and Recommendations for Future Work

8.0 Conclusions

Silicalite-1/carbon-graphite, NaA/carbon-graphite composite membranes and blank carbon-graphite membranes have been prepared. It was found that chemical oxidation of the carbon-graphite material was required to obtain a uniform coating of zeolite. But it was also found that zeolite growth did occur on non-oxidized carbon-graphite platforms but the resulting membranes had non-uniform zeolite coverage. For the removal of the templating agent/water from the pores of the zeolites of the composite membranes it was found that the use of air should be avoided as the high temperatures (700°C) required for complete template/water removal from the pores lead to an almost complete decomposition of the carbon-graphite support material.

The separation behaviour of composite membranes towards separating methane, ethane and propane hydrocarbon mixtures was evaluated. It was found that composite membranes grown on 4 h oxidised carbon-graphites (SIL2 and SIL3) had the highest separation selectivities of all the membranes. It was also found that for both binary and ternary gas mixtures at 20°C there was preferential separation selectivity towards the lightest component in the mixtures and generally the magnitude of the separation selectivity depends on the feed gas composition. The blank carbon-graphite membranes showed the highest overall permeation fluxes but lower separation selectivities comparable to that seen for the 24 h oxidized carbon-graphite composite membranes. For the ternary gas mixtures all membranes showed preferential separation selectivity towards the methane regardless of the feed gas composition used.

The influence of temperature was investigated on the separation performance of the composite membranes. For the silicalite-1 composite membranes the pure gas permeances were found to either decrease with increasing temperature or in the cases of methane and propane showed minimums at 60°C but then increased at 100°C. For binary mixtures as the temperature was increased it was observed that for methane/propane and ethane/propane mixtures there was a reversal in the separation selectivity such that the propane was preferentially separated. The effect was found to become more significant with increasing temperature. For methane/ethane mixtures the reversal in the selectivity was found to only occur at 60°C and in increasing the temperature to 100°C the separation selectivities were found to change back towards methane. For the NaA composite membranes it was found that increasing temperatures resulted in a general increase in the pure gas fluxes of all three alkanes. In the binary mixtures the NaA composite membranes showed a separation selectivity towards the larger component but only for binary mixtures of methane/ethane and ethane/propane when the lighter components feed concentration was high (ratio of 9:1).

The bulk adsorption of pure and mixed components of n-alkanes in siliceous LTA, mordenite and silicalite-1 zeolites was investigated using both static and dynamic simulation methods. The predicted sorption sites and energies were in line with previous calculations and experimental work. The use of modified united atom potentials was found to be satisfactory for simulations involving temperature influence and increased molecular loadings per unit cell and in general suitable for molecular dynamics studies. It was found that the modified potentials successfully describe and model the behaviour of sorbed molecules in the three different zeolites studied.

It was found in LTA that methane, ethane and propane were located mainly in the α-cage just off the centre of the 8-ring window. In mordenite, they were found to prefer the 12-ring channel drifting towards the 8-ring side pockets. The centre of this side pocket channel was found to be a favourable site for methane. All the available 10-ring channels in silicalite-1 were found to be suitable sites of adsorption for methane and ethane, but the channel intersection appears to be preferred and most suitable energetically. Propane in silicalite-1, however, has a strong preference for the straight channel and least preference for the sinusoidal channel. The effect of molecular loading appears to have no significant effect on the heats of adsorption and the effect of temperature was also minimal. Preliminary results on the binary and ternary mixed component simulations suggest competitive adsorption in the channels that justify further work using a combination of static and dynamic methods.

Both hydroxylated and non-hydroxylated silicalite-1 and Na-mordenite surface configurations were generated. For the generated silicalite-1 surfaces the most stable surface was found to correspond to the {010} hydroxylated and non-hydroxylated surfaces with low surface energies of 2.010 and 1.532 J/m^2 respectively. For the Na-mordenite surfaces generated the most stable surface was found to correspond to the {010} code 35 non-hydroxylated surface with a surface energy of 0.992 J/m^2. It was interesting to find that the resultant hydroxylated surface ({010} code 35) had the highest surface energy (4.249 J/m^2) of all the Na-mordenite surfaces investigated. In general it was found that the hydroxylated surfaces have higher surface energies compared to their non-hydroxylated counterparts and that the greater the number of surface hydroxyl groups the higher the resultant surface energy.

For the adsorption of hydrocarbons and water onto silicalite-1 {010} surface it was found in general that the hydroxylated surface had the most favourable exothermic adsorption energies and greatest number of different adsorption sites compared to the non-hydroxylated surface which showed large positive adsorption energies indicating an unfavourable endothermic adsorption process.

With the adsorption of hydrocarbons onto the Na-mordenite {010} surface, it was found that both the hydroxylated and non-hydroxylated surfaces had a combination of favourable and non-favourable adsorption energies. While for the adsorption of water it was found that both the hydroxylated and non-hydroxylated surfaces had large favourable exothermic adsorption energies indicating that adsorption of water onto both types of surfaces is a favourable process. In general for the Na-mordenite surface investigated it was found that the adsorbate with the highest number of adsorption sites followed the general trend:

Water > Propane > Ethane > Methane

While for the silicalite-1 surface investigated it was found that the adsorbates followed the general trend:

Propane > Water > Methane > Ethane

The reason for the difference in the two trends is probably due to the fact that silicalite-1 is a purely siliceous zeolite and thus is highly organophilic and thus favourably adsorbs propane at many more sites compared to the other adsorbates investigated. Na-mordenite on the other hand due to the presence of Al and Na within the framework is highly hydrophilic and thus water is more favourably adsorbed and at many more sites compared to hydrocarbon adsorption.

The diffusional behaviour of pure and mixed alkane components in silicalite-1 has been simulated. The use of the modified united atom potential for the simulations was found to be satisfactory as the results are in agreement with the available published experimental and other simulation works.

For the pure component simulation it was found that the increase in temperature resulted in an increase in diffusion coefficients of molecules whereas an increase in molecular loading resulted in an overall decrease in the diffusion coefficients. This trend was observed for all the three alkanes studied.

For the mixed component simulations it is apparent that the influence of the molecular sizes and loadings in the mixtures plays a significant role in their diffusional behaviours and also influences their separations. For molecules of similar sizes e.g. methane/ethane and propane/ethane it was found and reported for the first time the diffusional behaviour of mixed components where molecules in the mixture were undergoing a diffusional reversal role as the loading was increased. This behaviour is attributed to both the size entropy and coupling effect between diffusing species such that at higher loadings (close to saturation) the size entropy effect prevails hence leading to preferential adsorption and easier separation of the smaller component in the mixture.

For binary mixtures with components of different sizes e.g. methane/propane it was observed that the smaller component methane diffuses faster across the entire loading range but with each successive increase in loading there is a general decrease in methane's overall diffusion coefficients compared to that of the propane components. Remarkably the propane's diffusion coefficient remains virtually constant across the entire loading range. This behaviour was attributed to the coupling effect between the components in the mixture.

For the ternary mixture it was observed that at 300 K methane diffuses faster within the channel while at 400 K, the ethane component has the highest diffusion coefficient in the sinusoidal channels, compared to the other components in the mixture.

The radial distribution functions show that all three alkane molecules tend to move along the centres of the channels. Whilst form the z-density plots it is seen all three alkanes have preference for the straight channels and channel intersections compared to that of the sinusoidal channels.

It may be that there are other factors such as lattice vibrations that may contribute and alter the diffusional behaviour of sorbed molecules in the silicalite-1 channels. There is no doubt as shown in this work that the coupling effect between molecules is more pronounced when temperature and loadings are increased.

8.1 Recommendations for future work

Several suggestions for future work are presented in this section:

The first part of this thesis was concerned with the synthesis of composite zeolite membranes followed by an evaluation of there separation abilities towards light linear hydrocarbon mixtures. In the present study the choice of support was a microporous carbon-graphite material which was found to also influence the separation of the hydrocarbons. Thus it is recommended that for future works that either mesoporous or macroporous carbon-graphite be used as a candidate support material which would eliminate separation occurring through the support layer. This would have possible benefits of increased permeation fluxes and separation occurring only through the zeolite layer.

For the evaluation of the composite membranes separation behaviour in this work pure, binary and ternary gas mixtures of methane, ethane and propane were used as feed streams. The separations were also carried out atmospheric pressure and modest temperatures in the range 20 to 100°C. Clearly it is necessary to investigate the separation abilities of these composite zeolite membranes at both operating conditions and with feeds streams containing both hydrocarbon and impurity compositions that are likely to exist in a commercial process. This would give a much clearer indication of composite zeolite membrane abilities to compete with or complement traditional light hydrocarbon separation processes.

It would also be beneficial to synthesis composite zeolite catalytic membrane reactors using zeolites with both different pore sizes ranging from micro to mesopore (H-ZSM5, MCM etc) and with a high concentration of acid sites. A potential usage of such composite zeolite catalytic membrane reactors would be the catalytic upgrading and separation of bio-oil.

The second part of this work was focused on the molecular simulation and modelling of zeolite/adsorbate systems. In this work it has been shown that molecular simulations can be used successfully to gain an understand how adsorbate molecules behave within and on the surfaces of the zeolites.

Surface simulations of zeolite/adsorbate systems are still new and emerging with very few available published works. Of the work available only highly symmetrical purely siliceous zeolite structures have been studied. Thus it is recommended that future simulations be focused on generating stable surfaces of realistic zeolite structures with a greater emphasis on simulation with zeolite structures containing full aluminium and cation compositions. In the current work only pure single component surface adsorption investigations were conducted. It would be more beneficial to simulate with the use of molecular dynamic simulation the adsorption and diffusional behaviour of mixtures of adsorbates at the stable generated surfaces of zeolites. From this the microscopic transport mechanisms at the surfaces of zeolites could be more clearly understood.

Nomenclature

a	Parameter controlling the width of the potential well (equation 3.5)
a_i	Acceleration of species *I* (m/s^2)
A	Surface area (m^2)
A_{ij}	Constant of repulsion between species *i* and *j* (equations 3.1 & 3.3)
b	Actual bond length (Å)
b_{eq}	Equilibrium bond length (Å)
b_0	Ideal bond length (Å)
b_0	Ideal bond length (Å)
B_{ij}	Constant of attraction between species *i* and *j* (equation 3.1)
C_{ij}	Dispersion effects constant (equation 3.3)
d	Distance between two atomic planes in the crystalline phase (Å)
dE	Difference in energy
D	Self diffusivity (m^2/s)
D_{eq}	The potential energy for bond formation
Đ_i	Maxwell–Stefan diffusivity (m^2/s)
Đ_{ij}	Interchange Maxwell–Stefan diffusivity coefficient (m^2/s)
E(latt)	Lattice energy (kJ/mol)
F	Correction factor (dimensionless)
F_i	Force acting on species *i*
K_b	Force constant (equation 3.4)
m_i	Mass of species *i*
n	Order of the diffraction
N_O	Number of occupied adsorption sites
N_T	Total number of possible adsorption sites
$(\text{Pure flux})_A$	Pure single component flux of component A ($mmol/m^2s$)
$(\text{Pure flux})_B$	Pure single component flux of component B ($mmol/m^2s$)
q_{st}	The enthalpy of adsorption (kJ/mol)
r_{ij}	Distance between species *i* and *j* (Å)
t	Time
t_0	Arbitrary starting time

U_b	Energy of an equal number of atoms of the bulk crystal (eV)
$U_{BOND\text{-}STRETCH}$	Harmonic potential energy
U_{BUCKS}	Buckingham potential energy
U_d	Energy of surface block, suitably hydrated (eV)
U_{H2O}	Self energy of bulk water (eV)
U_{LJ}	Lennard-Jones potential energy
U_{MORS}	Morse potential energy
U_s	Energy of the surface block of the crystal (eV)
v_i	Velocity of species i (m/s)
V	Volume of gas adsorbed at a relative pressure (P/P_o) (m^3)
V_m	Volume of gas required to cover entire adsorbing surface with a monomolecular layer (m^3)
W	Weight of adsorbate at a given relative pressure (P/P_o) (grams)
W_m	Weight of adsorbate in a monomolecular layer. (grams)

Greek Letters

$\alpha_{A/B}$	membranes separation selectivity for a binary mixture of components A and B
$\alpha^*_{A/B}$	Ideal separation selectivity
Γ	Thermodynamic correction factor (dimensionless)
Θ_{diff}	Incoming diffraction angle (degrees)
θ	fractional coverage of a surface
Θ_i	Fractional surface occupancy of species i
Θ	Actual bond angle (deg)
Θ_0	Ideal bond angle (deg)
ε	Constant in equation 3.2 (K)
σ	Constant in equation 3.2 (Å)
ρ_{ij}	Constant in equation 3.3
γ	Surface energy ($\mathrm{J/m^2}$)
$\Delta \mathrm{H_f}$	Ethalpy change of formation (kJ/mol)
$\mu(Z)$	potential energy of the zeolite
$\mu(mol)$	Self-energy of the isolated adsorbed molecule.

$\sum_{ij}\frac{q_i q_j}{r_{ij}}$	Term representing sum of all long-range electrostatic interactions for the zeolite lattice and the adsorbate molecule.
$\sum_{ij}V_{ij}$	Two-body potential term representing sum of all short-range interactions.
$\sum_{ijk}V_{ijk}$	Three-body potential term representing sum of all bond bending forces in the zeolite and the adsorbate molecules.
λ	X-ray wavelength (cm^{-1})
y_A	Mole fraction of component A
y_B	Mole fraction of component B

References

(1) DW Breck: Zeolite Molecular Sieves, John Wiley, New York, 1974.

(2) T Masuda, S Otani, T Tsuji, M Kitamura, SR Mukai: Preparation of hydrophilic and acid-proof silicalite-1 zeolite membrane and its application to selective separation of water from water solutions of concentrated acetic acid by pervaporation. Separation and Purification Technology 32 (2003) 181-89.

(3) JA Rabo, MW Schoonover: Early discoveries in zeolite chemistry and catalysis at Union Carbide, and follow-up in industrial catalysis. Applied Catalysis a-General 222 (2001) 261-75.

(4) PB Weisz, VJ Frilette: Intracrystalline and molecular-shape-selective catalysis by zeolite salts. J. Phys. Chem. 64 (1960) 382.

(5) CC Chu, Selective production of para-xylene. Mobil Oil Corporation, United States Patent 4,001,346, 1977.

(6) M Stocker: Gas phase catalysis by zeolites. Microporous and Mesoporous Materials 82 (2005) 257-92.

(7) JD Sherman: Synthetic zeolites and other microporous oxide molecular sieves. Proceedings of the National Academy of Sciences of the United States of America 96 (1999) 3471-78.

(8) Y Morigami, M Kondo, J Abe, H Kita, K Okamoto: The first large-scale pervaporation plant using tubular-type module with zeolite NaA membrane. Separation and Purification Technology 25 (2001) 251-60.

(9) A Nilchi, B Maalek, A Khanchi, M Ghanadi Maragheh, A Bagheri, K Savoji: Ion exchangers in radioactive waste management: Natural Iranian zeolites. Applied Radiation and Isotopes 64 (2006) 138-43.

(10) T Bein: Chem. Mater 8 (1996) 1636.

(11) A Tavolaro, E Drioli: Adv. Mater. 11 (1999) 975.

(12) J Caro, M Noack, P Kolsch, R Schafer: Zeolite membranes - state of their development and perspective. Microporous and Mesoporous Materials 38 (2000) 3-24.

(13) M Matsukata, F Kikuchi: Bull. Chem. Soc. Jpn. 70 (1997).

(14) W Xu, J Dong, J Li, F Wu: J. Chem. Soc., Chem. Commun. (1990) 755.

(15) MW Ackley, SU Rege, H Saxena: Application of natural zeolites in the purification and separation of gases. Microporous and Mesoporous Materials 61 (2003) 25-42.

(16) AF Ismail, LIB David: A review on the latest development of carbon membranes for gas separation. Journal of Membrane Science 193 (2001) 1-18.

(17) DJ Safarik, RB Eldridge: Olefin/paraffin separations by reactive absorption: A review. Industrial & Engineering Chemistry Research 37 (1998) 2571-81.

(18) RB Eldridge: Olefin Paraffin Separation Technology - a Review. Industrial & Engineering Chemistry Research 32 (1993) 2208-12.

(19) S Kulprathipanja, Separation of trans- and cis-olefins. UOP Inc., Des Plaines, I11., U.S.A., 1984.

(20) E Kantner, DW Savage, RJ Bellows, Zeolite composition for use in olefinic separations. Exxon Research & Engineering Co, U.S.A., 1994.

(21) WJW Bakker, F Kapteijn, J Poppe, JA Moulijn: Permeation characteristics of a metal-supported silicalite-1 zeolite membrane. Journal of Membrane Science 117 (1996) 57-78.

(22) RM Barrer: Porous crystal membranes. J. Chem. Soc., Faraday. Trans 86 (1990) 1123-30.

(23) K Tanaka, R Yoshikawa, C Ying, H Kita, K Okamoto: Application of zeolite membranes to esterification reactions. Catal. Today. 67 (2001) 121.

(24) EE McLeary, JC Jansen, F Kapteijn: Zeolite based films, membranes and membrane reactors: Progress and prospects. Micropor. Mesopor. Mater. 90 (2006) 198-220.

(25) H Suzuki, Patent 4699892, United States Patent, 1987.

(26) TC Bowen, RD Noble, JL Falconer: Fundamentals and applications of pervaporation through zeolite membranes. J. Memb. Sci 245 (2004) 1-33.

(27) YS Lin: Microporous and dense inorganic membranes: current status and prospective. Sep. Purif. Technol. 25 (2001) 39-55.

(28) KL Yeung, LTY Au: An investigation of the relationship between microstructure and permeation properties of ZSM-5 membranes. J. Memb. Sci 194 (2001) 33-55.

(29) MP Bernal, J Coronas, M Menendez, J Santamaria: On the effect of morphological features on the properties of MFI zeolite membranes. Micropor. Mesopor. Mater. 60 (2003) 99-110.

(30) A Berenguer-Murcia, J Garcia-Martinez, D Cazorla-Amoros, A Linares-Solano, AB Fuertes: Silicalite-1 membranes supported on porous carbon discs. Microporous and Mesoporous Materials 59 (2003) 147-59.

(31) GTP Mabande, G Pradhan, W Schwieger, M Hanebuth, R Dittmeyer, T Selvam, A Zampieri, H Baser, R Herrmann: A study of Silicalite-1 and Al-ZSM-5 membrane synthesis on stainless steel supports. Microporous and Mesoporous Materials 75 (2004) 209-20.

(32) F Bonhomme, ME Welk, TM Nenoff: CO2 selectivity and lifetimes of high silica ZSM-5 membranes. Microporous and Mesoporous Materials 66 (2003) 181-88.

(33) F Kapteijn, WJW Bakker, GH Zheng, J Poppe, JA Moulijn: Permeation and Separation of Light-Hydrocarbons through a Silicalite-1 Membrane - Application of the Generalized Maxwell-Stefan Equations. Chemical Engineering Journal and the Biochemical Engineering Journal 57 (1995) 145-53.

(34) M Arruebo, J Coronas, M Menendez, J Santamaria: Separation of hydrocarbons from natural gas using silicalite membranes. Separation and Purification Technology 25 (2001) 275-86.

(35) MP Bernal, J Coronas, M Menendez, J Santamaria: Characterization of zeolite membranes by temperature programmed permeation and step desorption. Journal of Membrane Science 195 (2002) 125-38.

(36) J Garcia-Martinez, D Cazorla-Amoros, A Linares-Solano, YS Lin: Synthesis and characterisation of MFI-type zeolites supported on carbon materials. Microporous and Mesoporous Materials 42 (2001) 255-68.

(37) PS Tin, T-S Chung, L Jiang, S Kulprathipanja: Carbon-zeolite composite membranes for gas separation. Letters to the Editor / Carbon 43 (2005) 2025-27.

(38) A Berenguer-Murcia, E Morallon, D Cazorla-Amoros, A Linares-Solano: Preparation of silicalite-1 layers on Pt-coated carbon materials: a possible electrochemical approach towards membrane reactors. Microporous and Mesoporous Materials 78 (2005) 159-67.

(39) M Pan, YS Lin: Template-free secondary growth synthesis of MFI type zeolite membranes. Microporous and Mesoporous Materials 43 (2001) 319-27.

(40) R Ryoo, SH Joo, M Kruk, M Jaroniec: Ordered mesoporous carbons. Advanced Materials 13 (2001) 677-81.

(41) T Kyotani: Control of pore structure in carbon. Carbon 38 (2000) 269-86.

(42) K Okamoto, H Kita, K Horii, K Tanaka, M Kondo: Zeolite NaA membrane: preparation, single-gas permeation, and pervaporation and vapour permeation of water/organic liquid mixtures. Ind. Eng. Chem. Res. 40 (2001) 163.

(43) AWCVd Berg, L Gora, JC Jansen, M Makkee, T Maschmeyer: J. Memb. Sci 224 (2003) 29-37.

(44) AWCVd Berg, L Gora, JC Jansen, T Maschmeyer: Micropor. Mesopor. Mater. 66 (2003) 303-09.

(45) S Yamazaki, K Tsutsumi: Synthesis of A-type zeolite membrane using a plate heater and its formation mechanism. Microporous and Mesoporous Materials 37 (2000) 67-80.

(46) E Kikuchi, K Yamashita, S Hiromoto, K Ueyama, M Matsukata: Synthesis of a zeolitic thin layer by a vapor-phase transport method: appearance of a preferential orientation of MFI zeolite. Microporous Materials 11 (1997) 107-16.

(47) I Kumakiri, T Yamaguchi, S-I Nakao: Preparation of zeolite A and faujasite membranes from a clear solution. Industrial and Engineering Chemistry Research 38 (1999) 4682-88.

(48) I Kumakiri, T Yamaguchi, S-i Nakao: Ind. Eng. Chem. Res. 38 (1999) 4682-88.

(49) K Aoki, K Kusakabe, S Morooka: J. Memb. Sci 141 (1998) 197-205.

(50) K Kusakabe, T Kuroda, A Murata, S Morooka: Ind. Eng. Chem. Res. 36 (1997) 649.

(51) X Zhang, H Liu, TH Wang, AJ Wang, KL Yeung: Modification of carbon membranes and preparation of carbon-zeolite composite membranes with zeolite growth. Carbon 44 (2006) 501-07.

(52) X Zhang, W Zhu, H Liu, TH Wang: Novel tubular composite carbon-zeolite membranes. Materials Letters 58 (2004) 2223-26.

(53) G Xomeritakis, A Gouzinis, S Nair, T Okubo, M He, R Overney, M Tsapatsis: Chem. Eng. Sci. 54 (1999) 3521-31.

(54) MP Bernal, G Xomeritakis, M Tsapatsis: Catal. Today. 67 (2001) 101-07.

(55) LC Boudreau, JA Kuck, M Tsapatsis: J. Memb. Sci 152 (1999) 41-59.

(56) S Mintova, J Hedlund, V Valtchev, B Schoeman, J Sterte: J. Mater. Chem. 10 (1998) 2217.

(57) A Berenguer-Murcia, E Morallon, D Cazorla-Amoros, A Linares-Solano: Preparation of thin silicalite-1 layers on carbon materials by electrochemical methods. Microporous and Mesoporous Materials 66 (2003) 331-40.

(58) B Oonkhanond, ME Mullins: J. Memb. Sci 194 (2001) 3-13.

(59) T Mohammadi, A Pak: Micropor. Mesopor. Mater. 56 (2002) 81-88.

(60) W Shan, Y Zhang, W Yang, C Ke, Z Gao, Y Ye, Y Tang: Electrophoretic deposition of nanosized zeolites in non-aqueous medium and its application in fabricating thin zeolite membranes. Microporous and Mesoporous Materials 69 (2004) 35-42.

(61) Y Han, H Ma, SL Qui, FS Xiao: Preparation of zeolite A membranes by microwave heating. Microporous and Mesoporous Materials 30 (1999) 321-26.

(62) Y Li, H Chen, J Liu, W Yang: Microwave synthesis of LTA zeolite membranes without seeding. Journal of Membrane Science In Press, Corrected Proof.

(63) J Dong, YS Lin, MZ-C Hu, RA Peascoe, EA Payzant: Template-removal-associated microstructural development of porous-ceramic-supported MFI zeolite membranes. Microporous and Mesoporous Materials 34 (2000) 241-53.

(64) S Mintova, J Hedlund, V Valtchev, BJ Schoeman, J Sterte: ZSM-5 films prepared from template free precursors. Journal of Materials Chemistry 8 (1998) 2217-21.

(65) J Hedlund, M Noack, P Kolsch, D Creaser, J Caro, J Sterte: ZSM-5 membranes synthesized without organic templates using a seeding technique. Journal of Membrane Science 159 (1999) 263-73.

(66) EE McLeary, EJW Buijsse, L Gora, JC Jansen, T Maschmeyer: Phil. Trans. R. Soc. A. 363 (2005) 989-1000.

(67) J Hedlund, J Sterte, M Anthonis, AJ Bons, B Carstensen, N Corcoran, D Cox, H Deckman, WD Gijnst, PPd Moor, F Lai, J McHenry, W Mortier, J Reinoso, J Peeters: High flux MFI membranes. Micropor. Mesopor. Mater. 52 (2002) 179.

(68) ZP Lai, G Bonilla, I Diaz, JG Nery, K Sujaoti, MA Amat, E Kokkoli, O Terasaki, RW Thompson, M Tsapatsis, DJ Vlachos: Microstructural optimization of a zeolite membrane for organic vapour separation. Science 300 (2002) 456.

(69) JM van de Graaf, E van der Bijl, A Stol, F Kapteijn, JA Moulijn: Effect of Operating Conditions and Membrane Quality on the Separation Performance of Composite Silicalite-1 Membranes. Ind. Eng. Chem. Res. 37 (1998) 4071-83.

(70) M Arruebo, JL Falconer, RD Noble: Separation of binary C5 and C6 hydrocarbon mixtures through MFI zeolite membranes. Journal of Membrane Science 269 (2006) 171-76.

(71) JM van de Graaf, M Zwiep, F Kapteijn, JA Moulijn: Application of a silicalite-1 membrane reactor in metathesis reactions. Applied Catalysis A: General 178 (1999) 225-41.

(72) L Whitmore, B Slater, CRA Catlow: Adsorption of benzene at the hydroxylated (111) external surface of faujasite. Physical Chemistry Chemical Physics 2 (2000) 5354-56.

(73) SA Ojo, L Whitmore, B Slater, CRA Catlow: Understanding nucleation and growth using computer simulation. Solid State Sciences 3 (2001) 821-26.

(74) B Slater, JO Titiloye, FM Higgins, SC Parker: Atomistic simulation of zeolite surfaces. Current Opinion in Solid State and Materials Science 5 (2001) 417-24.

(75) S Sugiyama, S Yamamoto, O Matsuoka, H Nozoye, J Yu, G Zhu, S Qiu, O Terasaki: AFM observation of double 4-rings on zeolite LTA crystals surface. Microporous and Mesoporous Materials 28 (1999) 1-7.

(76) B Slater, C Richard, A Catlow, Z Liu, T Ohsuna, O Terasaki, MA Camblor: Surface structure and crystal growth of zeolite Beta C. Angewandte Chemie-International Edition 41 (2002) 1235-+.

(77) M Chandross, EB Webb, GS Grest, MG Martin, AP Thompson, MW Roth: Dynamics of exchange at gas-zeolite interfaces I: Pure component n-butane and isobutane. Journal of Physical Chemistry B 105 (2001) 5700-12.

(78) B Jagoda-Cwiklik, L Cwiklik, M Frankowicz: Theoretical study of the influence of confinement and channel blocking on adsorption and diffusion of n-butane in silicalite-1. Applied Surface Science
Fifth International Symposium, Effects on surface heterogeneity in adsorption and catalysis on solids - ISSHAC-V 252 (2005) 699-706.
(79) Y Zhang, S-I Furukawa, T Nitta: Computer simulation studies on gas permeation of propane and propylene across ZSM-5 membranes by a non-equilibrium molecular dynamics technique. Separation and Purification Technology
Seventh International Conference on Inorganic Membranes 32 (2003) 215-21.
(80) J Lin, S Murad: A computer simulation study of the separation of aqueous solutions using thin zeolite membranes. Molecular Physics 99 (2001) 1175-81.
(81) CE Ramachandran, S Chempath, LJ Broadbelt, RQ Snurr: Water adsorption in hydrophobic nanopores: Monte Carlo simulations of water in silicalite. Microporous and Mesoporous Materials
Dedicated to the late Denise Barthomeuf, George Kokotailo and Sergey P. Zhdanov in appreciation of their outstanding contributions to zeolite science 90 (2006) 293-98.
(82) C Beauvais, A Boutin, AH Fuchs: Adsorption of water in zeolite sodium-faujasite: A molecular simulation study. Comptes Rendus Chimie
Crystalline and organized porous solids 8 (2005) 485-90.
(83) FM Higgins, NH de Leeuw, SC Parker: Modelling the effect of water on cation exchange in zeolite A. Journal of Materials Chemistry 12 (2002) 124-31.
(84) JO Titiloye, SC Parker, FS Stone, CRA Catlow: Simulation Studies of the Structure and Energetics of Sorbed Molecules in High-Silica Zeolites .1. Hydrocarbons. Journal of Physical Chemistry 95 (1991) 4038-44.
(85) MAC Nascimento: Computer simulations of the adsorption process of light alkanes in high-silica zeolites. Journal of Molecular Structure-Theochem 464 (1999) 239-47.
(86) R Rungsirisakun, T Nanok, M Probst, J Limtrakul: Adsorption and diffusion of benzene in the nanoporous catalysts FAU, ZSM-5 and MCM-22: A molecular dynamics study. Journal of Molecular Graphics and Modelling 24 (2006) 373-82.
(87) E Garcia-Perez, IM Torrens, S Lago, D Dubbeldam, TJH Vlugt, TLM Maesen, B Smit, R Krishna, S Calero: Elucidating alkane adsorption in sodium-exchanged zeolites from molecular simulations to empirical equations. Applied Surface Science
Fifth International Symposium, Effects on surface heterogeneity in adsorption and catalysis on solids - ISSHAC-V 252 (2005) 716-22.
(88) JP Fox, V Rooy, SP Bates: Simulating the adsorption of linear, branched and cyclic alkanes in silicalite-1 and AlPO4-5. Microporous and Mesoporous Materials 69 (2004) 9-18.
(89) JMB Ndjaka, G Zwanenburg, B Smit, M Schenk: Molecular simulations of adsorption isotherms of small alkanes in FER-, TON-, MTW- and DON-type zeolites. Microporous and Mesoporous Materials 68 (2004) 37-43.
(90) R Krishna, D Paschek: Molecular simulations of adsorption and siting of light alkanes in silicalite-1. Physical Chemistry Chemical Physics 3 (2001) 453-62.

(91) JM van Baten, R Krishna: Entropy effects in adsorption and diffusion of alkane isomers in mordenite: An investigation using CBMC and MD simulations. Microporous and Mesoporous Materials 84 (2005) 179-91.

(92) P Demontis, ES Fois, GB Suffritti, S Quartieri: Molecular-Dynamics Studies on Zeolites .4. Diffusion of Methane in Silicalite. Journal of Physical Chemistry 94 (1990) 4329-34.

(93) P Demontis, GB Suffritti, ES Fois, S Quartieri: Molecular-Dynamics Studies on Zeolites .6. Temperature-Dependence of Diffusion of Methane in Silicalite. Journal of Physical Chemistry 96 (1992) 1482-90.

(94) S Fritzsche, M Wolfsberg, R Haberlandt: The importance of various degrees of freedom in the theoretical study of the diffusion of methane in silicalite-1. Chemical Physics 289 (2003) 321-33.

(95) F Leroy, B Rousseau, AH Fuchs: Self-diffusion of n-alkanes in silicalite using molecular dynamics simulation: A comparison between rigid and flexible frameworks. Physical Chemistry Chemical Physics 6 (2004) 775-83.

(96) DI Kopelevich, HC Chang: Does lattice vibration drive diffusion in zeolites? Journal of Chemical Physics 114 (2001) 3776-89.

(97) R Krishna, JA Wesselingh: The Maxwell-Stefan approach to mass transfer. Chemical Engineering Science 52 (1997) 861-911.

(98) LJP Vandenbroeke, R Krishna: Experimental-Verification of the Maxwell-Stefan Theory for Micropore Diffusion. Chemical Engineering Science 50 (1995) 2507-22.

(99) R Krishna, JM van Baten: Linking the loading dependence of the Maxwell-Stefan diffusivity of linear alkanes in zeolites with the thermodynamic correction factor. Chemical Physics Letters 420 (2006) 545-49.

(100) R Krishna, JM van Baten: Influence of isotherm inflection on the diffusivities of C5-C8 linear alkanes in MFI zeolite. Chemical Physics Letters 407 (2005) 159-65.

(101) TJH Vlugt, W Zhu, F Kapteijn, JA Moulijn, B Smit, R Krishna: Adsorption of linear and branched alkanes in the silicalite-1. Journal of the American Chemical Society 120 (1998) 5599-600.

(102) R Krishna, R Baur: Analytic solution of the Maxwell-Stefan equations for multicomponent permeation across a zeolite membrane. Chemical Engineering Journal 97 (2004) 37-45.

(103) R Krishna, D Paschek: Verification of the Maxwell-Stefan theory for tracer diffusion in zeolites. Chemical Engineering Journal 85 (2002) 7-15.

(104) R Krishna: Predicting transport diffusivities of binary mixtures in zeolites. Chemical Physics Letters 355 (2002) 483-89.

(105) MJ Sanborn, RQ Snurr: Diffusion of binary mixtures of CF4 and n-alkanes in faujasite. Separation and Purification Technology 20 (2000) 1-13.

(106) R Krishna: Diffusion of binary mixtures across zeolite membranes: Entropy effects on permeation selectivity. International Communications in Heat and Mass Transfer 28 (2001) 337-46.

(107) F Kapteijn, JA Moulijn, R Krishna: The generalized Maxwell-Stefan model for diffusion in zeolites: sorbate molecules with different saturation loadings. Chemical Engineering Science 55 (2000) 2923-30.

(108) JM van de Graaf, F Kapteijn, JA Moulijn: Modeling permeation of binary mixtures through zeolite membranes. Aiche Journal 45 (1999) 497-511.

(109) R Krishna, TJH Vlugt, B Smit: Influence of isotherm inflection on diffusion in silicalite. Chemical Engineering Science 54 (1999) 1751-57.

(110) GW Meindersma, AB de Haan: Economical feasibility of zeolite membranes for industrial scale separations of aromatic hydrocarbons. Desalination 149 (2002) 29-34.

(111) V Van Hoof, L Van den Abeele, A Buekenhoudt, C Dotremont, R Leysen: Economic comparison between azeotropic distillation and different hybrid systems combining distillation with pervaporation for the dehydration of isopropanol. Separation and Purification Technology 37 (2004) 33-49.

(112) AB Hinchliffe, KE Porter: A comparison of membrane separation and distillation. Chemical Engineering Research & Design 78 (2000) 255-68.

(113) M Born, K Huang: Dynamical Theory of Crystal Lattices, Oxford University Press, Oxford, 1954.

(114) MP Allen, DJ Tildesley: Computer simulation of liquids, Clarendon Press, Oxford, 1989.

(115) DE Parry: The electrostatic potential in the surface region of an ionic crystal. Surface Science 49 (1975) 433–40.

(116) BG Dick, AW Overhauser: Phys. Rev. 112 (1958) 90.

(117) B Smit: Simulating the Adsorption-Isotherms of Methane, Ethane, and Propane in the Zeolite Silicalite. Journal of Physical Chemistry 99 (1995) 5597-603.

(118) JP Ryckaert, A Bellemans: Molecular-Dynamics of Liquid Alkanes. Faraday Discussions (1978) 95-106.

(119) RL June, AT Bell, DN Theodorou: Molecular-Dynamics Studies of Butane and Hexane in Silicalite. Journal of Physical Chemistry 96 (1992) 1051-60.

(120) WL Jorgensen, JD Madura, CJ Swenson: Optimized Intermolecular Potential Functions for Liquid Hydrocarbons. Journal of the American Chemical Society 106 (1984) 6638-46.

(121) MJ Sanders, M Leslie, CRA Catlow: Interatomic Potentials for Sio2. Journal of the Chemical Society-Chemical Communications (1984) 1271-73.

(122) NH de Leeuw, SC Parker: Molecular Dynamics simulation of MgO surfaces in liquid water using a shell model potential for water. Physical Review B 58 (1998) 13901–08.

(123) CRA Catlow: Proc. Royal Soc. London, Ser. A, 1977, 353, 533.

(124) JE Post, CW Burnham: Ionic Modeling of Mineral Structures and Energies in the Electron-Gas Approximation - Tio2 Polymorphs, Quartz, Forsterite, Diopside. American Mineralogist 71 (1986) 142-50.

(125) NH de Leeuw, SC Parker: Surface-water interactions in the dolomite problem. Physical Chemistry Chemical Physics 3 (2001) 3217-21.

(126) TR Forrester, W Smith, DLPOLY Package, CCLRC, Daresbury Laboratory, Daresbury, UK, 1993.

(127) GW Watson, ET Kelsey, NH deLeeuw, DJ Harris, SC Parker: Atomistic simulation of dislocations, surfaces and interfaces in MgO. Journal of the Chemical Society-Faraday Transactions 92 (1996) 433-38.

(128) PW Tasker, The surface energies, surface tensions and surface structure of the alkali halide crystals., Philosophical Magazine A, 1979, p. 119–36.

(129) FM Higgins-Bos: Towards cation exchange; atomistic simulation study of zeolites, University of Bath, 2000.

(130) ZH Duan, N Moller, JH Weare: Molecular-Dynamics Simulation of Water Properties Using Rwk2 Potential - from Clusters to Bulk Water. Geochimica Et Cosmochimica Acta 59 (1995) 3273-83.

(131) JH Harding, NC Pyper: The Meaning of the Oxygen 2nd-Electron Affinity and Oxide Potential Models. Philosophical Magazine Letters 71 (1995) 113-21.

(132) RK Iler: The chemistry of silica; solubility polymerisation, colloid and surface properties, and biochemistry, John Wiley, New York, 1979.

(133) RC Weast, MJ Astle: CRC Handbook of chemistry and physics, CRC Boca Raton, 1981.

(134) SA Greenberg: Thermodynamic functions for the solution of silica in water. J Phys Chem 61 (1957) 196-97.

(135) S Brunauer, LS Deming, WS Deming, E Teller: On a Theory of the van der Waals Adsorption of Gases. J. Amer. Chem. Soc. 62 (1940) 1723.

(136) I Langmuir: The adsorption of gases on plane surfaces of glass, mica and platinum. J. Amer. Chem. Soc. 40 (1918) 1361 - 403.

(137) I Langmuir: Vapour pressures, evaporation, condensation and adsorption. J. Amer. Chem. Soc. 54 (1932) 2798 - 832.

(138) S Brunauer, P Emmett, E Teller: Adsorption of Gases in Multimolecular Layers. J. Amer. Chem. Soc. 60 (1938) 309.

(139) RW Grose, EM Flanigen., United States Patent 4,061,724, United States, 1977.

(140) RW Thompson, MJ Huber: Analysis of the Growth of Molecular-Sieve Zeolite Naa in a Batch Precipitation System. Journal of Crystal Growth 56 (1982) 711-22.

(141) H Kalipcilar, A Culfaz: Synthesis of submicron silicalite-1 crystals from clear solutions. Crystal Research and Technology 35 (2000) 933-42.

(142) W Zhu, F Kapteijn, Bvd Linden, JA Moulijn: Equilibrium adsorption of linear and branched C-6 alkanes on silicalite-1 studied by the tapered element oscillating microbalance. Phys. Chem. Chem. Phys. 3 (2001) 1755-61.

(143) DW Savage, Process for the separation of contaminants from feed streams using magnetic beds, United States Patent 4283204, 1981.

(144) S Brunauer, PH Emmett, E Teller: Adsorption of Gases in Multimolecular Layers. J. Am. Chem. Soc 60 (1938) 309-19.

(145) MM Dubinin, LV Radushkevich: Proc. Acad. Sci. USSR 55 (1947) 331.

(146) G Horvath, K Kawazoe: Method for the calculation of effective pore size distribution in molecular sieve carbon. J. Chem. Eng. Japan 16 (1983) 470-75.

(147) C Moreno-Castilla, F Carrasco-Marin, FJ Maldonado-Hodar, J Rivera-Utrilla: Effects of non-oxidant and oxidant acid treatments on the surface properties of an activated carbon with very low ash content. Carbon 36 (1998) 145-51.

(148) C Baerlocher, WM Meier, DH Olson: Atlas of Zeolite Framework Types, Elsevier, New York, 2001.

(149) JN Watson, AS Brown, LE Iton, JW White: Detection of TPA-silicalite precursors nucleated during the room temperature aging of a clear homogeneous synthesis solution. Journal of the Chemical Society-Faraday Transactions 94 (1998) 2181-86.

(150) BJ Zhang, SA Davis, NH Mendelson, S Mann: Bacterial templating of zeolite fibres with hierarchical structure. Chemical Communications (2000) 781-82.

(151) Z Wang, ML Larsson, M Grahn, A Holmgren, J Hedlund: Zeolite coated ATR crystals for new applications in FTIR-ATR spectroscopy. Chemical Communications (2004) 2888-89.

(152) YN Huang, EA Havenga: Why do zeolites with LTA structure undergo reversible amorphization under pressure? Chemical Physics Letters 345 (2001) 65-71.

(153) EM Flanigen, H Khatami, HA Szymanski: Molecular Sieve Zeolites. ACS Ser. 101 (1971) 201.

(154) T Kyotani, N Shimotsuma, S Kakui: FTIR-ATR study of the surface of a tubular zeolite NaA membrane ultrasonically reacted with water and acetic acid. Analytical Sciences 22 (2006) 325-27.

(155) V Crupi, D Majolino, V Venuti: Diffusional and vibrational dynamics of water in NaA zeolites by neutron and Fourier transform infrared spectroscopy. Journal of Physics-Condensed Matter 16 (2004) S5297-S316.

(156) I Hussain, JO Titiloye: Molecular dynamics simulations of the adsorption and diffusion behavior of pure and mixed alkanes in silicalite. Microporous and Mesoporous Materials 85 (2005) 143-56.

(157) B Beagley, JO Titiloye: Modeling the Similarities and Differences between the Sodalite Cages (Beta-Cages) in the Generic Materials - Sodalite, Zeolites of Type-a, and Zeolites with Faujasite Frameworks. Structural Chemistry 3 (1992) 429-48.

(158) RW Triebe, FH Tezel, KC Khulbe: Adsorption of methane, ethane and ethylene on molecular sieve zeolites. Gas Separation & Purification 10 (1996) 81-84.

(159) HJF Stroud, NG Parsonage, Molecular Sieve Zeolites-II, 1971, p. 138-43.

(160) DM Ruthven, KF Loughlin, RI Derrah, Molecular Sieves, 1973, p. 330-44.

(161) CE Webster, A Cottone, RS Drago: Multiple equilibrium analysis description of adsorption on Na-mordenite and H-mordenite. Journal of the American Chemical Society 121 (1999) 12127-39.

(162) YH Ma, C Mancel, Molecular Sieves, 1973, p. 392-402.

(163) TJH Vlugt, R Krishna, B Smit: Molecular simulations of adsorption isotherms for linear and branched alkanes and their mixtures in silicalite. Journal of Physical Chemistry B 103 (1999) 1102-18.

(164) JR Hufton, RP Danner: Chromatographic Study of Alkanes in Silicalite - Equilibrium Properties. Aiche Journal 39 (1993) 954-61.

(165) TA Nijhuis, LJP van den Broeke, MJG Linders, M Makkee, F Kapteijn, JA Moulijn: Modeling of the transient sorption and diffusion processes in microporous materials at low pressure. Catalysis Today 53 (1999) 189-205.

(166) R Krishna, D Paschek: Separation of hydrocarbon mixtures using zeolite membranes: a modelling approach combining molecular simulations with the Maxwell-Stefan theory. Separation and Purification Technology 21 (2000) 111-36.

(167) J Caro, M Bulow, W Schirmer, J Karger, W Heink, H Pfeifer, SP Zdanov: Microdynamics of Methane, Ethane and Propane in Zsm-5-Type Zeolites. Journal of the Chemical Society-Faraday Transactions I 81 (1985) 2541-50.

(168) AK Nowak, CJJ Denouden, SD Pickett, B Smit, AK Cheetham, MFM Post, JM Thomas: Mobility of Adsorbed Species in Zeolites - Methane, Ethane, and Propane Diffusivities. Journal of Physical Chemistry 95 (1991) 848-54.

(169) D Dumont, D Bougeard: A Molecular-Dynamics Study of Hydrocarbons Adsorbed in Silicalite. Zeolites 15 (1995) 650-55.

(170) R Krishna, D Paschek: Self-diffusivities in multicomponent mixtures in zeolites. Physical Chemistry Chemical Physics 4 (2002) 1891-98.

(171) L Bolton (BP). (2003). Challenges in separations: A perspective from the petrochemical industry. Crystal Faraday Partnership Separations Workshop, St Albans, 3-4 April 2003.

Appendix A – Scanning Electron Microscopy Pictures

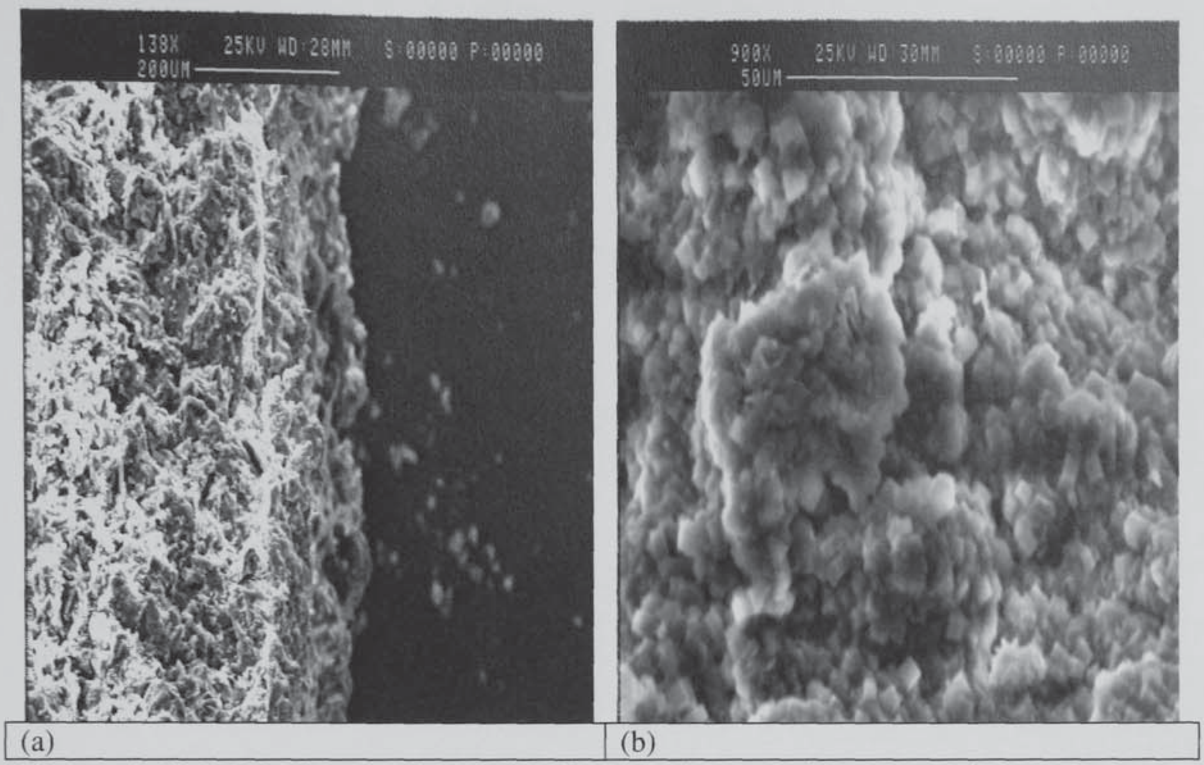

(a) (b)

Figure A.1 SEM micrographs of silicalite-1/carbon-graphite composite membrane SIL1: (a) Cross section view; (b) Top view.

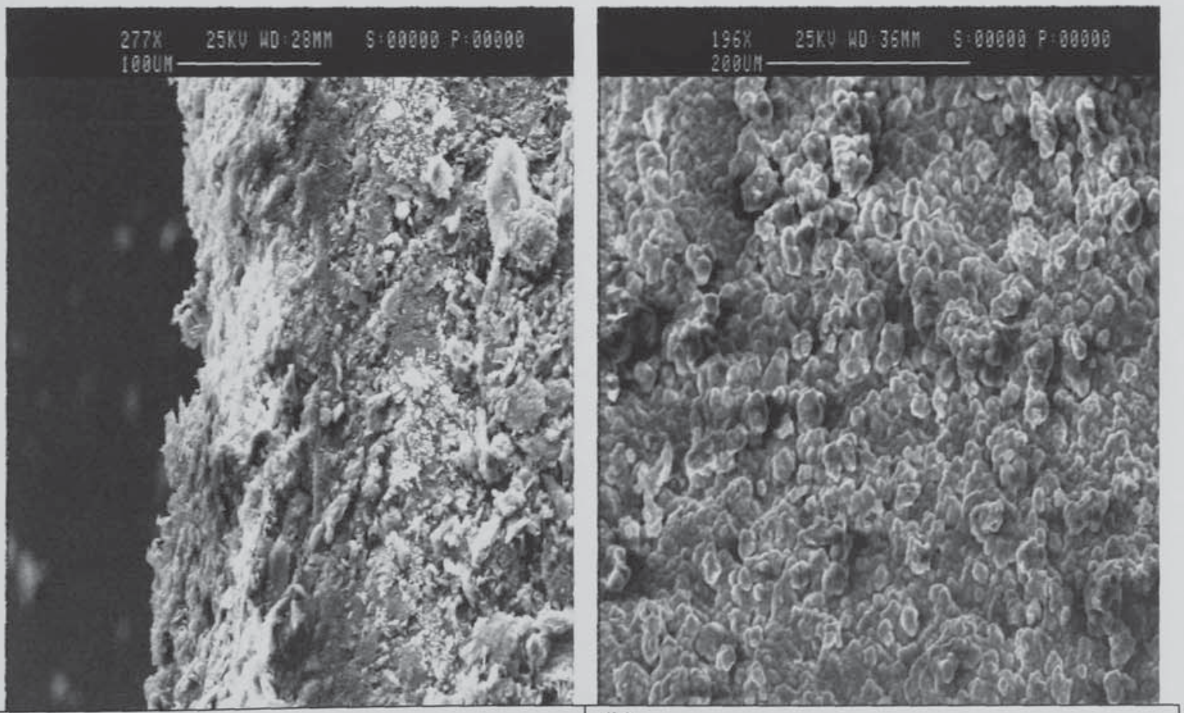

(a) (b)

Figure A.2 SEM micrographs of silicalite-1/carbon-graphite composite membrane SIL2: (a) Cross section view; (b) Top view.

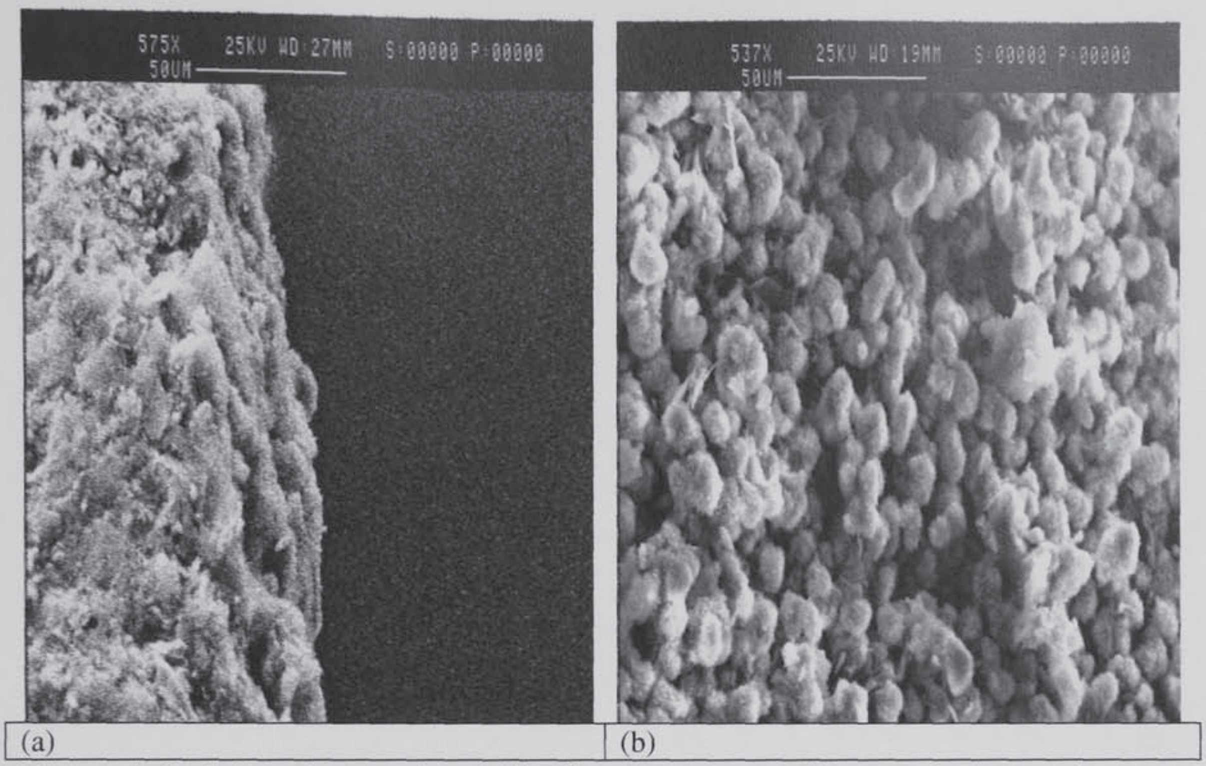

(a) (b)

Figure A.3 SEM micrographs of silicalite-1/carbon-graphite composite membrane SIL5: (a) Cross section view; (b) Top view.

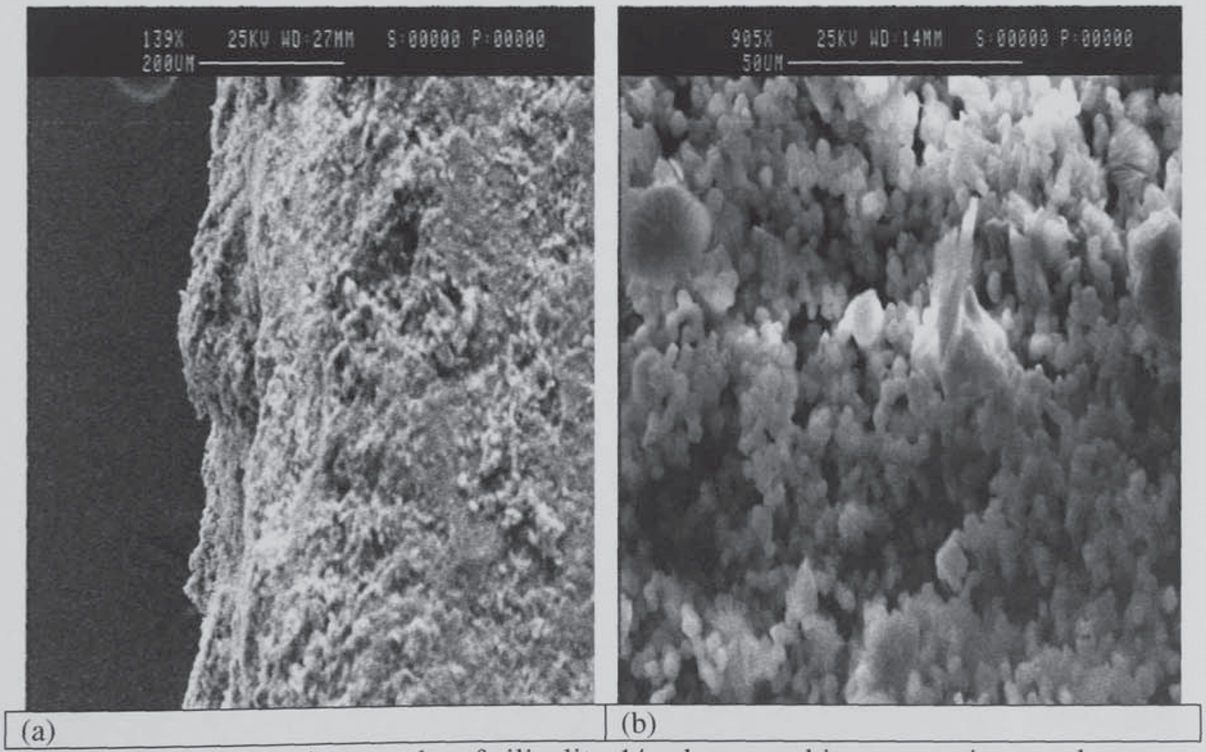

(a) (b)

Figure A.4 SEM micrographs of silicalite-1/carbon-graphite composite membrane SIL6: (a) Cross section view; (b) Top view.

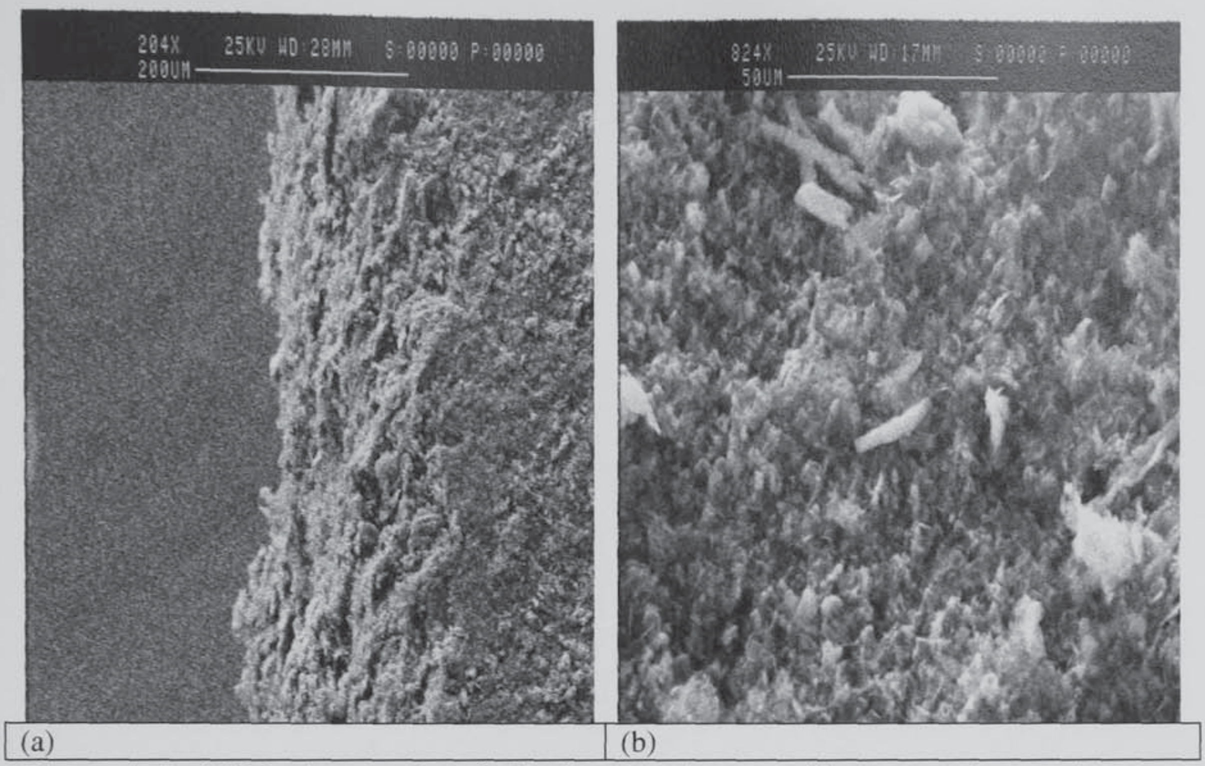

(a) (b)

Figure A.5 SEM micrographs of silicalite-1/carbon-graphite composite membrane SIL8: (a) Cross section view; (b) Top view.

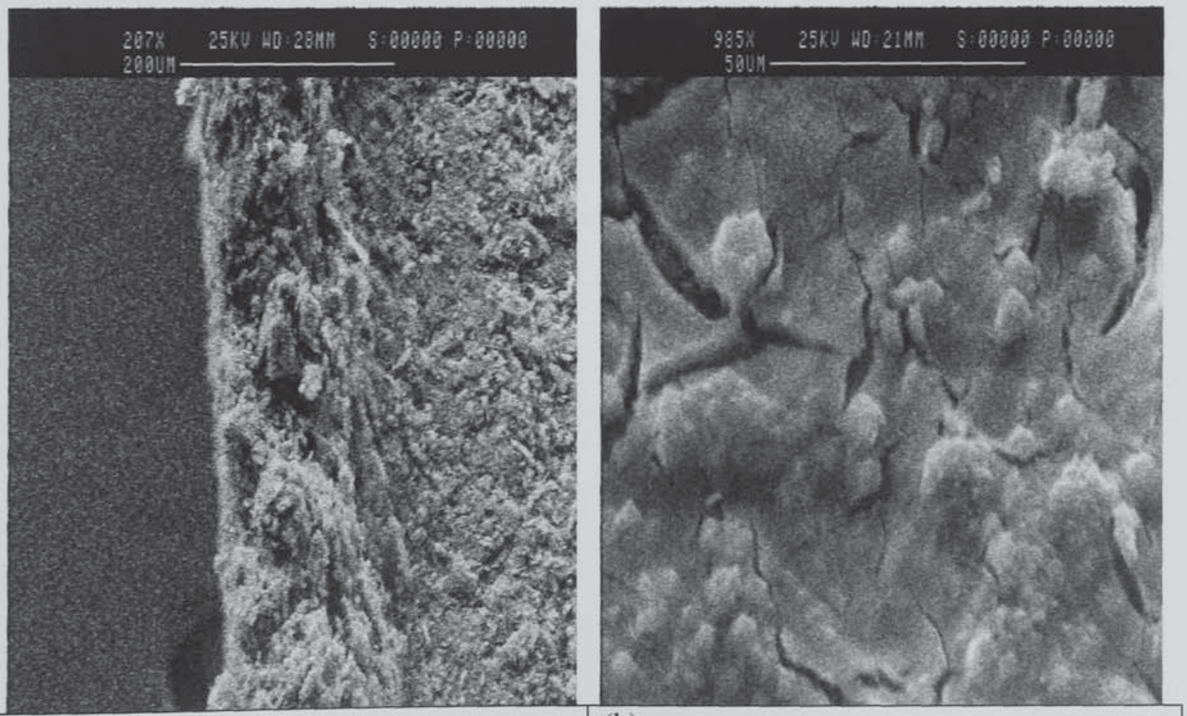

(a) (b)

Figure A.6 SEM micrographs of silicalite-1/carbon-graphite composite membrane SIL9: (a) Cross section view; (b) Top view.

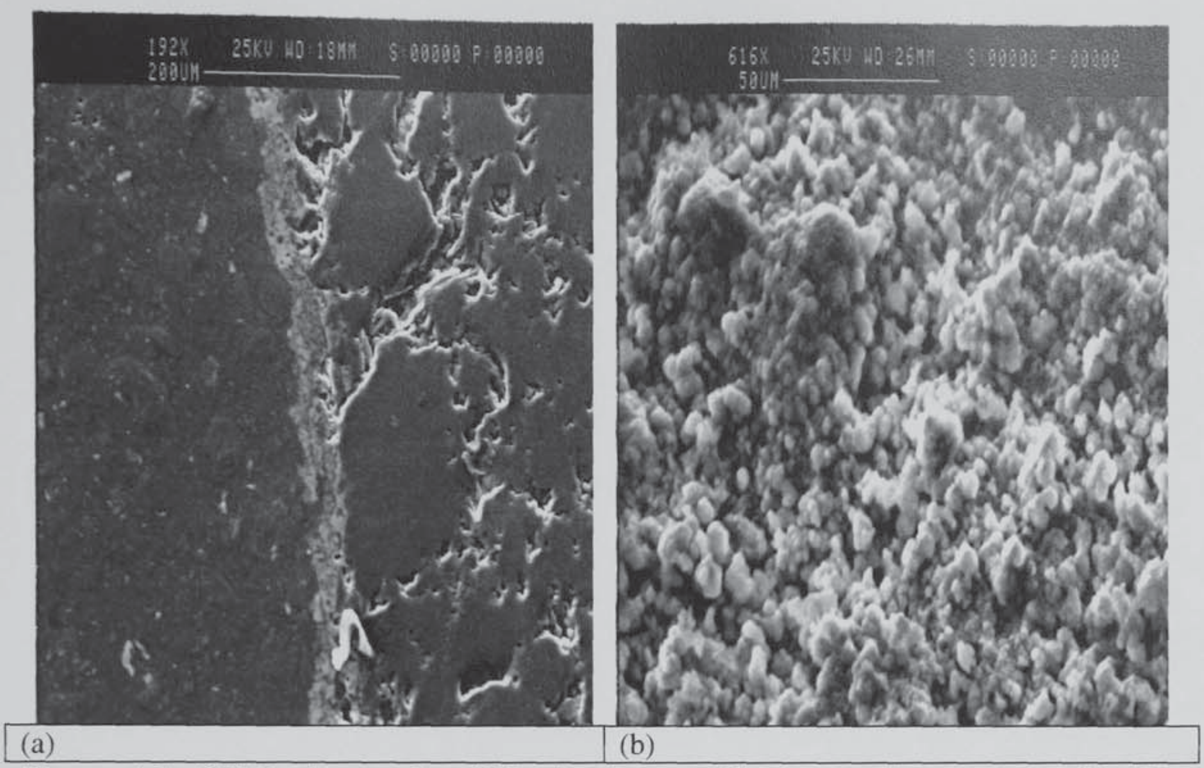

Figure A.7 SEM micrographs of NaA/carbon-graphite composite membrane NaA2: (a) Cross section view; (b) Top view.

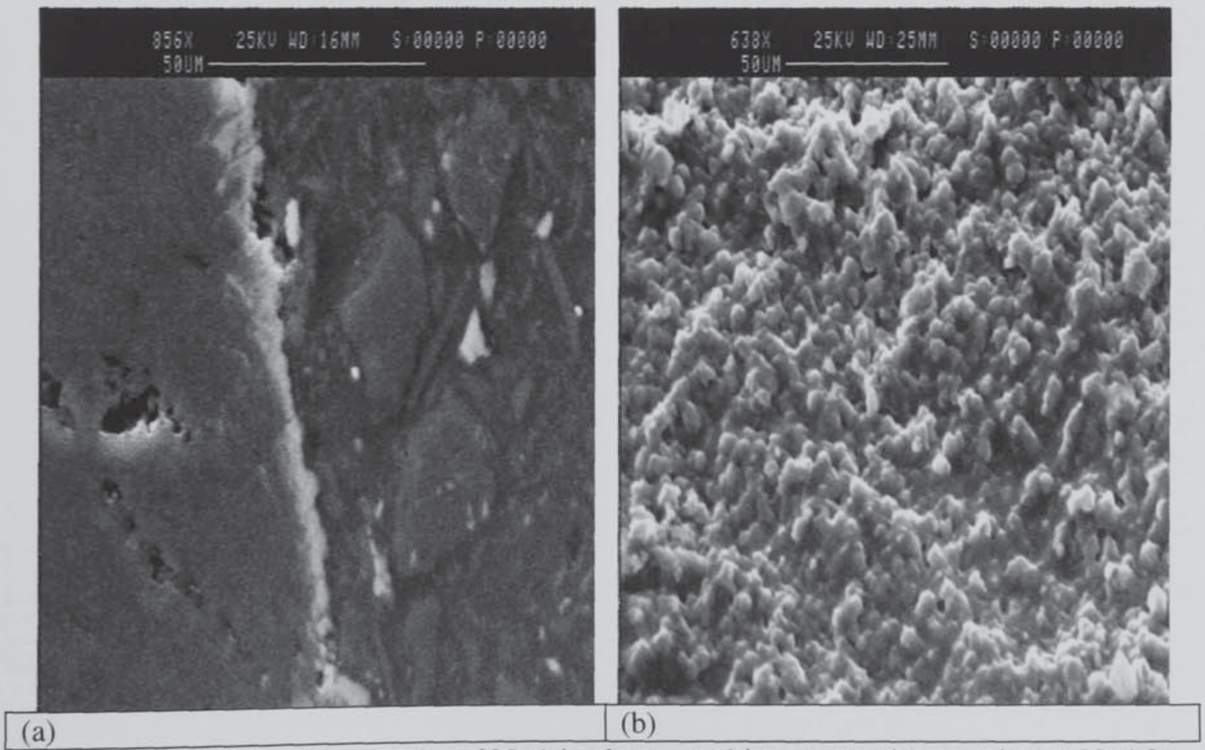

Figure A.8 SEM micrographs of NaA/carbon-graphite composite membrane NaA3: (a) Cross section view; (b) Top view.

Appendix B – XRD Diffractograms

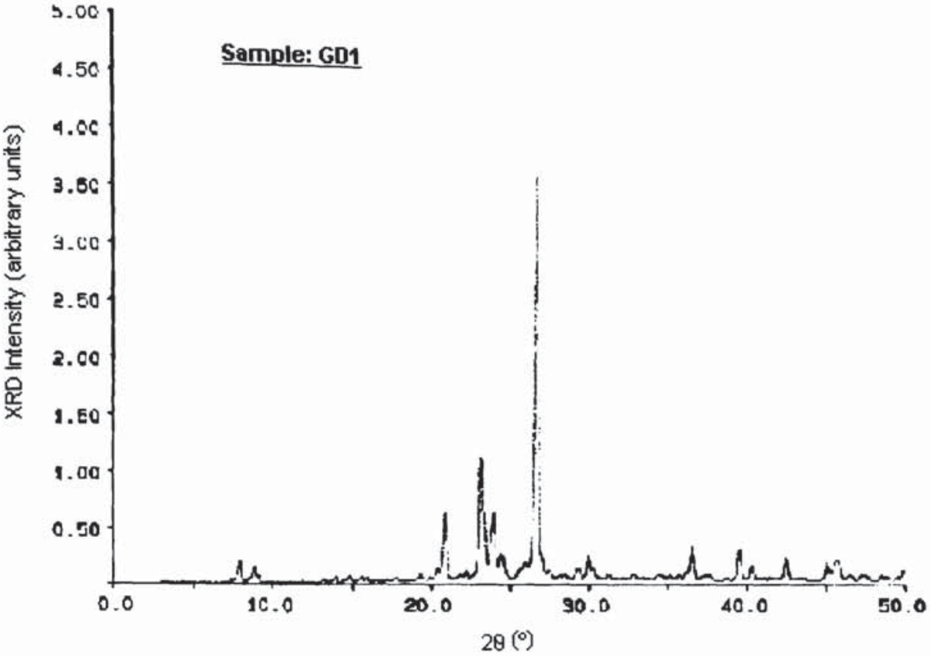

Figure B.1 XRD pattern for the synthesized silicalite-1 powder (Sample: SIL1)

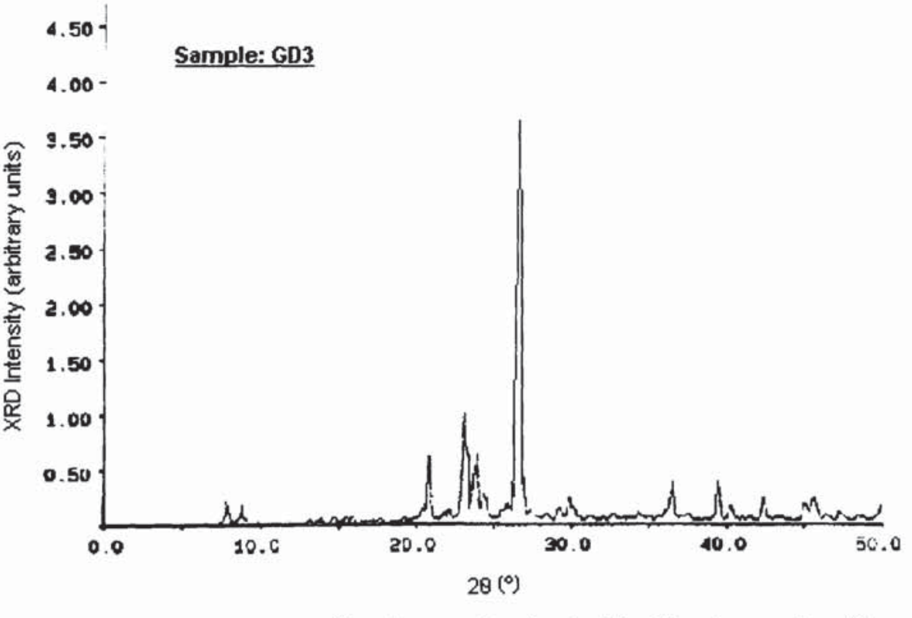

Figure B.2 XRD pattern for the synthesized silicalite-1 powder (Sample: SIL3)

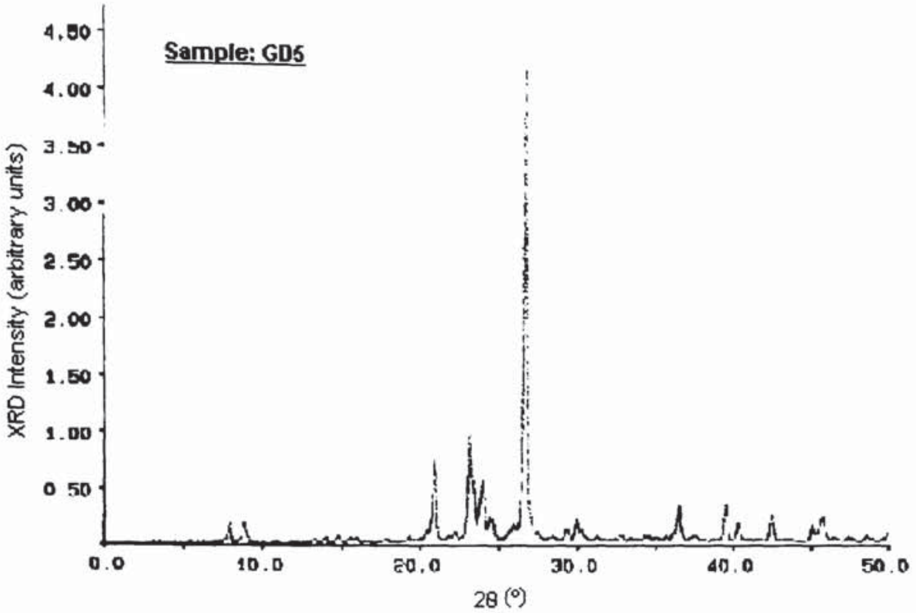

Figure B.3 XRD pattern for the synthesized silicalite-1 powder (Sample: SIL5)

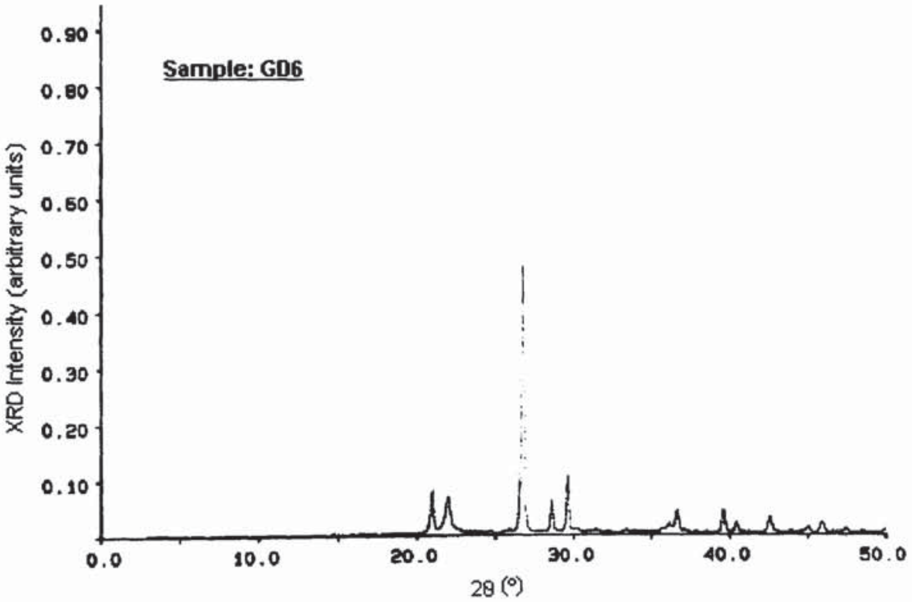

Figure B.4 XRD pattern for the synthesized silicalite-1 powder (Sample: SIL6)

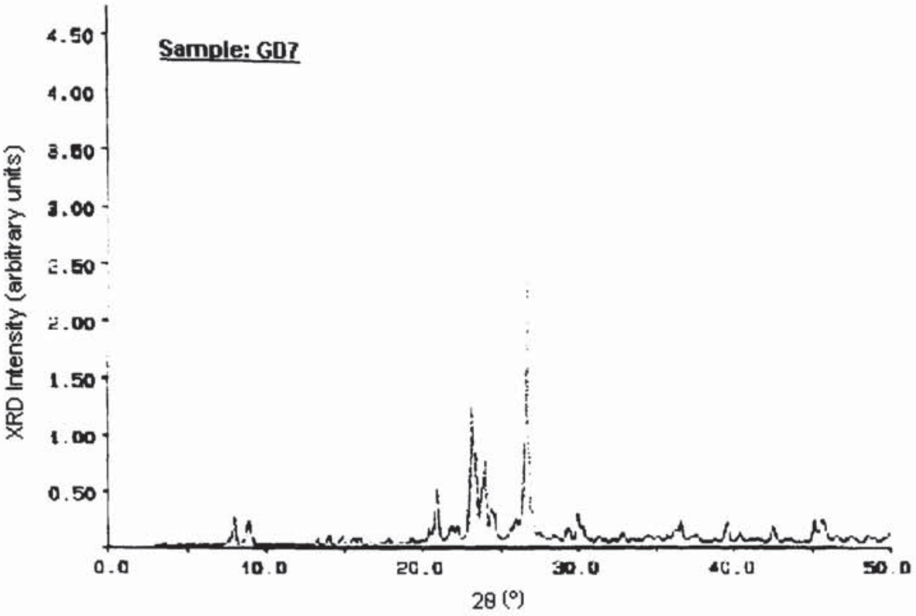

Figure B.5 XRD pattern for the synthesized silicalite-1 powder (Sample: SIL7)

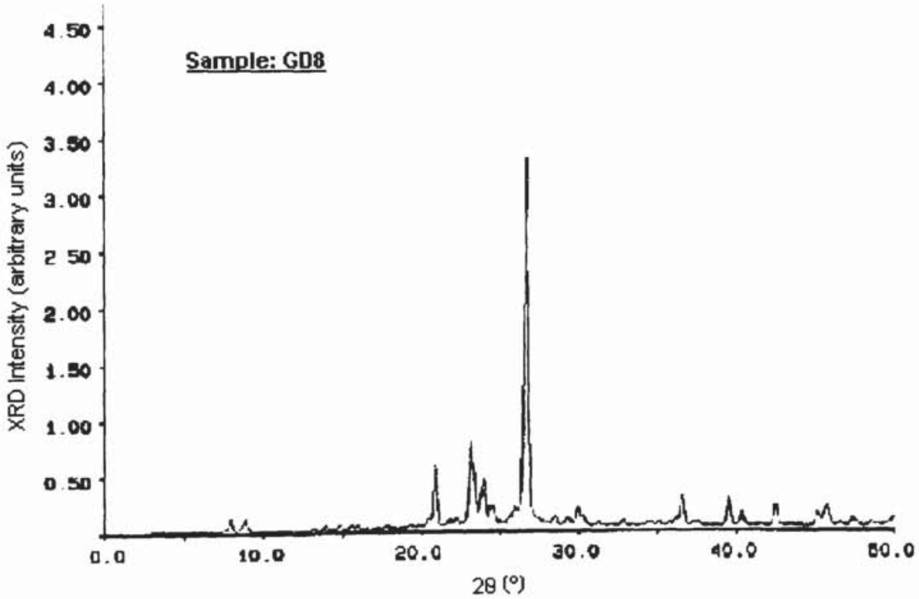

Figure B.6 XRD pattern for the synthesized silicalite-1 powder (Sample: SIL8)

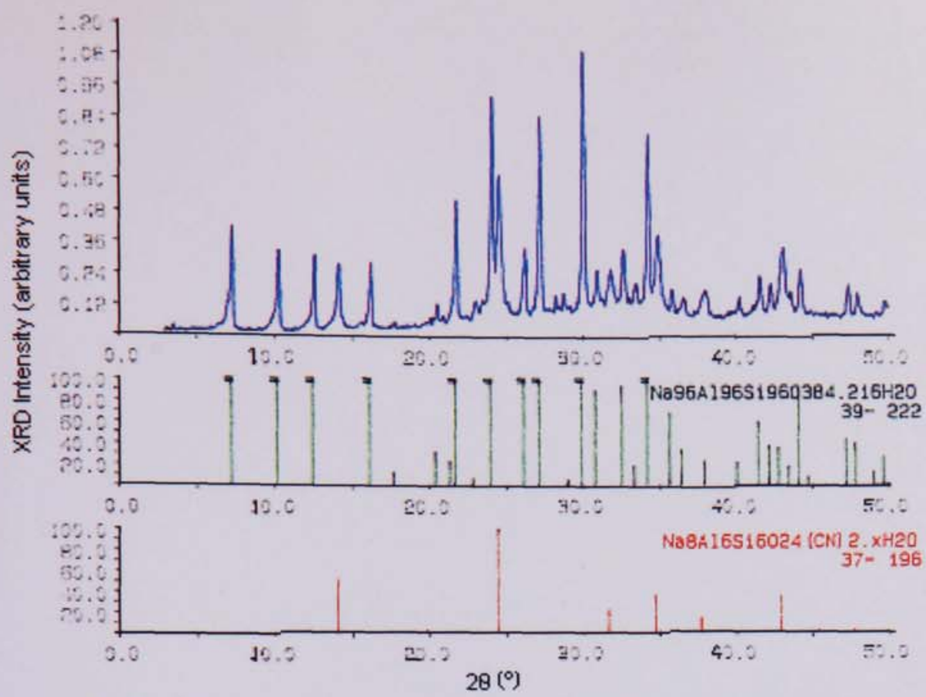

Figure B.7 XRD pattern for the synthesized NaA powder (Sample: NaA1)

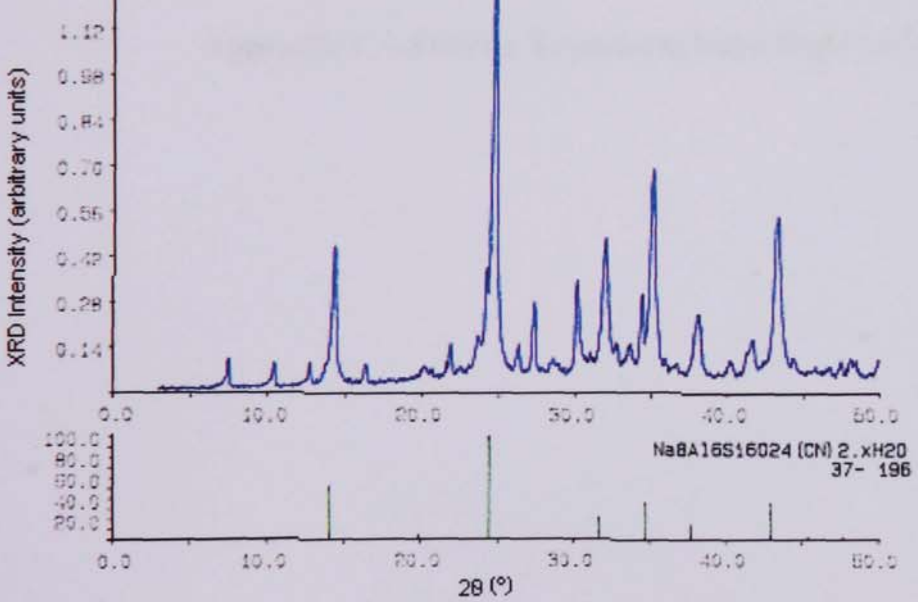

Figure B.8 XRD pattern for the synthesized NaA powder (Sample: NaA2)

Appendix C – Fourier Transform Infra Red Curves

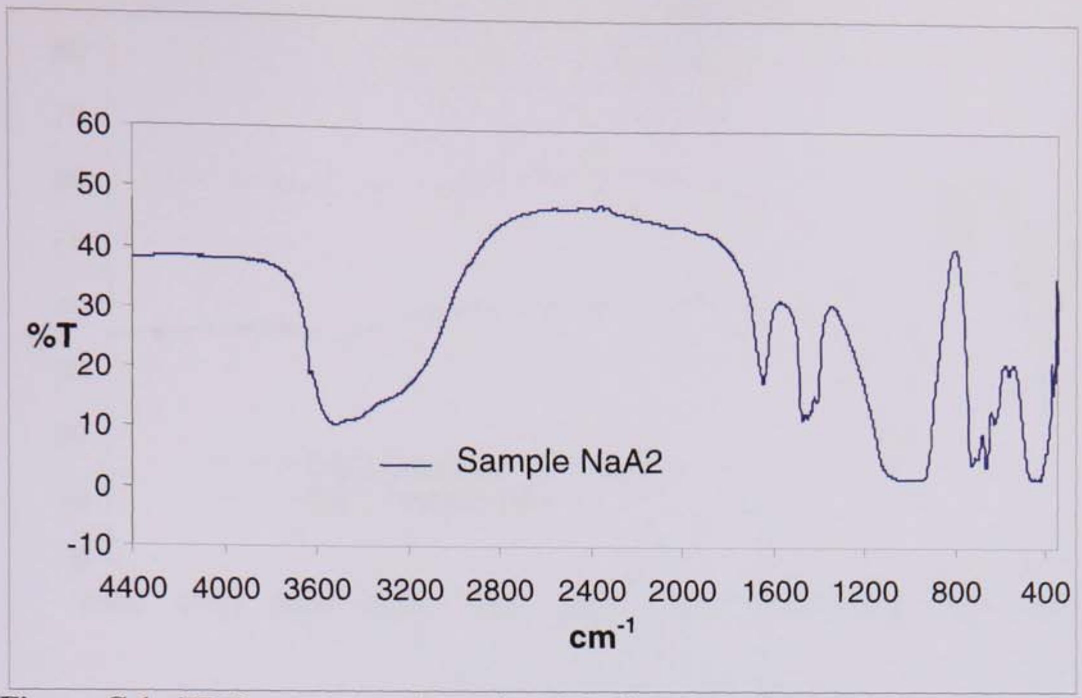

Figure C.1 FTIR spectrum of powder taken from sample NaA2. Experiment conducted at room temperature and atmospheric pressure.

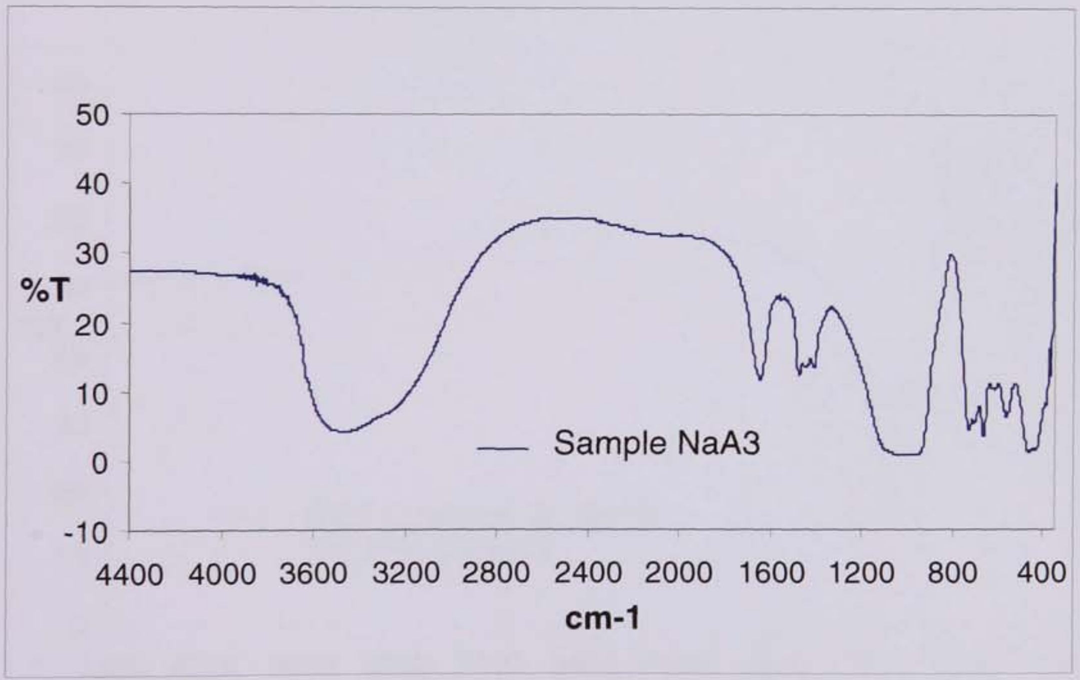

Figure C.2 FTIR spectrum of powder taken from sample NaA3. Experiment conducted at room temperature and atmospheric pressure.

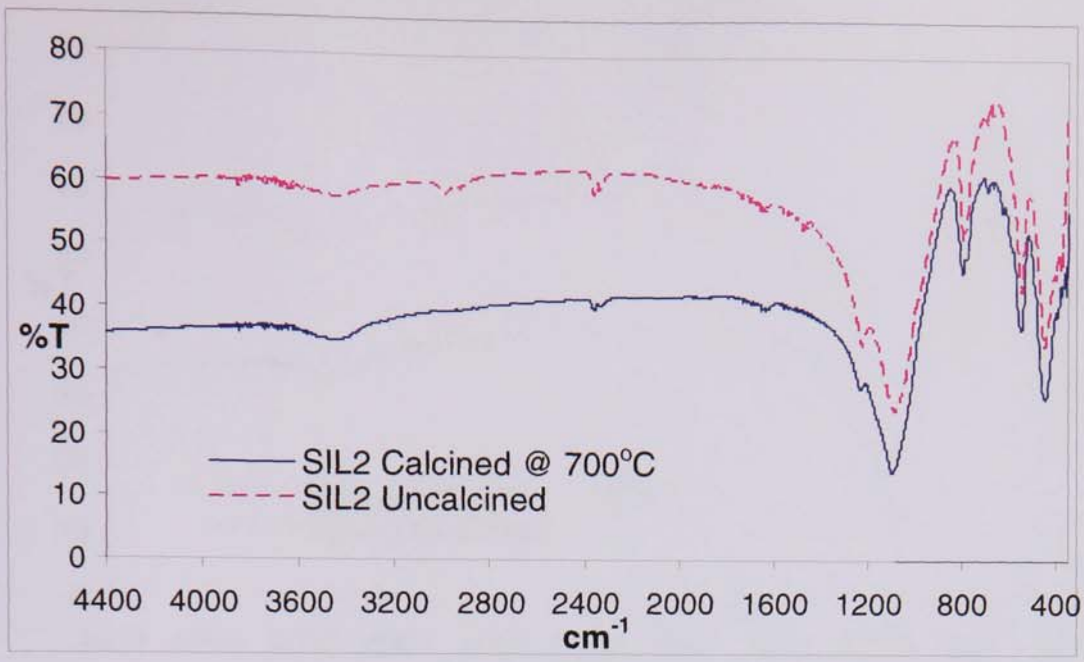

Figure C.3 FTIR spectrum of powder taken from sample SIL2. Experiment conducted at room temperature and atmospheric pressure.

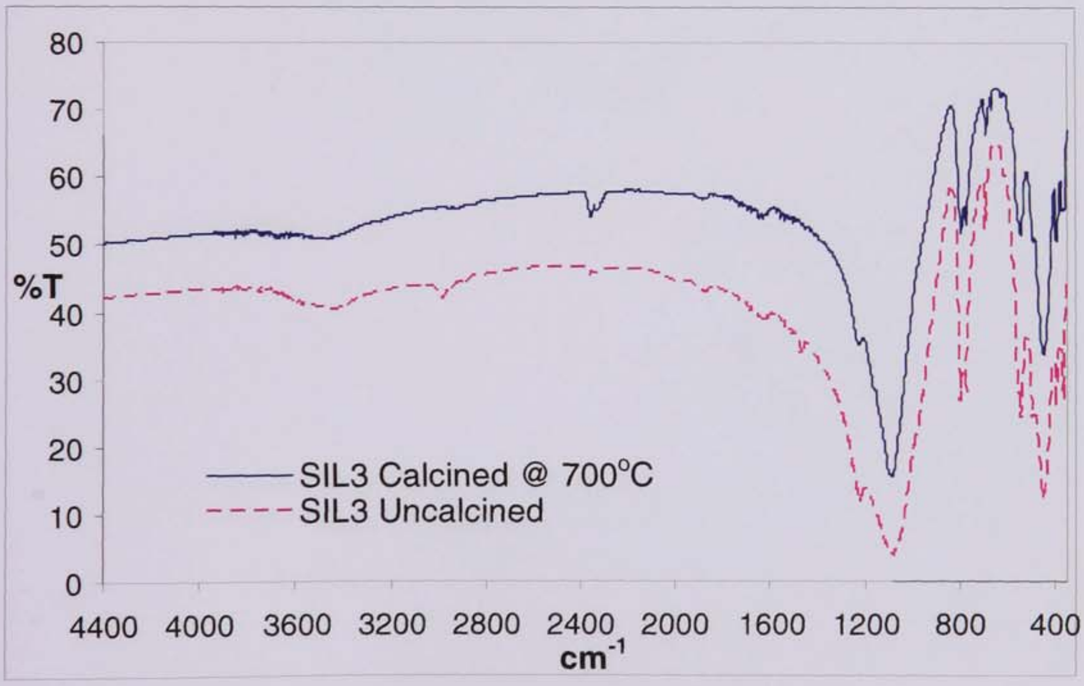

Figure C.4 FTIR spectrum of powder taken from sample SIL3. Experiment conducted at room temperature and atmospheric pressure.

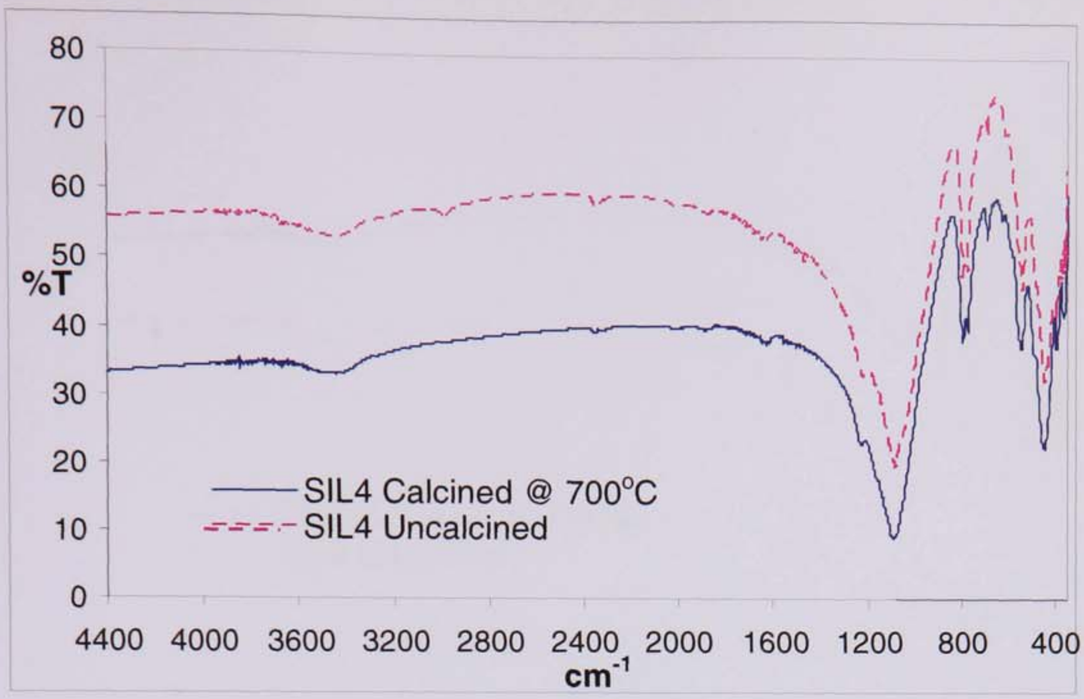

Figure C.5 FTIR spectrum of powder taken from sample SIL4. Experiment conducted at room temperature and atmospheric pressure.

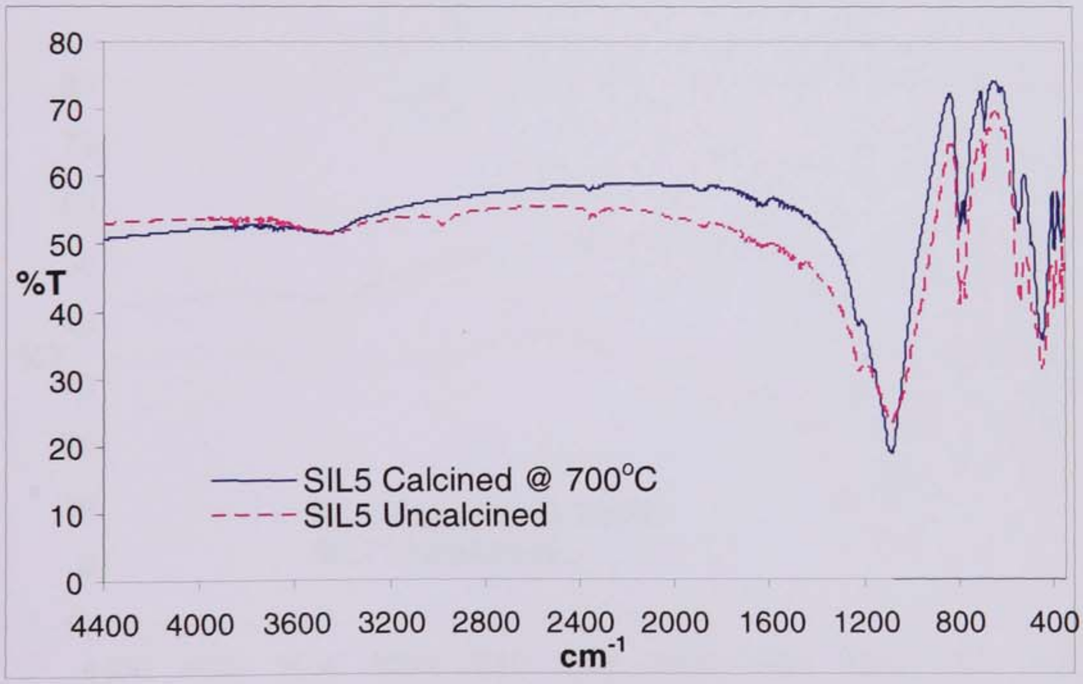

Figure C.6 FTIR spectrum of powder taken from sample SIL5. Experiment conducted at room temperature and atmospheric pressure.

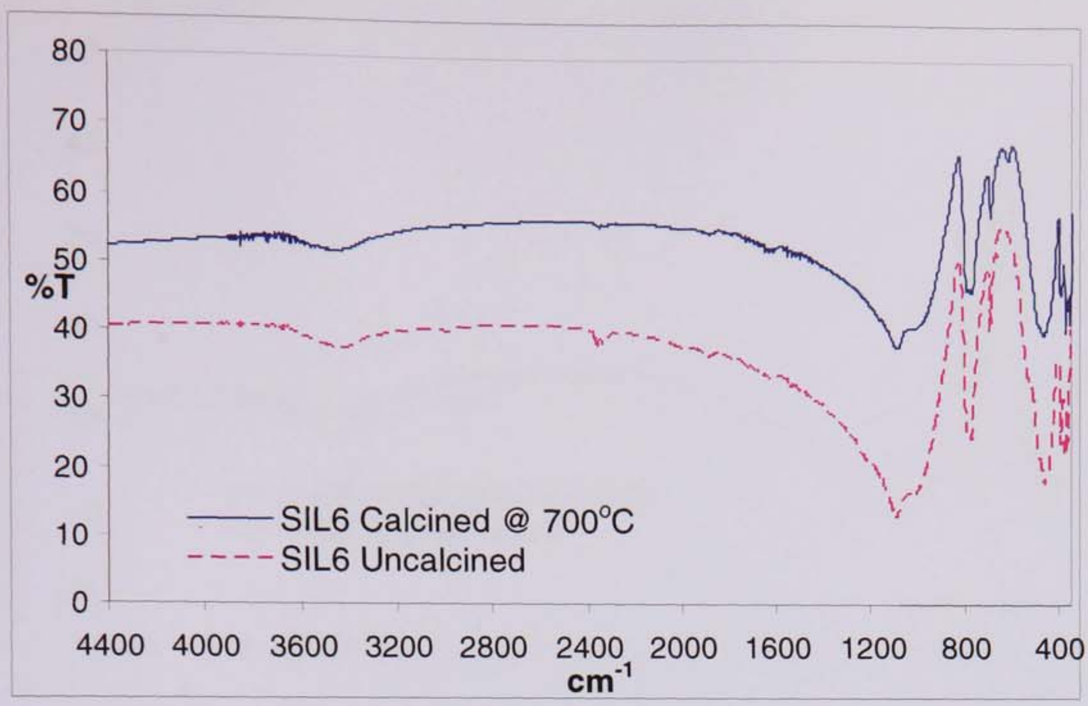

Figure C.7 FTIR spectrum of powder taken from sample SIL6. Experiment conducted at room temperature and atmospheric pressure.

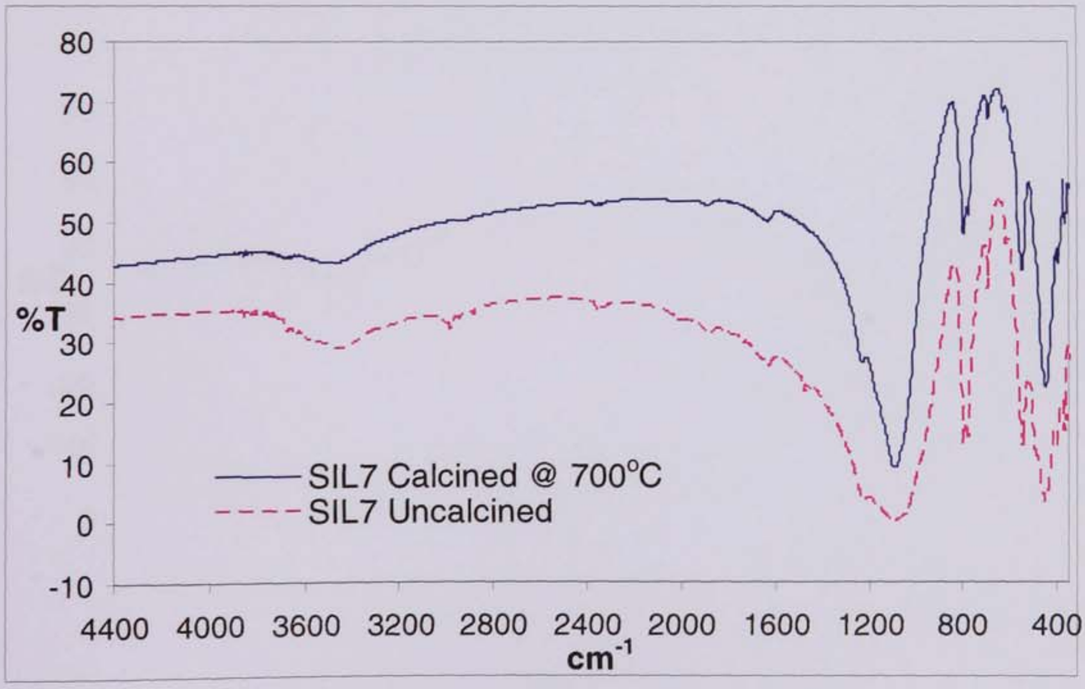

Figure C.8 FTIR spectrum of powder taken from sample SIL7. Experiment conducted at room temperature and atmospheric pressure.

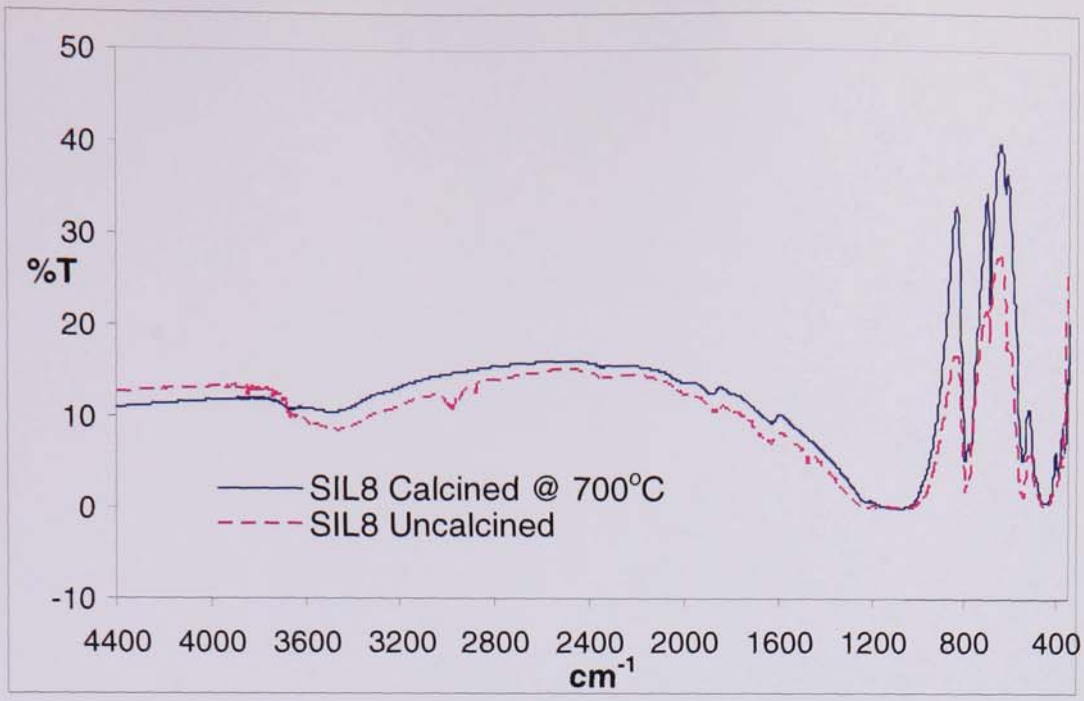

Figure C.9 FTIR spectrum of powder taken from sample SIL8. Experiment conducted at room temperature and atmospheric pressure.

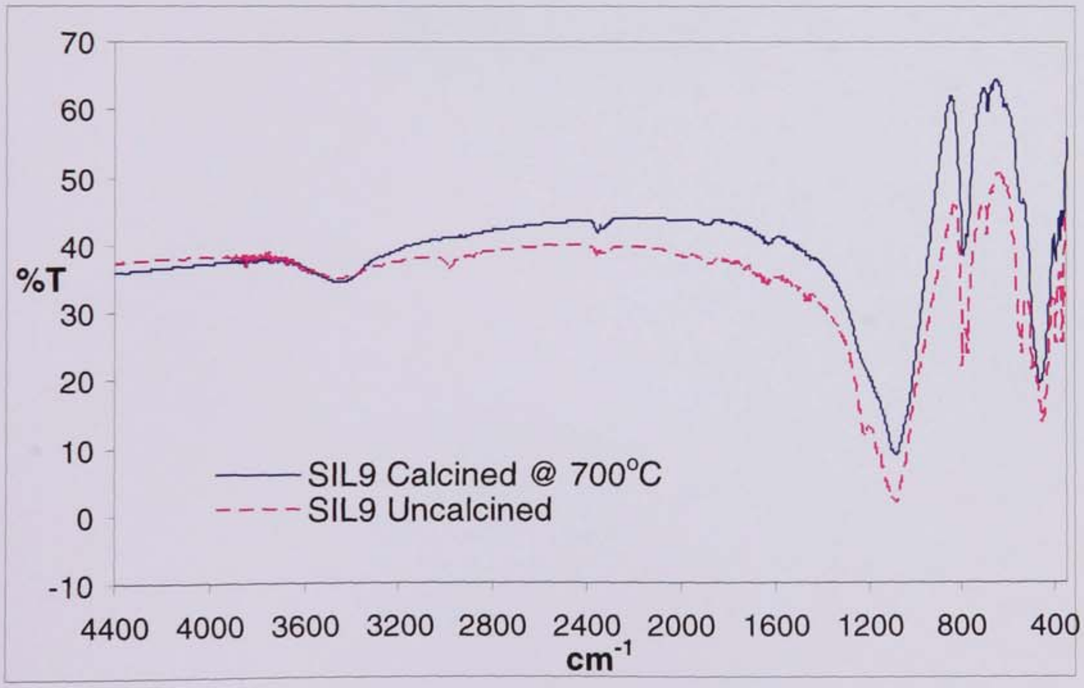

Figure C.10 FTIR spectrum of powder taken from sample SIL9. Experiment conducted at room temperature and atmospheric pressure.

Appendix D – Publications

The following is a list of publications that were produced during the course of this work.

I. Hussain and J.O. Titiloye., "Molecular Dynamics Simulations of the Adsorption and Diffusion Behaviour of Pure and Mixed Alkanes in Silicalite." Microporous and Mesoporous Materials., 85 (2005) 143–156.

I. Hussain and J.O. Titiloye., "Permeation and separation of light hydrocarbons through silicalite-1/carbon-graphite composite membranes" (Submitted).

Appendix E – Compact Disc (Containing Example Excel Spread Sheets)